Soil-structure interaction of horizontally loaded piled-raft foundations

Louw, Hendrik

Soil-structure interaction of horizontally loaded piled-raft foundations

Louw, Hendrik

A thesis submitted in partial fulfilment of the requirements for the degree of

PHILOSOPHIAE DOCTOR (CIVIL ENGINEERING)

in the

FACULTY OF ENGINEERING, BUILT-ENVIRONMENT AND INFORMATION TECHNOLOGY

UNIVERSITY OF PRETORIA

February 2024

Thesis summary

Soil-structure interaction of horizontally loaded piled-raft foundations

Louw, Hendrik

Supervisor:

Kearsley, Elsabe P.

Department:

Civil Engineering

University:

University of Pretoria

Degree:

Philosophiae Doctor (Civil

Engineering)

Wind turbine power generation has gained significant popularity over the past few decades as an option for cleaner energy production amidst growing climate change concerns. However, the design of a turbine's foundation, capable of supporting tall structures subject to large horizontal forces and overturning moments, remains challenging. The current focus with many new wind farm constructions is on taller wind towers, allowing for the same generation capacity from fewer wind turbines. Complex dynamic wind loading, which is amplified for taller wind turbines, and intricate soil-structure interaction between the foundation and the supporting soil require consideration to obtain foundation solutions that are both economical and sustainable.

Although raft foundations are preferred for supporting onshore wind turbines due to cost and ease of construction, many researchers have recently favoured the use of piled-raft foundations. Not only do these foundations adequately support wind turbines when these towers are constructed on less favourable soils, susceptible to large settlements or low bearing capacities, but they also provide a substantial and more economical solution for resisting the significant overturning moment acting on the foundation. Yet, the response of these support

structures is not well understood, especially considering that vertical loading is no longer the driving force in determining the size of these foundations, with loads dominated by the dominant horizontal load and overturning moment from the wind. Thus, given the increase in the dependency on these renewable energy structures and their size, the need to investigate this is important, given the strict design criteria and allowances.

In this thesis, a full-scale onshore wind turbine piled-raft foundation supporting a 117 m high wind turbine located on a newly constructed wind farm near Wesley in South Africa was instrumented and monitored for an extended period of time. The data presented includes those obtained during construction, turbine installation, and during turbine operation. In addition, finite element (FE) modelling was also conducted on piled-raft foundations under these unusual load combinations, considering soil-structure interaction and foundation rigidity. The full-scale testing showed that the foundation response was dominated by the dynamic horizontal load and overturning moment, compared to the vertical self-weight of the turbine, as expected, with the loads shared by both the raft and the piles. As the number of wind cycles increased, the results from the instrumented foundation socketed into bedrock indicated that a greater portion of the applied loads were distributed amongst the piles. Given the significant rigidity of the pile connecting raft, the response of the piles was dominated by the push-pull effect. Seasonal temperature changes also affect foundation response, which is usually neglected due to the foundations being buried. Additionally, from the FE modelling, apart from the soil-structure interaction concepts that were considered, the relative stiffness between the pile and the raft proved valuable towards analysing the rotational stiffness of the foundation for wind turbine application, also allowing for the potential axial forces in the trailing piles to be limited, given the large horizontal loads and the significant overturning moments.

Based on the responses observed from the full-scale testing and the results from the relevant FE models, it is clear that the upper limit has been reached regarding our current approaches to designing these foundations. In addition to the regular checks for restricting foundation settlement, differential settlement, horizontal displacement and meeting the minimum rotational stiffness requirements of the foundation, larger wind turbine models have presented additional critical design checks that cannot be ignored. These include the potential cracking of the raft under loading and the development of significant tensile forces in the trailing piles, both of which must be limited. Especially for larger turbine models, considering a balanced soil-structure interaction approach was shown to be beneficial. However, as mentioned previously, consideration should still be given to the constructability of these foundations, as larger foundations might result in more significant thermal gradients within the concrete section.

DECLARATION

I, the undersigned hereby declare that:

I understand what plagiarism is and I am aware of the University's policy in this regard;

The work contained in this thesis is my own original work;

I did not refer to work of current or previous students, lecture notes, handbooks or any other study material without proper referencing;

I have not allowed anyone to copy any part of my thesis;

I have not previously in its entirety or in part submitted this thesis at any university for a degree.

_____

Hendrik Louw

14303737

12 February 2024

ACKNOWLEDGEMENTS

TABLE OF CONTENTS

LIST OF TABLES

LIST OF FIGURES

xiii

xiv

LIST OF SYMBOLS

SYMBOL	DESCRIPTION	UNITS
A	Cross-sectional area	L^2
A_{eff}	Reduced foundation area between raft base and soil	L^2
A_t	Cross-sectional area of the bottom turbine tower section	L^2
B_r	Raft width (equal to $2R_r$ for a circular raft)	L
C_1	Coefficient of thermal expansion of the VWSG steel wire	$°C^{-1}$
C_2	Coefficient of thermal expansion of concrete	$°C^{-1}$
d_p	Pile diameter	L
E	Young's modulus	$M L^{-1} T^{-2}$
E_b	Young's modulus of the bearing stratum	$M L^{-1} T^{-2}$
E_p	Young's modulus of the pile	$M L^{-1} T^{-2}$
E_r	Young's modulus of the raft	$M L^{-1} T^{-2}$
E_s	Young's modulus of the soil	$M L^{-1} T^{-2}$
E_t	Young's modulus of the turbine tower	$M L^{-1} T^{-2}$
e	Load eccentricity between raft centre and load centre	L
e_{allow}	Allowable load eccentricity	L
F	Axial force	$M L T^{-2}$
F_{cr}	Critical column compressive force (Euler load)	$M L T^{-2}$
F_p	Axial force experienced by the pile/pile group	$M L T^{-2}$
$F_{p,max}$	Axial force experienced by the pile/pile group	$M L T^{-2}$
F_r	Axial force experienced by the raft	$M L T^{-2}$
F_{res}	Horizontal load acting through turbine rotor hub	$M L T^{-2}$
F_t	Axial force experienced by the turbine tower	$M L T^{-2}$
F_z	Vertical load from turbine self-weight	$M L T^{-2}$
G	Shear modulus of the soil	$M L^{-1} T^{-2}$
G_0	Small strain stiffness of the soil	$M L^{-1} T^{-2}$
g	Gravitational acceleration	$L T^{-2}$
H	Applied horizontal load	$M L T^{-2}$
h	Horizontal foundation displacement	L
h_h	Hub height	L
I	Second moment of area	L^4
I_p	Second moment of area of the pile	L^4
K_h	Horizontal foundation 'spring' stiffness	$M T^{-2}$
K_{ps}	Pile-soil stiffness ratio	-
K_R	Pile-flexibility factor	-
K_{rs}	Raft-soil stiffness ratio	-

K_v	Vertical foundation 'spring' stiffness	M T^{-2}
K_0	At-rest lateral earth pressure coefficient	-
K_θ	Rotational (rocking) foundation 'spring' stiffness	M L^2 T^{-2} rad^{-1}
$\overline{K}$	Member bending stiffness	M L^2 T^{-2}
k_p	Overall stiffness of the piled group	-
k_{pr}	Overall stiffness of the piled raft	-
k_r	Overall stiffness of the raft in isolation	-
L	Length	L
L_e	Effective column length	L
L_p	Pile length	L
L_r	Raft length	L
M	Applied bending moment	M L^2 T^{-2}
M_{crack}	Cracking moment	
M_p	Bending moment experienced by the pile	M L^2 T^{-2}
$M_{p,max}$	Maximum bending moment experienced by the pile	M L^2 T^{-2}
$M_{p,per}$	Permanent bending moment experienced by the pile	M L^2 T^{-2}
M_{res}	Bending moment at the base of the turbine tower	M L^2 T^{-2}
M_t	Bending moment experienced by the turbine tower	M L^2 T^{-2}
M_z	Torsional bending moment at the base of the turbine tower	M L^2 T^{-2}
n	Number of piles	-
q	Soil bearing pressure	M L^{-1} T^{-2}
R_d	Raft diameter	L
R_m	VWSG strain at any given time m	-
R_r	Raft radius	L
R_0	Initial VWSG strain	-
r	Radius of gyration	L
s	Pile spacing	L
T_m	VWSG temperature at any given time m	°C
T_0	Initial temperature at VWSG	°C
t_r	Raft thickness	L
u_x	x translational direction	-
u_y	y translational direction	-
u_z	z translational direction	-
V	Applied vertical load	M L T^{-2}
v	Vertical foundation settlement	L
v_{rd}	Raft differential settlement	L
v_{rh}	Raft horizontal displacement	L
v_{rv}	Raft vertical settlement/deflection	L
y	Distance from the neutral axis to extreme fibre of an area	L
Z_t	Sectional modulus of the bottom turbine tower section	L^3
α_{rp}	Interaction factor of the pile group on the raft	-

ΔF_p	Change in axial force	M L T^{-2}
ΔM_p	Change in bending moment	M L^2 T^{-2}
$\Delta\mu\varepsilon$	Change in strain	-
ε	Strain	-
$\varepsilon_{mechanical}$	Mechanical strain in concrete	-
$\varepsilon_{thermal}$	Thermal strain in concrete	-
$\varepsilon_1, \varepsilon_2$	Temperature-compensated strain at opposite ends of tower	-
θ	Angular foundation distortion	rad
θ_r	Rotation of raft pedestal	rad
v	Poisson's ratio	-
v_r	Poisson's ratio of the raft	-
v_s	Poisson's ratio of the soil	-
ρ	Density	M L^{-3}
$\Sigma\overline{K}$	Connection rotational stiffness	M L^2 T^{-2}
σ_{cr}	Critical column compressive stress (Euler stress)	M L^{-1} T^{-2}
σ	Stress	M L^{-1} T^{-2}
σ_r	Horizontal stress at the base of the raft	M L^{-1} T^{-2}
$\sigma_{r,max}$	Maximum horizontal stress at the base of the raft	M L^{-1} T^{-2}

LIST OF ABBREVIATIONS

ABBREVIATION	DESCRIPTION
APPRAF	Analysis of Piles and Piled Raft Foundations
B	Bottom
CSW	Continuous Surface Wave
C3D10	10-Noded Quadratic Tetrahedron
DOF	Degrees of Freedom
EPC	Engineering, Procurement and Construction
FBG	Fibre Bragg Grating
FE	Finite Element
L	Local Coordinate
LC	Load Centre
LVDT	Linear Variable Differential Transformer
P	Pile
PLF	Partial Load Factor
MPC	Multi-Point Constraint
M&O	Maintenance and Operations
R	Raft
Ra	Radial Direction
SC	Clayey Sand with Plastic Fines
SHM	Structural Health Monitoring
SLS	Serviceability Limit State
SPT	Standard Penetration Test
T	Top
Tr	Transverse Direction
ULS	Ultimate Limit State
USC	Unified Soil Classification
VWSG	Vibrating Wire Strain Gauge
W	Wind Turbine
WBSG	Wheatstone-Bridge Strain Gauge
WTG09	Wind Turbine Generator 09
1-D	One-Dimensional
2-D	Two-Dimensional
3-D	Three-Dimensional

1   INTRODUCTION

1.1   BACKGROUND

In many civil engineering structures, the governing force driving the design, selection and size of most structural foundations is vertical loading, primarily resulting from the self-weight of the structure and any imposed live loads, with limited consideration typically given to horizontal forces and its impact on the supporting foundation. Horizontal forces usually only become critical in areas where winds of significant magnitude and duration are present, or where structures are constructed in regions susceptible to earthquake activity. However, even in these areas, with the exception of tall and super-tall buildings, horizontal loading on structures is still considered modest compared to vertical loads, with the self-weight of the structure generally assisting in reducing its impact. This results in foundation design mainly focusing on the dominant static vertical load, simplifying the process to some extent.

The increased reliance on renewable energy alternatives to combat climate change challenges is a rising trend globally. Wind energy power generation, both onshore and offshore, has especially gained popularity within this field, with South Africa investing heavily in the onshore technology market (Wojtowitz & Foster, 2020). Over the years, wind turbine design has substantially changed to reduce cost and maximise performance, which has been met with wind turbines increasing in height, blade size and power rating, seeking steadier wind at higher elevations whilst capturing more wind with longer blade lengths. This results in fewer wind turbines to satisfy the electricity demand, effectively reducing the costs of purchasing and installing these structures. Yet, the vertical load and the already dominating horizontal load and overturning moment, caused by the wind, acting on these foundations increase significantly that needs to be accounted for.

For years, designing the foundations for supporting these dynamically sensitive structures has been based on simplified and semi-empirical methods not initially developed for wind turbine application, raising several concerns given modern technologies, developments, and computational power. Therefore, with the increase in popularity of these structures, the need to reconsider how we design these foundations economically and efficiently is important. Generally, conventional raft foundations are preferred for supporting onshore wind turbines as the science is well-established, and the construction is more straightforward. However, with the increase in wind turbine heights, foundation designs are drawn towards deep foundations, including piled-raft foundations, as they provide multiple benefits towards load-sharing capacity, settlement reduction and foundation stiffness, with researchers also claiming that it proves a more economical use of material in resisting the overturning moment from the

turbine (Burton *et al.*, 2011; Knappett & Craig, 2012). However, the current understanding of how these foundations respond, as well as interact with the soils supporting them, under dominant horizontal loads and overturning moments is limited.

It is well-known that any foundation's response depends on soil-structure interaction, and the relative stiffness between the foundation and the soil, with the use of soil-structure interaction principles in modern design on any structure proving advantageous (Morgan & Ntambakwa, 2008; Reese & Wang, 2008). Apart from raft foundations, where only the raft-soil interaction is considered, soil-structure interaction is slightly more complicated concerning piled-raft foundations, with the inclusion of piles creating additional concerns and complications in design that need to be accounted for. Raft-pile, pile-pile and pile-soil interaction all play a crucial role in the response of these foundations, regardless of the load combinations, making for a complex foundation problem, which, in the case of wind turbines, have to adhere to strict design criteria to ensure a safe and stable structure. Due to the limited research available, particularly concerning soil-structure interaction, and the lack of full-scale instrumentation and testing on these foundations, designs of these support structures still tend to be conservative, resulting in uneconomical structures that are not sustainable. In addition, many of the design approaches that utilise these principles, primarily focus on the soil component of the soil-structure interaction problem, assuming that the foundation is rigid. Little consideration is typically given to the flexibility of the foundation, and how it potentially affects the overall response of the foundation-soil system, which can be problematic, especially considering that most foundation are constructed from reinforced concrete, a highly non-linear material, that experiences a reduction in stiffness after cracking. Thus, given the increased size of wind turbine models, the need arises to physically determine the effect of dominant horizontal loads and overturning moments on the response of piled-raft foundation systems, also considering how soil-structure interaction influences foundation rigidity and response when exposed to these load combinations.

1.2   OBJECTIVES

The main focus of this thesis was to investigate the response of piled-raft foundations supporting onshore wind turbines where horizontal loads and overturning moments have a substantially larger impact on the foundation than vertical loading. Due to several advantages, these foundations have gained significant popularity recently, especially when turbine structures are to be constructed on soils susceptible to settlements exceeding serviceability limit state conditions, potentially affecting turbine stability (Burton *et al.*, 2011; Wojtowitz & Foster, 2020). However, the true foundation response from wind loading and the effect of pile inclusion on foundation stiffness is not necessarily well understood, resulting in conservative

and uneconomical support structures. This led to the research question of whether the conventional soil-structure interaction models used for analysing and predicting piled-raft foundation response under vertical loading are still relevant when horizontal loading and overturning moments become the dominant foundation actions (for example, in the case of wind turbines).

The primary objectives of the study included:

- establishing the current assumptions regarding the design of onshore wind turbine foundations with emphasis on piled rafts in particular;
- determining the actual response of an in-service piled-raft foundation supporting an onshore wind turbine;
- establishing the limits to current wind turbine foundation size and design models, including wind turbine sizes; and,
- identifying any critical foundation responses under wind turbine loading, especially in light of future larger wind turbine models.

The secondary objectives of the study include providing recommendations for engineers when designing foundations for onshore wind turbines comprising piled rafts and turbine models increasing in size.

1.3   SCOPE OF STUDY

In this study the response of piled-raft foundations for onshore wind turbine applications was investigated. The scope of the study was restricted to reinforced-concrete foundations constructed on dense silty-sand soil, having a circular raft and piles, with the water table located well below the foundation and piles resting on bedrock (socketed). The study was primarily based on full-scale site measurements taken from a newly constructed wind turbine foundation in South Africa. Numerical finite element (FE) modelling followed to further investigate the research objectives, evaluating the response of piled-raft foundations to varying serviceability limit state (SLS) load conditions, foundation size and soil properties.

The scope of the study was limited in the following ways:

- For the full-scale testing:
  - A single piled-raft foundation was instrumented and monitored for an extended period of time.
  - Only static foundation monitoring was considered when full-scale site measurements were taken. Dynamic load effects on the external wind turbine structures and foundation were not investigated.

o Torsional forces and moments present in the wind turbine tower structures and how they potentially affect foundation response did not form part of this study.

o The fatigue behaviour of the concrete foundation under repeated cyclic loading caused by the wind fell outside the scope of the study.

- For the FE modelling and recommendations set for designers:

o The radius of the circular raft varied between 5.5 m and 15 m.

o Only raft thicknesses between 0.7 m and 3 m were considered.

o The Young's modulus of the soil was varied between 10 MPa and 450 MPa.

o Given that the piles are socketed, only two pile lengths, or two compressible soil layer depths, were considered, namely 10 m and 20 m, with the diameters of the piles varying between 600 mm and 1200 mm.

o The study was restricted to 10 piles spaced equally towards the outer edge of the circular raft.

1.4 METHODOLOGY

The methodology followed in this thesis is described below and was based on addressing the study objectives set out in Section 1.2.

- To establish the current assumptions regarding the design of onshore wind turbine foundations comprising piled rafts, a literature study was conducted, focusing on wind turbines and establishing the factors driving the design and selection of the foundations supporting them. These discussions included wind turbine loading and future wind industry prospects, including how these prospects and the cyclic nature of the loading influence foundation response. As the response of any foundation is governed by soil-structure interaction and foundation rigidity, a great deal of the literature was focused on exploring these interactions, especially for piled-raft foundations under dominant horizontal loads and overturning moments. Research specific to previously instrumented onshore wind turbine foundations was also addressed, as well as numerical work, including FE modelling.

- Determining the actual response of an in-service piled-raft foundation supporting an onshore wind turbine, a full-scale wind turbine foundation was instrumented and monitored on a newly constructed wind farm in South Africa. The foundation was monitored for a period of 33 months and included responses during foundation casting and construction, during turbine installation and during turbine operations. Careful design of the experimental work was required before the installation

commenced to ensure an effective foundation monitoring system. The instrumentation design included the following:

- o instrument selection based on ease of installation and durability due to time constraints and casting environments during construction;
- o instrument placement according to recommendations from the literature and preliminary FE modelling; and,
- o selection of long-term remote monitoring and logging infrastructure.

- Numerical FE work was undertaken to establish the current limits on wind turbine foundation design and turbine sizes, identifying any critical foundation responses for larger wind turbine models. This also allowed for the soil-structure interaction and relative stiffness concepts to be further explored, enabling a list of recommendations to be compiled for engineers to design piled-raft foundations for larger turbine models. The numerical work was carried out by:
  - o setting up a representative FE model of a piled-raft foundation and supporting soil in Abaqus based on published models and recommendations found in the literature;
  - o calibrating and comparing the model outputs against known responses obtained from the full-scale instrumented foundation measured during the experimental work and;
  - o conducting a parametric study using the calibrated model investigating the influence of foundation size, soil properties and load magnitude of the response of these foundations under loading.

1.5   ORGANISATION OF REPORT

The thesis consists of the following chapters:

- Chapter 1 serves as an introduction to the thesis, describing the background, objectives, scope, and methodology of both the experimental and numerical work undertaken for this thesis.
- Chapter 2 contains a technical introduction based on a literature study. Relevant literature can be found in this chapter that supports the experimental and numerical work and aids in all discussions.
- In Chapter 3, the experimental work conducted for this thesis is presented, describing the instrumentation and monitoring system installed on a newly constructed full-scale onshore wind turbine and supporting piled-raft foundation. Measured concrete and soil properties are also included, as well as all the physical measurements taken from the foundation and wind turbine structure over two years during different phases.

These phases included the foundation's construction, wind turbine installation and commercial operation.

- Chapter 4 contains the appropriate steps for setting up a comprehensive and representative FE model of a piled-raft foundation and supporting soil, with the foundation subjected to dominant horizontal loads and overturning moments as with wind turbines. The chapter also calibrates the developed FE model against the full-scale site measurements presented in Chapter 3.

- In Chapter 5, a parametric study was conducted using the developed FE model in Chapter 4 to determine the pile-raft-soil system's response by varying the supporting soil's properties, the size of the two foundation components, and the magnitude of the applied loads and moments. This chapter aimed to build on the experimental responses presented in Chapter 3, investigating alternative scenarios.

- In Chapter 6, relative stiffness and pile-raft-soil interaction concepts were explored and discussed, investigating wind turbine foundation design criteria under serviceability limit state conditions. This investigation was based on some of the results presented in Chapter 5 when the parametric study was conducted.

- Chapter 7 contains the conclusions and recommendations of the study.

- References contain all source material accompanying the research.

- The Appendix contains information supporting the experimental work and full-scale measurements presented in Chapter 3.

2 LITERATURE REVIEW

2.1 INTRODUCTION

Wind energy power generation, both onshore and offshore, is a fast-growing industry that has, over the last 30 years, become a mainstream source of electricity generation globally in light of growing climate change concerns. According to Wiser & Bolinger (2011), by the end of 2010, roughly 2% of the world's electricity contribution came from wind, with GWEC (2022) later reporting that this number increased to about 9% in 2022. With the evolution of modern technology and the development of stronger, more durable materials, wind turbine manufacturers have, over the years, substantially changed and improved the design of their turbines to reduce costs and maximise performance and efficiency, resulting in wind turbines becoming a more viable and competitive option for electricity generation. These improvements have, however, been met by increasing turbine height, blade size and power rating, seeking steadier, more consistent winds at higher heights while harvesting more wind with longer blade lengths, even at lower wind speeds. Thus, given the increase in the demand for these renewable energy technologies, both locally and internationally, and the growing sizes of wind turbines, the need to understand these complex dynamic structures and the foundations supporting them is a subject of great importance (Bu, 2005).

Following in the footsteps of other developed nations, South Africa has started investing heavily in onshore wind turbine technologies to reduce carbon dioxide emissions, as about 90% of the country's electricity generation currently comes from burning fossil fuels. Only 2.5% of electricity is generated from the wind (GWEC, 2022), with the remaining 7.5% generated from solar farms, nuclear power plants and hydropower plants. Over 30 onshore wind farms have been erected in parts of South Africa, with this number set to grow significantly in the coming years, given the country's rapid population growth. The future focus with these wind farms is on taller wind turbines, effectively requiring fewer structures to deliver the same electricity output, ultimately reducing purchasing costs and infrastructure investment (Wojtowitz & Foster, 2020). However, simultaneously placing enormous pressure on the foundations supporting them.

Generally, onshore wind turbines are either supported by a raft or piled foundation, with the geotechnical properties and depth of the supporting soil or rock being the deciding factors. Although raft foundations are preferred primarily due to cost and ease of construction (DNV/RisØ, 2002; Wojtowitz & Foster, 2020), piled foundations are selected only when concerns regarding the bearing capacity of the supporting soil and excessive settlement arise.

However, some literature has indicated the benefits of using piles over a conventional raft for larger turbine structures (Burton *et al.*, 2011). Limited research and instrumentation have been conducted on full-scale onshore wind turbine foundations, especially piled foundations, resulting in the designs of these support structures being conservative, relying on simplified and semi-empirical numerical models not initially developed for wind turbine application. Given the increase in the size of wind turbines, Morgan & Ntambakwa (2008) and Reese & Wang (2008) also argued that the conventional simplified way of design, not utilising modern technologies of soil-structure interaction concepts, would result in inefficient and uneconomical foundations. Additionally, wind turbine foundations are susceptible to loads, design criteria and tolerances, unlike those typically encountered when designing foundations for large buildings and structures that fall outside the scope of general design codes (Morgan & Ntambakwa, 2008). The main difference lies in the magnitude and the dynamic nature of the horizontal shear load and overturning moment caused by the wind being the driving force in determining the size of foundations, compared to the self-weight, which is usually only a fraction of that. With the focus on taller wind turbines, an increase in the vertical and especially the horizontal loads and overturning moments acting on turbine foundations are to be expected and needs to be sufficiently supported, with Shrestha *et al.* (2018) mentioning that wind energy is directly proportional to wind speed cubed, which substantially affects the magnitude of the loads applied to the underlying foundation. The main aim of this literature review is to examine piled foundations, in particular piled rafts, for supporting onshore wind turbines, investigating the mechanisms associated with analysing these support structures under loading, observing typical responses, and focusing on soil-structure interaction as this governs behaviour, with the effect of increased turbine sizes also being on the forefront.

In the first section of the literature review, a brief background is given on wind turbines and wind turbine foundations, introducing the different types of foundations and discussing the main aspects that concern wind turbine foundation design. With the focus being on piled-raft foundations and soil-structure interaction concepts, the principles and typical responses of these foundations under loading are discussed, highlighting the relative stiffness concepts, including load transfer and distribution, and the various analysis models used in history. Discussions regarding end-bearing piles are also provided, as the study is limited to piles socketed in bedrock. Additionally, this section summarises and considers modern finite element (FE) models of piled-raft foundations. The discussion regarding FE modelling pivots around model sizes, elements and material behaviour, as well as how to realistically capture the interaction characteristics between the foundation and the soil of this complex three-dimensional (3-D) problem. In light of the similarities between piled-raft foundations and portal frames, the relative stiffness between the different foundation components (between the

raft and connecting piles) was further explored by considering structural analysis concepts and moment distribution theories. In addition, as wind turbine foundations are susceptible to dynamic horizontal loads and overturning moments, the cyclic response of piled-raft foundations and their interaction with the surrounding soil was also considered, looking at scaled models in the geotechnical centrifuge. The chapter concludes with a section that discusses past structural health monitoring (SHM) projects of wind turbine foundations, as a large portion of the thesis is centred around SHM, highlighting any shortcomings, followed by a short discussion on the thermal conductivity of soils.

2.2   WIND TURBINES AND SUPPORTING FOUNDATIONS

2.2.1   Wind turbine terminology and foundation types

Understanding the mechanisms driving the design of wind turbine foundations is critical to the stability of turbines and ensuring the long-term durability of foundations under the large number of load cycles imposed by the wind. However, before dealing with these mechanisms for onshore wind turbine foundations, it is worthwhile first introducing the various components that make up a wind turbine system as a whole, as it will be helpful with discussions and explanations in the remainder of this document. An onshore wind turbine system can broadly be classified into two parts: the superstructure, or wind turbine, visible above the ground and responsible for electricity generation, and the substructure, or foundation, typically located below the ground surface, responsible for turbine support and stability (see **Figure 2-1**). The wind turbine comprises a tower, rotor hub, nacelle, drive train and rotor blades, with the most common wind turbine having three blades. Apart from the turbines' power rating, general terms such as hub height and rotor diameter, highlighted in bold in **Figure 2-1**, typically describe a wind turbine's size and ultimately determine the magnitude of loading exerted on the foundation. Hub height refers to the distance from the base of the turbine tower to the position of the rotor hub, whereby rotor diameter refers to the diameter in which the blades rotate around the central rotor hub and is roughly twice the length of a rotor blade.

In terms of the substructure, or foundation, for onshore wind turbines, these foundations typically consist of a raft (gravity-base) or piled foundation constructed from reinforced concrete (see **Figure 2-2**). The only difference between the two foundations is the inclusion of piles, with the selection depending not only on the geotechnical and environmental conditions at the wind turbine location (Burton *et al.*, 2011; Cools, 2015; Wymore *et al.*, 2015), but also on the magnitude of the loading at the foundation level under extreme wind conditions (Burton *et al.*, 2011). According to DNV/RisØ (2002) and Wojtowitz & Foster

(2020), raft foundations are preferred due to the ease of construction and standardisation across the entire farm (using a single design for the whole farm), ultimately saving construction costs and time. However, this is only possible if competent soil exists near the soil surface, having sufficient bearing capacity to sustain the applied loads without excessive settlement and foundation rotation. Piled foundations are typically only introduced for either one of two reasons. First, the topsoil is softer, with loads exceeding the soil's bearing capacity, thus having to be transferred to deeper depths (DNV/RisØ, 2002; Bu, 2005). The second reason is that the foundation suffers large settlements under loading even if the soil has adequate bearing capacity under the raft, with piles typically extending to the rock socket (Wojtowitz & Foster, 2020). However, where depth for piling is sufficient, both Burton *et al.* (2011) and Knappett & Craig (2012) have mentioned the benefit of using piled foundations rather than the conventional raft foundations for larger turbine models due to the more efficient use of materials in resisting the applied moment (discussed in Section 2.2.4). Similarly, Poulos (2016) also indicated this about tall buildings, mentioning that as modern buildings increase in height, horizontal loads and moments will not be adequately resisted by only rafts.
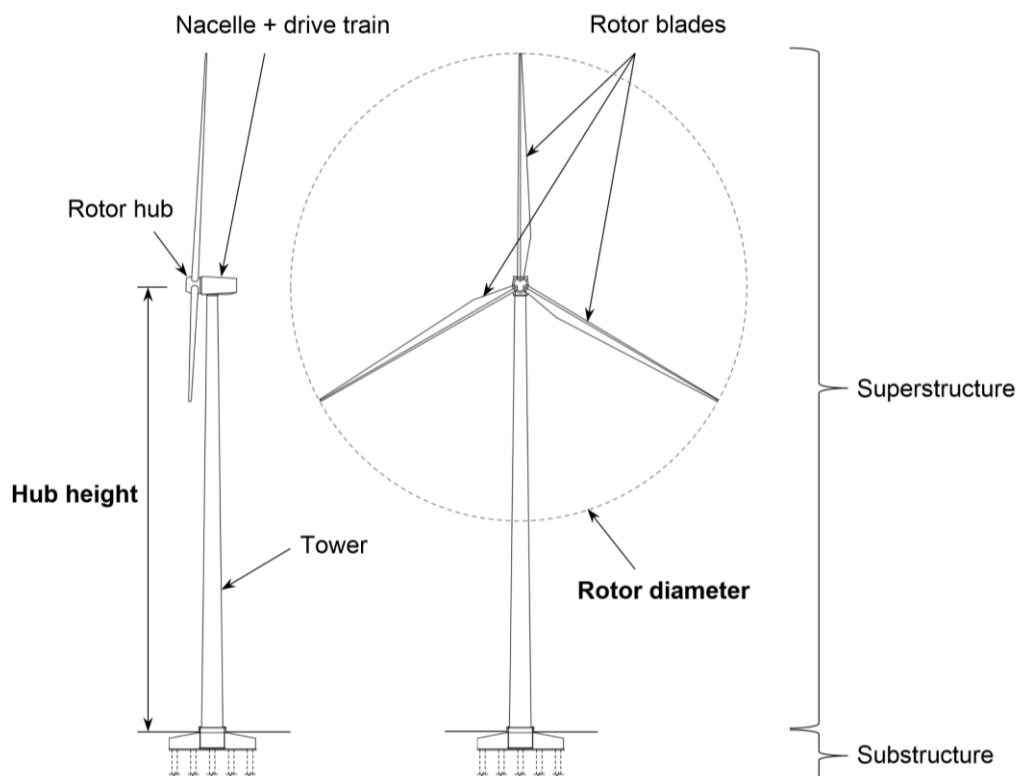
Figure 2-1: Superstructure components of a wind turbine system

As illustrated in **Figure 2-2** for both foundation types, a pedestal usually extends from the top of the raft to which the wind turbine is connected using either an anchor cage (ring of bolts) or, in some turbine models, an embedment can (Currie *et al.*, 2013). The anchor connection

comprises bolts attached to the flange at the base of the wind turbine tower, with the bolts extending the thickness of the raft that is terminated in the mass of the reinforced concrete foundation using a steel ring plate, washers and nuts (ASCE/AWEA RP2011). Alternatively, an embedment can connection comprises a short tower section cast into the reinforced-concrete foundation, which is then bolted to the remainder of the tower through a conventional flange-to-flange link.
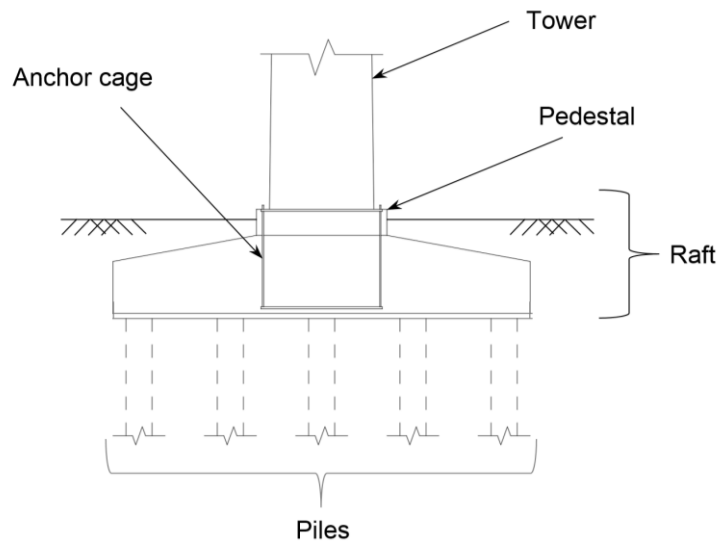
Figure 2-2: Substructure components of a wind turbine system

Foundations are typically either octagonal or circular in shape, with Mawer & Kalumba (2016) indicating that circular foundations are generally preferred since wind turbine rotors can rotate around the tower axis to account for changing wind directions. However, some literature has indicated the popularity of using an octagonal shape foundation due to the ease of removing shuttering. Foundation diameters typically range between 16 m and 20 m for smaller turbine units, increasing to 23.5 m for larger turbines (Tinjum & Christensen, 2011; Wojtowitz & Foster, 2020; Yilmaz *et al.*, 2022). However, it should be highlighted that these sizes depend mainly on the geotechnical site conditions and the magnitude of the loads applied to the foundation.

2.2.2 Future wind turbine prospects

Over the years, wind turbine manufacturers have improved designs to reduce costs and maximise turbine performance, developing more advanced turbine components that result in greater efficiency and reduced generation losses (Lantz *et al.,* 2012). However, these improvements have been met with wind turbines increasing in height, size and power rating, seeking steadier, more consistent wind sources at higher hub heights, with larger rotor diameters also allowing for turbine electricity generation capacity to be increased. **Figure 2-3**

illustrates the growth of wind turbine hub heights in history from 1980 to 2010, as presented by Lantz *et al.* (2012), also showing the increase in the rotor diameter and corresponding electricity generation capacity of turbines. Although the appropriate selection of wind turbine size is site-specific, future planned installations, particularly in South Africa, are focused on hub heights exceeding 130 m (see **Figure 2-3**), with rotor diameters over 145 m and a generation capacity of between 4 MW to 5 MW per turbine (Wojtowitz & Foster, 2020; REVE, 2023). It should be emphasised that this places enormous pressure on engineers to design efficient foundations to accommodate these increased loadings, raising the need to understand the complex mechanisms involved with wind turbine loading on supporting foundations.
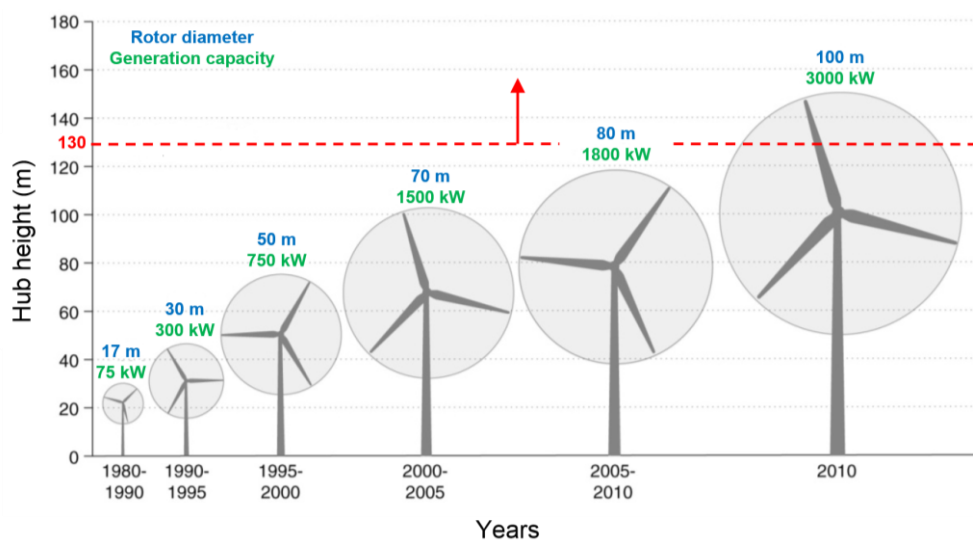
Figure 2-3: Approximate wind turbine sizes from 1980 to 2010 (adapted from Lantz *et al.,* 2012)

2.2.3 Wind turbine foundation loading

Apart from the vertical self-weight of a wind turbine structure and its various mechanical components, wind turbine foundation design is primarily driven by aerodynamic forces caused by the wind interacting with the turbine tower and rotor blades. The magnitude and intensity of these aerodynamic forces typically depend, amongst others, on the wind speed, turbulence in the airflow, the rotational speed of the rotor, air density, the shape of the rotor blades, and interactive effects between the rotor blades and the airflow, such as drag (DNV/RisØ, 2002). Since wind turbines are both dynamically sensitive and complex structures, for foundation design purposes, loads are generally simplified into four static load types (two forces and two moments), generated by both gravity and the wind acting on the external wind turbine structure. The direction of these loads and moments is indicated in **Figure 2-4** as presented by ASCE/AWEA RP2011. F_{res} refers to the horizontal load acting through the turbine rotor hub caused by aerodynamic forces. F_z is the vertical downward load

consisting of the self-weight of the wind turbine and wind turbine components. M_{res} is the corresponding moment at the base of the tower caused by F_{res} acting at the rotor hub (turbine hub height), and M_z is an additional torsional moment caused by the rotation of the turbine itself. Although these loads and moments are specified as static by the wind turbine manufacturers for design purposes, dynamic load effects must still be considered. More on this will be presented in Section 2.2.4 regarding the wind turbine system's natural frequency and the foundation's rotational stiffness.
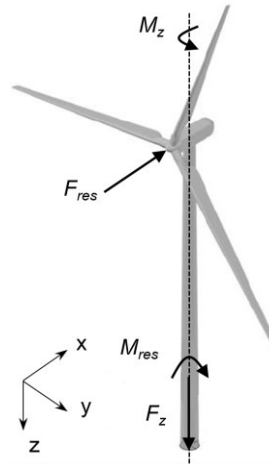
Figure 2-4: Typical loads on wind turbine structures (adapted from ASCE/AWEA RP2011)

The magnitude of the loads and moments are usually site and turbine-specific, with the design values provided by the turbine manufacturers considering different load cases. These load cases include serviceability (SLS) and ultimate limit state (ULS) load conditions for either normal or extreme operation scenarios, also considering additional crucial events such as if the turbine is parked or during start-up and shutdown. For this thesis in particular, the focus will only be on SLS conditions, with the difference between SLS and ULS simply being the application of a partial load factor (PLF). **Table 2-1**, although limited, indicates approximate SLS and ULS load values found in the literature and is included to give a rough indication of the loads and moments expected at the foundation level for different turbine sizes and hub heights. However, as mentioned, hub height is not the only contributing factor to load and moment magnitude but was considered to be for discussion purposes. Additionally, **Figure 2-5(a)** and **(b)** illustrate the relationship between hub height and the overturning moment at the foundation level, as well as the relationship between turbine power rating and the same overturning moment, respectively, with the overturning moment determined from the maximum operating wind speed of each tur. This information was presented by Cools (2015) and is based on technical data from various wind turbine models, with both figures indicating a reasonably linear relationship concerning the applied overturning moment. The significant variation in the data investigating the influence of hub height on the overturning moment,

Cools (2015) argued, could be attributed to the difference in power ratings of the wind turbines, where the variation in data investigating the influence of power rating could be attributed to the differences in hub heights. These turbines might have varying self-weights that ultimately affect the magnitude of the moments at the structure's base.
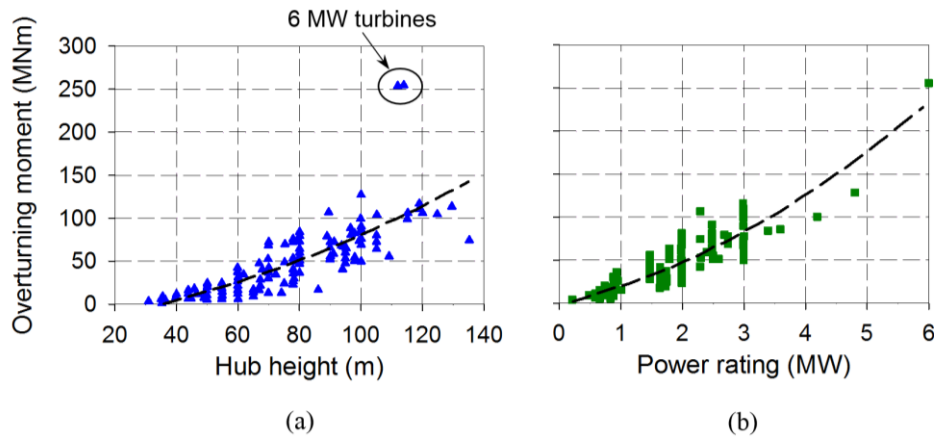
Figure 2-5: Relationship between tower base overturning moment and (a) turbine hub height; (b) turbine power rating (adapted from Cools, 2015)

Bu (2005) and Reese & Wang (2008) indicated that gravity (F_z) is typically modest compared to the loads from the wind, as seen in **Table 2-1**, and thus not the driving force in foundation design. Higher wind turbines resulted in larger vertical loads and significantly larger horizontal loads and overturning moments, which, as mentioned, places enormous pressure on engineers to design adequate foundations to support these loads. Although F_{res} is dependent on wind speed, upon observation, these loads at the SLS and normal ULS conditions amount to about 10% of the self-weight of the turbine structure, with the value increasing to about 20% under extreme ULS conditions. Compared to M_{res}, M_z is substantially smaller and, as Bu (2005) indicated, practically negligible under service and normal operating conditions. Thus, M_z will not be considered in the remainder of this study.

Table 2-1: Typical wind turbine foundation loads for different hub heights found in literature

Turbine hub height (m)	F_z (kN)	F_{res} (kN)	F_{res}/F_z (%)	M_{res} (kNm)	M_z (kNm)	SLS or ULS	Reference
80	1256	289	23	20250	-	ULS (extreme)	Reese & Wang (2008)
80	3510	482	14	35108	303	SLS	Mohamed & Austrell (2018)
	3510	797	23	63825	1642	ULS (normal)	
94	4620	554	12	49100	731	SLS	Mawer *et al.* (2017)
	4590	695	15	66700	353	ULS (normal)	
	4500	1031	23	85100	1551	ULS (extreme)	
-	1800-2000	-	-	25000-80000	-	-	Yilmaz *et al.* (2022)

2.2.4   Wind turbine foundation design and design criteria

Wind turbines constitute a particular type of structure that strongly depends on the efficiency of the foundation system (Pham *et al.*, 2018). This dependency is a consequence of the extremely high levels of eccentricity generated at the base of the tower, resulting from the uncommon combination of high flexural moment and relatively low vertical forces. Due to the unique loading characteristics under which wind turbine foundations operate and the variety of soil conditions within the optimal wind farm location corridors, Cools (2015) and Mawer & Kalumba (2016) indicated that designing efficient foundations for these structures poses several complex challenges. Upon the successful selection of the type and shape of the foundation, numerous design criteria need to be considered to ensure a foundation that has sufficient stability and strength. According to ASCE/AWEA RP2011 and Bu (2005), this process revolves around checks for ULS conditions, SLS conditions and, due to the cyclic nature of the loading, fatigue limit state conditions, addressing all geotechnical issues that may arise. Although the thesis focuses on piled-raft foundations, the principles for designing and analysing raft foundations are also included, as they are valuable to overall discussions.

Depending on whether the foundation consists of a raft or a piled raft (piles with a ground-connecting pile cap), ULS checks are based on how the foundation involved resists the applied overturning moment. A raft foundation alone relies on the weight of the wind turbine structure, the concrete footing and the overburden soil to resist the applied moment with checks including stability against overturning, sliding and soil bearing capacity (Bu, 2005; ASCE/AWEA RP2011; Burton *et al.*, 2011). Stability calculations against overturning and sliding are usually carried out to ensure a minimum factor of safety of 1.5 (ASCE/AWEA RP2011). In addition, the bearing capacity of the soil is checked on a reduced foundation area using Meyerhof's effective area method, as indicated by DNV/RisØ (2002) (see **Figure 2-6**). This method assumes a reduced area (A_{eff}) between the base of the raft and the supporting soil, adopting the theory that the overturning moment acting on the foundation causes the vertical load applied through the centre of the raft to work eccentrically (e) through the load centre (LC), which is also indicated in **Figure 2-6**. Thus, e is calculated by dividing M_{res} by the sum of the vertical weight of the wind turbine, concrete raft footing, and the overburden soil, with the uniformly distributed ellipse-shaped reduced area, then resisting the vertical load. Allowable eccentricities (e_{allow}) are usually considered less than $B_r/6$, with anything larger potentially causing an uplift at the foundation's edge, also called gapping, with B_r referring to the width of the raft and is taken as $2R_r$ (two times the raft radius) in the case of a circular raft. Given the significant rise in the size of wind turbines and the magnitude of the

overturning moment acting on the foundation, the risk of e becoming significantly larger increases, dictating the need for more significant foundation sizes.
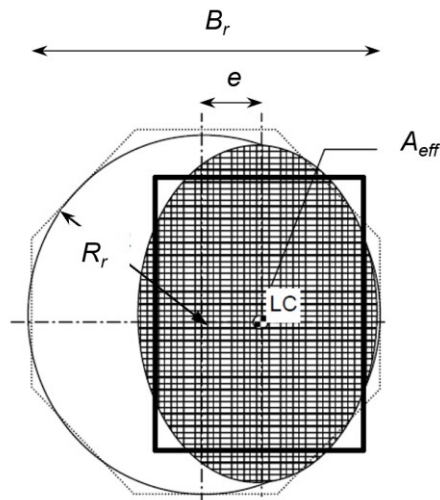
Figure 2-6: Effective foundation area – bearing capacity calculations (adapted from DNV/RisØ, 2002)

In some circumstances, providing a raft foundation as a solution requires a diameter of significant magnitude and volume to meet bearing capacity and stability requirements. Morgan & Ntambakwa (2008) argued that this is not necessarily logical, economical or efficient, especially considering the additional problems encountered when casting such sizeable concrete masses. They highlighted two of the biggest concerns are the practical limits of concrete placement (lengthy concrete pours) and thermal cracking caused by heat of hydration. Regarding thermal cracking, DNV/RisØ (2002) has indicated that, to minimise this risk, concrete temperatures may not exceed 70ºC during curing and differences in temperatures must be minimised, indicating that temperature differences greater than 12ºC to 15ºC are generally not allowed. Also suggested by Knappett & Craig (2012), simply increasing the plan area or thickness of the raft would help, but it is not always the most economical option and is sometimes difficult to construct. However, if the soil depth allows, Burton *et al.* (2011) and Knappett & Craig (2012) mentioned that a more attractive alternative would be to use a piled raft rather than just a raft, as it makes for more efficient use of materials to resist, in this case, the applied overturning moment, which is the main aim of this research.

A piled foundation uses axial friction, end-bearing resistance, and lateral earth pressure resistance to counteract the applied overturning moment (Morgan & Ntambakwa, 2008), with piles generally located towards the perimeter of the pile cap. Thus, the axial and lateral capacity of piles is usually checked under ULS conditions with the assumption that the piles carry all the loads and the raft (or pile cap) only acts as a connection between the wind turbine

and the piles. This is a reasonably conservative design approach, however, not considering the contribution of the ground-contacting pile cap, with the foundation then referred to as a piled-raft foundation, in carrying the applied loads and moments could, in some instances, be uneconomic (Burland *et al.*, 1977). Although generally not included in calculations, DNV/RisØ (2002) highlighted that it should still be appreciated how the superstructure, in this case, the wind turbine, connects to the supporting piles, i.e. the pile cap, as this largely influences the distribution of loads between the piles in the group and affects the overall stiffness of the foundation. Burton *et al.* (2011) later also mentioned that the lateral loads in the piles result from the moment acting at the head of each pile. Thus, full moment continuity between the piles and pile cap is required (concerning the relative stiffness between the pile and the pile cap). Both DNV/RisØ (2002) and Burton *et al.* (2011) highlighted the pile cap's importance in the overall foundation's response and can, therefore, not be neglected. The general assumption in practice is that piles are rigidly fixed to the wind turbine, thus having a relatively rigid pile cap connecting the piles to the wind turbine. The author, however, questions this assumption, which will be discussed in detail in the following paragraphs.

Regarding piled foundations, additional conditions should also be considered. As indicated by several researchers (DNV/RisØ, 2002; Bu, 2005; Reese & Wang, 2008; ASCE/AWEA RP2011, Burton *et al.*, 2011), axial and lateral capacity checks should also include group effects, referred to as pile-to-pile interaction, as this could potentially reduce the contribution of each pile in the overall resistance of the group or can lead to larger settlements. Novak & Sheta (1982) have raised concerns regarding dynamic pile group effects and how they differ from static pile group effects. However, Bu (2005) and Reese & Wang (2008) have indicated that although wind turbines are dynamic structures, the natural frequency of these turbines is in the lower range, which results in static pile group effects considered sufficient for practice.

Lateral soil resistance on embedded caps can also be included in calculations but is not usually taken into account because these soils can potentially be removed. Under the applied overturning moment, piles on the leading end (leeward side) of the foundation will experience an increased compression force (initial compression due to the self-weight of the wind turbine and connecting pile cap). In addition, piles on the trailing end (windward side) of the foundation will experience a reduced compression force (see **Figure 2-7**), with the combined action known as the push-pull effect. Although ASCE/AWEA RP2011 specifies that no tension is allowed within piles, the risk of tension forces developing within the trailing piles increases as turbine sizes increase. Furthermore, although the bearing capacity under the pile cap is not included in calculations, Wojtowitz & Foster (2020) argued that the diameter of the pile cap cannot be too small as it will also increase the risk of large tensile forces developing in the piles. Thus, a balanced optimisation between pile cap diameter and resultant tension

forces within the piles should be considered in the design. It should be highlighted that the severity of the push-pull effect of the piles under the applied moment is also highly dependent on the rigidity of the raft (pile cap), which affects the amount of rotation possible at the pile-raft interface. More on this will be discussed in Sections 2.3 and 2.4, respectively. The fatigue behaviour of the raft and piles should also be considered under ULS and fatigue limit state requirements (Zeevaert, 1991; ASCE/AWEA RP2011; Wojtowitz & Foster, 2020). However, this does not form part of this thesis and will not be further discussed.
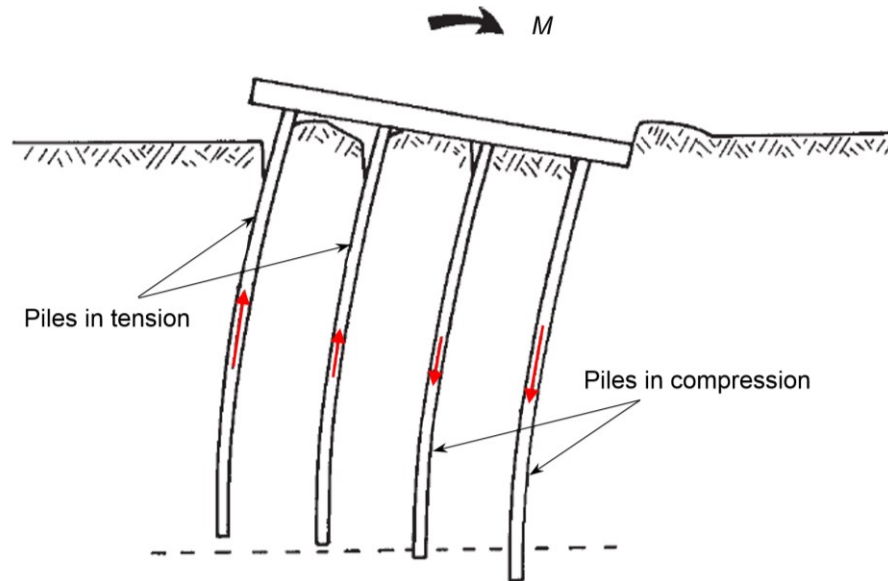
Figure 2-7: Pile response under applied overturning moment (adapted from Fleming *et al.*, 2009)

Concerning SLS conditions, checks for all wind turbine foundation types usually include foundation settlement (total and differential), crack width, foundation stiffness and ground gapping/tilt (Morgan & Ntambakwa, 2008; ASCE/AWEA RP2011). Due to the dynamic nature of wind turbines, with an operating frequency of less than 1 Hz (Bu, 2005), foundation stiffness and ground gapping are typically considered the most important and drive the size of foundations to avoid resonance of the foundation-turbine system (Bu, 2005; Reese & Wang, 2008; Wojtowitz & Foster, 2020). Resonance refers to the dynamic amplification of responses and is a function of the natural frequency of the turbine system, which, in turn, is dependent on the overall stiffness and mass of the foundation and the stiffness and cyclic characteristics of the supporting soil or ground (Wojtowitz & Foster, 2020; Yilmaz *et al*., 2022), and how these two components interact with one another (DNV/RisØ, 2002; ASCE/AWEA RP2011). To ensure that the natural frequency of the turbine system is high enough, wind turbine manufacturers typically specify a minimum foundation 'spring' stiffness, along with the applied foundation loads, depending on the turbine size. These stiffnesses generally are vertical (K_v), horizontal (K_h) and rotational (K_θ), with the rotational (rocking) stiffness being the most important due to the stability of the foundation against overturning. K_v is defined as

the ratio of the applied vertical load to vertical settlement (V/v), K_h as the ratio of the applied horizontal load to horizontal displacement (H/h) and K_θ as the ratio of the applied overturning moment to the angular distortion (M/θ), in radians, of the foundation.

Although these stiffnesses can be determined using FE modelling (Wojtowitz & Vorster, 2014), DNV/RisØ (2002) provides numerous idealised formulas for predicting them depending on the soil supporting conditions (resting on stratum over bedrock, resting on stratum over half-space or embedded in stratum over bedrock). The general formulas for predicting K_v, K_h and K_θ for circular raft foundations are indicated by **Equation 2-1**, **Equation 2-2** and **Equation 2-3**, respectively, where G refers to a representative shear modulus of the soil, R_r to the radius of the raft, and v_s to the Poisson's ratio of the soil.

$$K_v = \frac{4GR_r}{1 - v_s} \qquad (2\text{-}1)$$

$$K_h = \frac{8GR_r}{2 - v_s} \qquad (2\text{-}2)$$

$$K_\theta = \frac{8GR_r{}^3}{3(1 - v_s)} \qquad (2\text{-}3)$$

Although soil is highly nonlinear, DNV/RisØ (2002) have indicated that G is generally approximated using the small strain stiffness (G_0) of the soil in question and the corresponding shear strain in the soil (typically 10^{-3} for foundations). In addition, assumptions regarding these formulas are that footings are always in full contact with the soil and considered rigid relative to the soil, thus neglecting the thickness and Young's modulus of the raft. However, this raises questions as to what the thickness or Young's modulus value of the concrete needs to be before the raft can be considered rigid, especially considering that the deflection of any structural member is a function of both these parameters. The Young's modulus of concrete depends, amongst other things, primarily on the concrete mix's composition, especially the aggregate type used (BS EN 1992-1-1:2004+A1:2014; Alexander & Mindess, 2005) and typically varies between 20 GPa to 40 GPa. Thus, a foundation constructed of concrete with a lower Young's modulus requires a larger thickness to remain 'rigid' than one with a higher Young's modulus. Additionally, aggregate sourcing for concrete is site-specific and can thus not be omitted from these equations.

In the case of a piled-raft foundation, adding piles to the raft further influences the response of the foundation and, ultimately, the foundation system's vertical, horizontal and rotational

stiffness. Reese & Wang (2008) indicated that the slenderness of piles affects the response for piled foundations, especially when having a depth-to-width ratio larger than 2. They also mentioned that piles could increase the wind turbine tower's natural frequency and foundation stiffness and reduce vibration amplitude, proving beneficial in supporting wind turbines. Similarly, DNV/RisØ (2002) indicates several formulas for predicting pile foundation stiffnesses, including the coupled horizontal-rotational stiffness, assuming $L_p/d_p > 10$ and all the piles are flexible, with L_p and d_p referring to pile length and pile diameter, respectively. The formulas consider the Young's modulus of the soil and that of the pile, as well as the diameter of the pile, with soil profiles either being homogenous, increasing linearly with depth or increasing with the square root of depth. As with the capacity calculations, these formulas neglect the contribution of the raft, which, in some instances, can result in inefficient designs as the raft can potentially increase the stiffness of the foundation and play a crucial role in the foundation's response (DNV/RisØ, 2002; Burton *et al.*, 2011). Pile-to-pile interaction is also not considered, which should be flagged, given that the response of a piled foundation is affected by it.

In addition, the lateral response of piles is typically based on an equation from Poulos & Davis (1980) (see **Equation 2-4**). This equation is known as the pile-flexibility factor (K_R) and combines the Young's modulus of the pile (E_p), the second moment of area of the pile cross-section (I_p), the Young's modulus of the surrounding soil (E_s) and the length of the pile (L_p) to predict its reaction under loading. Given that the dominating loads on pile foundations for wind turbines are horizontal loads and bending moments, one can argue that this formula might be a better fit for predicting the overall response of these piles compared to those presented by DNV/RisØ (2002). However, this theory is also based on single piles, not considering potential pile-to-pile interaction. Using this equation, Poulos (1982) indicated that a pile under horizontal loading can be regarded as stiff if $K_R > 0.1$, whereas a $K_R < 10^{-5}$ is considered flexible.

$$K_R = \frac{E_p I_p}{E_s L_p^{\,4}} \tag{2-4}$$

Based on the assumption above that $L_p/d_p > 10$ is considered flexible according to DNV/RisØ (2002), conducting a simple calculation using the equation from Poulos & Davis (1980), for a pile to be considered flexible under horizontal loads, the pile should have an L_p/d_p ratio of greater than 30. This value was calculated by taking a pile diameter of 600 mm, the Young's modulus of a concrete pile as 30 GPa, and the Young's modulus of dense sand as 100 MPa (Fang, 1991). Thus, the assumption should be reconsidered, given that, in this case, the

dominant loads on foundations are horizontal loads and overturning moments, and the response of rigid piles differs from that of flexible piles (Poulos & Davis, 1980). Similarly, taking a pile diameter of 600 mm and an L_p/d_p ratio equal to 10, for a pile to be considered flexible, the Young's modulus of the surrounding soil needs to be less than 15 GPa (E_p/E_s = 2), which is impossible.

Furthermore, **Table 2-2** shows typical manufacturer limits on K_v, K_h and K_θ for different hub heights found in literature. These values are site and turbine-specific but were included as an indication of approximate design values. Maximum vertical deflection and rotational tilt are also indicated. As a general rule of thumb, ASCE/AWEA RP2011 mentioned that should the rotational tilt of the foundation not be specified by the wind turbine manufacturer, 3 mm/m can be adopted under extreme load cases, with Cools (2015) indicating 1 mm/m under service loads.

Table 2-2: Typical SLS design criteria values for wind turbine foundation design found in literature

Turbine hub height (m)	Maximum vertical deflection (mm)	Rotational tilt (rad)	K_v (MN/m)	K_h (MN/m)	K_θ (GNm/rad)	Reference
80	5	0.001	-	-	25	Reese & Wang (2008)
94	-	-	5000	5000	57	Mawer *et al.* (2017)
-	-	-	-	500-1000	60-120	Cools (2015)

Because the supporting soil will be subjected to a large number of load cycles of varying magnitudes and frequencies over the lifespan of the turbine, Mawer *et al.* (2017), Wojtowitz & Foster (2020) and Yilmaz *et al.* (2022) have indicated that, when determining a representative rocking stiffness for design, potential changes and strain accumulation in the supporting soil also needs to be accounted for. Burton *et al.* (2011), Currie *et al.* (2013), and Wojtowitz & Foster (2020) indicated that the excessive number of load cycles could lead to soil stiffness degradation over time, which can reduce the natural frequency of the wind turbine system, increasing the risk of the turbine becoming destabilised and resonating. However, Yilmaz *et al.* (2022) mentioned that strain accumulation properties for wind turbine foundations had not yet been characterised sufficiently, making SLS design challenging. Similar to the pile capacity checks, stiffness calculation checks concerning piled-raft foundations should also include group effects and pile-to-pile interaction.

Lastly, ground gapping refers to the temporary uplift between the foundation's tail and the supporting ground when the foundation is subjected to overturning moments during operation and can potentially be due to the footing being too small. The foundation partially loses

contact with the supporting ground, effectively bearing the applied load on a reduced area and is typically more common for raft foundations, as mentioned previously. Gapping limits vary between wind turbine manufacturers but are generally taken to be zero (Wojtowitz & Foster, 2020), with some gapping allowed only under extreme load conditions, which do not occur often. By assuming zero gapping, it can be accepted that the foundation stiffness remains adequate during normal operations and contributes to preventing potential cyclic degradation of the foundation-bearing materials. However, if gapping is allowed, the rotational stiffness of the foundation needs to be recalculated to accommodate the rotation caused by gapping. Regarding piled and piled-raft foundations, gapping is potentially less of a problem due to the added benefit of piles acting 'frictionally', ensuring minimal uplift and distributing the load to deeper depths.

2.3   PILED-RAFT FOUNDATIONS AND SOIL-STRUCTURE INTERACTION

As highlighted in Section 2.2, pile foundations are considered for supporting onshore wind turbines when concerns regarding low bearing capacity of the soil or excessive settlement of the foundation arise. Typically, these foundations are designed assuming the piles carry all the load, with the pile cap only acting as a rigid platform connection, distributing the loads onto the underlying piles. Under pure vertical loading, calculating these loads and the corresponding stiffness of the foundation is a reasonably well-established procedure. However, as indicated by Sakellariadis & Anastasopoulos (2022), the behaviour and design are much more complex when these foundations are subjected to combined loading, including horizontal loads and bending moments, in addition to the applied vertical loads. The interaction between the piles, the rotational restraint and the additional resistance the pile cap provides further complicate the response, with soil-foundation interaction and the relative stiffness between the foundation and the soil playing a pivotal role.

It should be appreciated that, more often than not, pile caps are cast onto existing soil, resulting in the foundation's response being different than that of the conventional pile foundation, with the pile cap working in conjunction with the piles and the loads shared by both foundation components through pile-soil and raft-soil contact stresses, respectively (Poulos & Davis, 1980; Randolph, 1983; Tomlinson, 1986; Katzenbach *et al.*, 1998; Reul & Randolph, 2003; Vorster & Wojtowitz, 2019). These 'hybrid' foundations are known as piled rafts and have recently gained popularity due to their numerous advantages, with the ground-contacting pile cap or raft providing additional benefits, effectively contributing to the overall response of the foundation. The original idea behind piled-raft foundations was based on the fact that the soil offers sufficient bearing capacity under the raft, with a limited number of piles included below the raft only acting as settlement reducers (Burland *et al.*, 1997;

Randolph, 1983; Katzenbach *et al.*, 1998). Poulos (2002), on the other hand, mentioned that the raft's performance could be improved by including piles, with Poulos also later indicating in 2016 that strategic placement of piles in areas where loads are more significant can provide additional load-carrying capacity, regardless of whether the soil below the raft has sufficient bearing. For wind turbine foundations, these piles are typically located towards the outside perimeter of the raft to counteract the applied overturning moment. Katzenbach *et al.* (1998) and Knappett & Craig (2012) have summarised several benefits of using piled-raft foundations compared to conventional pile foundations or pile groups, all proving valuable for wind turbine applications given the strict serviceability requirements. These benefits included the following:

- reduced absolute settlement, differential settlement and tilt;
- reduction in bending moment in the raft due to the presence of the piles;
- increased overall stability of the foundations; and,
- centralisation of actions and resistances if there are large eccentricities.

Regarding wind turbines, differential settlement and tilt are two of the most critical parameters that must be controlled as they influence the foundation's rotational stiffness. Differential settlement (the difference between the settlement at the raft centre and the raft edges) is often more essential to control than absolute settlement, as foundation distortion can damage the superstructure (Horikoshi & Randolph, 1997). In the case of piled-raft foundations, differential settlement can be managed by either increasing the raft's thickness or introducing piles in areas where larger settlements occur. However, it should be noted that increasing the thickness of the raft results in higher bending moments (Brown, 1969a), which is not desirable. Knappett & Craig (2012), on the other hand, indicated that it is more economical to include piles to reduce the differential settlement of the raft rather than increase the thickness. Thus, the design should incorporate a balance between these parameters. In addition, Vesic (1969) and Randolph (1994) have also highlighted the importance of considering pile group interaction and efficiency and how these effects may influence the foundation's response when piles are introduced. Both publications showed that the effectiveness of piles, particularly concerning their stiffness, is reduced by the proximity of other piles, all concerning soil-structure interaction. Winterkorn & Fang (1975), Tomlinson (1986) and Fleming *et al.* (2009) later indicated that the interaction amount depends on the loading type, pile spacing, and pile-soil properties, with a group of widely spaced piles potentially having the same stiffness as many closely spaced piles. BS EN 1992-1-1:2004+A1:2014 also specifies pile group interaction under special requirements for foundations in Clause 5.1.2 of the standard and Annex G, indicating that these interactions,

along with the interactions with the pile cap (raft) and the soil, need to be taken into consideration when these interactions and the properties of the soil have a significant influence on the action effects in the structure it is supporting. However, concurrently, the standard specifies that no simple approach is yet available for analysing the problem of piled-raft foundations, as additional interactions need to be accounted for. These interaction effects between the piles are commonly ignored when pile spacing exceeds two pile diameters.

Although significant progress has been made in recent years regarding the analysis of these foundations (Hain & Lee, 1978; Fleming *et al.*, 2009), design approaches still assume that all loads are carried entirely by the piles (Randolph, 1983; Horikoshi & Randolph, 1998; Fleming *et al.* 2009; Poulos, 2016; Sinha & Hanna, 2016; Vorster & Wojtowitz, 2019), which Burland *et al.* (1977) argued is illogical. In addition, the stiffness of the foundation is also taken as the stiffness of the pile group (Horikoshi & Randolph, 1998), disregarding the contribution of the ground-contacting raft, with two of the main questions still arising being what portion of the applied load is carried by the piles and raft, and to what extent the piles influence absolute and differential settlement. Randolph (1983) and Sinha & Hanna (2016) argued that all this uncertainty is mainly due to the complexity of the problem, the limited understanding of the pile-raft-soil interaction, the lack of field data and the scarcity of validated methods of analysing this intricate 3-D problem. Novak *et al.* (2005) and Vorster & Wojtowitz (2019) also indicated that adding to the difficulty of adequately understanding the response of these foundations, apart from soil-structure interaction, is the dynamic response of these structures to wind loads and seismic activity, settlement and creep effects and the long-term response of the ground. Additionally, Vorster & Wojtowitz (2019) mentioned that many factors, including site geology, type of loading, foundation installation methods, pile group effects, cyclic soil degradation and relative soil-foundation rigidity, influence foundation design.

Thus, given that the overall response of piled-raft foundation, especially under horizontal loads and overturning moments, is highly dependent on soil-structure interaction and the data available on this complex 'hybrid' foundation is reasonably limited, the need to further investigate and understand the mechanisms is important. Although designs are still based on the assumption that the piles carry all the loads, it should be appreciated that, given the ground-contacting pile cap, the foundation would respond as a piled raft, with the potential contribution of the raft to foundation stiffness not to be neglected. The following sections provide a brief background on the main principles of soil-structure interaction relating to piled-raft foundations. Specific emphasis was also placed on how these interactions influence the overall foundation stiffness and load sharing and how it can be used towards analysing and designing future wind turbine foundations comprising piled rafts. In addition, typical

responses of how these foundations respond under loading are also addressed, identifying potential shortcomings in research. The focus was mainly on circular piled rafts. However, given the limited information available, general observations for square and rectangular piled rafts were also included.

2.3.1 Soil-structure interaction principles and piled-raft foundation stiffness

Soil-structure interaction is not a new concept, yet it has gained significant popularity recently due to the construction of new infrastructure focusing on more economical and sustainable designs whilst meeting critical design specifications. Soil-structure interaction defines and investigates the boundary where soil and structures meet and predicts the behaviour between the two components through the relative stiffness concept, which establishes the stiffness and geometrical properties of the structure relative to the stiffness and properties of the soil. Other examples of the relative stiffness concept published in research include the works of Westergaard (1926) on the behaviour of a slab on subgrade for use in pavement engineering, Rowe (1952) for retaining structures, and Klar *et al.* (2005) for predicting the response of a pipe-soil system. Regarding piled-raft foundations, the soil-structure interaction problem becomes slightly more complicated as many factors simultaneously play a role in the overall foundation response. Typically, predicting the response of the piles and the raft in isolation is a relatively simple procedure. However, when considering the combination of the piles and raft as a single unit, not only does the interaction of these two components with the soil need to be considered, but additional interactions between the raft and the connecting piles and between the piles themselves arise that need to be addressed.

The soil-structure interaction and foundation rigidity principles for piled-raft foundations date back to the initial works of Brown (1969a, 1969b), who conducted numerical analyses on uniformly loaded circular rafts resting on elastic layers of soil of finite and deep depths. His research was based on the works of Borowicka (1939), who obtained solutions for the distribution of contact pressures beneath a strip subjected to uniform pressure. Regarding the research from Brown (1969a, 1969b), special consideration was given to raft flexibility and soil layer depth, investigating the soil reaction, bending moment distribution and vertical displacement in raft foundations under vertical loading, which ultimately contributed to our current understanding of piled rafts. Brown (1969a, 1969b) was seeking an alternative approach to the popular subgrade reaction method commonly used, which assumes that the reaction pressure between the raft and the soil is dependent solely and directionally proportional to the displacement of the soil at that point. He argued that this method might give adequate results when the raft is flexible but will fail when the raft is rigid. Under a uniformly distributed pressure, the displacement of a rigid raft will be uniform, with the soil

reaction also being uniform, resulting in the bending moment in the raft being zero, which is incorrect. He indicated that analysis must be based on more complicated and realistic assumptions, such as the elastic behaviour of the foundation material with the formula presented below. This research was later extended by many researchers (Butterfield & Banerjee, 1971; Poulos & Davis, 1980; Randolph, 1983; Clancy, 1993) with the inclusion of piles below the raft, investigating the response of piled-raft foundations through numerical analysis.

As indicated by Katzenbach *et al.* (1998) and also highlighted by Clancy & Randolph (1993), the main soil-structure interactions that need to be considered between the foundation components and the supporting soil that dictate the response of piled-raft foundations are as follows:

- raft-to-soil interaction;
- pile-to-soil interaction;
- raft-to-pile interaction; and,
- pile-to-pile interaction.

According to Clancy & Randolph (1993), these interactions can broadly be described using four dimensionless parameters: the raft-soil stiffness ratio (K_{rs}), the pile-soil stiffness ratio (K_{ps}), the pile slenderness ratio and the pile spacing ratio. These dimensionless parameters are listed in **Table 2-3**, along with the formulas for calculating each and the practical values typically encountered in practice. Brown (1969a) originally proposed the equation for calculating the K_{rs} for circular rafts. However, this equation was later adapted by Clancy (1993), including Poisson's ratio of the raft based on elastic plate theory in bending (Timoshenko & Woinowsky-Krieger, 1959) and the flexural rigidity of the plate.

Table 2-3: Dimensionless parameters for piled-raft foundation (adapted from Clancy & Randolph, 1993)

Dimensionless group	Definition	Practical range
Raft-soil stiffness ratio, K_{rs}	$\dfrac{E_r t_r^{\,3}(1 - \nu_s^{\,2})}{E_s R_r^{\,3}}$ * $\quad$ $\dfrac{E_r t_r^{\,3}(1 - \nu_s^{\,2})}{E_s R_r^{\,3}(1 - \nu_r^{\,2})}$ **	0.01 – 10
Pile-soil stiffness ratio, K_{ps}	$\dfrac{E_p}{E_s}$	100 – 10000
Pile slenderness ratio	$\dfrac{L_p}{d_p}$	10 – 100
Pile spacing ratio	$\dfrac{s}{d_p}$	2.5 – 8

*Brown (1969a) **Clancy (1993)

According to Hain & Lee (1978) and Clancy & Randolph (1993), rafts with a K_{rs} value greater than 10 are considered stiff, and less than 0.01 are flexible. In addition, piles with a K_{ps} value greater than 10^5 are considered rigid and, smaller than 10^2, flexible. Similar values for K_{ps} were recorded by Zhang & Small (2000). For the equations listed in **Table 2-3**, E_r refers to the Young's modulus of the raft, t_r refers to the raft thickness, R_r is the raft radius, E_s is the Young's modulus of the soil, v_r is the Poisson's ratio of the raft, v_s is the Poisson's ratio of the soil, E_p refers to the Young's modulus of the pile, L_p is the pile length, d_p is the pile diameter, and s is the spacing between the piles.

In assessing the overall combined stiffness of a piled-raft foundation, a paper published by Randolph in 1983 is probably the most well-known and used. This paper describes a way of assessing the overall stiffness of a piled-raft foundation and the load distribution between the raft and the piles by considering the stiffnesses of each component in isolation, using the flexibility matrix, allowing for interaction between them. This method uses an analytical study of a single pile-raft unit (see **Figure 2-8**), assuming a rigid pile cap with diameter, R_d, pile length, L_p, and pile diameter, d_p, assuming equal displacement in each pile, ignoring the interaction between piles.
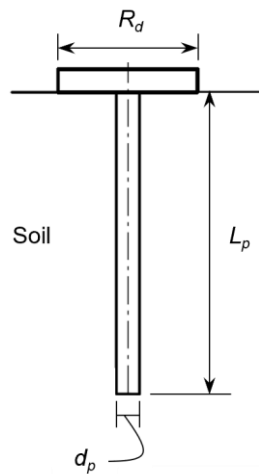
Figure 2-8: Simplified representation of a single pile-raft unit from Randolph (1983) (adapted from Poulos, 2001)

Equation 2-5 and **Equation 2-6** indicates the formulas Randolph (1983) derived for assessing the piled-raft foundation's overall stiffness (k_{pr}) and the load distribution between the piles and the raft, respectively. From **Equation 2-5**, k_p is defined as the overall stiffness of the pile group, k_r is the overall stiffness of the raft in isolation, and α_{rp} is the interaction factor of the pile group on the raft. Furthermore, F_p in **Equation 2-6** is defined as the load carried by the pile group, and F_r is the load carried by the raft, respectively.

$$k_{pr} = \frac{k_p + k_r(1 - 2\alpha_{rp})}{1 - (\frac{k_r}{k_p})\alpha_{rp}{}^2} \qquad \textbf{(2-5)}$$

$$\frac{F_r}{F_r + F_p} = \frac{(1 - \alpha_{rp})k_r}{k_p + k_r(1 - 2\alpha_{rp})} \qquad \textbf{(2-6)}$$

Calculating the values of k_r and k_p can typically be carried out using elastic theory methods presented by Fraser & Wardle (1976) or Mayne & Poulos (1999) for the rafts, and Poulos & Davis (1980), Poulos (1989) and Fleming *et al.* (2009) for pile groups. Although the initial analysis was based on a single pile-raft unit, ignoring pile interaction effects, the methods presented for pile groups above allow for an interaction factor to incorporate the group's contribution based on group efficiency. Although α_{rp} can be calculated, Clancy & Randolph (1993) and Randolph (1994) have indicated that this value tends to converge to 0.8 for larger piled rafts, regardless of pile spacing, slenderness, or compressibility.

2.3.2 Piled-raft foundation analysis techniques and typical response

Most initial trends and responses recorded regarding soil-structure interaction of piled-raft foundations were based on analyses using various numerical methods. Poulos (2001) summarised and broadly classified these methods into four categories. He referred to the first category as simplified methods, which includes the works of Poulos & Davis (1980) and Randolph (1983, 1994), as presented previously. The remaining three categories are as follows (including references to the relevant published works), with Hain & Lee (1978) combining boundary element techniques and finite element modelling:

1. Approximate computer-based methods – Clancy & Randolph (1993), employing a 'plate on spring' approach.
2. Rigorous methods – Butterfield & Banerjee (1971) and Kuwabara (1989), employing boundary element analysis based on elastic theory.
3. 3-D finite element analysis methods – Katzenbach *et al.* (1998).

Probably the most popular method is that presented by Clancy & Randolph (1993), which was based on the original works of Griffiths *et al.* (1991), using a 'plate on springs' hybrid finite element continuum-load transfer approach in which the raft is represented by a plate and the supporting soil by springs. Additionally, this method considered the load transfer treatment of individual piles and the elastic interaction between the piles and the raft, combining finite elements to model structural components and analytical solutions to model the soil's response. Furthermore, this approach allowed for investigating variable geometry, soil

stiffness and pile and raft stiffnesses. One-dimensional (1-D) rod finite elements were used for modelling the axially loaded piles (Smith & Griffiths, 1988), with the pile-soil contact represented by non-linear load transfer springs at node points (Randolph, 1977; Chow, 1986). In addition, the raft was subdivided into two-dimensional (2-D) thin plate-bending finite elements (Smith & Griffiths, 1988), with the raft-soil contact lumped onto equivalent soil springs at each node (Giroud, 1968). The interaction between the node pairs was then calculated using the elastic solution of Mindlin (1936). This method was applied to the foundation under vertical loading, with **Figure 2-9** illustrating the different components that make up the hybrid analysis method. However, one of the significant drawbacks experienced by many of these analysis methods was the lack of computational resources.

1. One-dimensional pile element
2. Lumped soil response at each pile node-load transfer spring
3. Two-dimensional plate-bending finite element raft mesh
4. Lumped soil response at each raft node – Giroud (1968)
5. Pile-soil-pile interaction effects calculated between pairs of nodes – Mindlin (1936)
6. Raft-soil-raft interaction
7. Pile-soil-raft interaction
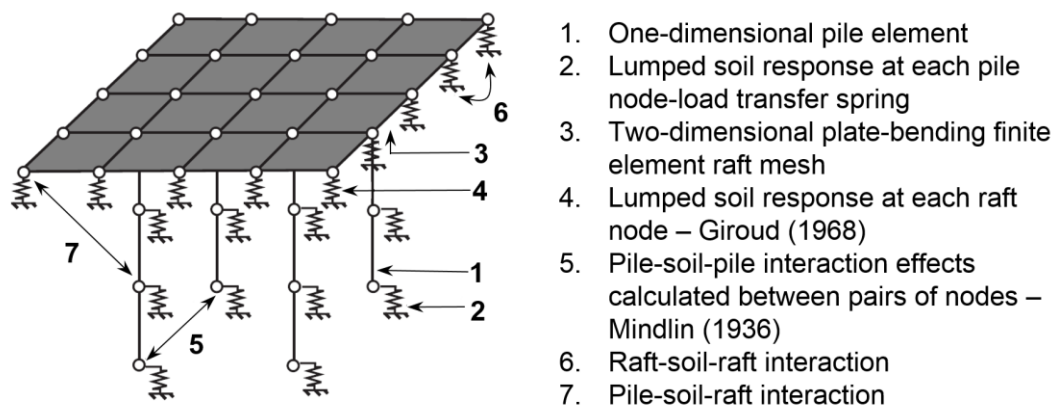
Figure 2-9: Numerical representation of piled-raft foundation from Griffiths *et al.* (1991) (adapted from Clancy & Randolph, 1996)

Given the complexity of the problem and the number of factors that play a role in the response of these foundations, some of the main conclusions reached by these researchers are summarised in **Table 2-4**. Note that only the most critical aspects are presented, relating mainly to wind turbine foundations, including bending moment in the raft, load distribution among the foundation components, foundation stiffness and differential settlement of the foundation, and how it pertains to soil-structure interaction concepts of piled-raft foundations. It should be emphasised that these observations were made for foundations subjected to vertical loading only, with all analyses regarding piles being conducted on floating piles, with little consideration given to end-bearing piles or piles socketed into bedrock. As before, most of these results also considered that the piled raft consists of a rigid pile cap (assuming that the displacements in all the piles are identical), compared to a flexible cap, which typically takes the load acting on each pile as equal.

Table 2-4: Summary of piled-raft response to vertical loading, considering soil-structure interaction

Reference	Foundation type (loading)	Main conclusions
Brown (1969a)	Circular raft, perfectly smooth, resting on a finite layer of isotropic elastic material underlain by a rough rigid base (uniform vertical loading)	• The maximum bending moment in the raft increased rapidly, and differential settlement decreased as K_{rs} increased from 0.1 to 2. No significant increase was observed for K_{rs} values greater than 10 (starting plateauing at $K_{rs} = 2$). As soil layer depth increased, the maximum bending moment increased. However, it remained relatively constant for layer depths greater than $2R_r$. • Central deflection of the raft depends on layer depth, K_{rs} and Poisson's ratio of the soil (v_s). More significant deflections were observed when layer depth was high and v_s and K_{rs} were low. • For deep soil layers ($> 5R_r$), an increase in K_{rs} caused a significant decrease in central deflection, with v_s having little effect. • Alternatively, for shallow soil layers ($< 2R_r$), the v_s caused a considerable increase in central raft deflection, whereby K_{rs} had almost no effect. • Varying the Poisson's ratio of the raft (v_r) had little effect on the behaviour of the raft (decreasing v_r slightly decreased bending moments and increased differential settlement).
Brown (1969b)	Circular raft, perfectly smooth, resting on a deep layer of isotropic elastic material (uniform vertical loading)	• The same general trends as Brown (1969a) were observed for bending moments. A reduction in v_r had little effect on raft bending moments. • Differential settlement changed rapidly when K_{rs} was near 1. • A significant change in the maximum bending moment in the raft occurred when K_{rs} was near 0.2, requiring a substantial increase in raft thickness to produce any considerable decrease in raft stresses. • v_s no longer influenced bending moments in the raft and differential settlement of the raft.
Butterfield & Banerjee (1971)	Square and rectangular rafts (rigid) supported by circular piles, perfectly smooth, embedded in semi-infinite ideal elastic half-space (vertical loading)	• Depending on pile group size and pile spacing, the presence of the pile cap produced only a slight increase (5%-15%) in the vertical stiffness of the foundation for all but short piles ($L_p/d_p < 20$). This slight increase was mainly due to interaction/group effects between the piles. As K_{ps} increased, the vertical stiffness of the foundation increased more significantly. • Although the effect of the pile cap on the stiffness was small, for L_p/d_p values between 20 and 40, the pile cap carried between 15% and 25% of the vertical load, with the percentage increasing as pile spacing and pile group size increased and pile length decreased. • Lower K_{ps} values resulted in a higher percentage of the load carried by the pile cap for $L_p/d_p > 20$. • Doubling the pile spacing resulted in the vertical stiffness of the foundation increasing between 5% and 10%. • Higher L_p/d_p values produced greater vertical foundation stiffnesses. • A higher number of piles and higher K_{ps} values increased foundation stiffness. • Increasing s/d_p resulted in interaction/group effects between the piles decreasing, with the presence of the raft becoming more significant.

Author	Model	Findings
Hain & Lee (1978)	Square raft supported by circular piles embedded in elastic soil model (vertical loading)	• As s/d_p increased, the interaction between piles decreased, as expected. • A reduction in settlement with an increase in K_{ps} and L_p was observed. This was expected as a more significant portion of the applied load was resisted by the longer piles through shaft friction, ultimately reducing settlement. • Differential settlement increased as raft rigidity decreased, but bending moments decreased. • The piles carried a larger percentage of the load when K_{ps} was larger and were more prominent when the piles were closely spaced. • As pile spacing increased, the influence of the raft became greater. • As mentioned, a higher L_p/d_p ratio resulted in a more significant portion of the load being carried by the piles.
Randolph (1983)	Rigid circular pile cap supported by circular piles (vertical loading)	• See **Figure 2-10(a)** and **(b)**. Results compared well with those from Poulos & Davis (1980). • Small pile diameters had virtually no effect on the foundation's overall stiffness (k_{pr}), with the foundation's overall stiffness being dictated by the stiffness of the pile group (k_p). • Higher L_p/d_p values increased the stiffness of the pile group compared to the raft stiffness. • The pile group carries a more significant portion of loads for smaller raft diameters, with longer and larger diameter piles also carrying higher loads. • Closely spaced piles may increase settlement due to interaction/group effects. Thus, increased spacing of piles is beneficial.
Katzenbach *et al.* (1998)	Square rafts supported by circular piles (vertical loading)	• Initially, a larger portion of the vertical load was carried by the piles but decreased as displacement of the piled raft occurred, resulting in the raft starting to carry higher loads. • The effect of shaft friction was observed. • Higher pile lengths reduced the settlement amount, but the number of piles (n) and pile diameter (d_p) also influenced settlement simultaneously. No significant reduction was observed for $n(L_p/d_p) > 500$. However, as $n(L_p/d_p)$ increased from 0 to 500, settlement reduced between 55% and 85%.
Kuwabara (1989)	Square raft supported by circular piles (vertical loading)	• The reduction in overall settlement due to the presence of the raft was small. However, the raft transferred between 20% and 40% of loads to the supporting ground when s/d_p was less than 10 (percentages somewhat lower than what Butterfield & Banerjee (1971) observed previously).
Clancy & Randolph (1993)	Square raft supported by circular piles embedded in homogeneous soil (vertical loading)	• Results align with those observed by Kuwabara (1989) and build on the model initially presented by Randolph (1983). • As pile spacing increased, the pile group had less influence on the raft, but the raft had a more significant impact on the piles. • As L_p/d_p increased, the effect of K_{ps} was more noticeable. However, as K_{ps} increased, the pile group had a more significant effect on the raft. • Increasing L_p/d_p merely increased the spread of pile compressibility values at a given pile spacing, with pile compressibility being more critical for longer piles. • Interaction between the piles and raft increased as the size of the pile group increased, leading to a reduction in the

2-25

		overall foundation stiffness. Simultaneously, the effect of pile compressibility and slenderness was also reduced.
		• As s/d_p increased, k_r and k_p increased. k_p increased at a lower rate than k_r, thus resulting in the portion of the load taken by the piles decreasing and that carried by the raft increasing.
		• Differential settlement decreased as K_{rs} increased, with greater settlements observed when piles had lower compressibilities.
		• Due to increased shaft friction, lower settlements were observed for a higher L_p/d_p ratio. As s/d_p decreased, settlements also reduced. The same trends were observed for differential settlements.
		• Lower K_{ps} values resulted in higher settlements, and as s/d_p increased, raft settlement increased.
Clancy & Randolph (1996)	Square raft supported by circular piles embedded in homogeneous soil (vertical loading)	• Differential settlement tends to decrease with increased K_{ps}, K_{rs} and L_p/d_p values, with an increase in s/d_p values resulting in an increased differential settlement. • The amount of load carried by the raft decreased as K_{ps} increased. • K_{rs} seemed to have little effect on the load carried by the raft and the pile. • Increased L_p/d_p ratio resulted in the piles carrying higher loads, with the raft taking more loads when s/d_p increased.
Horikoshi & Randolph (1997)	Square raft supported by circular piles embedded in homogeneous soil (vertical loading)	• See **Figure 2-11(a)** and **(b)**. Results compared well with that from Brown (1969a). L_r refers to the length of the rectangular raft, B_r to the width of the raft, v_{rd} to the differential settlement of the raft, v_{rv} to the average vertical settlement, and q to the bearing pressure in the soil below the raft. • Differential settlement decreased with increased K_{rs} values. • The maximum bending moment in the raft increased as raft thickness and K_{rs} increased.
Horikoshi & Randolph (1998)	Square raft supported by circular piles embedded in homogeneous soil (vertical loading)	• Differential settlement can be minimised by concentrating piles in the central 16%-25% of the raft area.

Figure 2-10: Foundation stiffness and load transfer: (a) effect of the ground-contacting raft on single pile stiffness (b) proportion of load carried by raft (adapted from Randolph, 1983)
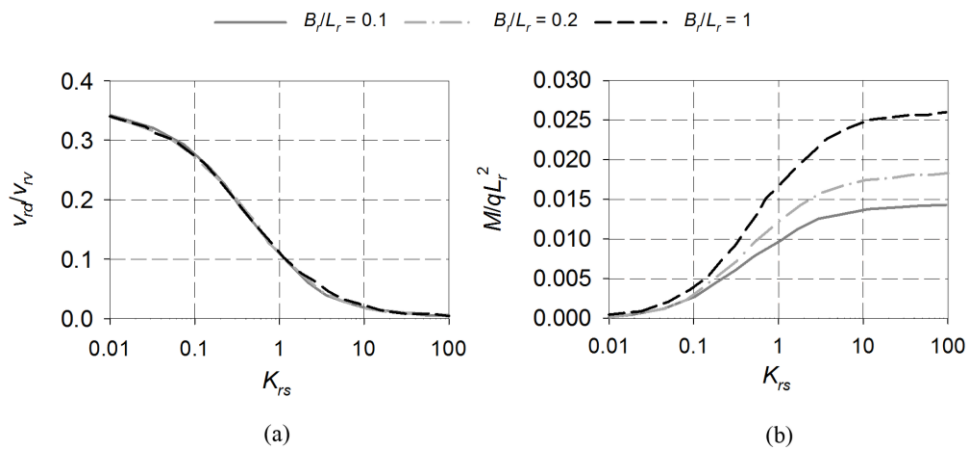
Figure 2-11: Foundation response to changing raft-soil ratio, K_{rs}: (a) normalised differential settlement (b) normalised maximum bending moment (adapted from Fleming *et al.*, 2009)

Furthermore, Randolph (2003) indicated that, based on works from Viggiani (2001), the response of pile groups can either be defined as 'small' ($B_r/L_p < 1$) or 'large' ($B_r/L_p \geq 1$), where B_r refers to the width of the raft and L_p to the length of the pile. For 'small' pile groups, the stiffness of the pile group is greater than the stiffness of the raft. Thus, the pile cap will contribute little to the overall response of the foundation. The piles carry most of the load with these foundations, and the raft can be made infinitely stiff to minimise differential settlement. However, the raft often provides sufficient bearing capacity for 'large' pile groups, transferring the loads to the underlying ground, with the piles included to minimise differential settlement and reduce the bending moment in the raft. Thus, the stiffness of the foundation approaches the stiffness of the raft, which was also observed by Randolph (1983).

In light of turbines increasing in height needing foundations that are not too small in diameter to result in large tensile forces in the piles, 'large' pile groups would be preferred, resulting in

2-27

the stiffness of the raft having to be considered and not neglected. In addition to the results presented in **Table 2-4**, Fleming *et al.* (2009) made the following remarks:

- Piles spaced closer together result in higher pile group stiffness. However, as s/d_p increases, the stiffness of the raft becomes more profound.

- Piles have higher interaction and lower efficiencies when spaced closer together. Efficiency also decreases as the number of piles increases.

- The central piles will settle more for piles supported by a flexible cap, with piles at the edges experiencing higher loads if loaded through a rigid cap.

- For a rigid pile cap, piles settle equally. Hence, differential settlement is negligible.

Regarding piled-raft foundations subjected to combined vertical and horizontal loads, Zhang & Small (2000) investigated the response of pile groups (off-ground cap) and Small & Zhang (2002) for piled rafts (ground contacting cap). Both used a combination of thin plates for modelling the raft and elastic beams for modelling the piles, with the soil treated as horizontal layers. Finite layer theory and the APPRAF (Analysis of Piles and Piled Raft Foundations) finite element software program were used to solve equations, with Zhang & Small (2000) and Small & Zhang (2002) indicating that this method improved on previous approaches for modelling the raft-pile, raft-soil, pile-pile and pile-soil interaction. Sinha & Hanna (2016) argued that these methods still neglect the 3-D nature of the problem, where typically most of the interaction takes place.

Some of the main conclusions reached by Zhang & Small (2000) and Small & Zhang (2002) included the following:

- Under horizontal loading, K_{ps} played a vital role in resisting the lateral displacement of the pile group for K_{ps} values less than 1000, with lateral displacement increasing sharply with decreasing K_{ps}. In addition, higher displacements were observed when the cap was not in contact with the ground.

- Under vertical loading, K_{ps} affected the amount of vertical settlement for K_{ps} less than 100, after which the effect was negligible.

- Pile length affected vertical settlement but had less effect on horizontal displacement.

- Under lateral loading, low s/d_p values (less than 6) not only resulted in larger displacements of a capped pile group but also caused significant moments in the piles.

- At greater pile spacings, larger sagging moments were observed in the raft under vertical loading and greater hogging moments in the raft over the piles.

- The vertical settlement of the foundation reduced as pile spacing decreased, with a greater portion of the loads being carried by the piles.
- Under horizontal loading, greater hogging moments were observed over the leading piles and sagging moments over the trailing piles.

2.3.3 Piles socketed into bedrock

In the case of piles founded on rock (socketed into bedrock), Tomlinson (1986) indicated that the response of the pile is governed by its strength, with the pile being regarded as a column, owing a great deal of its resistance to end bearing, not primarily dependent on the shaft friction between the pile and the soil. However, he indicated that caution should still be exercised as the properties of different bedrocks vary and can potentially alter during construction due to pile driving or augering. Given that the piles can be regarded as columns, in structural engineering, the compressive strength of any columns is primarily related to the potential buckling that can occur under compressive loading. The principles on which column buckling is based on the Euler curve. These principles define the maximum theoretical compressive stress (σ_{cr}), or Euler stress, that an idealised column (a column that is centrically loaded with small deflections and perfect construction, with the material following Hooke's Law) can resist under loading. These stresses are a function of the column's length (L) and flexural stiffness (EI), which comprise the product of the Young's modulus and the second moment of area. As an explanation, **Equation 2-7** and **Equation 2-8** indicates the formulas for determining the critical compressive stress (σ_{cr}) of a column pinned at the top and bottom boundaries (Gere & Goodno, 2013), where F_{cr} is the critical compressive load and A, the column's cross-sectional area. The critical compressive stress for columns with different boundary conditions can easily be determined by applying factors based on the columns' effective length (L_e). Stresses in the column greater than σ_{cr} would result in an unstable structure, with the converse being stable.

$$\sigma_{cr} = \frac{F_{cr}}{A} = \frac{\pi^2 E}{(L_e/r)^2} \tag{2-7}$$

$$F_{cr} = \frac{\pi^2 EI}{L_e^2} \tag{2-8}$$

Ugural & Fenster (2012) have sketched the typical relationship between the critical compressive stress and slenderness ratio (L_e/r) of columns, where r is the radius of gyration ($\sqrt{I/A}$) of the column (see **Figure 2-12**). According to **Figure 2-12**, columns can be

classified into three regions: short, intermediate and long. Typically, short columns have a slenderness ratio of less than 30 for structural steel or 50 for reinforced concrete ('A' in **Figure 2-12**) (Mosley *et al.*, 2012; Ugural & Fenster, 2012). The response of these columns is usually characterised as being able to resist larger compressive loads. It has low instability, with the crushing of the material being the primary failure mechanism when the compressive strength limit has been reached. Failure of long columns is typical through elastic buckling at much lower loads and is typically encountered when the slenderness ratio is greater than 110 for reinforced concrete columns and 100 for structural steel ('B' in **Figure 2-12**) (Mosley *et al.*, 2012; Ugural & Fenster, 2012). Intermediate columns fail due to a combination of direct compression and elastic buckling and typically occur within the tangent-modulus portion of the curve (see **Figure 2-12**). The tangent-modulus curve is introduced as the limit of the Euler curve. It is capped by the material's compressive strength, as solely relying on the Euler curve would imply that column members become infinitely strong as the slenderness ratio of the columns reduces.
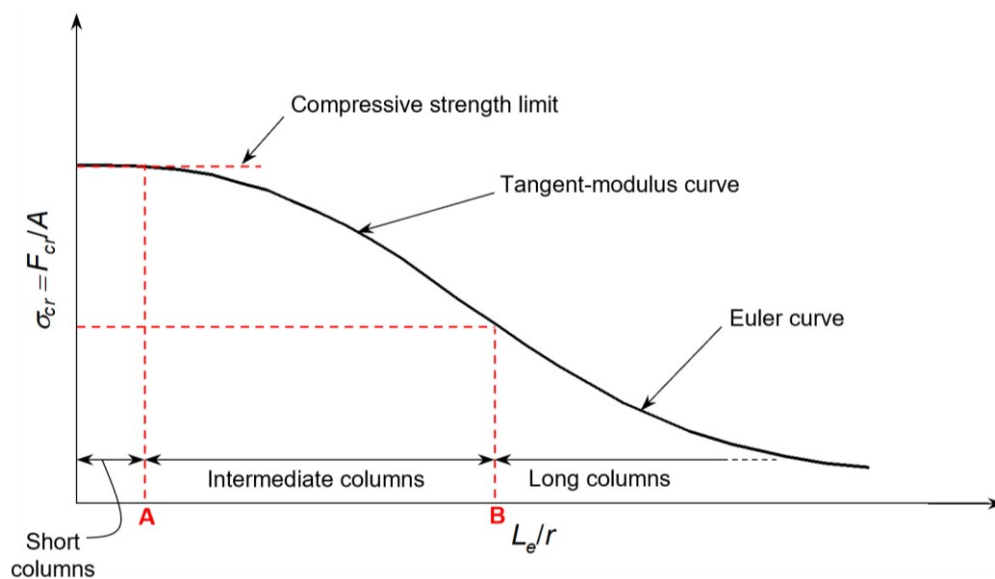
Figure 2-12: Critical stress versus slenderness ratio (adapted from Ugural & Fenster, 2012)

Thus, contrary to the response of the floating piles observed in Section 2.3.2, which typically acquires much of its resistance from shaft friction, the response of piles bearing on bedrock differs. Poulos & Mattes (1969) investigated the behaviour of axially loaded end-bearing piles in an ideal elastic soil through numerical analysis. They found that the response of the piles was influenced mainly by the L_p/d_p ratio and the relative stiffness between the Young's modulus of the pile (E_p), that of the surrounding soil (E_s) and the bearing stratum (E_b). Higher pile-soil stiffness ratios (E_p/E_s) resulted in piles carrying higher loads, with the E_b having a negligible effect. As L_p/d_p increased, as expected, less load was transferred to the bearing stratum, even if the bearing stratum had a high Young's modulus. The pile started acting as a

floating pile, with the effect higher when the pile-soil stiffness ratio was low. The axial load transferred to the bearing stratum increased as E_s/E_b decreased, though when E_s/E_b increased from 100 to infinity, it was nearly identical, with the effect being less when L_p/d_p was higher. The more slender the pile, the greater the load transfer to the soil and the lower the load transfer to the bearing stratum, as in the case of longer columns. All of this is comparable to the structural response observed previously, with shorter, stockier piles carrying higher loads due to the reduction in potential buckling that might occur.

2.3.4   3-D FE modelling of piled-raft foundations

Based on the relatively rigorous approximations of the responses of piled-raft foundations mentioned in Sections 2.3.2 and 2.3.3, with the increased power of modern software and computer capabilities over recent years, advanced 3-D FE modelling enabled the study of many complex engineering problems. A lot of the existing methods presented in the past have been considerably limited by the number of equations that could be solved simultaneously, which resulted in problems being simplified to a large extent. Several researchers have investigated piled-raft foundations using various FE software packages with reasonable success (Reul, 2004; Sinha & Hanna, 2016; Ravichandran & Shresta, 2019), allowing for the interaction between the foundation and the soil to be captured more realistically. In addition, FE permitted modelling to better understand this intricate problem and the load sharing between the different foundation components. The complexity increased with the addition of dominant horizontal loads and overturning moments.

Poulos (2010) indicated that, although the conventional simplified analytical methods for assessing the foundation's stability proved adequate when vertical loading is present, other outcomes might be achieved when the dominant load is no longer vertical. However, Poulos amended this argument in 2016, stating that these traditional methods can no longer be applied confidently for structures increasing in height and size since they require extrapolation well beyond the realms of past experiences. Additionally, Reul (2004), Sinha & Hanna (2016) and Ravichandran & Shresta (2019) highlighted that these methods might work well under vertical loading but not under general loading conditions since the soil-structure interaction concepts are not fully captured. This effectively encourages using FE modelling to improve our understanding of how these support structures respond to various loadings. Novak *et al.* (2005) provided two reasons for using 3-D modelling. These reasons were as follows:

1. Piled-raft foundation problems are so complex that simplified methods cannot model the issues correctly.

2. Codes for the FE modelling are available, powerful and capable of being run on a personal computer. Thus, using FE modelling, modelling the raft, piles, and the surrounding soil as a soil-structure interaction problem is feasible.

In addition, Poulos (2016) indicated that for any FE software programs to prove valuable in providing representative models of piled-raft foundations under loading, these programs should have the following capabilities:

- For overall stability, the program should be able to consider the following:
    o non-homogeneous and layered soil profiles;
    o non-linearity of pile and, if appropriate, raft behaviour;
    o geotechnical and structural failure of piles (and the raft);
    o vertical, lateral and moment loading (in all directions), including torsion; and,
    o piles having different characteristics within the same group.
- For serviceability analysis, the above characteristics are also desirable, and in addition, the program should have the ability to consider the following:
    o pile-to-pile interaction, and if appropriate, raft-to-pile and raft-pile-soil interaction;
    o the flexibility of the raft of pile-cap; and,
    o some means by which the stiffness of the supported structure can be considered.

Literature available on 3-D FE modelling of piled-raft foundations is still relatively limited, especially considering scenarios where foundations are subjected to horizontal loads and overturning moments, as in the case of wind turbine support structures. Apart from the 3-D FE modelling conducted by Katzenbach *et al.* (1998) and presented in Section 2.3.2, the first comprehensive 3-D FE model of a piled-raft foundation was that proposed by Prakoso & Kulhawy (2001) and Reul & Randolph (2003). Reul & Randolph (2003) investigated the overall settlement, differential settlement and load carried by the piles of three piled-raft foundations under vertical loading resting on overconsolidated clays using FE modelling, comparing it to field measurements. The main idea behind the research was to check whether an improved layout of the piles cannot reduce both the maximum differential settlement and the overall loading of the piles. Results obtained from the FE model showed good agreement with field measurements, although FE analysis generally showed a higher portion of the applied load being carried by the piles. However, Reul & Randolph (2003) highlighted that only 15% of the piles were instrumented, which may not be sufficient for monitoring all aspects of the pile group behaviour. On the other hand, Prakoso & Kulhawy (2001) found that 2-D modelling of piled-raft foundations overestimated the displacement for different raft

rigidities compared to 3-D models. Their investigations, however, focused on settlement and bearing pressure in the soil, neglecting soil-structure interaction concepts.

Sinha & Hanna (2016) conducted 3-D modelling of vertically loaded piled-raft foundations resting on clay soil, accounting for pile-pile, raft-pile, pile-soil and raft-soil interaction. The study's main objective was to examine the effects of foundation geometry, soil properties, pile spacing, length, shape and diameter, and raft thickness on the foundation's response and the load-sharing mechanisms involved. Sinha & Hanna (2016) calibrated their numerical FE modelling against the conventional method results presented by Poulos (2001), highlighted in Section 2.3.2, and found they were in good agreement. Some of the main observations included:

- Pile cross-sectional shape (rectangular, octagonal or circular) does not affect the results.
- As with previous observations, the raft settlement increased with increased pile spacing and decreased pile size and length. For s/d_p greater than 6, the foundation system tends to function as a raft.
- Increasing the pile spacing offsets the benefits of increasing pile size and length to reduce settlement. However, one can argue that this significantly benefits large overturning moments. A trade-off between the pile spacing, size and length should thus be examined to achieve an economical design.
- A thinner raft may lead to non-uniform load sharing between the piles, which is a departure from the principles of the design of pile foundations. Accordingly, significant settlement within the raft may also take place.
- A thicker raft will minimise or eliminate differential settlement. However, it may impose an additional load on some of the piles, leading to unexpected excessive uniform settlement of the raft.

More recently, Deb & Pal (2021) investigated the response of piled rafts in layers of silty clays and sand using 3-D FE modelling, examining the settlement, raft-soil contact behaviour, bending moments, axial stresses in the piles and soil stresses in different directions. The piled raft was subjected to vertical loading only, with the following conclusions reached:

- As mentioned before, the piles acted as settlement reducers under the raft. The normalised average settlement was reduced between 3% to 10% by increasing the piles from 9 to 16. The effect was also more significant when s/d_p was less. Bhaduri & Choudhury (2020) also made similar observations, although this will result in the piles carrying higher loads.

- Differential settlement can be controlled by increasing the raft's thickness or the number of piles. Piles, however, became less effective when the spacing was increased. Differential settlement decreased between 30% and 60% when the number of piles increased from 9 to 25.

- Increasing the raft thickness by 1.5 times, the differential settlement was reduced between 12% and 17%, and increasing the thickness by 2 times resulted in a reduction between 25% and 30%.

- Hogging moments were present in the raft at the location of the piles. Hogging moments were decreased between 15% and 25% by increasing the number of piles from 9 to 16, respectively, and between 28% and 39% by adding 25 piles. In addition, the piles beneath the raft reduced the sagging moments by more than 26%.

- Larger pile spacings increased the hogging and sagging moments in the raft.

- The portion of the load carried by the piles increased with pile number, pile spacing and diameter of the raft but reduced as the raft thickness increased.

In addition, Bhaduri & Choudhury (2020) also found that greater pile spacings resulted in more significant foundation settlements, with larger raft thicknesses, resulting in less absolute and differential settlement. Similar results were observed by Chanda *et al.* (2020). Regarding foundations subjected to horizontal loads and overturning moments, Ravichandran & Shrestha (2019) conducted numerical modelling of piles raft in clayey soil for wind turbine application and compared it to simplified analytical models as presented by Poulos (2001) and Small & Poulos (2007). Some of the main conclusions they found were that vertical settlement and horizontal displacement were higher for the analytical solutions, with differential settlement and rotation being smaller than that presented by the 3-D model. Additionally, some of the other conclusions reached were that the design requirements for wind turbine foundations can be met by increasing the number of piles, pile lengths, or the radius of the raft when the wind speed is increased. However, as with previous models, little consideration was given to investigating soil-structure interaction. In a separate publication, Shrestha & Ravichandran (2019) indicated that piles contributed more towards reducing settlement, with the raft contributing more to reducing horizontal displacement. Under applied overturning moments, only the piles contributed towards reducing the rotation and differential settlement, unlike when piled rafts are subjected to only vertical loading. **Table 2-5** summarises models found in literature, highlighting the typical material models used for representing the piles, raft and soil. Additionally, model sizes, elements, interaction properties, and assumptions are emphasised, all providing background for developing a comprehensive FE model.

2-34

Table 2-5: 3-D FE models of a raft foundation, piled foundation and piled-raft foundations found in literature

References	Software program	Study considered	Elements	Material models	Soil model size	Loading	Interaction modelling
Lee *et al.* (2002)	Abaqus 2-D and 3-D	Pile foundations embedded in layers of soft clay and sand	*Soil and piles:* 27-node quadratic hexahedral bricks (3-D)	*Soil:* Mohr-Coulomb *Piles:* Linear elastic	Square (1/4 symmetry – with boundary conditions) *Length:* NS* *Width:* NS* *Height:* 25 m	Vertical	-
Reul & Randolph (2003)	Abaqus 3-D	Piled raft embedded in overconsolidated clay underlain by limestone	*Soil:* Linear solid hexahedron brick *Piles:* Linear solid triangular prisms *Raft:* Linear triangular and square shells	*Soil:* Linear elasto-plastic cap model *Piles and raft:* Linear elastic	Square (1/8 symmetry – with boundary conditions) *Length*: 120 m ($2B_r$) *Width*: 120 m ($2B_r$) *Height*: 130 m	Vertical	Thin solid continuum elements instead of interface elements Perfectly rough
Reul (2004)	Abaqus 3-D	Pile raft embedded in a layer of clay underlain by limestone	*Soil:* Linear solid hexahedron brick *Piles:* Linear solid triangular prisms *Raft:* Linear triangular and square shells	*Soil:* Linear elasto-plastic cap model *Piles and raft:* Linear elastic	Square *Length*: NS* *Width*: NS* *Height*: 113 m	Vertical	Thin solid continuum elements instead of interface elements Perfectly rough
Lee *et al.* (2010)	Abaqus 3-D	Rectangular piled raft foundation embedded in soft clay underlain by rock	*Soil, piles and raft:* 27-node quadratic hexahedral	*Soil:* Mohr-Coulomb *Piles and raft:* Linear elastic	Square (1/4 symmetry – with boundary conditions) *Length*: 20 m ($4B_r$) *Width*: 20 m ($4B_r$) *Height*: 24 ($1.5L_p$)	Vertical	Surface-to-surface contact Master-slave contact (Coulomb friction model)

2-35

Sinha & Hanna (2016)	Abaqus 3-D	Piled raft embedded in a clay soil	*Soil, raft and piles:* 8-node hexahedral bricks	*Soil:* Drucker-Prager cap plasticity *Piles and raft:* Linear elastic	Square (1/4 symmetry – with boundary conditions) *Length*: $30d_p$ *Width*: $30d_p$ *Height*: $2L_p$	Vertical	Surface-to-surface contact Master-slave contact (Coulomb friction model)
Mohamed & Austrell (2018)	Abaqus 3-D	Rafts embedded in medium clay	*Soil and raft:* 20-node quadratic brick	*Soil:* Mohr-Coulomb *Raft:* Linear elastic	Circular *Diameter:* $2R_r + 5R_r$ *Height:* $6R_r$	Vertical-Horizontal-Moment	Surface-to-surface contact Master-slave contact (Coulomb friction model)
Ravichandran & Shrestha (2019)	Abaqus 3-D	Piled raft embedded in clayey soils	*Soil, piles and raft:* Linear 8-node hexahedral	*Soil:* Drucker-Prager cap plasticity *Piles and raft:* Linear elastic	Circular *Diameter:* 50 m ($6.67R_r$) *Height:* 56 m ($2L_p$)	Vertical-Horizontal-Moment	Master-slave surface-to-surface contact (Coulomb friction model)
Chanda *et al.* (2020)	Plaxis 3-D	Rectangular piled raft embedded in sand soil	*Soil:* 15-node wedge *Piles:* 8-node quadrilaterals *Raft:* 6-node triangular	*Soil:* Mohr-Coulomb *Piles and raft:* Linear elastic	Square *Length:* 28 m ($7B_r$) *Width:* 28 m ($7B_r$) *Height:* 16 m ($1.8L_p$)	Vertical-Horizontal-Moment (including torsional)	-
Deb & Pal (2021)	Abaqus 3-D	Piled-raft foundations embedded in layers of silty clay and sand	*Soil and raft:* 20-node hexahedral brick *Piles:* 15-node tetrahedral prism	*Soil:* Modified Drucker-Prager *Piles and raft:* Linear elastic	Square (1/4 symmetry – with boundary conditions) Length: $3B_r$ Width: $3B_r$ Height: $3B_r+L_p/3$	Vertical	Surface-to-surface Contact Master-slave constraint (Coulomb friction model)

*Not specified

2-36

Although piled-raft foundations are both cost-effective and sustainable foundation solutions, providing a high level of redundancy (Poulos, 2010; Vorster & Wojtowitz, 2019) and many benefits, there is a knowledge gap regarding the response of these foundations to large horizontal forces and overturning moments. Regardless of whether the piles act as settlement reducers or are included for load-carrying capacity, the overall response and stiffness of the foundation is governed by soil-structure interaction and the relative stiffness between the foundation components and these components and the surrounding soil (Poulos & Davis, 1980; Tomlinson, 1986; Knappett & Craig, 2012).

Given that wind turbine sizes are increasing, the dependency on piled-raft foundations is also growing, providing a more economical use of material than the conventional raft foundation that requires significantly large plan areas to resist the applied overturning moment. As indicated, the pile cap or raft might have a negligible effect on the response of a piled-raft foundation when subjected to vertical loading and when the raft is small. However, it might present a different outcome when horizontal loads and overturning moments dominate, as tilting and rotation of the foundation are highly dependent on the stiffness of the raft in addition to that of the piles.

Even though numerous methods and interaction models exist to investigate foundation stiffness, the relative stiffness between the pile group and the raft is typically neglected. The raft is mostly assumed to be rigid, which is not necessarily representative. The primary focus has to date been on the interaction between the piles and the soil. Given that both the piles and the raft contribute towards load carrying, the size of foundations can also be reduced whilst meeting critical rotational stiffness requirements, resulting in the potential saving of concrete required for casting. Piles reduce the bending moments in the raft whilst simultaneously providing benefits against differential settlement and tilt – all desirable characteristics for wind turbine application. The presence of potential tension forces in trailing piles caused by the push-pull effect and how it relates to soil-structure interaction also requires further investigation, especially considering the size increase of wind turbines.

2.4   BASIC PORTAL FRAME PRINCIPLES AND DISTRIBUTION FACTORS

Although the response of a piled-raft foundation is primarily governed by soil-structure interaction (discussed in Section 2.3), the structural response of these foundations can, given the typical shape and orientation of wind turbine foundations (piles located towards the edge of the raft to counteract the overturning moment), in the simplest 2-D form, be compared to that of a portal frame under loading. Portal frames are a type of rigid frame consisting of two vertical columns fixed or pinned at the bottom, with a third member connecting the top of the

two columns (see **Figure 2-13**). As shown in **Figure 2-13**, the connections (joints) between the columns and the top beam are moment-resisting (rigid), which means that the angles between members (in this case being 90º for a rectangular portal frame) remain constant as the structure deforms under loading (Norris *et al.*, 1976). By accepting a rigid connection, forces (axial and shear) and moments can be transmitted from one member to another, similar to the connection assumptions between the piles and raft of a piled-raft foundation. Several structural analysis methods from the past explain the basic principles of how portal frames respond under loading and how, internally, members interact with one another. Two classical methods are the slope-deflection method, initially introduced by Maney (1915), and the moment distribution method, published by Cross (1932).
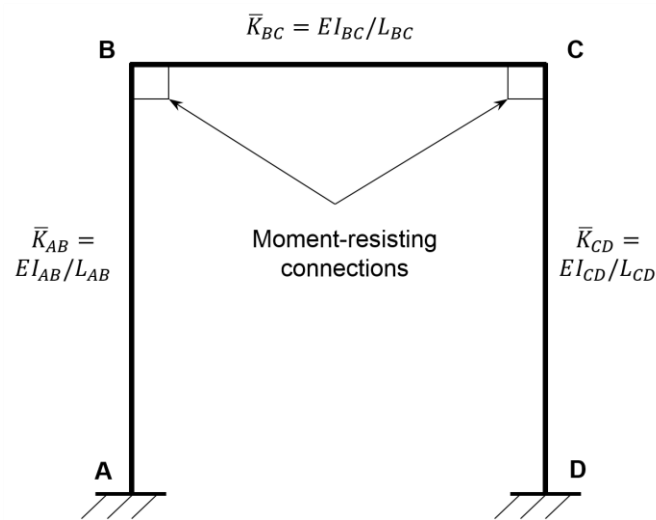
Figure 2-13: Typical rectangular 2-D portal frame with fixed supports

Both methods are based on the bending deformation of frames, assuming that the entire frame is continuous, with the overall deformation governed by member bending stiffness and joint rotational stiffness. The bending stiffness of members is typically denoted in structural analysis using the symbol, $\bar{K}$, and is calculated as the ratio of member flexural stiffness (EI) and length (L) (see members AB, BC and CD in **Figure 2-13**). On the other hand, joint rotational stiffness is taken as the sum of all the member bending stiffnesses ($\Sigma\bar{K}$) at a particular joint and is defined as the moment required to cause a unit rotation (Kassimali, 2015). Thus, the stiffness of each member relative to the stiffness of the joint can be expressed as $\bar{K}/\Sigma\bar{K}$, which is also referred to as a distribution factor. **Equation 2-9** indicates the formula for obtaining the amount of rotation at a joint of a portal frame and is a function of both the applied bending moment at that joint and the rotational stiffness of the connection, with total rotation being reduced for higher bending member stiffnesses and, ultimately, combined joint stiffness. This equation is similar to the one presented in Section 2.2.4 for calculating a foundation's rotational 'spring' stiffness ($K_\theta = M/\theta$). Yet, this equation combines

the stiffness of both connecting members. In addition, **Equation 2-9** highlights that the amount of rotation depends on the stiffness of all connecting members, raising the argument whether a similar approach should not be followed when designing wind turbine foundations where the applied horizontal load and overturning moment are dominating.

$$\theta = \frac{M}{\Sigma \overline{K}} \qquad \qquad \textbf{(2-9)}$$

Building on the statement from Wojtowitz & Foster (2020) that the diameter of the piled raft cannot be too small as it will result in potentially significant tension forces in the piles located at the edges, larger diameter rafts (L in **Figure 2-13**) might also result in the stiffness of the member decreasing, effectively reducing the rigidity of the connection, which needs to be considered. To better illustrate these basic principles, **Figure 2-14** shows typical deflected shapes of a portal frame under loading, highlighting the influence of member bending stiffnesses on the overall response. **Figure 2-14(a)** indicates the deflected shape under vertical loading, and **Figure 2-14(b)** under coupled horizontal load and moment, with profiles based on examples from Reynolds & Steedman (1988) and Kassimali (2015). Keeping the lengths of all the members and EI_{AB} and EI_{CD} the same, it is evident that increasing EI_{BC} drastically reduces the rotation of joints and members of the portal frame. Although not affecting the bending moments experienced within members significantly, due to the balance between the increased rotational stiffness and decreased rotation of the frame, the increased rotational stiffness of joints affects the axial force in column members. Stiffer connections potentially increase vertical displacements at joints compared to less stiff connections, increasing axial forces in vertical column members. For a piled raft, increasing the raft stiffness increases the bending moment in the raft and reduces settlement. However, the potential of higher axial forces (tension and compression) developing in piles is more significant.

Similar to the deflected shapes, typical bending moment diagrams of a portal frame under an applied vertical load and a coupled horizontal load and moment are indicated in **Figure 2-15(a)** and **(b)**, respectively, with the magnitude of the bending moments dependent on load size. These diagrams were based on examples from Reynolds & Steedman (1988) and Kassimali (2015), with bending moments drawn on the tensile side of members. Given the moment-resisting connections, moments at member intersections are equal ($M_{BA}=M_{BC}$, $M_{CB}=M_{CD}$). Additionally, the moment fixity at the bottom of column members results in bending moments within this region (similar to what piles would experience being socketed into bedrock). Although not indicated, combining these bending moment diagrams through superposition can be achieved to simulate the effect of the combined vertical, horizontal and moment load, which, depending on the magnitude and direction of individual bending

moments, can either increase or decrease the moments experienced by the members. For example, moments at joint B tend to increase with the addition of the applied horizontal load and overturning moment. It should be pointed out that given the interaction with the soil, the shape of the bending moments in the raft and piles might differ slightly from those of portal frames. However, similar behavioural trends will still be achieved but need further investigation.
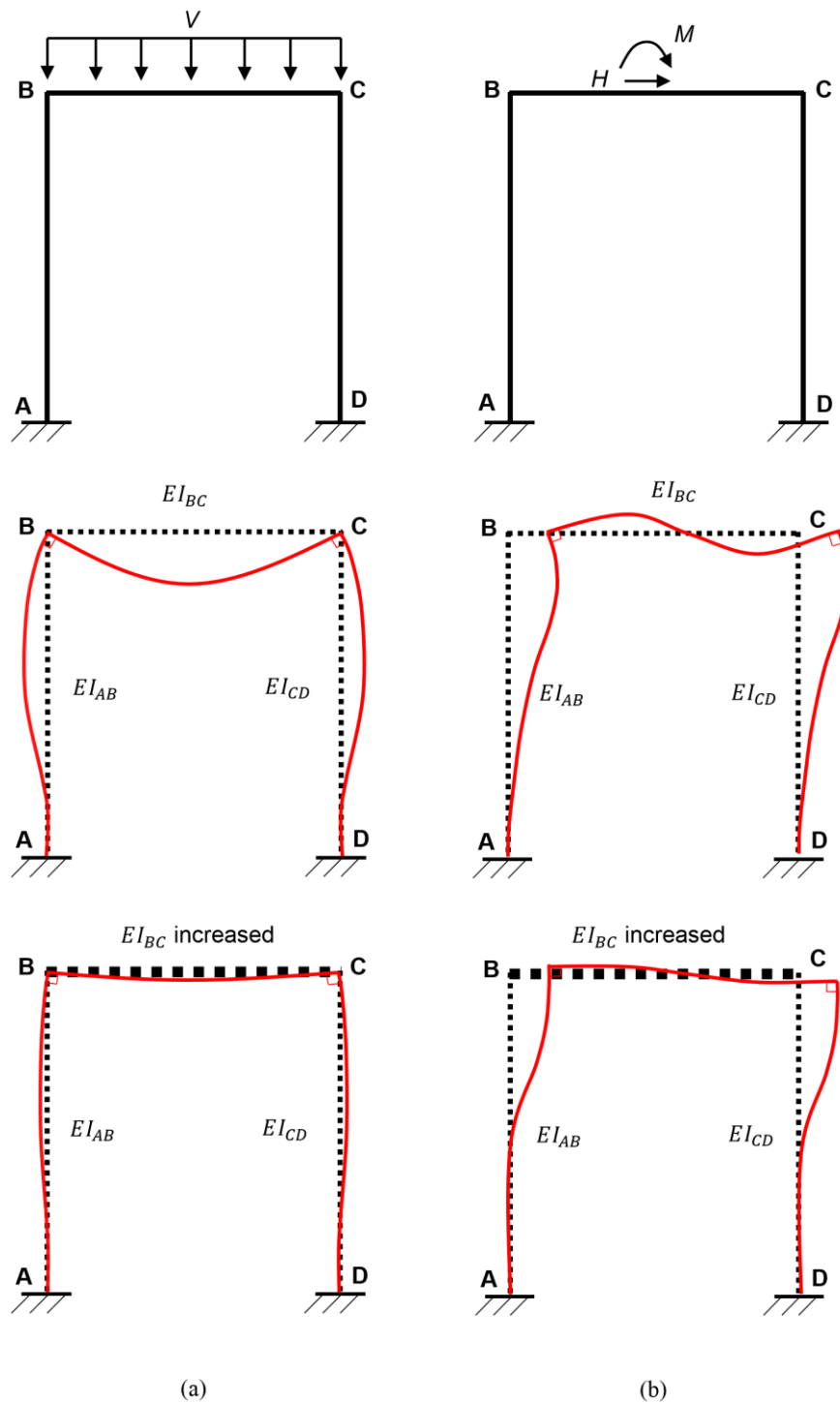
Figure 2-14: Portal frame deflected shapes: (a) vertical load; (b) horizontal load and applied moment

2-40
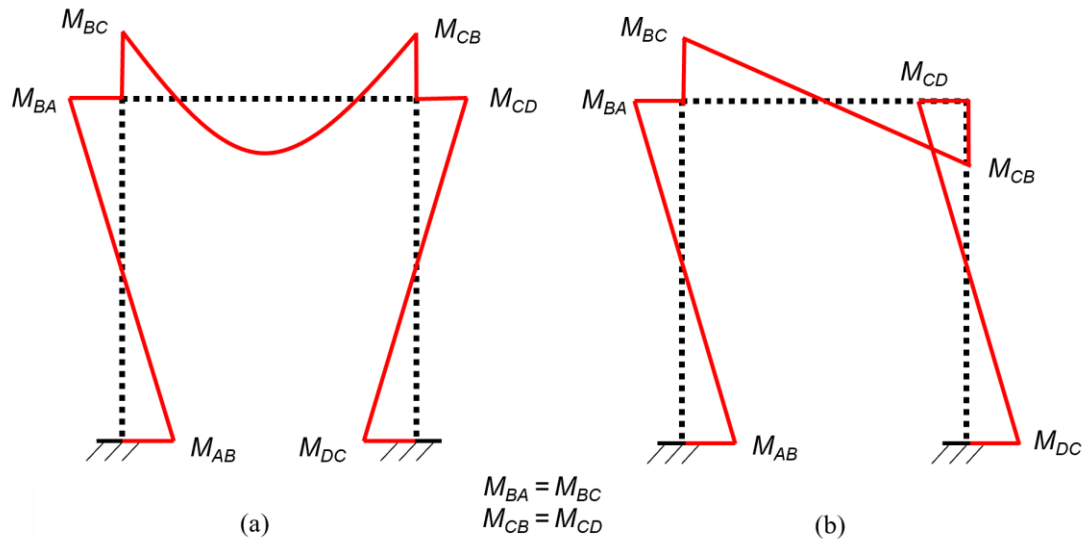
Figure 2-15: Typical portal frame bending response: (a) vertical load; (b) horizontal load and applied moment

2.5 RESPONSE OF FOUNDATIONS UNDER CYCLIC LOADING

As mentioned in Section 2.2.4, due to the non-linear characteristics of soil and the cyclic nature of the applied wind loads on turbine foundations, potential changes and strain accumulation in the supporting soil must be accounted for. Cyclic loading could likely lead to soil degradation, altering the rotational stiffness of the foundation, reducing the natural frequency of the wind turbine system and ultimately increasing the risk of the turbine becoming destabilised. Moss *et al.* (1998) indicated that the cyclic response of soils and foundations is highly complex and likely misunderstood, resulting in most design methods still being based on a conservative rule of thumb.

Due to the cost and difficulty associated with full-scale testing, many researchers have resorted to using small-scale models to improve their understanding of the behaviour of complex engineering problems (Sabnis *et al.*, 1983; Noor & Boswell, 1992). Similarly, soil-structure interaction problems have typically been investigated using scaled models in a geotechnical centrifuge (Schofield, 1980), which is an experimental technique whereby a scaled model is spun up to an accelerated *g*-level, with centrifugal forces ensuring that realistic soil stresses and strains are generated despite the small size of the models. Thus, in an attempt to investigate the cyclic response of foundations under loading, several researchers conducted tests using this method.

One such example of scaled testing conducted on piled-raft foundations in a geotechnical centrifuge is based on the works by Horikoshi *et al.* (2003a; 2003b), who investigated the static and dynamic response of piled-raft foundations in sand under one-way vertical and

horizontal loading. They explored the load-displacement relationship and load sharing between the pile and raft, giving particular attention to the effects of pile head connection rigidity on the foundation response. Some of the main conclusions were as follows:

- The stiffness and resistance of a pile in proximity to other nearby piles in a piled-raft foundation differ substantially from those observed from a single pile in isolation. They argued that this was mainly due to the differences in the confining stress conditions around the piles, linking to the arguments discussed in Section 2.3.

- The horizontal resistance of the piles in the piled raft with a hinged pile head connection was slightly smaller than that observed in the isolated pile despite the higher confining pressures around the piles beneath the raft. This was thought to be due to the interactions between the raft and the piles.

- As before, the piles played an essential role in increasing the horizontal resistance of the piled-raft foundation under loading. The initial horizontal stiffness of the piled-raft foundation was not always higher than that of the raft in isolation. The piles potentially reduced the contact pressure between the raft and the soil, effectively reducing the stiffness towards the top of the soil.

- Greater horizontal loads were transferred to the piles in the piled-raft foundation when the pile head connection was rigid, resulting in a higher horizontal foundation stiffness than a more flexible (hinged) pile head connection. Initially, the raft carried more of the applied horizontal loads. However, these loads decreased as horizontal displacements increased, resulting in the piles working harder. They argued that it is thus vital to consider the soil's non-linear response/permanent deformation in design. Given the higher horizontal loads in the piles, a greater bending moment was also observed when the pile head connection was rigid.

- Apart from the horizontal loads carried by the piles increasing as the horizontal displacement of the piles increased, the proportion of the vertical load carried by the piles in the piled-raft foundation remained unchanged during horizontal loading. Hinged pile head connection models resulted in the change in vertical load sharing between the raft and the piles being smaller.

These observations were made based on horizontal loads being the governing load on the piled-raft foundation. In the case of wind turbine foundations, apart from the significant cyclic horizontal loads acting on these foundations, the response of these foundations is also primarily governed by the sizeable cyclic overturning moment. One can thus argue that not only the horizontal displacement of the foundation caused by the horizontal force but also the vertical settlement of the foundation caused by the overturning moment rotating the raft and

the piles need to be investigated. In addition, Hanna & Vakili (2021) indicated through centrifuge testing on scaled piled-raft foundations that pile spacing and settlement both governed load-sharing mechanisms between the piles and the raft, with pile-soil-pile interaction being a function of pile geometry and conditions of the surrounding soil, all of which are relevant to wind turbine foundations having rigid rafts connecting the piles. This response was also highlighted previously in an article by Tang *et al.* (2014).

Similarly, Niemann *et al.* (2019) investigated the effect of cyclic horizontal loading on pile groups supporting integral bridge abutments in a geotechnical centrifuge, where daily and seasonal temperature variations generate horizontal loads. They found that the bending moment in the centre and trailing row of piles was approximately the same but lower than the maximum bending moment in the leading row due to the shadowing effects caused by the geometry of the pile group. However, as the number of load cycles increased, Niemann *et al.* (2019) found that the load distribution, and hence the bending moment, within the pile group gradually shifted from the leading piles to the trailing piles. More significant displacement was observed when piles were more closely spaced and when the cyclic load magnitude was higher.

Additionally, other researchers have indicated the effect of cyclic lateral loading on the response of single piles (Poulos, 1982; Verdure *et al.*, 2003; Leblanc *et al.*, 2010; Li *et al.*, 2010; Louw *et al.*, 2022a). As with the piled rafts and pile groups mentioned previously, bending moments typically develop within the piles under applied horizontal loading, with the maximum bending moment increasing with the number of load cycles. However, more notable results were recorded by Kirkwood & Haigh (2014), who indicated the presence of permanent (locked-in) bending moments in piles resulting from cyclic horizontal loads. Permanent bending moments are defined as the bending moments left in the piles after load removal and were said to be due to particle re-orientation around the piles causing locked-in soil stresses which develop in response to the applied cyclic loads. The soil condition surrounding the piles changed, with the magnitude of the permanent bending moments increasing as the number of load cycles increased. More recently, Truong *et al.* (2019) also emphasised the presence of permanent bending moments during cyclic horizontal load tests on single piles, resulting in the soil surrounding the piles changing and the piles having to work harder.

Regarding the cyclic response of soil and changing soil conditions, the shakedown concept has been used to describe the behaviour of many conventional engineering structures in contact with soil, investigating the extent of permanent soil deformation under repetitive loading. Johnson originally proposed this concept in 1986 when he studied the permanent

deformation of surface layer soils under rolling and sliding line contact. Depending on the magnitude of the applied loads and the number of load cycles, Johnson (1986) found that the response of the soil can be classified into four categories (see **Figure 2-16**). These categories were as follows:

1. Purely elastic
2. Elastic shakedown
3. Plastic shakedown
4. Incremental collapse/ratcheting
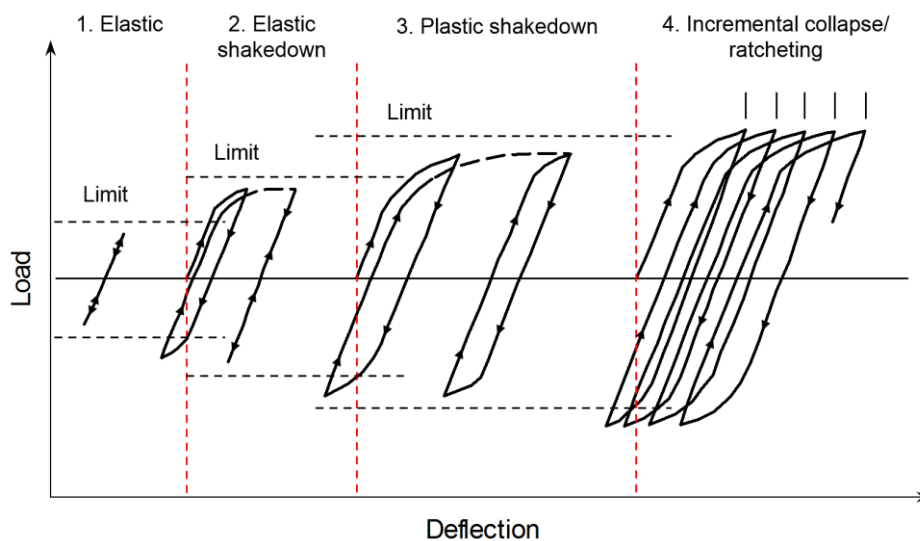
Figure 2-16: Shakedown effect (adapted from Johnston, 1986)

These categories were also later highlighted by Werkmeister *et al.* (2001), who investigated the response of cyclic loading on unbounded granular materials for pavement engineering using triaxial tests. Werkmeister *et al.* (2001) mentioned that purely elastic conditions (Category 1) exist when loads exerted on soil are sufficiently small and all deformations are fully recoverable. However, Werkmeister *et al.* (2004) later indicated that this region is rarely encountered in soil as all soils experience some form of permanent and resilient (recoverable) deformation under loading and unloading (see **Figure 2-17**). The elastic shakedown condition (Category 2) occurs when the applied load is slightly less than required to produce plastic shakedown. Within this region, the response of the soil is plastic for a finite number of load cycles, though the reaction of the soil is elastic, with no permanent strains occurring within the soil after that, regardless of the number of load cycles. The plastic shakedown region (Category 3) occurs at higher loads than an elastic shakedown, with the soil achieving long-term steady-state response (no accumulation of plastic strain, with each response being

hysteretic). The soil becomes resilient after a post-compaction/densification period, after which the number of load cycles no longer changes the reaction of the soil, similar to the elastic shakedown region. At greater applied loads, a significant zone in the soil is under the yielding condition, with plastic strains accumulating rapidly, leading to a large amount of soil degradation. Continuing incremental plastic deformation occurs for each additional load cycle at these loads, a process known as ratcheting (Category 4). Thus, usually, only at large applied loads does soil typically experience degradation. It should be mentioned that regardless of the magnitude of the applied loads, the response is also dependent on the properties of the soil, including previous stress history. As seen from the cyclic load tests conducted on foundations in the geotechnical centrifuge, this concept can be applied to the response of a piled raft, with the deformation depending on the magnitude of the applied load to the soil and the properties of that soil.
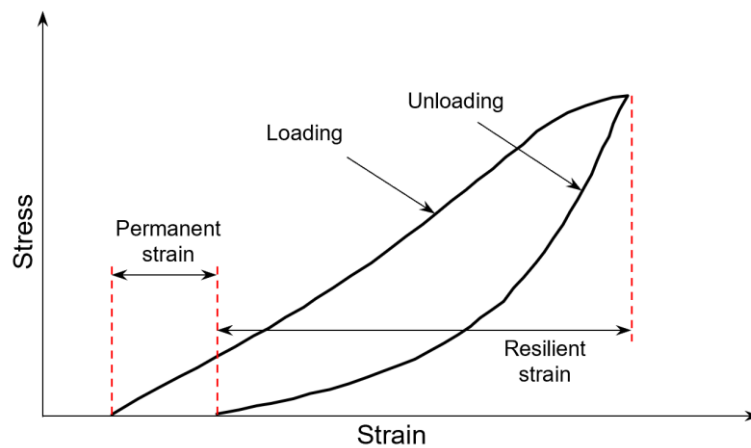
Figure 2-17: Typical stress-strain relationship of soils under loading (adapted from Werkmeister *et al.*, 2004)

Apart from the permanent bending moments in piles resulting from changing soil conditions, the concepts of soil densification and soil degradation/incremental collapse were also observed by several researchers investigating single piles (Hettler, 1981; Poulos, 1982; Little & Briaud, 1988; Long & Vanneste, 1994; Leblanc *et al.*, 2010, Li *et al.*, 2010; Louw *et al.*, 2022a) and pile groups (Niemann *et al.*, 2019) under cyclic lateral loads. As with the shakedown theory, apart from the density, load history and properties of the soil in question, the magnitude of the cyclic load being applied primarily dictated the response of the soil. Leblanc *et al.* (2010) and Li *et al.* (2010) have indicated that, depending on the magnitude of the applied load and the properties of the surrounding soil, the soil densifies rather than degrades. Regarding pile groups, Niemann *et al.* (2019) have found that for s/d_p = 4 and 5, displacements were low and stabilised within the first 20 cycles at low cyclic load amplitudes.

Higher displacements were observed at larger cyclic load amplitudes when the piles were closely spaced ($s/d_p = 3$), even at low cyclic load amplitudes.

Thus, in light of the observed responses, many questions arise regarding wind turbines supported by piled rafts. Given that the pile cap is in contact with the ground, effectively 'bridging' the span between the piles, will the piles start carrying greater loads under continued cyclic loading caused by the wind as the permanent deformation of the soil below the raft would potentially increase, forming a void, with the piles being unable to settle because they are end-bearing? Additionally, is the soil below the raft experiencing some form of degradation, or is densification taking place, which ultimately improves the overall stiffness of the foundation (rocking stiffness in particular for wind turbines)? Similarly, will the interaction between the raft and the piles affect the pile bending and permanent bending moments under cyclic horizontal loading and coupled overturning moments?

2.6 STRUCTURAL HEALTH MONITORING OF ONSHORE WIND TURBINE FOUNDATIONS

With the rise in popularity and size of wind turbines, the safety and security of these structures and the foundations supporting them are critical to the longevity of these structures as a renewable energy alternative (Currie *et al.*, 2013). Wind turbines operate under challenging dynamic loading conditions, which, over time, can potentially diminish their structural integrity (Burton *et al.*, 2011). Thus, in light of the questions raised in previous sections, understanding these complex structures and how these dynamic effects influence the foundations and soil supporting them requires further investigation, which can be achieved with full-scale testing. Although the behaviour can be explored using scaled models in a geotechnical centrifuge under a controlled environment, the efficacy of full-scale site testing remains, given that environmental and seasonal changes may also affect foundation response, which is typically neglected in laboratory testing.

Over the years, structural health monitoring (SHM), a process of in-service health assessment of a structure through an automated monitoring system, has gained significant traction in determining the integrity of structures. Chen (2018) noted that it is a vital part of cost-effective condition-based maintenance strategies and a powerful tool for damage assessment and performance evaluation of engineering structures over their lifespan. Alternatively, SHM provides the opportunity to improve the current understanding of how structures behave under working loads and changing environmental conditions (Hu *et al.*, 2015), allowing for more economical, secure and sustainable designs in future. Although SHM systems provide several advantages, they are typically neglected when constructing new infrastructure due to the high

cost of installing sensors and long-term monitoring systems (Swartz *et al.*, 2010). Concerns regarding sensor durability, accessibility and harsh installation conditions within construction environments have also been raised (Wymore *et al.*, 2015; Bai *et al.*, 2017; He *et al.*, 2019).

SHM has also been implemented in wind turbines and wind turbine foundations to determine the dynamic response. Currie *et al.* (2015) and Wymore *et al.* (2015) indicated that health monitoring of these structures provides various economic and other benefits to aid in wind energy growth, ensuring the safety and reliability of these structures. Several commercial and research monitoring systems have been implemented for wind turbines, focusing predominantly on structural damage of blades, gearboxes and towers, with limited information on the structural behaviour of wind turbine foundations (Currie *et al.*, 2013; Bai *et al.*, 2017). McAlorum *et al.* (2018) also mentioned this lack of information despite foundations being safety-critical structures. Of the foundation monitoring research available, offshore foundation monitoring has typically received significantly more attention than onshore wind turbine foundation monitoring. Wymore *et al.* (2015) argued that it is likely due to these foundations being more complex structures, exposed to challenging conditions, and due to many questions still surrounding the design and deployment of these turbines. However, McAlorum *et al.* (2018) mentioned that onshore wind turbine foundations are becoming a focus of SHM due to their increasing role in renewable energy generation. The need to revisit these foundations, especially in light of the rising size of turbines, is of great importance (Wang *et al.*, 2012), with foundations now having to operate at higher stress levels (Bai *et al.*, 2017) as turbines increase in size.

Regarding onshore wind turbine foundations, SHM has primarily been centred around failure mode-based monitoring and the development of early warning systems to detect these particular failure modes and the severity thereof. One such monitoring system has been demonstrated by Currie *et al.* (2015), who investigated the excessive movement around the bottom flange of embedded can-raft foundation connections. They indicated that these movements resulted from cyclic wind loading, eroding the concrete around the bottom flange of the can embedded in the foundation, creating a void within these regions, ultimately altering the stability and natural frequency of the wind turbine-foundation system. Displacement patterns were monitored using wireless linear variable differential transformers (LVDTs) positioned at the base of the wind turbine tower, with the tower having a hub height of 67 m, a rotor diameter of 80 m and a power rating of 2 MW. The supporting foundation was octagonal in shape and had a width of 15.4 m and a total thickness of 3.1 m, of which the base height was only 0.7 m. Results indicated significant movement during start-up and shutdown periods and during turbulent wind speeds, as expected. Structural cracks were also observed near the top of the pedestal, with Currie *et al.* (2015) mentioning that these cracks

result in water ingress, which can increase the sizes of voids and the corrosion potential of the embedded steel can. Monitoring these cracks and their deterioration using fibre Bragg grating (FBG) has also been illustrated by McAlorum *et al.* (2018).

Similar observations to Currie *et al.* (2015) were made by Bai *et al.* in 2017. Instead of using LVDTs, displacement patterns were measured using several embedded strain sensors positioned at specific locations near the bottom flange of the embedded can, which allowed them to capture the occurrence of cracks and monitor crack opening. In addition, ultrasonic testing was used to track the position of the cracks and identify their boundaries. The sensors were cast into a circular raft foundation with a diameter of 18 m and a total thickness of 4.2 m (1.8 m high pedestal), supporting a 1.5 MW wind turbine having a hub height of 75 m and a rotor diameter of 93 m. They argued that voids and cracks at the bottom flange of the embedded can already occur at an early age due to different shrinkage rates of the concrete around the inserted can, which gradually grows and fluctuates according to wind speed changes. Debonding between the concrete and the steel can was also considered possible. Overall, crack widths correlated well with wind speed, with cracks becoming wider under tensile stresses. This research was later further explored in a publication by He *et al.* (2019), using the same experimental set-up, comparing the measured strains around the bottom flange to a numerical finite element model, which modelled the interface between the embedded can and the concrete raft. A good correlation existed between the measured data and the model predictions, with the loads applied to the finite element model based on strain measurement obtained from the tower's base. They argued that slight differences were possibly related to variations in concrete strengths, voids near the bottom flanges, or how the embedded steel can was fastened to the steel supports before casting, potentially restraining deformation. It should, however, be pointed out that the deformation of the soil below the foundation was neglected in the finite element model. Rotation and displacement were restricted in all directions on the base of the raft, which would have affected the validity of the observed responses.

Although Wymore *et al.* (2015) indicated that failure mode-based monitoring is valuable, more general concrete monitoring should also prove helpful as it can significantly reduce the operating and construction cost of structures, as highlighted by Schiegg & Steiner (2010). Reese & Wang (2008) also noted the need for full-scale instrumentation and in-service wind turbine foundations monitoring. The available research, however, to date remains relatively limited. Perry *et al.* (2017) monitored the temperature of a large 20 m diameter, 3 m thick raft foundation during curing using a number of thermocouples. Temperature measurements are usually taken in the foundation to minimise thermal gradients causing stresses in the concrete of such large concrete masses after casting (Azenha & Faria, 2008; Conceicao *et al.*, 2014).

However, in the case of Perry *et al.* (2017), temperature measurements were used to improve understanding of strength development and estimate the initial performance of concrete using the 'maturity' method (the principle that temperature measured in the foundation during curing is caused by the chemical reactions responsible for strength development). Recent works from Rubert *et al.* (2018) showed real-time strain monitoring of an onshore wind turbine raft foundation using FBG sensors at various points. They also compared the measured strain to finite element models, with the foundation resting on linear springs and found a good correlation with sensors placed at two locations within the foundation.

In addition, research from Yilmaz *et al.* (2022) investigated the soil pressure distribution in lean clay foundation soils below two in-service raft foundations (16.5 m diameter, 1.7 m thick) supporting a 1.5 MW and 1.65 MW wind turbine, respectively. The primary focus of the research was comparing how the pressures correlate to assumptions adopted during conventional design practices of these foundations. Pressure distribution was measured using both pressure cells and soil deformation meters. As expected, pressure distribution varied from the centre of the raft to the sides under turbine operation, with the magnitude trending with wind speed and direction. Higher pressures were observed in the leeward end of the raft, with the extent decreasing towards the centre. They concluded from these measurements and corresponding triaxial testing results that the reduced shear modulus concept adopted in design is three times smaller than the measured in-situ values, resulting in the potential over-design of foundations, with the shear strain in the soil being significantly smaller than the assumed 10^{-3}. Thus, soil degradation is effectively less of a problem than what is assumed during design.

Although SHM projects have been around for years, providing a better understanding of many complex engineering problems, these projects have been lagging significantly in monitoring wind turbines and wind turbine foundations. Due to cost constraints, SHM of full-scale foundations remains scarce, apart from the rapidly expanding wind energy market. All research on full-scale wind turbine foundation tests has focused on raft foundations, leaving much to be investigated when piles are introduced. In addition, this research has primarily been focused on failure mode-based monitoring, giving little consideration to soil-structure interaction and how it can be used to improve our understanding of the design of future wind turbine foundations. Do the numerical models used for predicting the response of these structures, which were not initially developed for wind turbine application, still apply, and are there any additional factors, for example, environmental effects, that need to be considered?

2.7 THERMAL CONDUCTIVITY OF SOILS

Investigating the response of a piled-raft foundation supporting an onshore wind turbine is the main focus of this thesis. However, given that the foundation is buried below the ground and interacting with the surrounding soil, it is also of note to consider the thermal properties of soils, how they are linked to their physical properties, and how, ultimately, they change seasonally and affect the structure adjacent to it. Florides & Kalogirou (2007) mentioned that any structure located below the ground surface has the potential to be affected by surface temperature changes, daily and seasonally. This results in a structure potentially expanding when temperatures increase and contracting when temperatures decrease. Due to the high thermal inertia of soils, surface temperature fluctuations, however, also diminishes with depth into the ground, remaining nearly constant at a particular depth throughout the year. Thus, the part of the structure closest to the top of the soil surface would be most affected by temperature changes.

Florides & Kalogirou (2007) indicated that the factors influencing the distribution of temperatures in the ground are as follows:

- Structure and physical properties of the ground.
- Ground surface cover.
- Climate interaction determined by air temperature, wind, solar radiation, air humidity and rainfall.

Additionally, Barry-Macaulay *et al.* (2013) mentioned that the thermal conductivity of soils varied with soil moisture content, density, mineralogical composition and particle size. They indicated that coarse grained soils was observed to have higher thermal conductivity, with thermal conductivity also increasing with an increase in dry density and moisture content. Increasing moisture content, increases the contact between particles, similar to an increase in dry density, repacking of particles, allowing for greater inter-particle contact.

Regarding the distribution of temperatures within soils, Popiel *et al.* (2001) categorised the ground into three zones. The first zone is referred to as the surface zone, up to a depth of 1 m, with the temperatures in the ground being quite sensitive to short-term changes in weather conditions. The second zone is located between either 1 m and 8 m for dry light soils or between 1 m and 20 m for moist heavy sandy soils, and is referred to as the shallow zone. Within this zone, Popiel *et al.* (2001) mentioned that the temperature in the ground is almost constant and close to annual air temperature, with the distribution of temperature within the ground mainly depending on the seasonal cycle weather conditions. The last zone, referred to as the deep zone is located below depths of between 8 m and 20 m. Within this zone,

temperatures in the ground is practically constant, and rising very slowly with depth according to the geothermal gradient (average temperature increase in the ground of 30ºC/km).

2.8   SUMMARY

Using wind turbines as an alternative for electricity generation is a growing market internationally. With the future focus on taller wind turbines, engineers are under pressure to design adequate foundations to support them. This literature review discussed various aspects regarding wind turbines and their supporting foundations' design under serviceability and ultimate limit state conditions. These aspects included the different foundation types and future wind turbine prospects, including how these prospects would potentially influence the magnitudes of loads on turbine foundations. In addition, critical design parameters, including foundation rotational stiffness, differential settlement and tilt, were addressed, as these parameters dictate the size of wind turbine foundations under dynamic loading. It was found that, given the increase in the size of modern wind turbines, piled-raft foundations proved more economical and practical for supporting these structures compared to the conventional raft foundation. Traditional methods for analysing and assessing these foundations are limited and based on semi-empirical formulas, disregarding important parameters. The pile cap or raft connecting the piles is nearly always assumed to be rigid. The potential contribution of the ground-contacting cap in carrying some loads or increasing the foundation stiffness is neglected, with the stiffness typically assumed to depend solely on the pile group. Multiple researchers have emphasised that the pile cap contribution should be considered, especially when piled rafts are increasing in size. Additionally, under horizontal loads and overturning moments, the interface between the piles and the raft (relative stiffness between the piles and the raft) proved critical when considering structural analysis and portal frame theories. Larger wind turbines also result in potentially more significant tensile forces in trailing piles. This phenomenon can be counteracted by either increasing the raft radius or decreasing the thickness of the raft. Design should thus consider a balanced approach, which still needs further investigation.

Given that the response of a foundation is based on soil-structure interaction, a great deal of the literature reviewed focused on it, as many researchers also argued that the future of designing efficient foundations lies in appreciating these concepts. It was also found that these interactions are pivotal when the dominant forces are horizontal loads and overturning moments. The basic concepts of soil-structure interaction relating to piled-raft foundations were discussed, considering the typical responses of these foundations under loading. Methods for assessing the stiffness of a piled raft were also addressed. Yet, these methods

tend to neglect the 3-D nature of the problem and the various interaction mechanisms involved between the different foundation components and these components and the supporting soil. FE modelling proved valuable, allowing the different interactions to be modelled more realistically. However, these models have been limited, with little consideration given to soil-structure interaction and how it affects foundation response. It was evident from the literature that most of these analyses were also focused on vertical loading as the dominant force, with the effect of horizontal loads and overturning moments being minimal.

Structural health monitoring and full-scale testing of wind turbine foundations were also considered. The behavioural monitoring of these foundations under operations is limited, with the number of functioning sensors installed also being small. In addition, little consideration is given to soil-structure interaction. The SHM of full-scale wind turbine foundations has only been on raft foundations, leaving much to be investigated for piled-raft foundations. Although centrifuge testing allowed for the soil-structure interaction concepts to be explored for piled-raft foundations under static and cyclic vertical and horizontal loading, these models did not capture environmental effects and seasonal temperature variations. Thus, determining whether these variations influence foundation response through full-scale monitoring is necessary. Additionally, these models did not consider the coupled overturning moment with the horizontally applied loads.

The typical response of soil under cyclic loading was also discussed, and the amount of permanent deformation was highlighted, which is related to not only the properties of the soil but also the magnitude of the applied load and the number of load cycles. The piles of a piled-raft foundation supporting a wind turbine socketed into bedrock should be instrumented to determine whether an increase in the number of load cycles on the foundation causes an increase in pile stresses. Thus, given the increase in the size of wind turbines planned for the future, modern concepts of soil-structure interaction are becoming popular and prove vital in ensuring efficient and economic foundations to support these structures. The design of piled-raft foundations is intricate due to the complicated load transfer and relevant soil-structure interaction mechanisms. With limiting gapping and settlement, potential cyclic degradation of soil, and meeting minimum rotational stiffness requirements, wind turbine foundation poses several design challenges. The subsequent chapters include a description of the instrumentation and monitoring of a full-scale wind turbine piled-raft foundation and the numerical modelling of these foundations to address the abovementioned concerns.

3 MONITORING OF A PILED-RAFT FOUNDATION

3.1 INTRODUCTION

This research aims to investigate the response of circular piled-raft foundations subjected to dominant horizontal loads typically accompanied by significant overturning moments. As evident from the first two chapters of this thesis, an example of such a case is an onshore wind turbine foundation, which, depending on the properties of the underlying soil, can have a piled-raft foundation. Horizontal loads and overturning moments caused by the wind have a much higher impact on the underlying foundation than the vertical load acting on the foundation from the turbine's self-weight. An intricate loading scenario which, combined with the complex soil-structure interaction between the foundation and the supporting soil and the structure-structure interaction between the different piled-raft foundation components, needs further investigation. In light of several successful structural health monitoring projects in the Department of Civil Engineering at the University of Pretoria in recent years (Kusel *et al*., 2018; Skorpen *et al*., 2021), a full-scale reinforced concrete piled-raft foundation supporting a newly constructed onshore wind turbine was instrumented and monitored for an extended period of time. Numerous instruments were embedded in the turbine foundation during construction and monitored continuously afterwards for different phases in the life of the turbine. These phases broadly included:

- the early-age foundation response during the construction of the piles and raft;
- the foundation response during the installation of the wind turbine structure before commissioning and commercial operations; and,
- the foundation response during commercial operations after commissioning.

Additionally, to supplement the foundation data, measuring equipment was installed at the base of the turbine tower prior to turbine installation to monitor the actual loads and moments experienced by the tower caused by the turbine's own weight and the external wind, both of which are ultimately transferred to the supporting foundation and underlying soil. Measuring these loads and moments would allow for the calibration of the foundation system and assist with the estimation of load sharing between the different foundation components, improving understanding of wind turbine foundation response, particularly piled-raft foundation response.

In summary, this chapter presents all aspects and results of the wind turbine foundation instrumentation and monitoring process, starting with the construction of the foundation and ending with the installation and operation of the wind turbine. Section 3.2 gives some

background on the wind farm location, turbine specifications, and size. This section is followed by a description and size of the instrumented foundation in Section 3.3, with Section 3.4 briefly highlighting the foundation's construction sequence and the wind turbine installation process. Sections 3.5 and 3.6 discuss the sensors installed within the foundation and wind turbine tower, their respective positions, and the systems used to monitor and record their output. As it forms a critical part of the data analysis, foundation calibration and numerical work covered in later chapters, the properties of the concrete used to cast the foundation were also measured and included in Section 3.7. Furthermore, Section 3.8 summarises the geotechnical properties of the soil on which the foundation and wind turbine were constructed. The chapter concludes with Sections 3.9 and 3.10, discussing and summarising all the results obtained from the instrumentation and monitoring processes, focusing on the critical phases mentioned above and the points highlighted at the end of Chapter 2.

3.2   WIND FARM LOCATION AND WIND TURBINE DESCRIPTION

The instrumented foundation is located on the Wesley-Ciskei Wind Farm (see **Figure 3-1**) and is the foundation of one of ten newly constructed Vestas V126-3.45 MW wind turbines. The farm is next to the R72 provincial road near the town of Wesley in the Eastern Cape Province, South Africa, approximately 200 km North-East of Port Elizabeth (see **Figure 3-2**).

Figure 3-1: Wesley-Ciskei Wind Farm

Each turbine on the farm has a hub height of 117 m, a rotor diameter of approximately 126 m and a generating capacity of 3.45 MW, giving the entire wind farm a combined capacity of 34.5 MW, which is equivalent to powering around 22 400 South African households annually (EDF Renewables, 2022). The farm is owned by Riverbank Wind Power (RF) (Pty) Ltd and managed by EDF Renewables (Pty) Ltd [South Africa]. Vestas Southern Africa (Pty) Ltd was appointed and responsible for all Engineering, Procurement and Construction (EPC) processes, including all civil and electrical works, transportation and logistics, as well as the

supply and installation of the wind turbines. They are also acting as the Maintenance and Operations (M&O) contractors during the lifespan of these turbines.

Figure 3-2: Wind farm location (Google Maps, 2022)

3.3   FOUNDATION DESCRIPTION

Due to significant variations in the depth and properties of bedrock across the entire farm, turbine foundation types for the ten new wind turbines varied between the conventional raft (or gravity base) foundations and piled-raft foundations, all circular and constructed from reinforced concrete. Based on the aim of this study, the foundation selected for instrumentation was a piled-raft foundation, referred to as WTG09, for the remainder of this thesis.

Figure 3-3 shows a schematic of the WTG09 foundation, indicating the main foundation components and respective dimensions. The raft had a base diameter of approximately 15.5 m and a minimum thickness of 1.85 m. The top of the raft was not flat and had a slight inclination (or cross fall) of about 5°. A 7.2 m diameter pedestal extended 0.9 m from the top of the raft to which the turbine was connected through an anchor cage cast into the raft, with the cage extending the entire depth of the raft. Ten 900 mm piles were augered, positioned along a perimeter with a radius of about 6.675 m from the centre of the raft, extending down to bedrock. Piles were socketed into the bedrock (end-bearing) and were connected (tied) to the raft through reinforcing bars sticking out from the top of the cast piles exposed after trimming. Due to fluctuating depths of bedrock at the position of the WTG09 foundation, pile

lengths varied from 16.7 m to 17.9 m, with the depth of socketing varying between 1.5 m when sandstone was encountered and 2.5 m when either mudstone or siltstone were encountered.
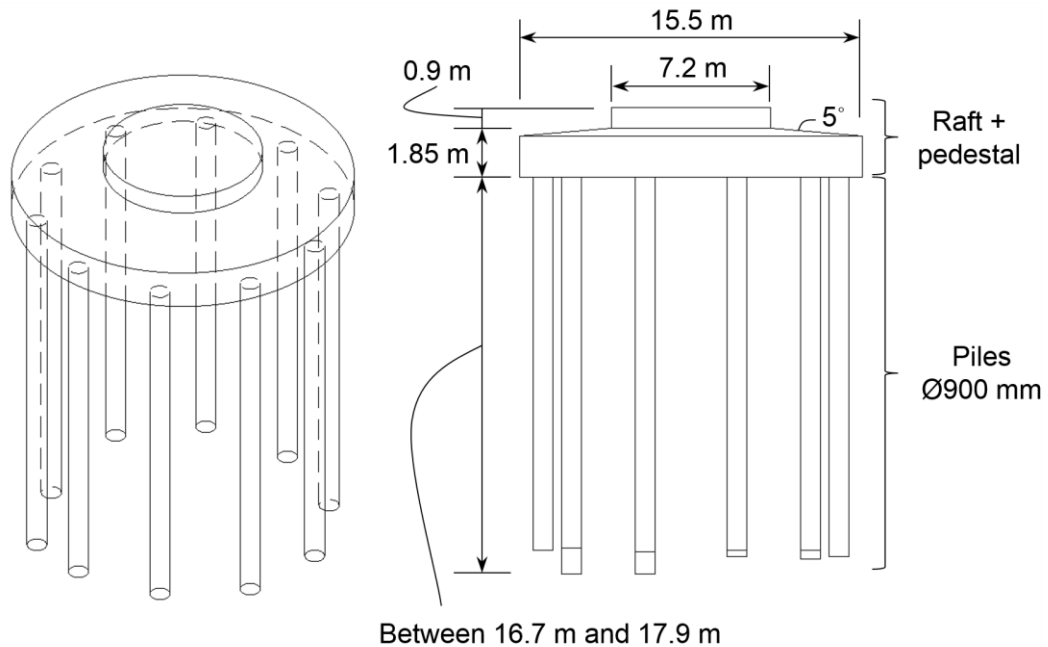
Figure 3-3: WTG09 foundation schematic

3.4 FOUNDATION CONSTRUCTION SEQUENCE AND TURBINE INSTALLATION

Construction on the entire wind farm began towards the end of 2019, with the preparations and casting of the WTG09 foundation only starting a few months later, in February 2020. All construction-related events on the WTG09 foundation were completed by August 2020, followed by final preparation and sign-off before turbine installation and commissioning. In summary, the construction process started with the casting of the piles after excavation, followed by pile trimming, casting of a blinding layer and the installation of the anchor cage that connects the wind turbine to the foundation. The raft reinforcing cage was then constructed on top of the blinding layer, around the pre-installed anchor cage, after which the raft was cast. Once the raft was cast, backfilling of the previously excavated soil followed. **Figure 3-4** indicates the completed foundation after casting, before backfilling about 1.1 m of soil, with the top portion of the anchor cage visible in the centre of the pedestal.

Wind turbine installation at WTG09 began in February 2021, with assembly completed within a few days. **Figure 3-5** indicates the completed wind turbine at WTG09 after installation, highlighting the various turbine components. The entire wind farm was commissioned in June 2021 and became fully operational in August 2021.

Figure 3-4: Completed WTG09 foundation
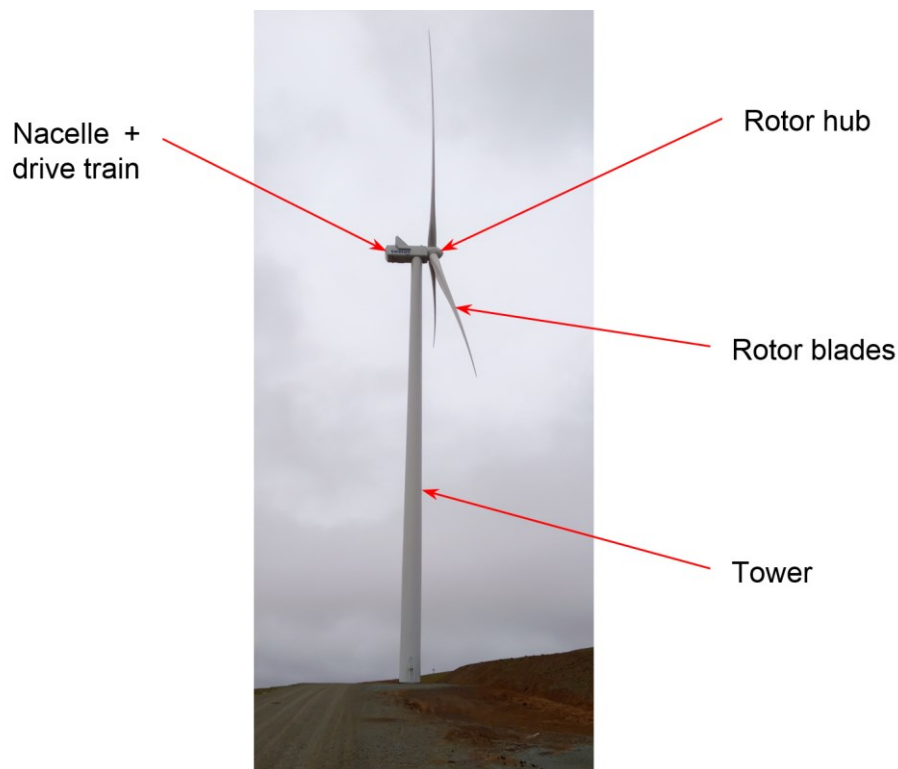
Figure 3-5: Completed WTG09 turbine installation

3.5   SENSORS, PLACEMENT AND LABELLING

During foundation construction and turbine installation, several instruments were embedded within the foundation or installed inside the turbine tower as part of the structural health monitoring system. With the research focusing on static monitoring of the foundation, sensors were selected based on long-term reliability, durability during harsh installation conditions and environments, and ease of installation to limit any delays during construction. This section introduces all the sensors installed, their respective positions, and the labelling convention used when plotting and presenting the data later in this chapter.

3.5.1 Foundation

For the foundation, a total of 31 concrete embedment vibrating wire strain gauges (VWSGs) with built-in thermistors were installed by the author as they proved to be best suited and most durable for this type of application based on past instrumentation projects conducted by the University of Pretoria (Kusel *et al.*, 2018; Skorpen *et al.*, 2021). Apart from that, VWSG also has the ability to measure the thermal and mechanical strain experienced by the concrete at a particular location from a single sensor. Thermal strain refers to the strain generated in the concrete due to temperature changes. In contrast, mechanical strain typically refers to strain caused by external load application, concrete shrinkage, or even differences between thermal strains at different parts of the structure. **Figure 3-6(a)** and **(b)** indicate examples of VWSGs installed within the piles and the raft, respectively, attached to the main reinforcing bars before being cast into the concrete.
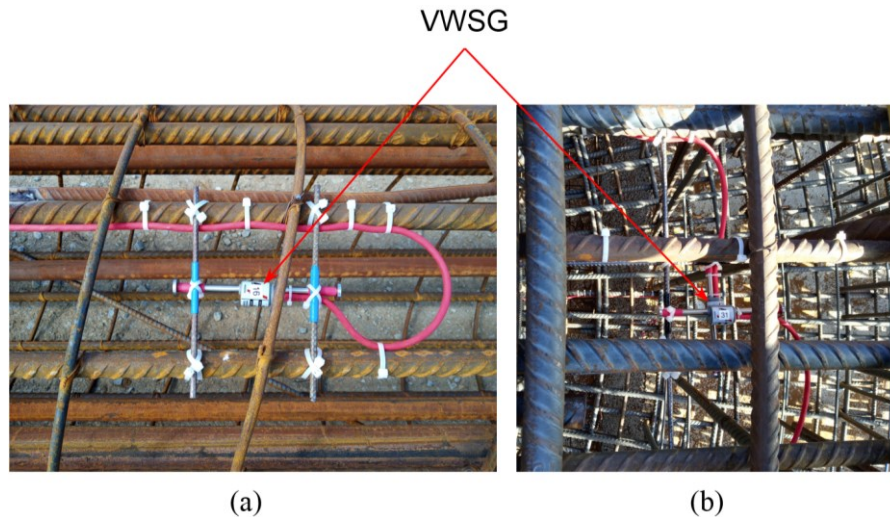
Figure 3-6: Installed VWSG: (a) pile; (b) raft

In order to distinguish between the mechanical and thermal strains experienced by the concrete, **Equation 3-1** and **Equation 3-2** were used on all the measured VWSG data, with the sum of the two strains typically referred to as the total strain experienced by the concrete.

$$\varepsilon_{mechanical} = (R_m - R_0) + (T_m - T_0)(C_1 - C_2) \tag{3-1}$$

$$\varepsilon_{thermal} = (R_m - R_0) + (T_m - T_0)(C_2) \tag{3-2}$$

where R_0 is the initial strain, R_m is the strain at any given time m, T_0 is the initial temperature, T_m is the temperature at time m, C_1 is the coefficient of thermal expansion of the VWSG steel wire (taken as 12.20 με/°C according to instrument calibration sheet), and C_2 is the coefficient of thermal expansion of the surrounding concrete.

For the piles, 17 of the 31 concrete embedment VWSGs were installed. A VWSG was located in each of the ten piles at a depth of 2.5 m below the bottom surface of the raft (see **Figure 3-7**). For the two piles in the prevailing wind direction (south-westerly according to initial investigative site reports), indicated by the dotted circles in **Figure 3-7(a)**, additional VWSGs were placed at depths of 0.5 m and 4.5 m, respectively (see **Figure 3-7(b)**). For Pile 54 P, in particular, sensors were placed on opposite sides of the pile at these three depths, allowing for the axial and bending stresses of the pile to be assessed. Based on initial numerical modelling and the literature covered in Chapter 2, the maximum bending moment was expected towards the top of the piles. Thus, sensors were concentrated and only installed within this region. For explanation purposes, **Figure 3-7(c)** was included to indicate the leading and trailing pile reference convention used in the remainder of the document. Based on the direction of the wind load, leading piles are considered as the piles located on the leeward side of the foundation, with trailing piles located on the windward side of the foundation.

A global labelling coordinate system was applied to all the sensors installed within the foundation. In the case of the piles, each pile in **Figure 3-7(a)** is labelled as indicated in black, with 'P' referring to 'Pile' and the accompanying number corresponding to the position of the pile from the centre of the raft relative to North, expressed in degrees. The following number in blue denotes the VWSG depth below the raft's bottom surface, either at 0.5 m, 2.5 m or 4.5 m, respectively. Lastly, the green portion indicates each sensor's position relative to the centre of each individual pile, with 'L' referring to 'Local Coordinate' and the corresponding number indicating the sensor's position relative to the outside of the pile facing away from the foundation centre, expressed in degrees. For example, if the value reads 'L 0', the sensor is located on the outermost point on the side of the pile facing towards the outside of the foundation. Additionally, if the value reads 'L 180', the position of the sensor in a pile is facing towards the foundation's centre and is the innermost point. Values of sensor positions between these extremes are obtained in a clockwise convention. For further explanation, these positions are also indicated by the circular red markers in **Figure 3-7(a)**.

The remaining 14 concrete embedment VWSGs were installed at four locations, in both the top and bottom of the raft, in either the radial or transverse directions, or both. **Figure 3-8(a)** and **(b)** present the position of the VWSGs installed within the raft part of the piled-raft foundation. The positions of the sensors were selected where, theoretically, the highest bending moment should occur within the raft, placed at locations in the prevailing wind direction and the direction perpendicular to that. Similar to the labelling system used for the piles, the position of the VWSGs was expressed in degrees relative to North, as indicated in black, with 'R' referring to 'Raft' in this case. Furthermore, 'B' and 'T' in blue refer to the

position of the sensor at either the 'Bottom' or 'Top' of the raft, whereas 'Ra' and 'Tr' in green indicate the sensor's placement in either the radial or transverse directions, respectively.
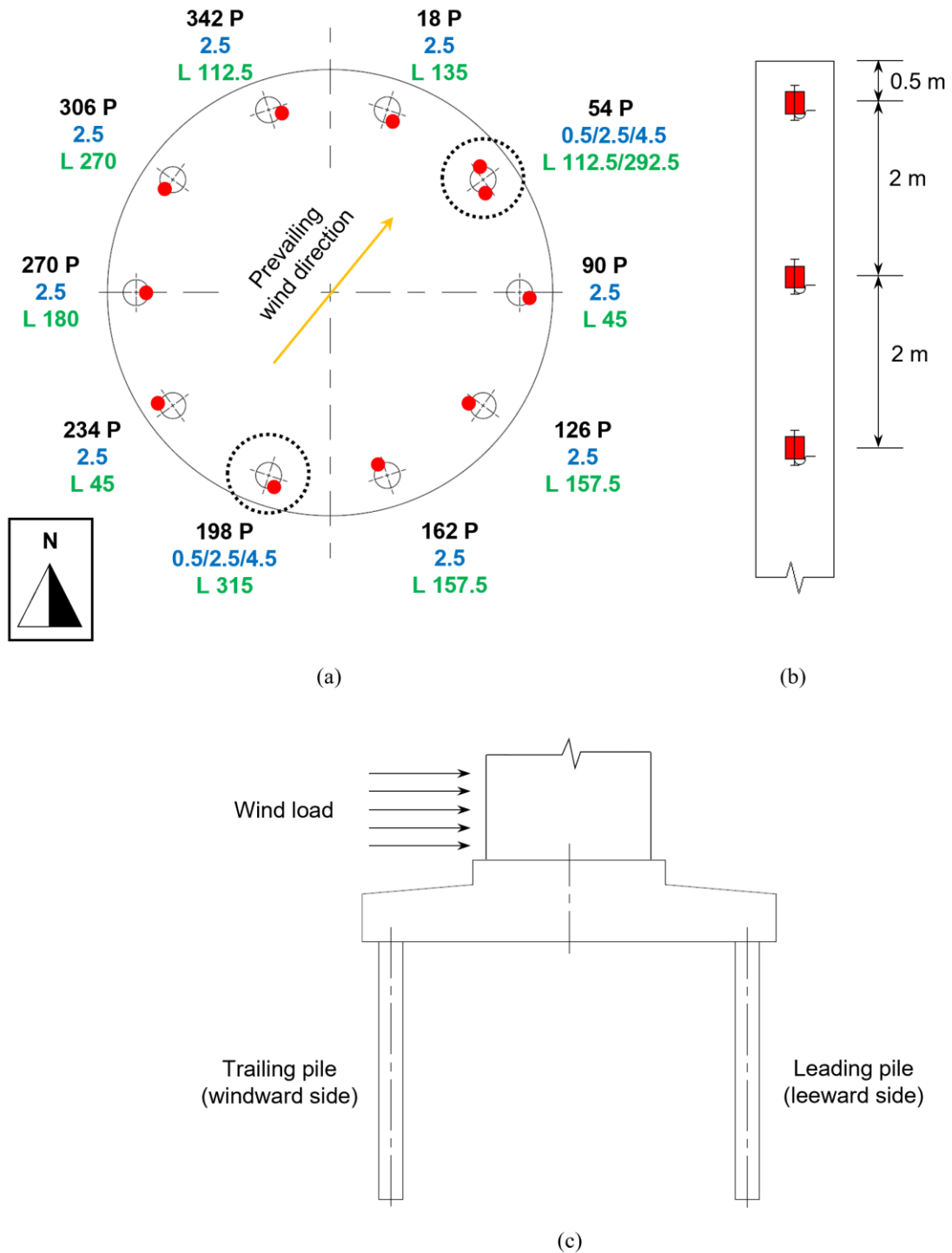
Figure 3-7: Instrumentation placement – piles: (a) plan view; (b) cross-section; (c) leading-trailing pile position relative to wind direction

3-8
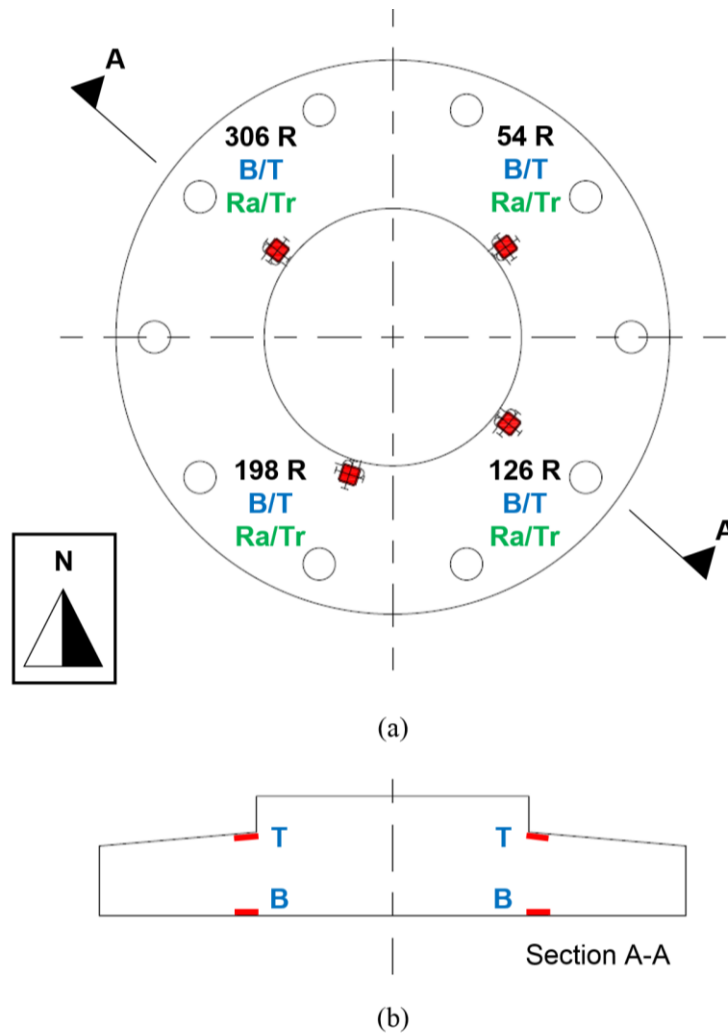
Figure 3-8: Instrumentation placement – raft: (a) plan view; (b) cross-section

3.5.2   Wind turbine tower

Sensors were installed inside the bottom section of the tower before the top portion of the turbine was constructed. The placement of these sensors allowed for the tower's response to be monitored during turbine installation and operation, aiding in quantifying the true magnitude of the loads and moments being transferred to the underlying foundation. Eight 120 Ohm quarter-Wheatstone bridge strain gauges (WBSGs) were installed at the base of the wind turbine tower to obtain independent strain readings (see **Figure 3-9**). WBSGs were positioned at four locations along the inside circumference of the bottom tower section (see **Figure 3-10(a)** and **(b)**), 1.5 m from the base of the tower. The location of the sensors was again selected to be in the prevailing wind direction and the direction perpendicular to that. At each position, two gauges were placed perpendicular to one another, with the vertical gauges measuring axial strain and the horizontal gauges only used for temperature compensation. Each location in **Figure 3-10(b)** is labelled as indicated in black, with 'W' referring to 'Wind

Turbine' and the accompanying number corresponding to the position of the strain gauges from the centre of the turbine and foundation relative to North, expressed in degrees. The height of 1.5 m was considered close enough to the bottom of the tower but not close enough to encounter possible stress concentrations near where the turbine tower connects to the underlying foundation.
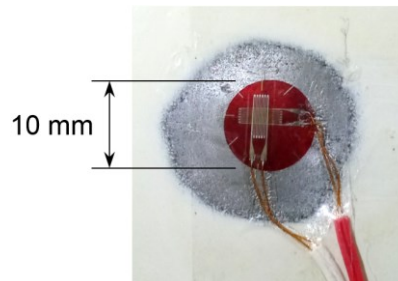
Figure 3-9: Installed WBSG - base of the turbine tower
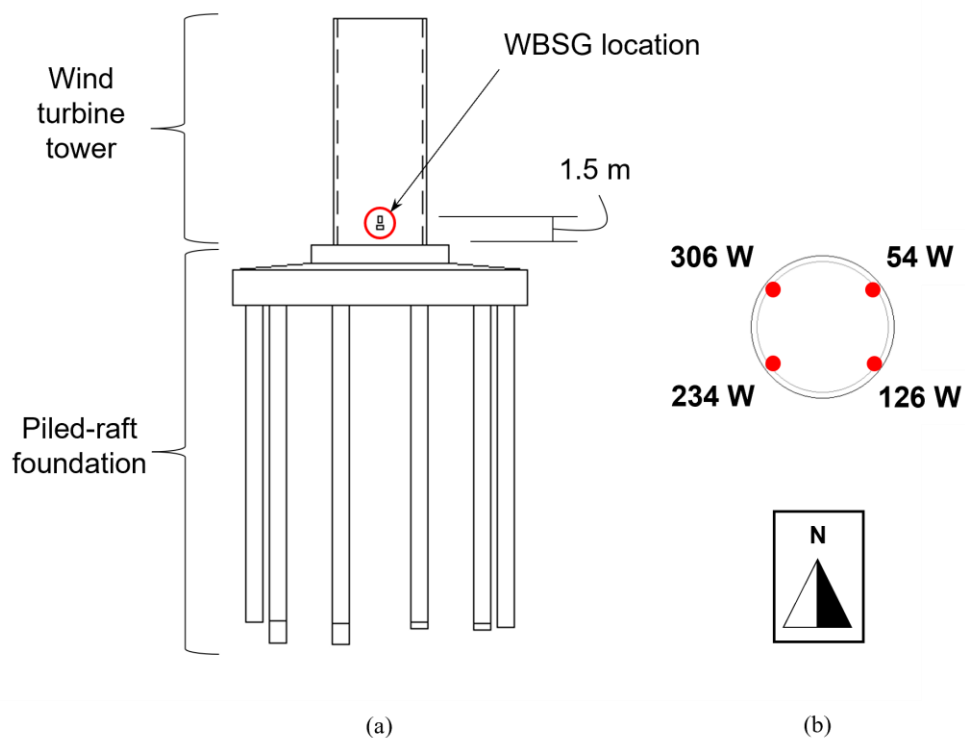
Figure 3-10: Instrumentation placement – base of the turbine tower: (a) cross-section; (b) plan view

By measuring independent strain (quarter-Wheatstone bridges) on opposite sides of the tower, it was possible to distinguish between axial forces caused by the weight of the turbine structure and bending moments experienced by the tower caused by the wind. **Equation 3-3** and **Equation 3-4** presents the formulas for calculating these forces and moments, respectively, and were used to interpret all the measured data from the tower.

$$F_t = \frac{(\varepsilon_1 + \varepsilon_2)E_t A_t}{2}$$ (3-3)

$$M_t = \frac{(\varepsilon_1 - \varepsilon_2)E_t Z_t}{2}$$ (3-4)

where F_t is the axial force experienced by the tower, E_t is the Young's modulus of the tower steel (taken as 210 GPa, Gere & Goodno, 2013), A_t is the cross-sectional area of the bottom section of the tower, M_t is the bending moment experienced by the tower, Z_t is the sectional modulus of the bottom section of the tower, and ε_1 and ε_2 is the temperature compensated strain measured on opposite sides of the tower.

3.6   MONITORING SYSTEMS

Measurements were only taken when construction activity allowed throughout the construction process of the foundation, as well as during turbine installation and after commissioning, to assess the foundation and turbine response under working load conditions (turbine operations). All measurements from the VWSG sensors embedded in the raft and piles were taken using a commercially available Campbell Scientific CR6 measurement and control datalogger (see **Figure 3-11**), accompanied by two AM 16/32B multiplexers to increase the number of channels available to log simultaneously.
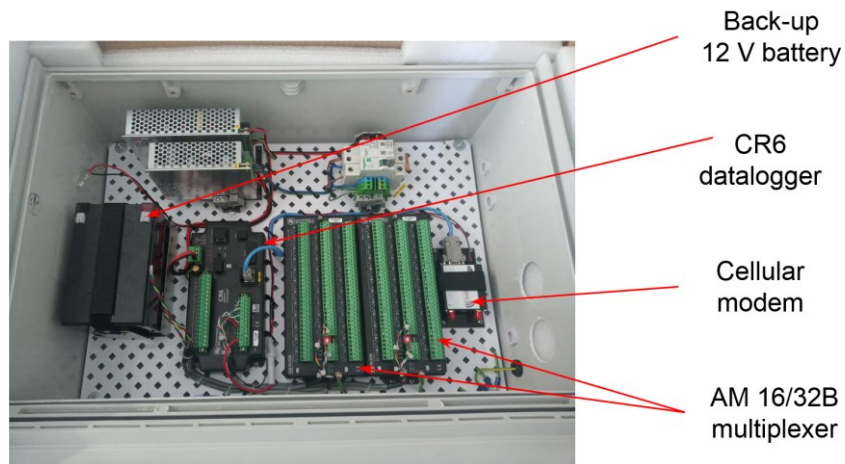
Figure 3-11: Campbell Scientific datalogger and remote monitoring system

A multi-channel Arduino-based differential voltage data acquisition system developed at the University of Pretoria was used to measure the output of the WBSG strain sensors at the bottom of the turbine tower (see **Figure 3-12**). The low-cost datalogger system combined an Arduino microcontroller as the primary data acquisition system, quantifying the differential voltage outputs associated with the WBSGs using high-resolution analog-to-digital

3-11

converters. A secondary simple single-board computer, known as a Raspberry Pi, was included to relay information from the Arduino microcontroller to two independent data platforms for storage and analysis. For more details on the development process, circuit design, data conversion and hardware costs, refer to Louw *et al*. (2022b).

With the focus on static monitoring of the wind turbine and wind turbine foundation, measurements on both systems were taken at 15-minute intervals. After turbine installation, both dataloggers were placed inside the wind turbine mast, connected to the electrical power supply of the turbine, with data monitored and downloaded remotely using cellular modems.
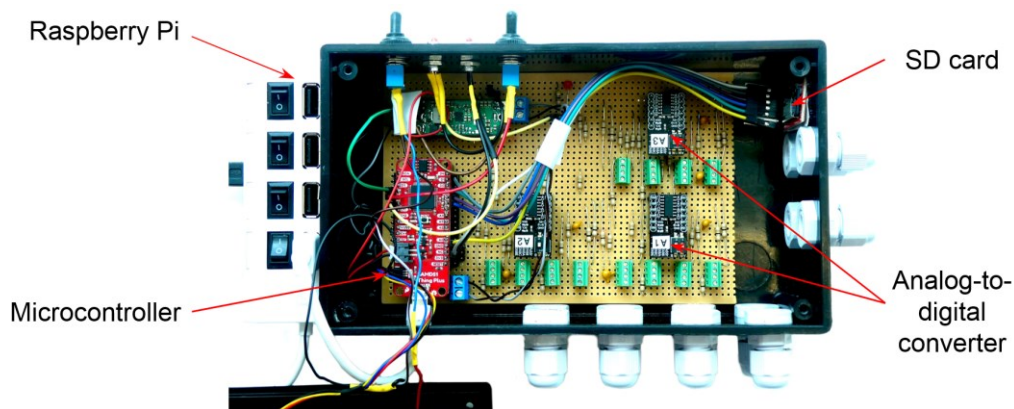
Figure 3-12: Arduino-based microcontroller datalogger developed at the University of Pretoria

3.7   MEASURED CONCRETE PROPERTIES

One of the critical aspects of this research project was soil-structure interaction. It was thus essential to determine the actual properties of the concrete used to construct the reinforced concrete foundation for data analysis, interpretation, and calibration. Samples of the fresh concrete used to cast the different foundation components (piles and raft) were taken on-site on the respective casting dates. The fresh concrete was then used to cast a number of test specimens to obtain the actual concrete properties. For concrete characterisation, properties including strength, stiffness, shrinkage and coefficient of thermal expansion, all of which were deemed important to address the objectives being studied. All pile and raft concrete mixes contained locally-sourced dolerite stone and crusher dust as aggregate components.

3.7.1   Concrete strength and stiffness properties

Measured concrete strength and stiffness properties included the compressive strength, indirect tensile strength, and modulus of elasticity, with sample preparation and testing methods in accordance with BS EN 12390-3:2019, BS EN 12390-6:2009 and BS EN 12390-13:2021, respectively. After casting the test specimens, the respective concrete samples were covered and cured overnight inside the mould next to the piles and raft, after which they were

demoulded and wrapped in plastic the following day. Samples were then transported to the Civil Engineering Laboratory at the University of Pretoria for testing at the respective ages. The indirect tensile strength was obtained by splitting 100 mm diameter cylinders, with the density and compressive strength measured by weighing and crushing 100 mm cubes. For determining the secant modulus of elasticity, 100 mm diameter cylinders, 200 mm long, were loaded to 40% of its compressive strength (typically assumed elastic zone for concrete), measuring the deformation of each cylinder using a standard collar over the central two-thirds of the cylinder. **Table 3-1** and **Table 3-2** summarise the measured concrete properties for the piles and the raft, respectively. Concrete samples were only tested in compression after 28 days as a reference according to standard testing procedures, whereby the long-term properties (> 180 days) included the indirect tensile strength and secant modulus of elasticity, along with the compressive strength and density of the concrete. These values are more representative of the actual properties of the concrete compared to 28-day strengths and will, therefore, be used for the remainder of this thesis.

Table 3-1: Concrete properties summary - piles

Property	28 days	Long-term (> 180 days)
Compressive strength (MPa)	52.9	84.4
Splitting tensile strength (MPa)	-	5.6
Secant modulus of elasticity (GPa)	-	43.5
Density (kg/m^3)	2517	2541

Table 3-2: Concrete properties summary - raft

Property	28 days	Long-term (> 180 days)
Compressive strength (MPa)	54.1	91.7
Splitting tensile strength (MPa)	-	5.4
Secant modulus of elasticity (GPa)	-	47.3
Density (kg/m^3)	2602	2622

Considering the long-term strengths in **Table 3-1** and **Table 3-2**, a significant increase in compressive strength was observed for both foundation components after 28 days. The measured secant moduli of elasticity for the piles and raft after 180 days were also high compared to normal-strength concrete mixes, with strengths typically ranging between 20 MPa to 80 MPa. According to Alexander & Mindess (2005), this high secant modulus of elasticity could be attributed to either the type and stiffness of aggregate used, the resulting packing density of the concrete matrix or the interface characteristics between the cement paste and aggregate. However, it should be mentioned that the measured secant modulus of elasticity values was still within the ranges for predicting the elastic modulus of concrete from its compressive strength for concretes made with South African aggregates (Alexander &

Mindess, 2005). In addition, by measuring the concrete's secant modulus, compressive strength and indirect tensile strength, it was possible to approximate the range of strains in which the foundation will behave 'elastically'. Applying Hooke's law to the concrete's indirect tensile strength and secant modulus, it was found that the piles and raft will crack at a tensile strain value of approximately 129 με and 114 με, respectively. Similarly, under compression, the piles and raft will remain in an elastic state up to a compressive strain of 775 με and 776 με, respectively, assuming 40% of the concrete's compressive strength and dividing it by the secant modulus. These calculated values will be used to assess the measured strains in the foundation presented later in this chapter.

3.7.2 Concrete shrinkage measurements – reference cylinders

Soutsos & Domone (2018) mentioned that the size and shape of concrete specimens significantly affect shrinkage. When concrete is curing, the only way water can be lost is through its surfaces, with the inner core of that specimen acting as a restraint against overall movement. The rate of moisture loss, and hence shrinkage, will depend on the rate of water transfer from the core to the surface. Thus, larger concrete specimens or masses will have longer diffusion paths, lowering shrinkage rates. Considering the size of the raft that was cast, it was necessary to estimate the shrinkage experienced by the concrete in the core of the raft, enabling its influence to be subtracted from the measured mechanical strains obtained from the foundation under working load conditions.

For this reason, two additional 250 mm diameter, 500 mm long reference cylinders were cast from the concrete samples taken from the raft mix. Each reference cylinder contained a VWSG positioned in the centre, midway from the bottom, enabling the measurement of strains as the concrete shrinks (see **Figure 3-13**). After casting, both cylinders were closed and sealed to prolong the shrinkage process, simulating conditions similar to that experienced by the core of the raft, where the shrinkage rate is restricted by both the size of the raft and the overburden and confining soil from backfilling. **Figure 3-14** presents the average concrete shrinkage data obtained from the two cylinders, measured from the start of the cast.

Initially, the fresh concrete experienced tensile (negative) strains due to the heat generated during the hydration process between the cement and the water, resulting in slight swelling of the cement paste. This normally occurs when the hydration reactions proceed most rapidly, typically within the first few days after cast (Soutsos & Domone, 2018). After achieving a peak of swelling (at about -50 με), the concrete started to shrink at a gradually decreasing rate, with shrinkage potentially contributing up to 120 με to the measured strain in the raft.

Figure 3-13: Reference cylinders

Shrinkage measurements within the first few months after casting appear to be 'noisy'. According to Skorpen (2020), this 'noise' can be attributed to the heat sync effect of the cylinder and the continually changing surface temperatures resulting in small temperature (thermal) gradients through the cylinder. Both cylinders were kept on-site for the first six months, thus experiencing the same day-night temperature changes as the turbine foundation. Similar to the concrete specimens cast for obtaining the strength properties, both reference cylinders were later transported to the University of Pretoria, where they were kept sealed in a temperature-controlled room at 25°C, with shrinkage measurements on both cylinders continuing.
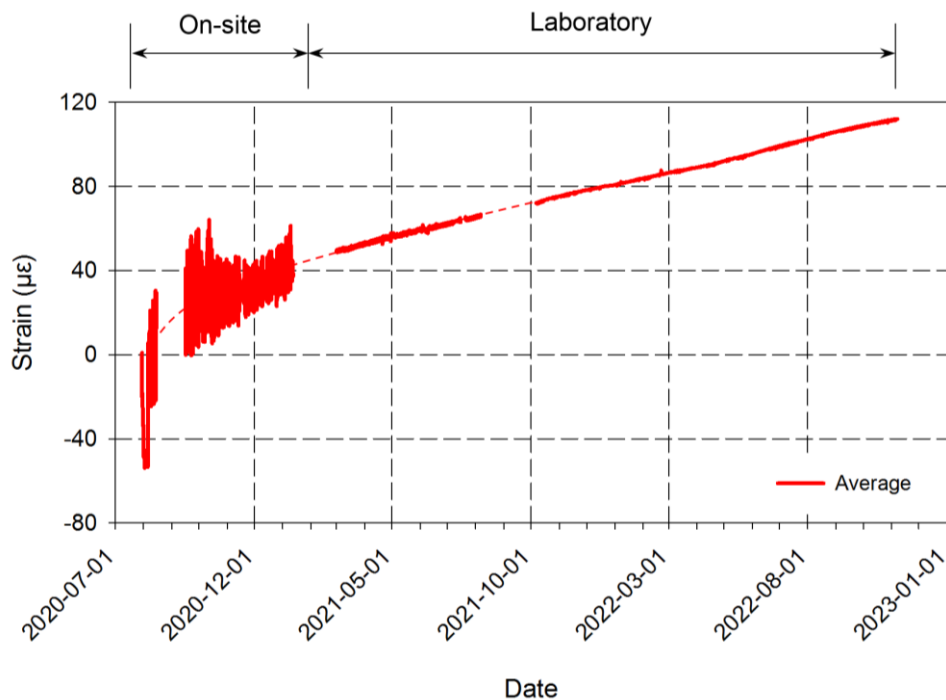
Figure 3-14: Shrinkage measurements

3.7.3 Thermal expansion coefficient

The thermal expansion coefficient of the concrete cast on-site was determined from the two instrumented reference cylinders used for measuring the concrete shrinkage. As mentioned in Section 3.5, VWSGs can simultaneously measure the mechanical and thermal strains experienced by the concrete. Thus, using the daily temperature changes measured from the built-in thermistor and the corresponding changes in mechanical and thermal strains in the concrete, a line of best fit could be plotted (see Appendix), with the gradient equalling the coefficient of thermal expansion. The coefficient of thermal expansion was determined as 8.46 $\mu\varepsilon$/˚C.

3.8 SITE CONDITIONS AND GEOTECHNICAL ASPECTS

All results presented in this section regarding the properties of the soil were obtained from the geotechnical site investigation report (Geotechnical Report, 2014) provided by the contractor. The report was compiled for the proposed Wesley-Ciskei Wind Farm before the start of construction. Only results about the soil conditions at the location of the instrumented foundation (WTG09) are summarised, and only properties applicable to the study are included.

The instrumented foundation is the southernmost wind turbine on the farm (see **Figure 3-15**). It is situated on a hill at an elevation of 130 m above sea level, with a thick layer of silty aeolian sands present to depths of about 22 m. Standard soil tests were conducted in a laboratory on samples taken from a number of test pits and boreholes, with test pits excavated to a maximum depth of three metres and boreholes drilled to bedrock, allowing for some extension into bedrock. According to the Unified Soil Classification (USC) System, the soil can be classified as clayey sand (SC) with plastic fines. Standard Penetration Test (SPT) results indicated medium-dense to dense soil conditions over a depth range between 0.8 m and 3 m. Borehole core samples indicated an in-situ dry and wet density of 1482 kg/m^3 and 1862 kg/m^3 at depths between 1.1 m and 1.3 m, and 1780 kg/m^3 and 2070 kg/m^3 at depths between 14.6 m and 14.9 m, respectively. To assess the variation in small strain stiffness (G_0) of the soil with depth, Continuous Surface Wave (CSW) testing was also conducted, with results summarised in **Table 3-3**. The underlying bedrock comprised alternating layers of mudstone, siltstone and sandstone, with the groundwater table located 25 m below the soil surface (based on standpipe piezometer measurements).
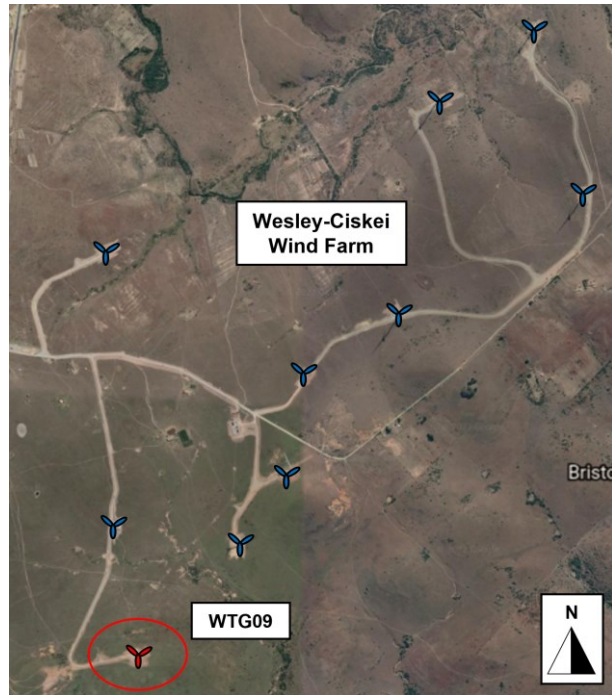
Figure 3-15: Wind turbine position - WTG09 (Google Earth, 2022)

Table 3-3: Continuous Surface Wave (CSW) testing results – small strain stiffness with depth

Soil depth (m)	G_0 (MPa)
0.0 – 8.2	200
8.2 – 14.1	350
14.1 – 18.1	1100
> 18.1	> 4000

3.9 RESULTS AND DISCUSSION OF FOUNDATION AND TURBINE MONITORING

This section presents and discusses all the results obtained from the static field monitoring of the instrumented wind turbine and foundation. The available data span a total of 33 months, covering several phases, starting with the early-age response of the foundation during construction and ending with the foundation response during wind turbine installation and initial operation. Given the provided on-site concrete and soil properties summarised in the previous sections, along with the foundation's dimensions, the rigidity of the foundation was determined to get an idea of the size and stiffness of the constructed foundation relative to that of the soil. These calculations were based on formulas presented by Clancy & Randolph (1993), with the values providing some background to the results and trends presented and observed in this section. Taking the thickness, radius, Young's modulus and Poisson's ratio of the raft as 1.85 m, 7.75 m, 47.3 GPa and 0.2, respectively, along with the Young's modulus and Poisson's ratio of the soil as 260 MPa and 0.3, respectively, the raft-soil stiffness ratio (K_{rs}) was calculated as 2.7. The soil Young's modulus was determined from the measured

3-17

G_0 values, which are discussed in more detail in Chapter 4. This raft-soil stiffness ratio can be considered relatively rigid based on the literature in Chapter 2. Furthermore, the pile-soil stiffness ratio (K_{ps}) was calculated as 182.7 and the pile slenderness ratio (L_p/d_p) as 19, taking an average between all the pile lengths. It should be emphasised that, given that the piles are socketed into bedrock, the average length of the piles also corresponds to the average depth of the compressible soil layer.

As a brief introduction and overview of what to expect in the following section, **Figure 3-16(a)** and **(b)** present all the strain measurements in the raft and piles for the entire monitoring period, highlighting the abovementioned phases. The data presents the total strain measured in the foundation, including the strains induced by external loads (in this case, the tower's self-weight and vibrations) and concrete shrinkage, as well as that caused by seasonal temperature changes. As seen in **Figure 3-16**, the monitoring schedule was interrupted from time to time before commercial turbine operation. These interruptions were attributed mainly to either construction activity on-site or the reliance on battery power for obtaining measurements, as the turbine and loggers were not yet connected to the grid at these times. To better understand the response of the wind turbine foundation, Sections 3.9.1 to 3.9.4 concentrate on each of the phases individually, discussing the measured results, including a brief overview of initial time effects. Apart from the strain measured during the construction phase of the raft, which is mainly thermal, the horizontal loads and overturning moments caused by the wind had a much higher impact on the supporting foundation than the loads induced by the self-weight of the turbine. Even though the foundation is buried below the soil after construction, seasonal variations (changes in thermal strain) can also be observed from the raft strains between the summer months starting in December and the winter months starting in June. Most of the data presented focus on mechanically induced strain. However, thermally induced strains are mentioned where they are deemed critical to the overall response of the foundation. Given the large amount of data measured, the section on turbine operations will focus only on the first year of operations, as indicated in **Figure 3-16**. The sign convention adopted for plotting the site data followed standard geotechnical practices, whereby positive strain is considered compressive and negative strain is considered tensile. Subsequently, negative loads are indicative of tensile loads, while positive loads represent compressive loads.

3.9.1   Early-age foundation response during raft construction

To investigate the early-age foundation response of the raft and piles after the raft was cast, strain and temperature data obtained from the installed VWSGs were recorded continuously for two weeks after the raft was cast.
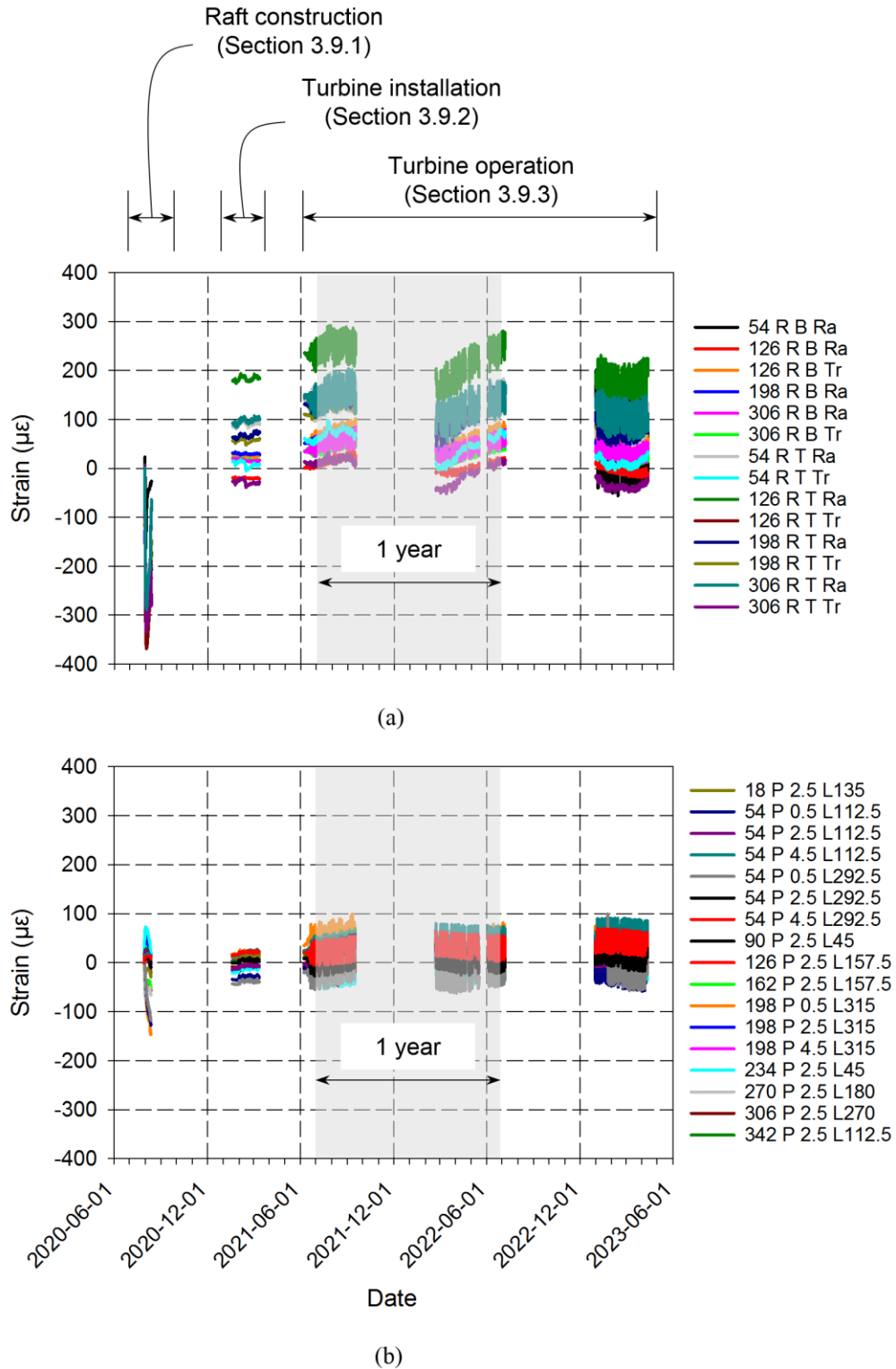
Figure 3-16: Total strain measurements: (a) raft; (b) piles

Figure 3-17(a) and **(b)** indicate the strain and temperature measurements for the sensors at the bottom and top of the raft, respectively. The strain data represents the total strain (sum of the mechanical and thermal strain) measured in the concrete. Within the first few days, the total strain measured in the raft was dominated by the thermal effects due to the exothermic

3-19

reaction caused by the heat of hydration process, resulting in tensile (negative) strains. The maximum temperature in the raft caused by the heat of hydration of the concrete only occurred after approximately five days from the start of the cast (see **Figure 3-17(a)** and **(b)**), with the maximum temperature towards the top of the raft being 10˚C higher than that experienced at the bottom. This temperature difference results in a slight thermal gradient within the concrete section (thermally induced mechanical strains), potentially causing premature concrete cracking if not controlled. Yet, these differences are less than the limits specified by DNV/RisØ (2002) of between 12ºC and 15ºC, respectively. Considerations should thus be given when casting even larger foundations, as this difference might become more significant.
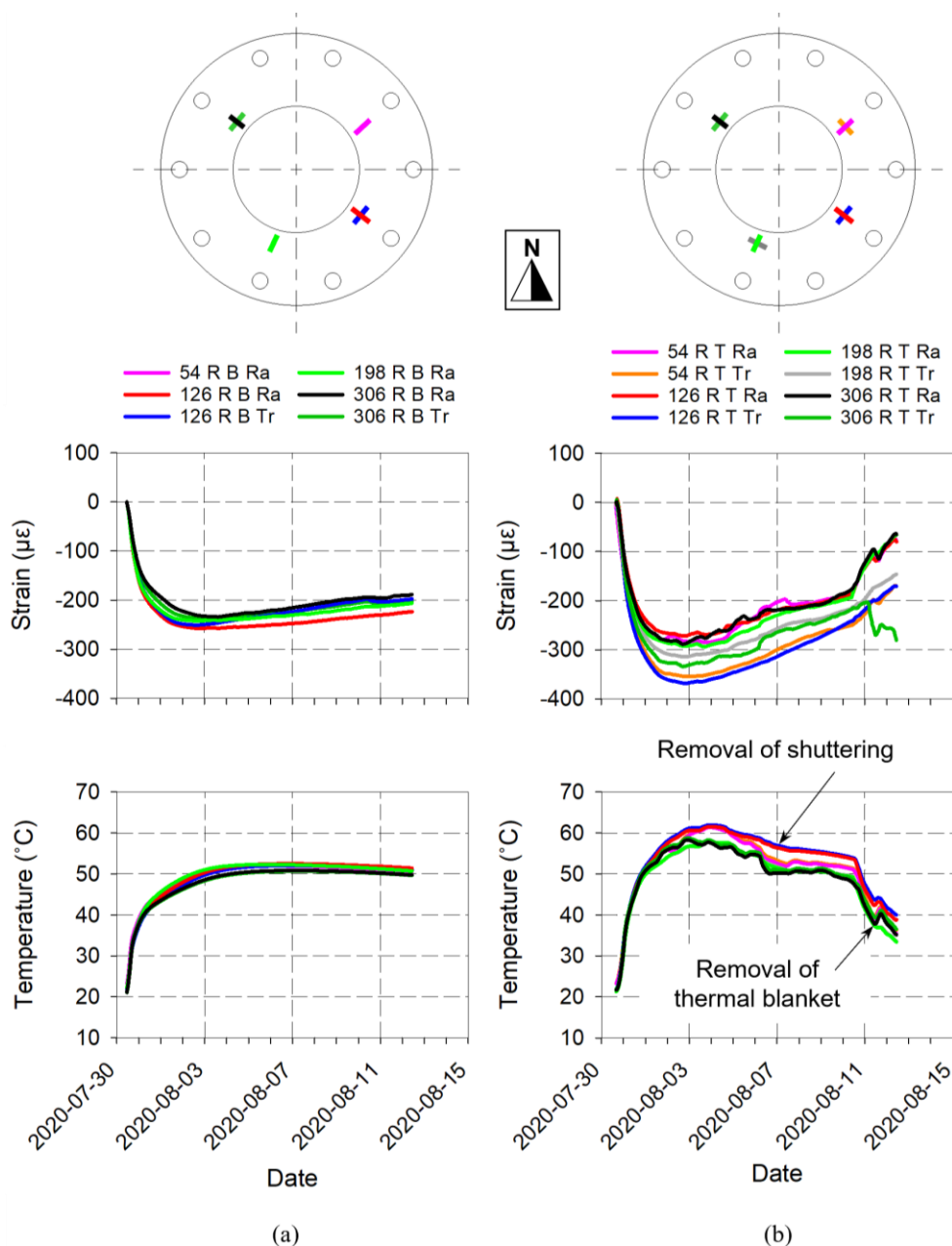
Figure 3-17: Total strain and temperature in the raft: (a) bottom; (b) top

Perry *et al.* (2017) also recorded similar temperature differences with a 20 m diameter, 3 m thick raft foundation after seven days. The rate at which the top of the raft started cooling was significantly higher than at the bottom, especially after removing the shuttering and thermal blanket, with the temperature at the bottom remaining relatively constant. For this raft, the shutters and thermal blanket remained in place for 8 days and 13 days, respectively, as indicated in **Figure 3-17(b)**.

By removing the thermal effects and only considering the mechanical strains at the bottom and top of the raft, it can be seen that strains were already present during the first two weeks after the start of the cast, even though no external loads were applied to the raft (see **Figure 3-18(a)** and **(b)**). These strains could potentially be due to the raft's shrinkage during curing or differences between the thermal strains at the top and bottom of the raft, as evident from **Figure 3-17** regarding the cooling rate at different parts of the raft.
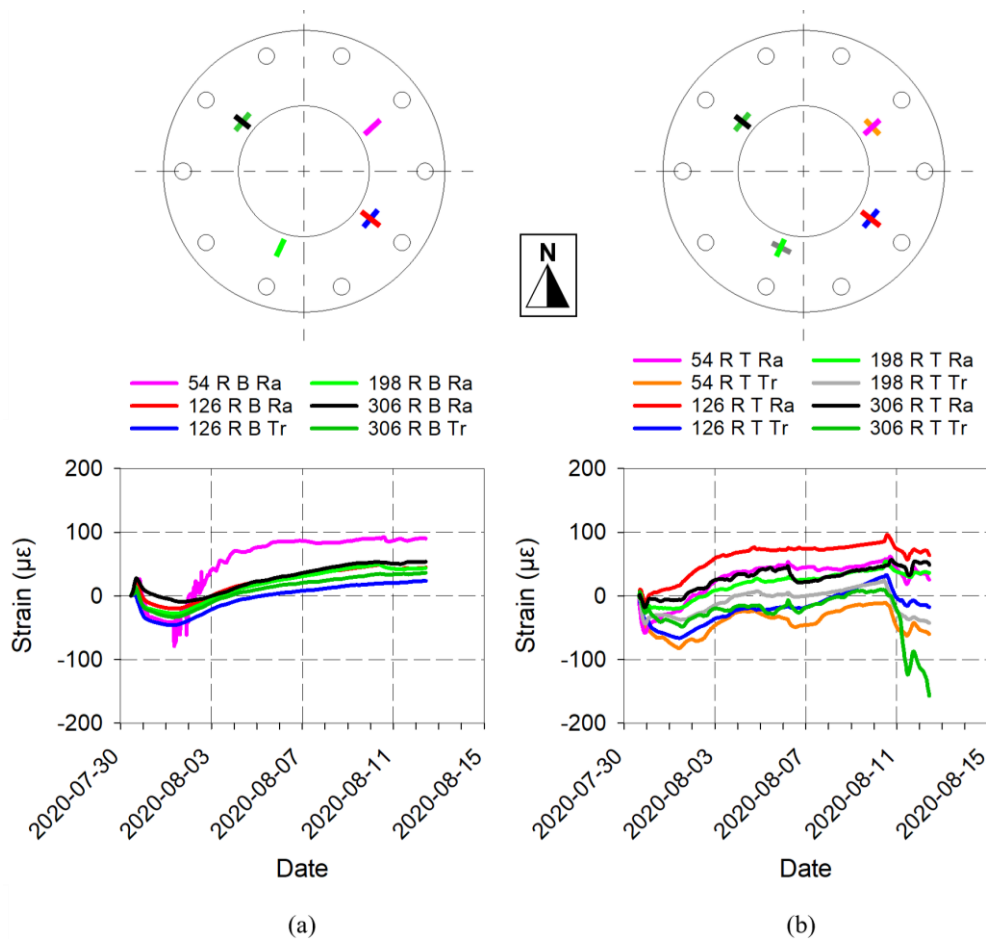
Figure 3-18: Mechanical strain in the raft: (a) bottom; (b) top

The casting of the raft had little effect on the existing piles cast earlier that year, as illustrated in **Figure 3-19**. **Figure 3-19(a)** and **(b)** indicate the mechanical strain and temperature in only the two piles in the prevailing wind direction (Pile 54 P and 198 P). In both these piles,

measurements were obtained at three different depths (0.5 m, 2.5 m and 4.5 m), with Pile 54 P having measurements at these depths on opposite sides of the pile compared to Pile 198 P having only measurements on a single side. A slight increase in strain (positive equals compressive) in both piles was observed due to the presence of the wet concrete from casting the raft. However, as the concrete started to cool and cure, a reversal of strains (becoming more negative) indicated the influence of raft concrete shrinkage on the piles through the steel bars extending from the top of the pile, binding the raft to the piles. Additionally, both piles experienced an increase in temperature towards the top of the pile (0.5 m below the bottom of the raft) resulting from the exothermic reaction from the heat of hydration process of the raft.
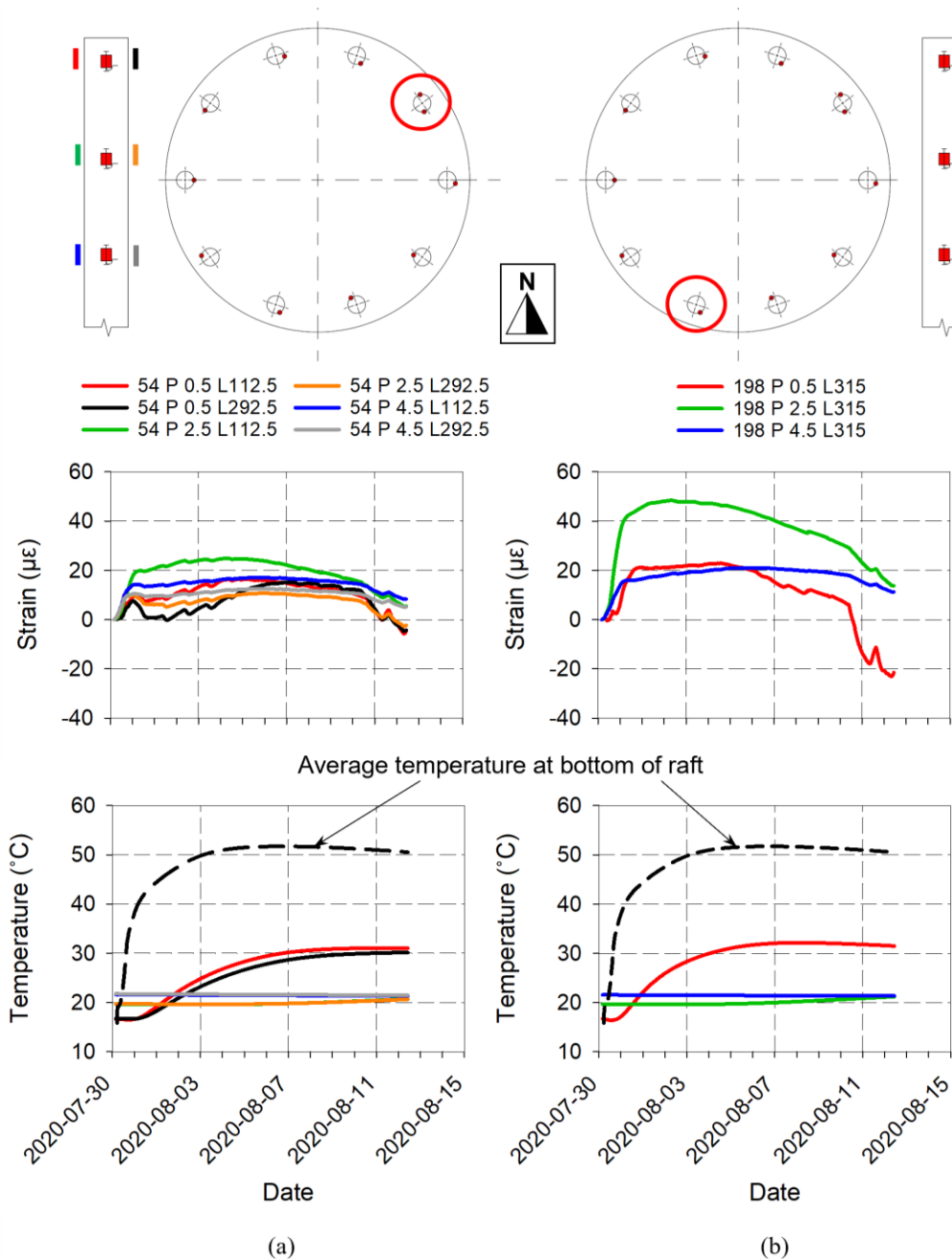
Figure 3-19: Mechanical strain and temperature in piles: (a) 54 P; (b) 198 P

In the case of Pile 54 P (see **Figure 3-19(a)**), the fact that the strains at the same depth but opposite sides of the pile differ significantly indicates the presence of bending moments. In order to obtain these bending moments, the measured strain data had to be converted. Similarly, to obtaining the axial forces and bending moments in the wind turbine tower, using **Equation 3-3** and **Equation 3-4** presented in Section 3.5.2, the axial force and bending moment in Pile 54 P could also be determined using the measured Young's modulus and sectional properties of the pile.

Figure 3-20(a) and **(b)** indicate the calculated axial forces (F_p) and bending moments (M_p) in Pile 54 P at the three depths based on uncracked section properties. As with the strains, an initial increase in the pile's axial force (compressive) occurred due to the presence of the wet concrete. However, a reversal of forces was observed after that when the raft started to cool and cure. This reversal could possibly be attributed to the concrete from the raft binding to the pile reinforcing bars, starting to pull on the pile as the concrete cures and shrinks. Furthermore, considering the bending moments, the maximum measured bending moment occurred 2.5 m below the bottom of the raft, with the bending moment closest to the bottom of the raft (0.5 m) moving back to zero compared to the bending moments at depths of 2.5 m ($\approx 2.8 D_p$) and 4.5 m, respectively.
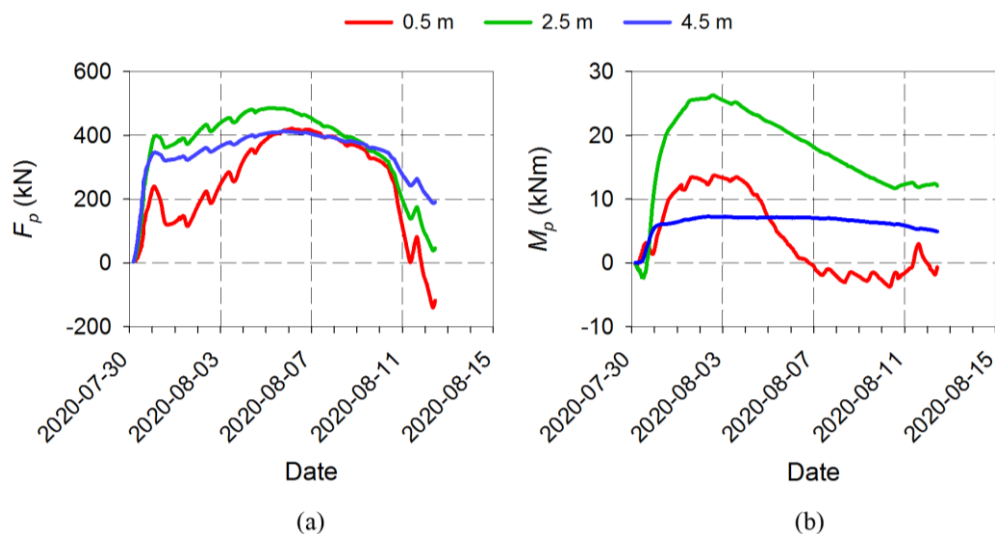
Figure 3-20: Pile 54 P response: (a) axial force; (b) bending moment

3.9.2 Wind turbine installation before commercial operation

Apart from monitoring the foundation response for the first 14 days after the raft was cast, no measurements were taken until the wind turbine was constructed. Upon arrival back on site, before the final turbine assembly, the foundation had already been backfilled, and the bottom section of the turbine tower had been connected to the anchor cage (see **Figure 3-21**). This

3-23

meant that the strain in the foundation measured from this point onwards included the strain induced by concrete shrinkage of the raft, the soil backfill, and the weight of the bottom turbine tower section. Strains were also not zeroed, with the measurements presented in the remainder of this document including all activities since foundation construction. With the bottom tower section standing, the 12 WBSGs for measuring axial forces caused by the tower's weight and bending moments caused by the wind, mentioned in Section 3.5.2, were only installed at this point.
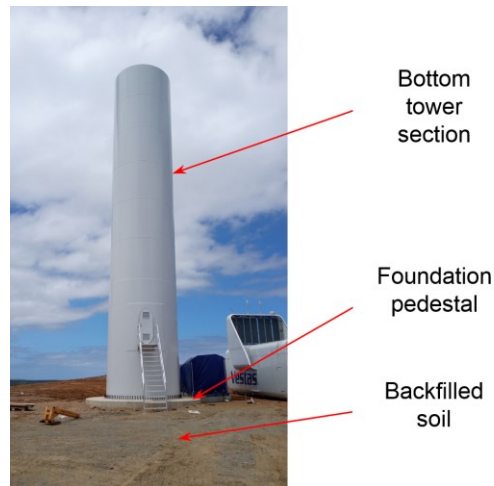
Figure 3-21: Installed bottom tower section

Installation of the rest of the wind turbine components (top tower sections, the nacelle, drive train, rotor hub and rotor blades) took place at the end of January 2021, with the assembly finished within about three days. **Figure 3-22(a)** and **(b)** indicate the measured axial force (F_t) and bending moments (M_t) measured at the base of the turbine tower during the period of turbine installation using the WBSGs at the base of the tower. Unfortunately, only the WBSG pair in the prevailing wind direction (54 W – 234 W) remained functional and will, therefore, be included in all analyses and discussions in the rest of this chapter. As expected, the axial force in the tower increased as the turbine was gradually erected. To calibrate these forces, the masses of each wind turbine component were obtained from the wind turbine manufacturer (see **Table 3-4**) and used to determine the theoretical total axial force expected at the base of the tower.

The expected axial force was calculated to be 3.61 MN (excluding the weight of the bottom tower section), as indicated in **Figure 3-22(a)**, and was in good agreement with the actual axial forces measured. The axial forces remained relatively constant after that, with some variation caused by either construction activity or the wind acting on the turbine tower and stationary blades in the following days. With the tower's bottom section already installed, the theoretical calculations neglected the contribution of that mass to the total theoretical axial

force. Furthermore, regarding the bending moment measured in the base of the tower, during the three days of installation, a near-zero bending moment was recorded, as expected, as these towers are typically erected on days with low wind speeds. After installation, small bending moments were observed, caused by the wind acting on the tower and stationary blades or some final construction activity on the tower.
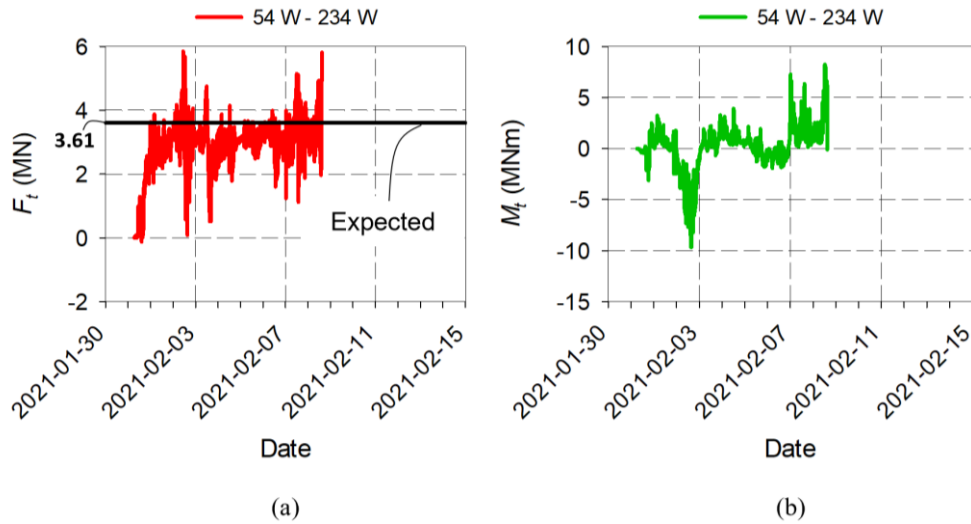
Figure 3-22: Turbine response: (a) axial force; (b) bending moment

Table 3-4: Turbine components and corresponding masses

Component	Mass (tonnes)
Bottom tower section	81
Top tower sections	163
Nacelle and drive train	130
Rotor hub and blades (3 blades)	75
Total mass of the turbine	**449**

For the strains in the foundation, focusing on the raft portion of the foundation first, almost no change in the mechanical strain could be observed in the bottom and top of the raft during turbine installation (see **Figure 3-23(a)** and **(b)**). Besides the significant rigidity of the raft, the measured strains were overshadowed mainly by the strains previously caused by concrete shrinkage, the soil backfill, and the weight of the bottom tower section. In order to assess the effect of turbine installation, for explanation purposes, strain results were zeroed before the three days of turbine installation and a few days after that (see shaded areas in **Figure 3-23(a)** and **(b)**). Measured data from sensor 54 R B Ra, located at the bottom of the raft, suggested that the sensor might have malfunctioned. Thus, readings from this sensor will not be included in the remainder of this section.

3-25
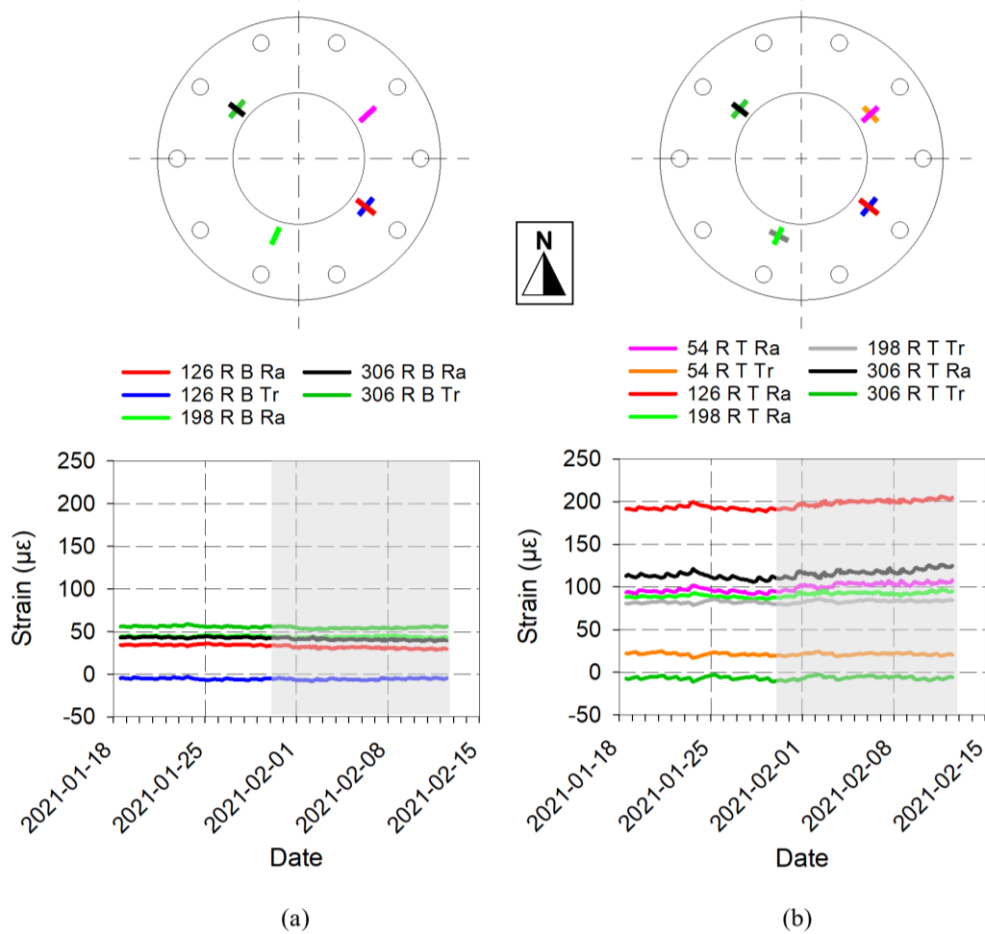
Figure 3-23: Raft mechanical strain response: (a) bottom; (b) top

Figure 3-24(a) and **(b)** indicate the zeroed strain at the bottom and top of the raft, respectively. All the sensors in both the radial and transverse directions at the bottom of the raft experienced tensile strains within the first three days of installation, or experienced a reduction in compressive strain with reference to **Figure 3-23(a)**. Subsequently, all the top sensors in the radial and transverse directions experienced compressive strains (or an increase in compressive strain with reference to **Figure 3-23(b)**), with the change in strains at the top of the raft measuring about twice the strains at the bottom. This difference suggests the influence of the supporting soil below the raft. Additionally, the bottom and top of the raft experienced 'tensile' and 'compressive' strains, respectively, indicating that the raft acts as a beam, with the applied load causing a bending moment in the concrete section. The largest strain changes after installation seemed to be due to day-night temperature variation, resulting in thermally-induced mechanical strain changes in the concrete section, as the bottom and top of the raft did not experience the same temperature change.

For the piles, the influence of the wind turbine installation was more visible. Only the two piles in the prevailing wind direction are presented as before. **Figure 3-25(a)** and **(b)** indicate the mechanical strains measured in Pile 54 P and 198 P, respectively. As illustrated, both piles

experienced increased compressive strain during installation, with the effect noticed at all three depths. Similar responses were observed from the other eight piles but are not presented here. Again, final construction activity and initial winds acting on the newly erected wind turbine were also visible after installation.
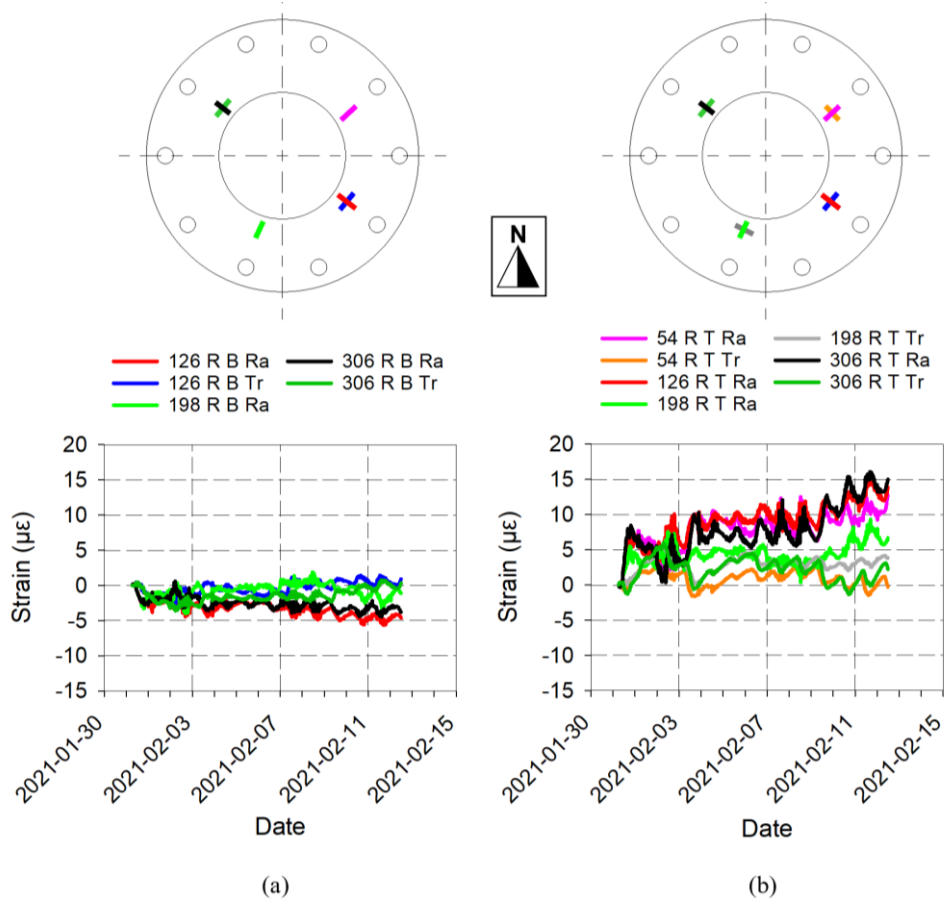
Figure 3-24: Raft mechanical strain response zeroed: (a) bottom; (b) top

Given that the raft could be considered rigid, based on approximations presented by Clancy & Randolph (1993) at the start of this section, limited rotation between the raft and the piles should occur during turbine installation (vertical loading). Thus, the change in strain in each pile, caused by the vertically imposed load, can be considered nearly entirely axial. Thus, considering the changes in strain ($\Delta\mu\varepsilon$) in all ten piles at a depth of 2.5 m below the bottom surface of the raft (see example in **Figure 3-25(a)**), the total vertical load carried by the piles can be estimated. **Table 3-5** indicates the changes in strain measured in each of the ten piles during turbine installation, respectively, along with the length of each pile.

The change in pile compressive force in the last column was obtained using Hooke's Law, the Young's modulus of the pile's concrete, as well as the cross-sectional area of the pile. An estimated 1262 kN (F_p) was calculated to be carried by the piles, with the load not equally distributed among the ten piles. Interestingly, the shorter piles embedded into bedrock did not

seem to carry higher loads than the longer piles, which can potentially be attributed to bearing conditions at the bedrock. Based on the 3610 kN (F_t) applied vertical load caused by the additional turbine components during installation, the piles carry approximately 35% (F_p/F_t) of the total self-weight of the wind turbine structure.
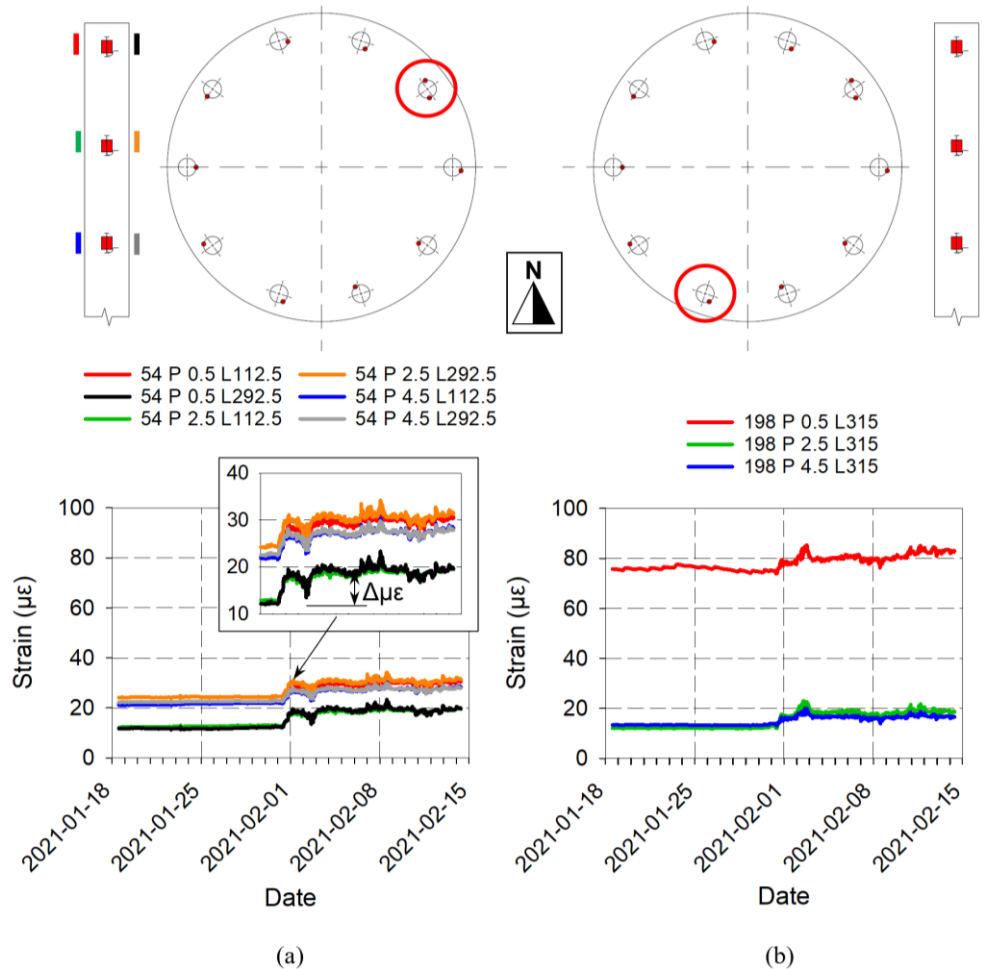
Figure 3-25: Pile mechanical strain response: (a) 54 P; (b) 198 P

Table 3-5: Vertical load approximations carried by each pile

Pile name	Pile length (m)	Δμε	Change in pile compressive force (kN)
18 P 2.5 L135	17.1	6.2	172
54 P 2.5 L112.5/292.5	17.2	5.9	163
90 P 2.5 L45	17.1	6.7	185
126 P 2.5 L157.5	16.8	2.2	61
162 P 2.5 L157.5	16.8	1.6	44
198 P 2.5 L315	17.9	5.7	158
234 P 2.5 L45	17.9	5.8	161
270 P 2.5 L180	16.8	2.1	58
306 P 2.5 L270	16.7	4.3	119
342 P 2.5 L112.5	16.9	5.1	141
Total weight carried by piles (F_p)			**1262**

Additionally, it should be noted that strain measurements in **Figure 3-25(a)** were not zeroed since the casting of the raft. Thus, the measured data suggest a possible built-in bending moment already present within the pile caused by the shrinkage of the raft before turbine installation. As before, the corresponding axial force (F_p) and bending moment (M_p) in Pile 54 P were plotted for the period of turbine installation (see **Figure 3-26(a)** and **(b)**). Similar to the strains, an increase in the compressive force in Pile 54 P was observed during turbine installation (see **Figure 3-26(a)**). Although designed as end-bearing piles, the change in force in the pile toward the top at 0.5 m proved the highest, followed by the change in force at 2.5 m and 4.5 m, respectively. This indicates the influence of shaft friction between the outside surface of the pile and the surrounding soil, with the average pile shaft friction mobilised calculated as 13.4 kN/m over a 4 m section of pile from the measured strains at 0.5 m, 2.5 m and 4.5 m. Before turbine installation, a built-in bending moment was present within the pile, as mentioned, and can be seen in **Figure 3-26(b)**. The largest bending moment by magnitude was measured at 2.5 m, followed by the bending moment at 0.5 m, having a slightly smaller magnitude but the opposite sign (change in the direction of the bending moment). Bending moments with depth differed in sign, indicating the influence of soil confinement. Turbine installation also seemed to have little effect on the bending moment in Pile 54 P. Thus, the assumption regarding the change in strain in the piles being nearly entirely axial during turbine installation seems valid.
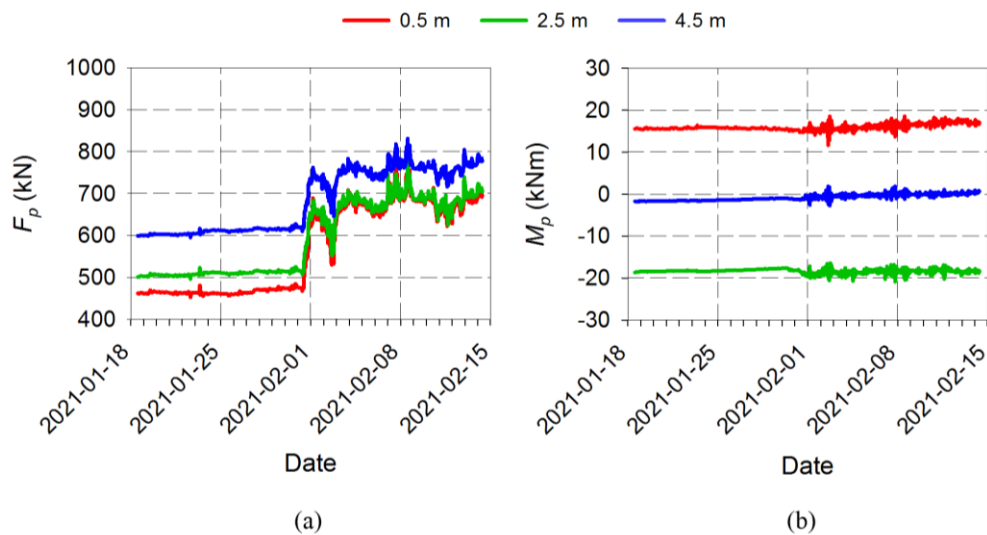
Figure 3-26: Pile 54 P response: (a) axial force; (b) bending moment

3.9.3   Commercial operation after commissioning

The data recorded during commercial operation presented in this thesis only considers the first year since the commissioning of the wind turbine, which will be referred to as the initial

operating phase. Although it does not seem like a long time, given the significant number of wind-induced load cycles turbines are exposed to over their lifespan, valuable trends could be observed from the large number of load cycles already imposed on the turbine and supporting foundation during the first year. Thus, initial time effects are also included in discussions.

Before considering the influence of the wind on the turbine and supporting foundation, it was necessary to first examine the wind speed and wind direction data obtained from the WTG09 tower. **Figure 3-27** indicates the wind speed information obtained from the weather station located on top of the nacelle for the WTG09 tower as supplied by the wind turbine manufacturer, with measurements taken every ten minutes. The data spans just over a year since the wind turbine became operational in June 2021, with the average wind speed calculated to be about 30.3 km/h and the standard deviation calculated to be 14.3 km/h. Correspondingly, the 95th percentile was calculated as 55.8 km/h, which is also indicated in **Figure 3-27**. Wind speeds seem fairly consistent over the year, with seasonal variations between summer and winter months being insignificant.
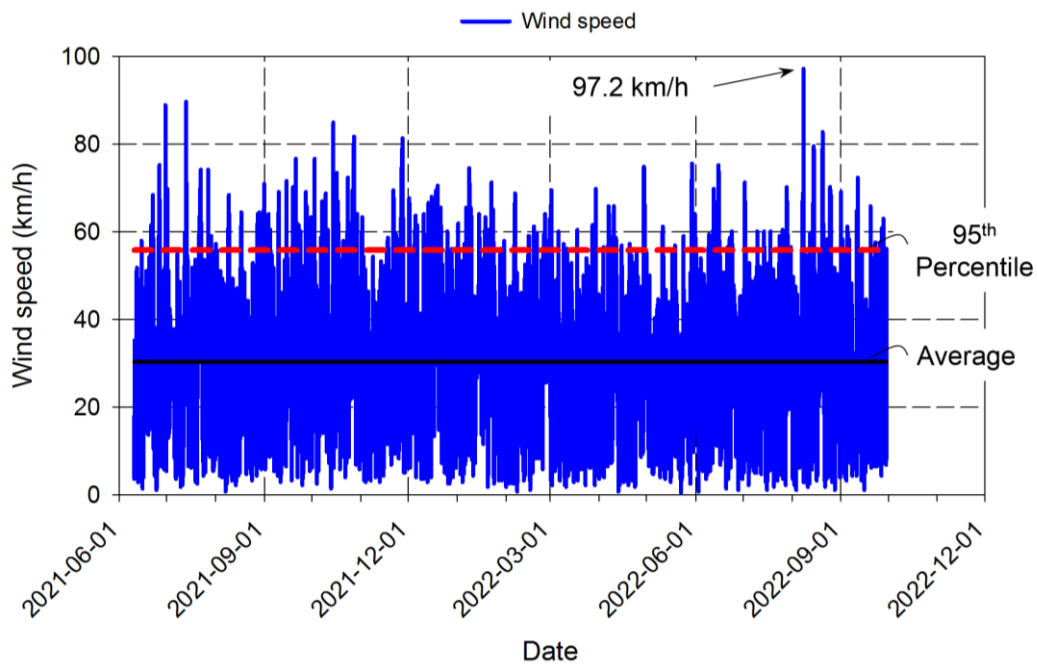
Figure 3-27: Wind speed information

The Beaufort scale is the most commonly used scale for classifying winds according to their speeds into 13 wind speed categories. The scale is an empirical measure that relates wind speed to typically observed conditions at sea or on land, ranging from calm and gentle breeze winds to gale-force winds, storms and hurricanes. The provided data in the scale is based on mean speeds, usually averaged over ten minutes by convention, with speeds measured at ten

metres above the ground. **Table 3-6** summarises all 13 Beaufort scale numbers, their equivalent speeds and short descriptions, as presented by WMO (1970).

Although the provided data from the site is based on wind measurements taken at hub height (117 m), for analysis purposes, the Beaufort scale should give a reasonably accurate indication of the wind speed as wind speeds at elevated heights usually are higher than closer to the ground. Based on the average wind speed calculated from the provided data, average wind speeds on-site can be classified as a fresh breeze (Beaufort scale number of 5). However, some days, these speeds exceed that for near gale and gale force winds, with the highest wind speeds measured as 97.2 km/h (see **Figure 3-27**).

Table 3-6: Beaufort scale classification of wind speeds (WMO, 1970)

Beaufort scale number	Equivalent speed (km/h)	Description
0	0-1	Calm
1	1-5	Light air
2	6-11	Light breeze
3	12-19	Gentle breeze
4	20-28	Moderate breeze
5	29-38	Fresh breeze
6	39-49	Strong breeze
7	50-61	Near gale
8	62-74	Gale
9	75-88	Severe gale
10	89-102	Storm
11	103-117	Violent storm
12	118-133	Hurricane

In terms of analysing the response of the wind turbine foundation due to different wind speeds, knowing the direction of these winds is also of great importance. **Figure 3-28(a)** and **(b)** indicate rose charts of the wind speed data plotted in **Figure 3-27**, sorted into the different wind directions. **Figure 3-28(a)** presents the frequency of the different wind speeds according to different directions, with **Figure 3-28(b)** indicating the corresponding average wind speeds in each of these directions. Contrary to the initial site investigative reports showing that the wind is dominantly blowing from the south-westerly direction, the data suggest the wind mainly blows from the westerly and easterly directions, with minimal winds blowing from the southern and northern directions. Similar to the average wind speed calculated from all the provided data, the average wind speed in most directions was about 30 km/h. In addition, isolating the data points for gale force winds and higher (wind speeds exceeding 50 km/h), it can be seen from the rose chart in **Figure 3-29** that the highest frequency of these wind speeds typically originates from the easterly direction with over 30% frequency.
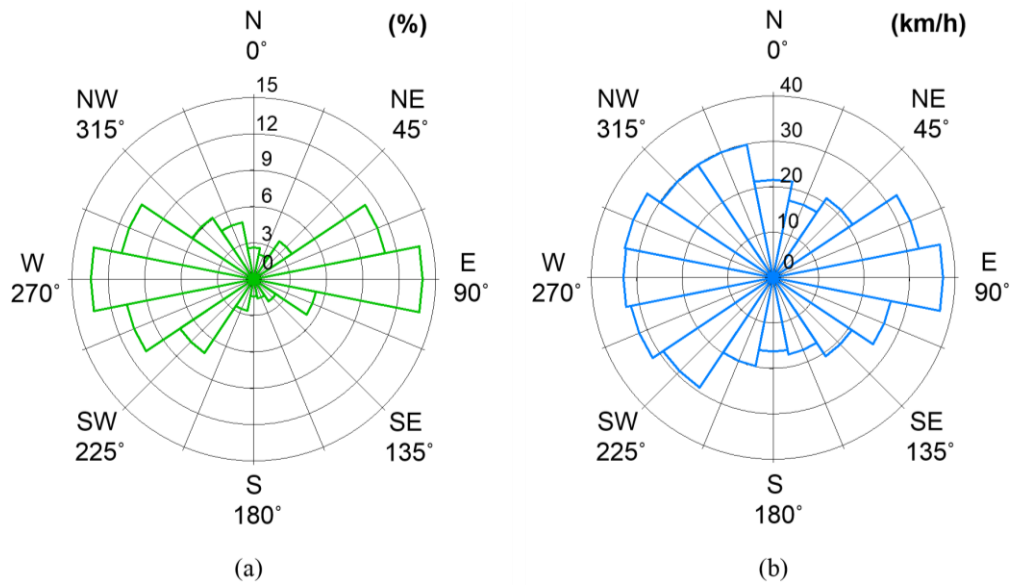
Figure 3-28: Wind data per direction: (a) frequency; (b) average wind speed
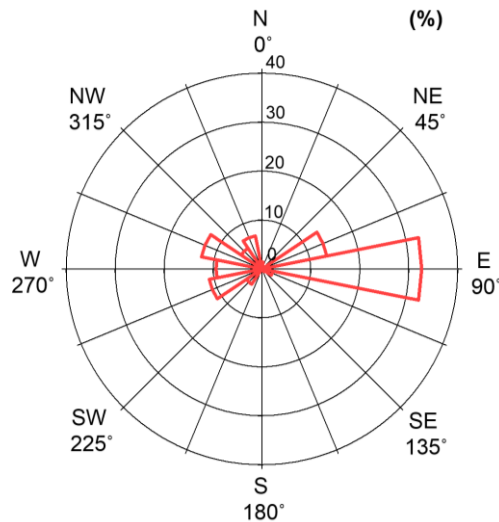
Figure 3-29: High wind speed frequency per direction

Moving on to the bending moment experienced in the tower during operations resulting from the wind, **Figure 3-30** presents the measured bending moment (M_t) at the bottom of the turbine tower since the start of operations at the beginning of June 2021. As before, the plotted data is only for the WBSG pair in the prevailing wind direction (54 W – 234 W), with the data representing the bending moment at the base of the tower in that direction, even if the wind is blowing from different directions. Thus, when the wind speeds on some days are near zero or blowing in the directions perpendicular to the WBSG pair, the bending moment in the tower should read close to zero. The expected theoretical SLS bending moment envelope is also indicated in **Figure 3-30**, based on the average values calculated from the data presented by Cools (2015) in **Figure 2-5**, with the measured operational data falling within this range. The envelope of ± 66.4 MNm is based on information obtained for a typical tower with a hub

3-32

height of 117 m and a rotor diameter of 126 m, respectively, with the measured data agreeing well with what was expected under service loads. The smaller bending moments measured at the tower's base from end-September 2021 to mid-October 2021 were due to the tower undergoing maintenance (not operational), with the wind acting on the tower and stationary blades.
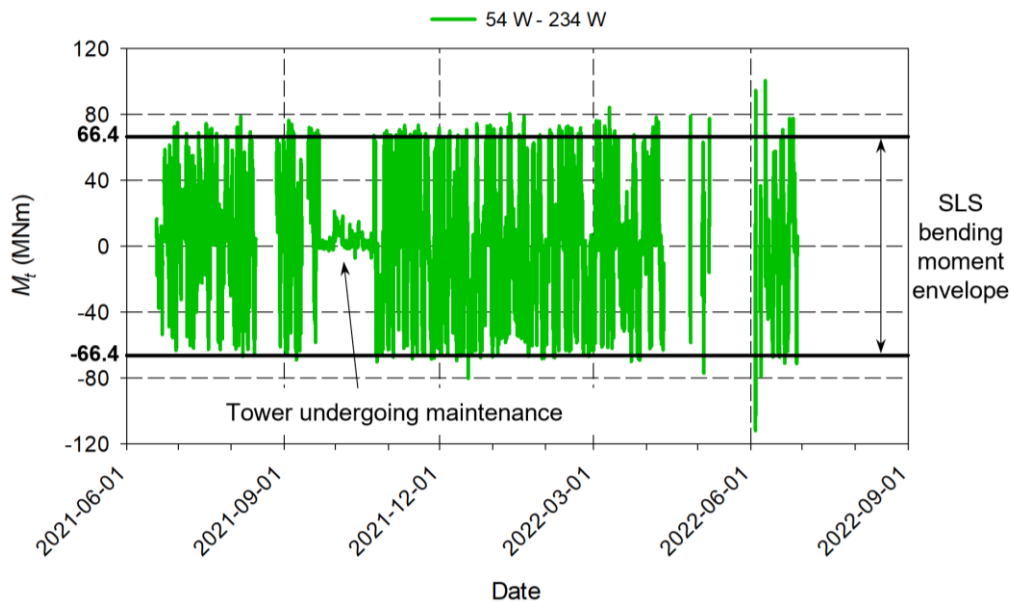
Figure 3-30: Bending moment response at the bottom of the turbine tower

To obtain the relationship between the wind speed and the expected bending moment (M_t) at the base of the tower, the wind speed results for the days when the wind was blowing from either the 54° or 234° directions were extracted. The relationships are plotted in **Figure 3-31(a)** and **(b)** for the 54° and 234° wind directions, respectively. Only a limited number of data points were available from the sensors installed in the south-westerly direction, given that the prevailing wind direction was between East and West. Although it is well known that the fundamental relationship between wind speed and loads on a structure is quadratic according to Bernoulli's principle (Kassimali, 2015), a linear regression line, passing through the origin, was fitted to both sets of data points. Both lines had similar gradients, as expected, with both lines also showing a good coefficient of determination. For wind speeds less than 30 km/h (see **Figure 3-31(a)** and **(b)**), the linear relationship was reasonably representative. However, the results were more varied as wind speeds passed 40 km/h. A quadratic trendline was added to the data points in **Figure 3-31(a)** for explanation purposes. Although not visible in **Figure 3-31**, it is necessary to highlight the typical cut-in and cut-out wind speeds for wind turbine models to know when the turbine will be operative. The cut-in wind speed is the speed at which the wind turbine starts generating electricity (blades start to rotate). On the other hand, the cut-out wind speed is defined as the wind speed at which the turbine blades are

stopped for safety reasons, and the turbine no longer generates electricity. Due to the turbine being stationary above these cut-out wind speeds, bending moments are still present at the tower's base. However, they are typically lower than the bending moments present when the turbine is fully operational and generating electricity. For this Vestas V126-3.45 MW wind turbine model, the cut-in and cut-out wind speeds are about 10 km/h and 72 km/h, respectively (Vestas, 2022).
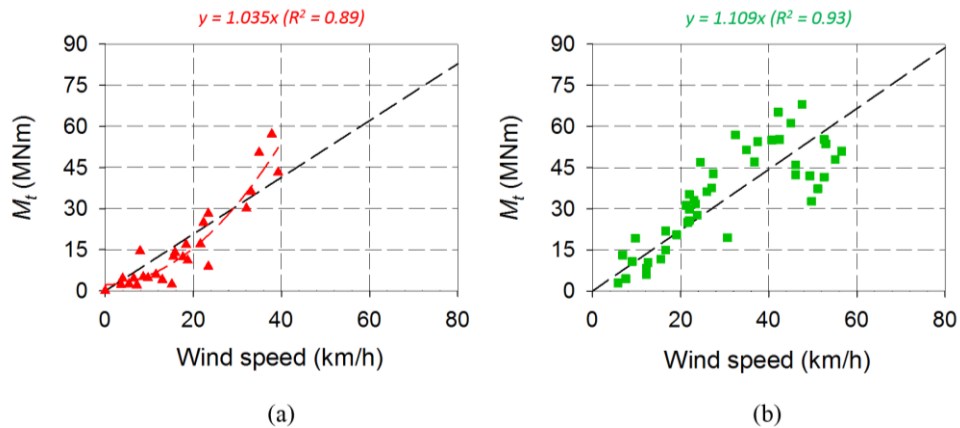
Figure 3-31: Relationship between wind speed and bending moment at the tower's base: (a) 54° wind direction; (b) 234° wind direction

Given the vast amount of measured data obtained, to investigate the relationship between the bending moment at the tower's base and the resulting strains experienced in the underlying foundation, an arbitrary 11 days in June 2021 and June 2022 were isolated and plotted for discussion purposes. **Figure 3-32** and **Figure 3-33** indicate the relationships between the wind-induced bending moments in the turbine tower and the response of the underlying foundation for June 2021 and June 2022, respectively. In each figure, **(a)** represents the wind speed and wind direction plotted on separate axes, **(b)** the bending moment at the tower's base (M_t), **(c)** the radial mechanical strain measured at the bottom of the raft and **(d)** the radial mechanical strain in the top of the raft. As before, **(e)** and **(f)** present the mechanical strain at three depths for the two piles in the prevailing wind direction, namely Pile 54 P and 198 P, respectively. **Figure 3-32** and **Figure 3-33** show a good agreement between the bending moments and the strains in the underlying foundation, with the bending moments (wind speed and direction) remaining in phase with all the strain measurements. In both instances (2021 and 2022), the largest absolute bending moments in the tower's base were measured when the wind was blowing in the direction of the WBSG pair and opposite to it. Near-zero readings were observed when the wind speeds were close to zero or blowing in the direction perpendicular to the positions of the WBSG pair. The influence of the wind was also noticed from the radial strains at the bottom and top of the raft in **Figure 3-32(c** and **d)** and **Figure 3-33(c** and **d)**.

3-34
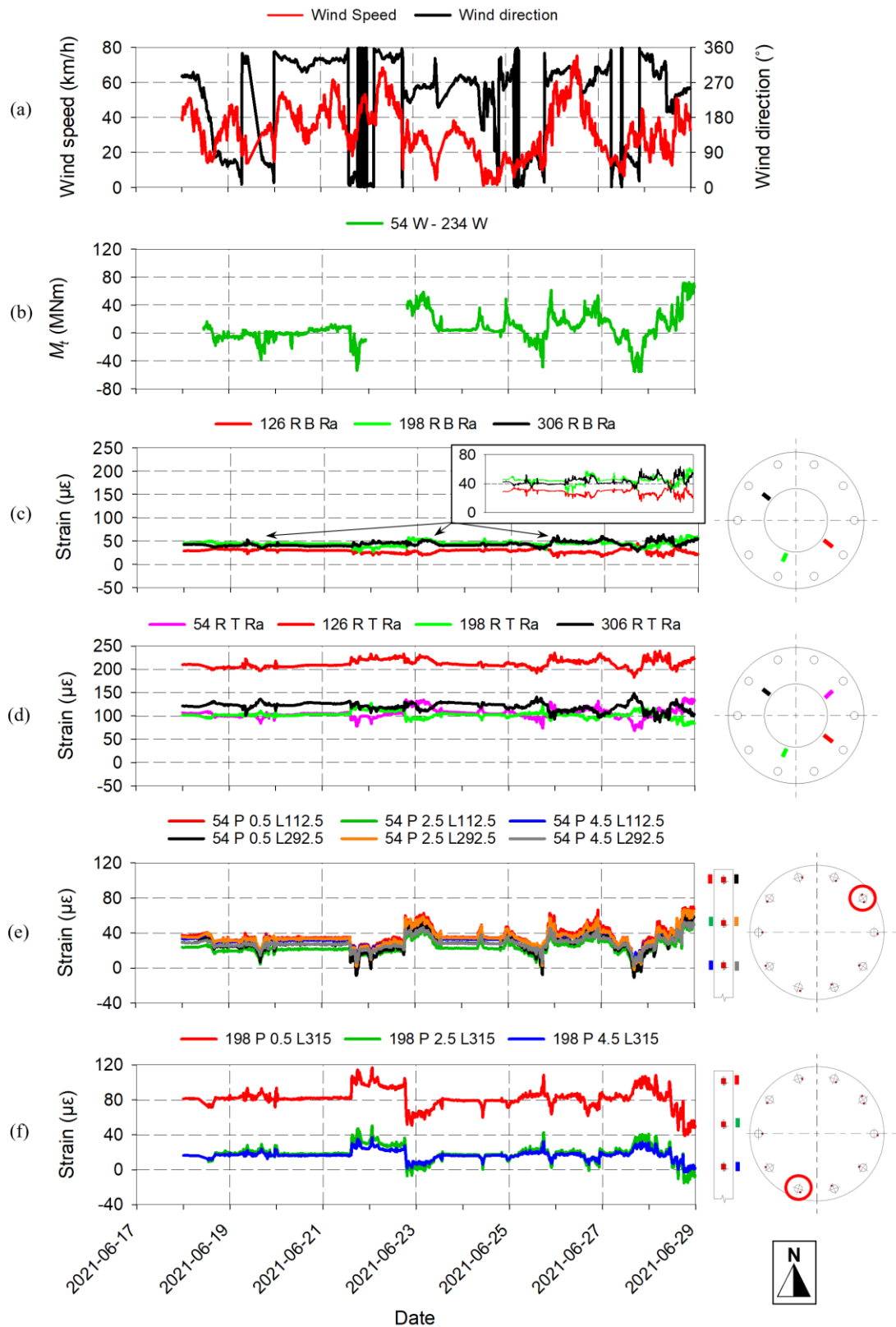
Figure 3-32: Operational response: (a) wind speed and wind direction; (b) tower base bending moment; (c) bottom raft radial strain; (d) top raft radial strain; (e) Pile 54 P stain; (f) Pile 198 P strain – June 2021
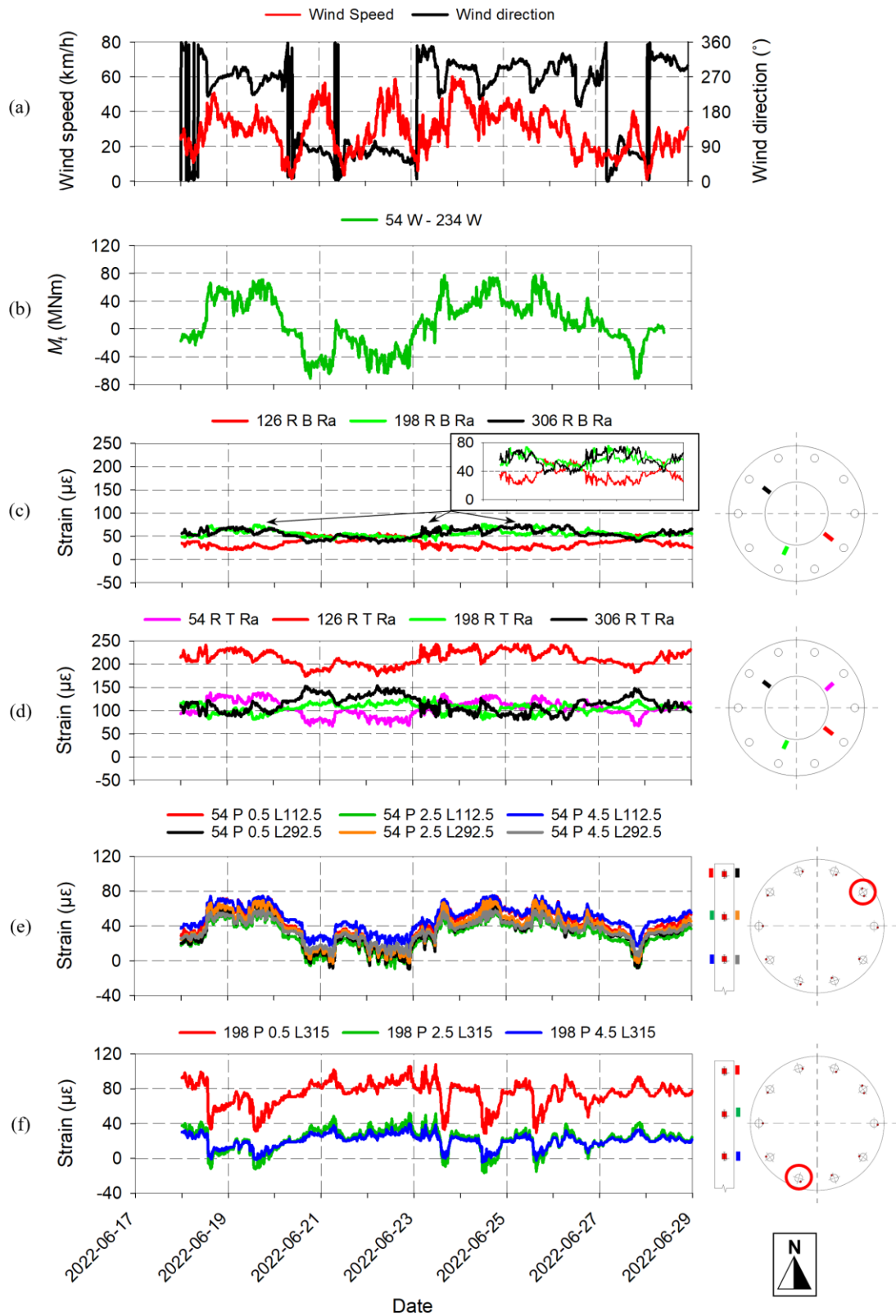
Figure 3-33: Operational response: (a) wind speed and wind direction; (b) tower base bending moment; (c) bottom raft radial strain; (d) top raft radial strain; (e) Pile 54 P stain; (f) Pile 198 P strain – June 2022

Depending on the direction of the wind, an increase or decrease in compressive strain was observed between gauges. VWSGs on opposite sides of the raft tend to respond inversely, with one sensor increasing by a certain magnitude and the other reducing by about the same magnitude. For example, when the wind was blowing from the 234° direction or nearby, top strains on the opposite end of the raft (54°) increased, becoming more compressive, whereas top strains on the same end (234°) decreased, becoming less compressive. These trends followed what Yilmaz *et al.* (2022) observed from the pressure sensors below the raft foundation they instrumented. Bottom strains showed a similar trend.

However, where top strains became more compressive under loading on one side, bottom strains became less compressive on the same side, which was expected when considering the raft as a beam subjected to a bending moment. Changes in the strain at the top and bottom of the raft being opposite in direction indicate an increase in bending moment within the raft section as the wind blows, with larger strain changes occurring when the applied bending moment and wind are larger. Bending moments at the opposite end from the wind direction tend to start 'sagging' more, and bending moments on the same end will tend to start 'hogging' more. Due to the circular nature of the raft and not having a constant moment of inertia throughout, bending moments were not calculated. The changes in strains at the top and bottom of the raft are also not equal in magnitude under the applied bending moment, suggesting the influence of the soil supporting and resisting some of the externally applied loads and moments.

Regarding the piles, similar results were observed. Piles located on the leading (leeward) end of the raft (see **Figure 3-32(e)** and **Figure 3-33(e)**) experienced an increase in compressive strain, given that the wind originates from the 234° direction. On the contrary, the piles on the trailing (windward) end of the raft experienced a decrease in compressive strain (see **Figure 3-32(f)** and **Figure 3-33(f)**). This shows the expected push-pull effect of the piles under bending when a rigid raft connects the piles, as Fleming *et al.* (2009) presented. Larger changes in the compressive strain in the piles were also linked to larger bending moments at the tower's base. Opposite responses in the raft and piles were observed when the direction of the wind changed, blowing, for example, from the 54° direction or nearby.

Although difficult to conclude whether bending moments occur within the pile under the applied external bending moments from only observing the strains in Pile 54 P in **Figure 3-32(e)** and **Figure 3-33(e)**, the corresponding axial force and bending moments were plotted for the two 11 day periods considered previously. **Figure 3-34(a)** and **(b)** present the axial force and bending moments in Pile 54 P for June 2021 and June 2022, respectively. The push-pull effect is reasonably noticeable when considering the axial forces in the piles under

loading, with more significant changes in the axial force occurring when the applied bending moment at the tower's base was higher (when the wind is blowing in the 54˚ or 234˚ directions).
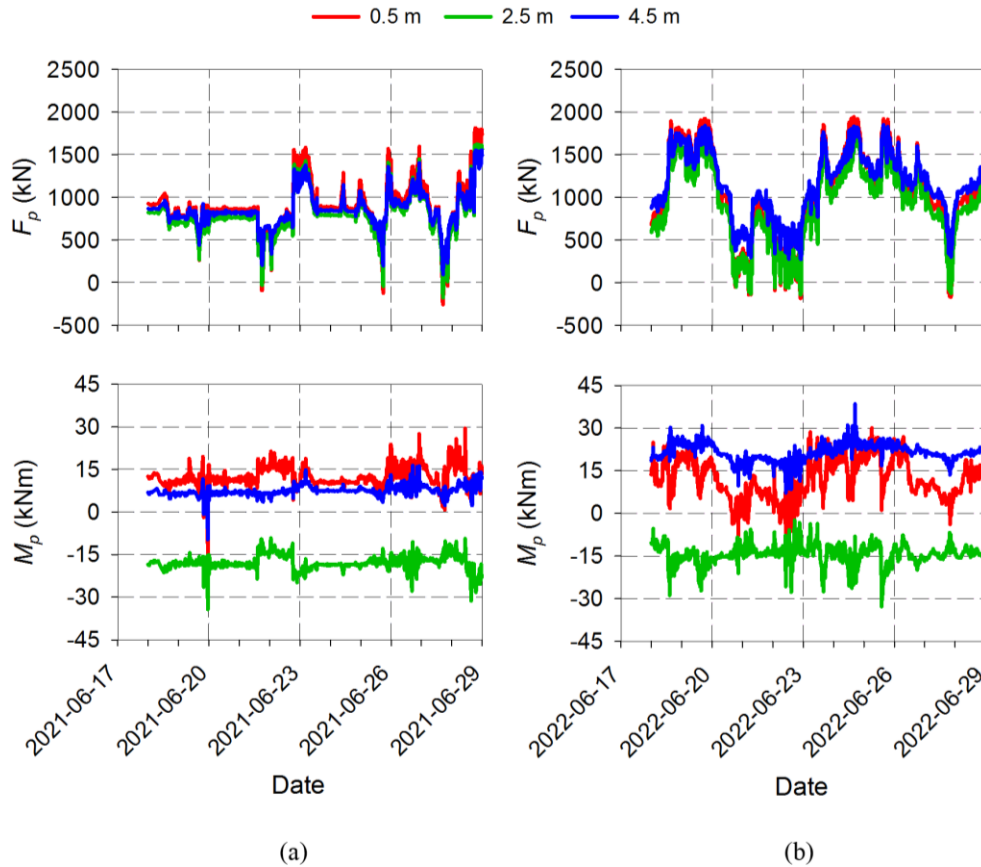
Figure 3-34: Pile 54 P F_p and M_p response: (a) June 2021; (b) June 2022

Similar to the responses observed during turbine installation, the shaft friction influence between the piles' outer surface and the surrounding soil was visible upon closer inspection. The VWSGs towards the top of the pile at 0.5 m experienced the highest increase or decrease in axial force under loading, followed by the sensors at 2.5 m and 4.5 m, respectively. Again, the average pile shaft friction mobilised was calculated over a 4 m section of pile from the measured pile strains at 0.5 m, 2.5 m and 4.5 m to determine whether a significant change occurred since turbine installation (pile shaft friction mobilised at installation = 13.4 kN/m). The average shaft friction mobilised for June 2021 and June 2022 was determined as 31.3 kN/m and 58.5 kN/m, respectively, indicating that, with increasing wind load cycles, the piles are taking up greater loads. Although changes in bending moments at different depths in the pile were observed during loading, axial changes seem to be more significant and can be considered the governing response, given the rigidity of the raft. However, the most significant changes in the bending moments were experienced towards the top of the pile at 0.5 m. The change was greater when the corresponding axial force was higher due to the

3-38

larger externally applied bending moment, with bending moments at a depth of 2.5 m, again, acting in the opposite direction.

To investigate whether a relationship exists between the externally applied bending moment at the tower's base and the change in axial force and bending moment in Pile 54 P, **Figure 3-35** was plotted. **Figure 3-35(a)** and **(b)** indicate the change in mechanical strain ($\Delta\mu\varepsilon$), change in axial force (ΔF_p) and change in bending moment (ΔM_p) in Pile 54 P against the bending moment (M_t) at the tower's base for June 2021 and June 2022, respectively.
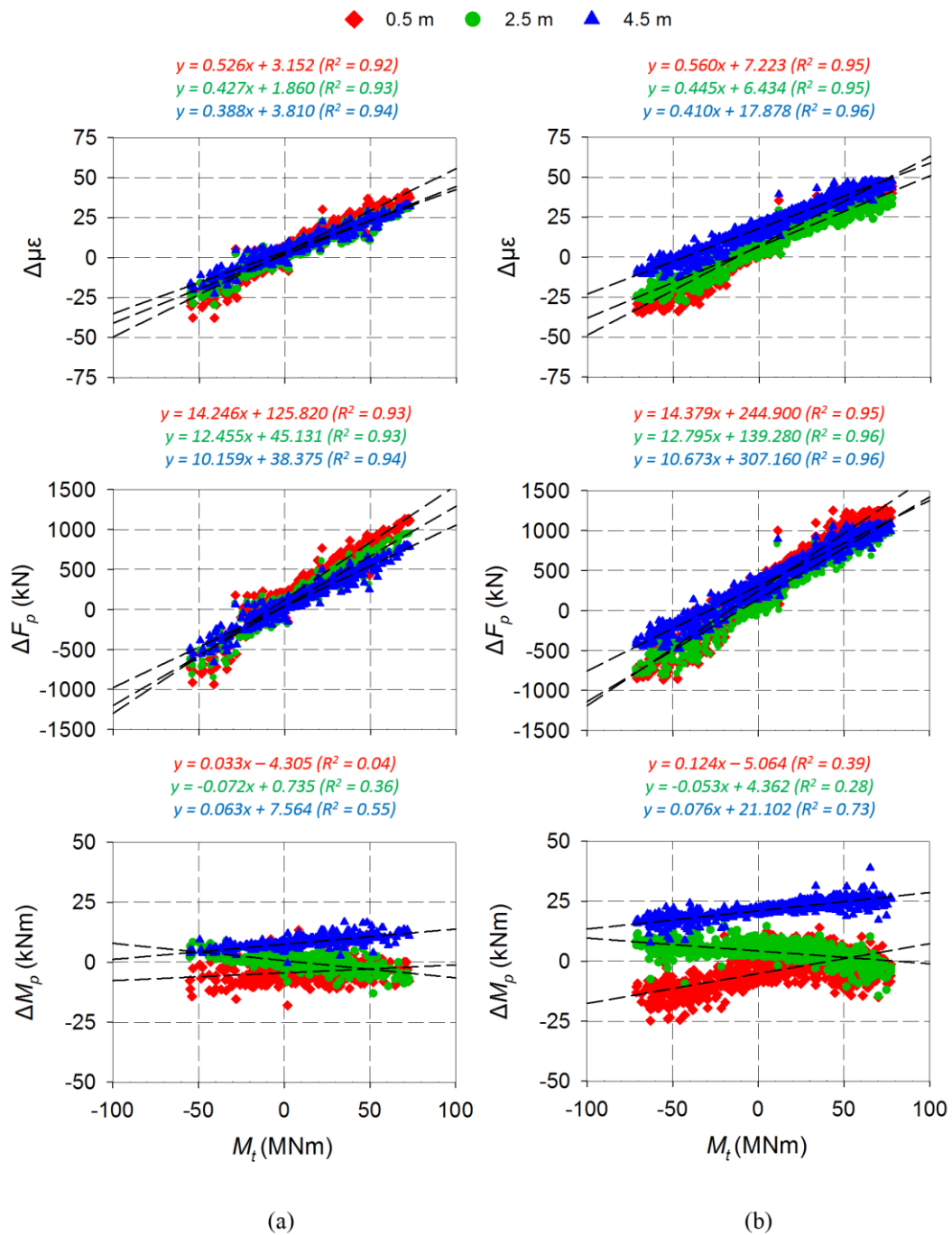
Figure 3-35: M_t versus ΔF_p, ΔM_p: (a) June 2021; (b) June 2022

3-39

A good correlation between the applied tower bending moment and the change in strain and axial forces was observed during both months. Larger positive tower bending moments resulted in larger changes in the compressive strain axial force in Pile 54 P, with the opposite being true when the direction of the bending moment changed. Considering the slopes of the linear regression lines fitted to the strain and axial force graphs, the largest change occurred towards the top of the pile, gradually decreasing downwards. Again, this indicates the influence of shaft friction between the pile surface and the surrounding soil. A poor correlation was observed regarding the changes in the bending moments in Pile 54 P due to the applied tower bending moment (see **Figure 3-35(a)** and **(b)**). However, by general observation, the positive bending moment at depths of 0.5 m and 4.5 m (from **Figure 3-34(a)** and **(b)**) tends to increase, becoming more positive when the bending moment in the tower's base increases positively. Additionally, the negative bending moment in Pile 54 P tends to also increase, becoming more negative. When the wind was blowing from the opposite direction, an inverse response of the pile was observed.

3.9.4 Time effects on foundation response

Although the wind turbine operational results considered in this thesis only summarise the first year after commissioning, some time effects were observed from the measured data caused by the large number of wind-induced load cycles that already acted on the underlying foundation. These effects are briefly presented and discussed in the following few paragraphs. To investigate whether the cyclically induced wind loads acting on the foundation over time affected the percentage of the total vertical turbine load carried by the piles, strain measurements in the piles were extracted on the days when the wind speeds measured below 5 km/h. The tower can be assumed stationary at these wind speeds, not generating electricity, with little bending moments at the tower's base, as the cut-in wind speed was only at 10 km/h. Similar procedures were performed, as presented in **Table 3-5**, calculating the change in strain in each pile at a given time based on the original strain in each pile prior to installation. **Figure 3-36** indicates the percentage of the total vertical wind turbine load carried by the piles (F_p/F_t) since the turbine was installed.

As indicated in **Figure 3-36** and presented in Section 3.9.2, the piles carried approximately 35% of the total vertical turbine self-weight after installation. However, upon initial cyclic loading in June 2021 (0.4 years since installation), this percentage seemed to have increased to about 50%. After an additional year, the percentage carried by the piles increases even further, suggesting a convergence to about 60%. This convergence justifies the argument raised in the literature review based on the works of Johnson (1986) and Werkmeister *et al.* (2001) that the induced cyclic nature of the load causes permanent deformation in the soil,

resulting in the soil below the raft becoming resilient after a post-compaction period, with the piles carrying higher loads as the raft is effectively 'bridging' this gap.

$y = 5.598\ln(x) + 56.562 \ (R^2 = 0.66)$
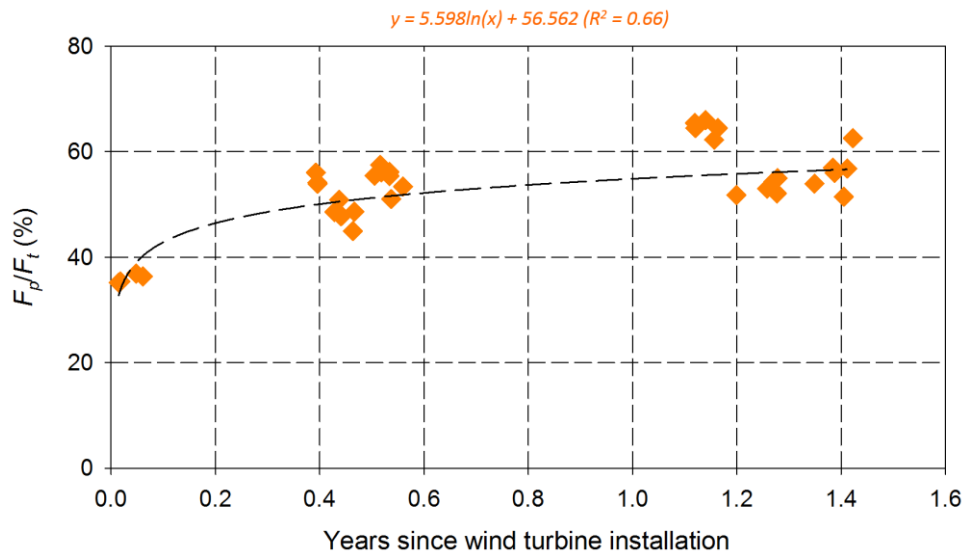
Figure 3-36: Percentage of total vertical wind turbine self-weight carried by the piles with time

As seen in **Figure 3-34(a)** and **(b)**, an increase in the overall average bending moment in Pile 54 P at a depth of 4.5 m was observed over the one-year investigative period from 2021 to 2022. Compared to the average bending moment measured in the pile before and after turbine installation (see **Figure 3-26(b))**, the measured data indicates the possible influence of cyclic wind loading on the built-in permanent bending moments in piles. These bending moments are typically left in a pile after load removal, as Kirkwood & Haigh (2014) indicated, and can be attributed to repetitive loading of piles, changing the soil conditions surrounding the pile. The permanent bending moments in Pile 54 P were plotted from the strains for the days when wind speeds were low (< 5 km/h) and the external bending moments at the tower's base were small. This indicates whether the permanent bending moment induced on the pile after the raft was cast was influenced by the cyclic wind loads, as turbine installation had little effect on this bending moment. **Figure 3-37** indicates the measured permanent bending moment ($M_{p,per}$) since the turbine was installed.

As mentioned in Section 3.9.2, raft shrinkage seemed to have caused a built-in permanent bending moment in Pile 54 P before turbine installation. A positive permanent bending moment was measured at a depth of 0.5 m before installation, and a negative permanent bending moment at 2.5 m, both similar in magnitude. The bending moment measured at a depth of 4.5 m was close to zero at that instance. As the number of wind load cycles increased over the one-year period, the largest increase in bending moment seemed to occur at a depth of 4.5 m, with the absolute bending moments at a depth of 0.5 m and 2.5 m slightly reducing.

This increased permanent bending moment at deeper depths compliments the results presented in **Figure 3-36** that piles tend to start working harder as the number of load cycles increases, with the raft gradually doing less.
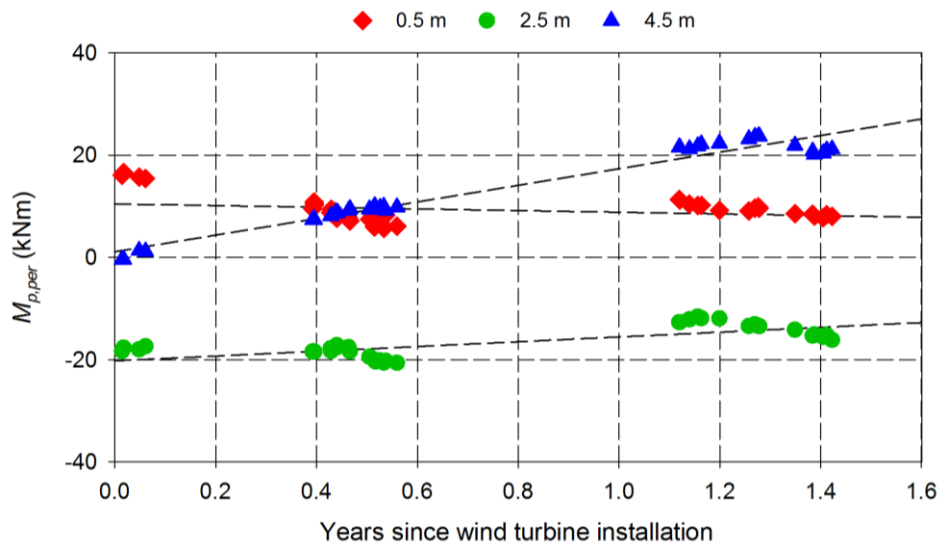
Figure 3-37: Permanent bending moment in Pile 54 P with time

Given the changes occurring in the piles over time, it was decided to investigate if the relationship between the applied foundation bending moment (M_t) and the corresponding change in axial forces and bending moments in Pile 54 P also changed. Similar to the graphs plotted in **Figure 3-35(a)** and **(b)**, sets of three graphs were also plotted for an arbitrary 11 days in July, August and September 2021, and February, March and April 2022. These graphs, along with the regression lines fitted to the data, can be seen in the Appendix. **Figure 3-38** indicates the rates of change ($\Delta F_p/M_t$ and $\Delta M_p/M_t$) of the regression lines fitted to the data over time. These rates of change show the relationship between the applied tower bending moment and the resulting change in both the axial forces (see **Figure 3-38(a)**) and bending moments (see **Figure 3-38(b)**) in Pile 54 P. Regarding the rate of change in the axial force, no significant changes were observed since the start of turbine operations, with the data suggesting the relationship between the tower's bending moment and the change in the axial force in Pile 54 P remaining constant. This can possibly be attributed to the fact that the total vertical load carried by the piles converged to a constant value (see **Figure 3-36**), resulting in the relationship remaining unaffected. Again, more significant changes were observed towards the top of the pile, indicating the influence of pile shaft friction.

Despite the correlation between the tower bending moment and the changes in the pile bending moment being poor, some trends were observed. As mentioned, the applied bending moment largely affected the change in bending moment at the top of the pile (0.5 m), which became more significant after many wind load cycles. Soil conditions surrounding the piles

changed due to the applied load cycles, similar to previously considered permanent bending moments. Time seemed to have little effect on the bending moment rates of change at 2.5 m and 4.5 m, respectively.
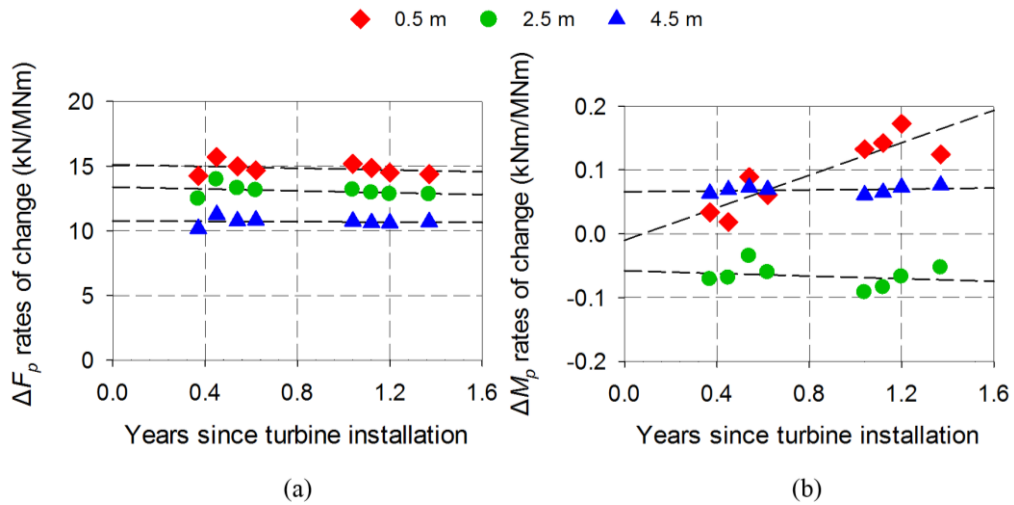
Figure 3-38: M_t versus pile response (a) rates of change in axial force; (b) rates of change in bending moment

Additionally, strain measurements in the bottom and top of the raft when the wind speeds were low (< 10 km/h) seemed unaffected by time (see **Figure 3-39(a)** and **(b)**), with no noticeable increase or decrease observed since wind turbine installation. A more extended measurement period is required to conclude whether the strains in the raft are affected by time and number of wind-induced load cycles.
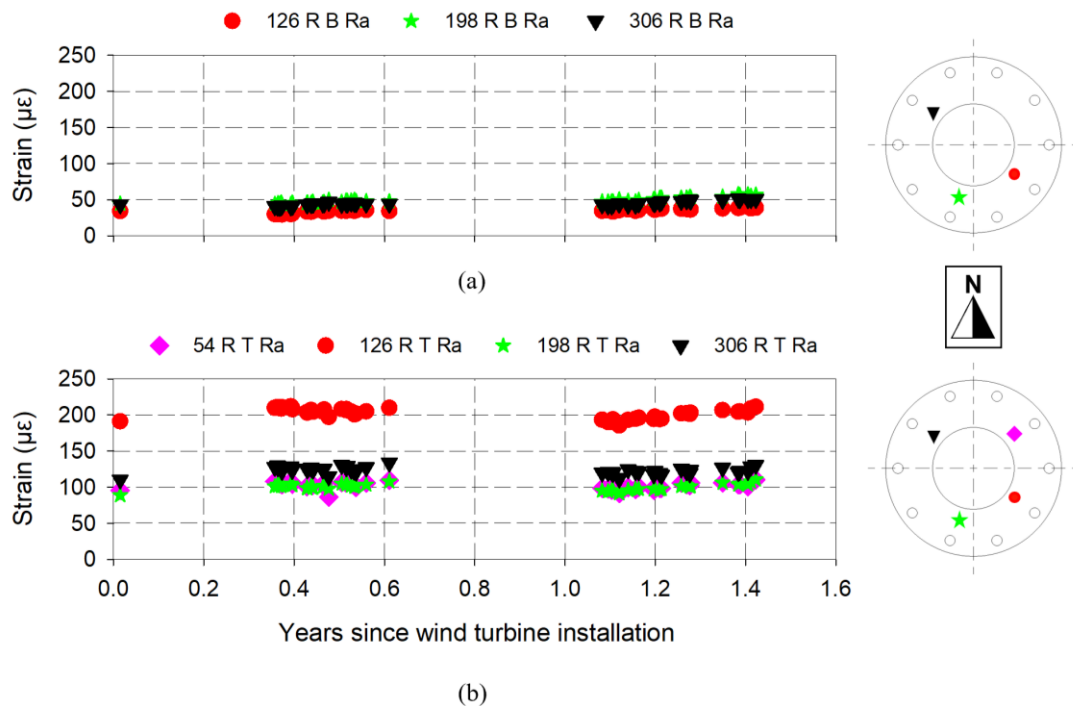
Figure 3-39: Low wind speed strains in the raft with time: (a) bottom; (b) top

Even though thermal strains in the foundation were initially thought to not be significant, given that the foundation is buried below the soil surface, seasonal variations were observed for the strain measured in the raft (see **Figure 3-16(a)**). No significant effect was observed from the strains measured in the piles deeper below the soil surface (see **Figure 3-16(b)**). To determine what influence these seasonal changes had on the raft, temperature and thermal strain data were extracted and plotted. **Figure 3-40(a)** and **(b)** indicate the temperature and corresponding thermal strain at the bottom of the raft, respectively, whereas **Figure 3-40(c)** and **(d)** indicate the temperature and thermal strain at the top of the raft, respectively. The presented values are only for the radial VWSGs, with data extending from February 2021, before the turbine was installed, to June 2022, when the turbine was already operational for about a year. During the seasonal changes from winter to summer, the bottom of the raft experienced a temperature increase of about 5˚C. This resulted in a thermally-induced strain change at the bottom of the raft of about 40 με.
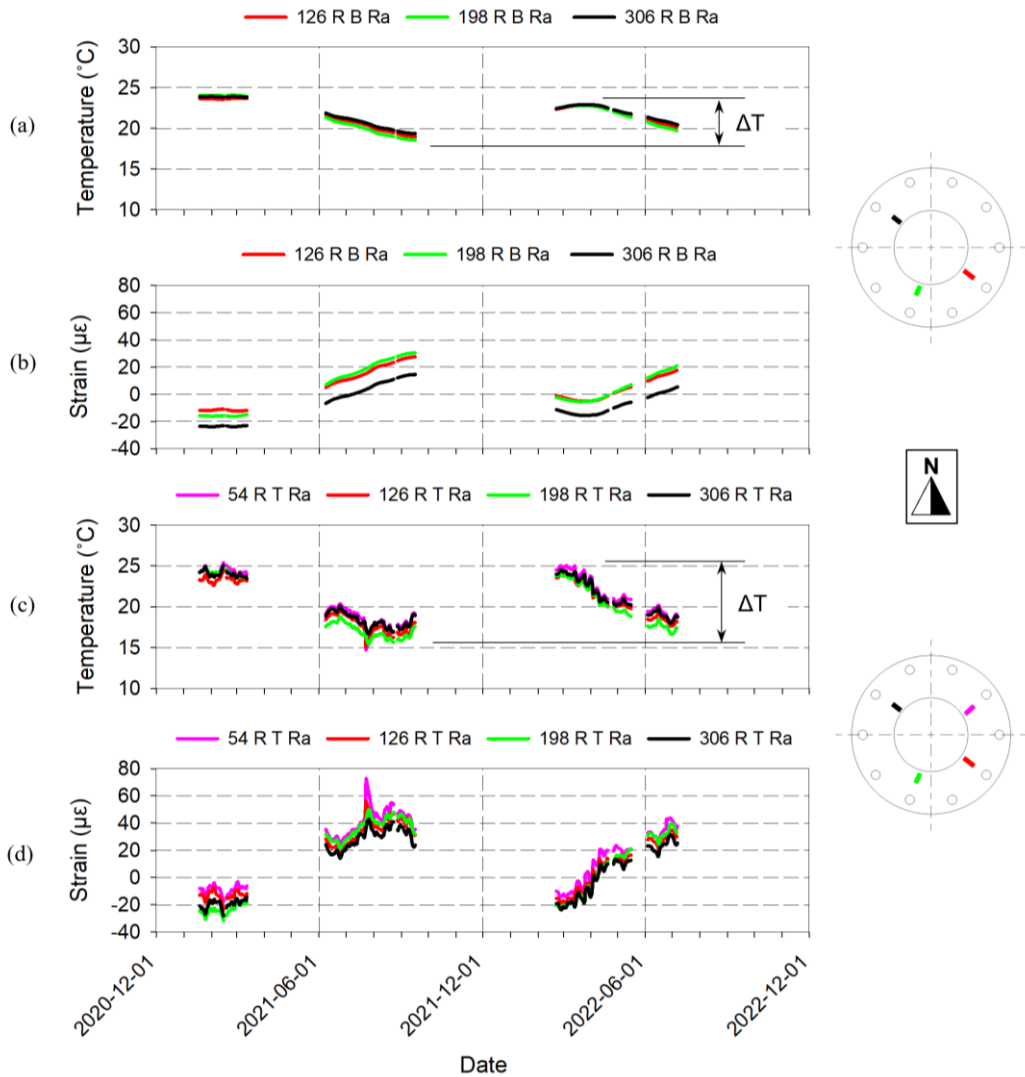
Figure 3-40: Seasonal effects of raft response: (a) bottom raft temperature; (b) bottom raft thermal strain; (c) top raft temperature; (d) top raft thermal strain

3-44

Additionally, at the top of the raft, closer to the soil surface, temperature changes of about 10°C were recorded, resulting in a thermally-induced strain change of about 60 με. These changes at both the top and bottom of the raft are significant and should be pointed out as they are higher than the strains mechanically induced on the raft during operations caused by the wind. Furthermore, with the thermal strain at the bottom and top of the raft not being equal, a temperature (thermal) gradient exists within the raft section, resulting in potentially thermally induced mechanical strains.

3.10   SUMMARY

This chapter illustrated the successful instrumentation and monitoring of an onshore wind turbine piled-raft foundation in South Africa. Wind turbine foundations are characterised by being exposed to horizontal load and overturning moments caused by the wind having a significantly higher impact than compared to the vertical load caused by the turbine's self-weight. An intricate load scenario, which combined with the complex soil-structure interaction between the foundation and the supporting soil, required further investigation.

Different phases affecting the foundation's response were considered, including the foundation's response during construction, during turbine installation, and during initial operations after commissioning. The presented data showed the possibility of calibrating the foundation system using known turbine weights, allowing for the estimation of load sharing between the raft and piles. Furthermore, quantifying the loads and overturning moments caused by the wind on the external turbine structure under normal working (SLS) load conditions was also considered, investigating its influence on the underlying foundation. The effect of wind speed and wind directions was also discussed.

During construction, the foundation's response was dominated by thermal effects caused by the concrete's heat of hydration process, with the raft's size contributing to thermal gradients in the concrete section. The full-scale testing showed that the foundation response was dominated by the dynamic horizontal load and overturning moment caused by the wind, compared to the vertical self-weight of the turbine, with the loads shared by both the raft and the piles. During turbine installation, the piles carried about 35% of the applied vertical load, increasing at a reduced rate to about 60% after one year of turbine operation. As the piles were socketed into bedrock, the data suggested that this load increase can be attributed to the soil below the raft settling relative to that of the pile, with the raft having to bridge the 'gap' spanning the piles. However, turbine installation had little effect on the strains measured in the raft. Before turbine installation, permanent bending moments were present in the piles, which was believed to be caused by shrinkage of the raft during concrete curing. Given the

3-45

significant rigidity of the pile connecting raft, the response of the piles was also characterised by the push-pull effect in the leading and trailing piles under the applied dynamic overturning moment, with the relationship between the moment and the axial forces in the piles remaining unaffected by number of load cycles. The magnitude of the push-pull effects depended on the wind's direction and speed. However, as load cycles increased, permanent bending moments developed towards the top of the piles. Although the actual relationship between the bending moment at the base of the tower and wind speed is quadratic, for wind speeds up to 30 km/h, this relationship seemed fairly linear, becoming more varied at higher wind speeds. Over time, due to many load cycles, the permanent bending moments present in the piles before turbine installation increased, with the largest increase being at a depth of 4.5 m. Wind-induced cyclic loading seemed to have no noticeable influence on the strain measured in the raft for the period of measurement. Seasonal temperature variations and thermally induced strains also affected foundation response, even more than the turbine operation, which is often neglected due to the foundation being buried.

In conclusion, the question, however, still arises as to whether the response of a piled-raft foundation would have been different if the size of the foundation or the overall rigidity of the pile-raft-soil system were any different. Additionally, considering the strive towards larger wind turbines, resulting in higher vertical loads, horizontal loads, and overturning moments that need to be carried by the underlying foundation, would the foundation's response change, and if so, what would be considered critical? To further investigate these questions, finite element (FE) modelling was undertaken, focusing particularly on the soil-structure interaction between the foundation and the supporting soil and the structure-structure interaction between the different foundation components. Based on the literature presented in Chapter 2 and the results summarised in this chapter, these interactions proved to be the governing factors driving foundation response and were, therefore, further explored. Chapter 4 to Chapter 6 contain all the FE modelling conducted for this thesis, building on the results presented in this chapter.

4 FINITE ELEMENT MODELLING OF A PILED-RAFT FOUNDATION

4.1 INTRODUCTION

As indicated by the literature covered in Chapter 2, the response of a piled-raft foundation under loading mainly depends on the interaction between the different foundation components (piles and raft), as well as the interaction between these components and the surrounding soil, jointly referred to as soil-structure interaction. However, most published research is based on scenarios where the main force acting on the foundation is vertical loading, with analysis primarily focused on it. As highlighted in Chapter 3, the opposite is true in the case of wind turbines. Horizontal loads and overturning moments caused by the wind on the external structures have a significantly higher impact on the underlying foundation than that created by the own weight of the turbine. Thus, given the current popularity of wind turbine technologies as a cleaner electricity production option amidst climate change concerns, the need to further investigate piled-raft foundation response under these load configurations, particularly regarding soil-structure interaction mechanisms, is of interest.

Finite element (FE) modelling has proven useful as an alternative for approximating solutions to complex engineering problems where analytical solutions cannot be obtained or, if obtainable, are highly empirical and oversimplified. Additionally, with the vast improvement of computer-based technologies, processing power and modern software programs, any engineering problem with complex geometries, load conditions or material properties can be modelled reasonably efficiently using FE modelling (Shrestha & Ravichandran, 2019). Therefore, FE modelling techniques were employed to better understand and investigate the soil-structure mechanisms. In this chapter, steps for constructing a comprehensive and representative FE model of a piled-raft foundation under dominant horizontal loads and overturning moments are discussed. Interaction between the different foundation components, as well as the interaction between these components and the supporting soil, was critical to this investigation. As a starting point, the dimensions and properties used in the developed FE model were based on that of the wind turbine foundation and soil resting on bedrock presented in Chapter 3 to, as far as possible, replicate the actual conditions, construction sequence and structural loadings on-site. Fortunately, knowing the expected response of that foundation (obtained from the results in Chapter 3), the simulated outputs of the developed model could be compared, and the FE model thus calibrated against known responses. Section 4.2 in this chapter summarises the steps for constructing the FE model, whereby Section 4.3 addresses the comparison of the developed model against known responses.

4.2   FE MODEL DEVELOPMENT

A three-dimensional (3-D) FE model of a piled-raft foundation and supporting soil was constructed in Abaqus/CAE Standard (Dassault Systèmes Simulia Corp., 2021). Abaqus is a FE software program widely used in both Civil and Mechanical Engineering research environments and has proven reliable in successfully modelling complex soil-structure interaction problems in the past. In addition, Abaqus has the ability to incorporate intricate constitutive material models and multi-directional load combinations, all of which were desirable features for investigating the study objectives. Although computationally more expensive, apart from the geometric and loading nature of the foundation problem being studied, 3-D modelling was selected primarily due to the pile-raft-soil interaction being captured more realistically than in two dimensions (2-D).

Constructing a computationally simple yet representative FE model is a product of several decisions and factors that need to be considered during the development phase of the model. Among these factors are selecting appropriate constitutive material models for the different parts and sections, deciding on part geometries and meshing (including element type and size), boundary conditions, loading and load application. In the case of modelling soil-structure interaction problems, an added factor of selecting appropriate interaction properties is vital and should also be incorporated into simulations. The following subsections discuss the various steps for developing an FE model of a piled-raft foundation and supporting soil resting on bedrock in Abaqus, highlighting the abovementioned factors. These steps aligned with previously published FE models of piled-raft foundations by Sinha & Hanna (2016) and Shrestha & Ravichandran (2019).

4.2.1   Model components

The two foundation components and the soil component of the FE model were each constructed individually. Dimensions of the raft and pile parts, including the position and length of the piles, resembled the actual full-scale piled-raft foundation dimensions, as presented in **Figure 3-3** in Chapter 3. As direction plays a vital role, especially considering the comparison of the FE model, East was taken in the positive *x*-direction, whereas North was taken in the positive *y*-direction. Based on the circular shape of the piles and raft, the soil part was also modelled as circular, mainly to assist with meshing. From preliminary investigative FE models, the diameter of the soil part was selected as four times the base diameter of the raft, which, in this case, corresponded to 62 m. This was to ensure that boundary effects did not influence the computed response of the foundation and could thus be neglected. In order to create and correctly position the holes where the piles and raft would

come into contact with the surrounding soil, the cut instance technique was used in the assembly module prior to assembly. As the soil was resting on bedrock and the piles were socketed into the bedrock, the total length of the soil part only equalled the sum of the longest pile length (17.9 m) and the base thickness of the raft (1.85 m), equalling 19.75 m. The 1.1 m soil backfill was not included in this dimension but instead modelled as a uniform vertical pressure equivalent to the weight of the backfilled material. This was done to simplify the model and reduce any potential numerical instabilities that might arise during computation. **Figure 4-1(a)**, **(b)** and **(c)** indicate the constructed parts for the raft, piles and soil, respectively. After individual part construction, each part was assembled at its respective locations in the assembly module before meshing. The application of the different loads and boundary conditions followed after this. Due to the geometric asymmetric placement of the piles, the problem was not modelled using symmetry.
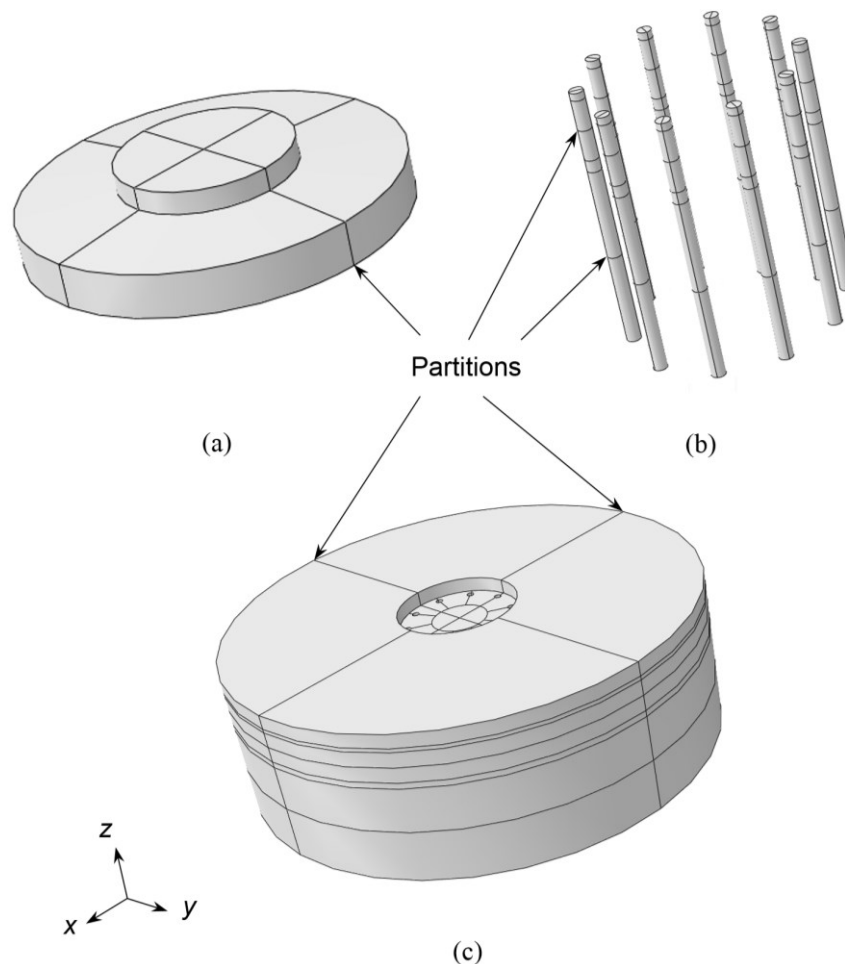
Figure 4-1: FE model parts: (a) raft; (b) piles; (c) soil

Partitioning was included in all the parts, as seen in **Figures 4-1(a)**, **(b)** and **(c)**, respectively, and placed at specific locations for three reasons. The first was to ensure uniform meshing at all the interfaces (boundaries) between the different parts, allowing for an equal number of

elements to be present at interacting faces. The second was for easy extraction of computed data for post-processing and model comparison, as the placement of these partitions coincided with the positions of the instruments installed in the full-scale piled-raft foundation. Finally, partitions were also placed at locations where the in-situ properties of the soil changed with depth. As this FE model replicates the on-site conditions, different material properties had to be applied to different sections in the same soil part, which was achieved through appropriate partitioning.

4.2.2 Constitutive material models

A linear elastic material model was chosen for modelling the raft and piles, even though it is well known that reinforced concrete exhibits highly nonlinear material behaviour even under SLS conditions (Mosley *et al.*, 2012). Although the nonlinear response of reinforced-concrete elements can and has been successfully modelled in Abaqus using built-in material models in the past, for simplicity, linear elastic behaviour was assumed, only requiring a density (ρ), Young's modulus (E) and Poisson's ratio (v) of the material as input. Modelling the intricate soil-foundation interaction was of greater importance in this study, which already required significant computational power.

The values for the density and Young's modulus corresponded to the actual material properties measured from the concrete samples taken on-site during the casting of the full-scale piled-raft foundation. Long-term property values were selected as they represent the foundation in its current state. The Poisson's ratio was assumed to be 0.2, which is valid for most concretes, according to Soutsos & Domone (2018). A summary of the long-term concrete properties used and assigned to the different parts of the FE model is provided in **Table 4-1** and corresponds to the values presented in Chapter 3.

Table 4-1: Constitutive material model properties – raft and piles

Component	Density (kg/m^3)	Young's modulus (GPa)	Poisson's ratio
Raft	2602	47.3	0.2
Piles	2541	43.5	0.2

It is well-known that soil is also a highly nonlinear material. However, Clayton (2011) and Knappett & Craig (2012) have indicated that, under SLS load conditions, the constitutive behaviour of soil can be approximated as linear elastic. They argued that any structure is designed to be far from failure, thus, the corresponding strains in the supporting soil will typically also be small. In the case of wind turbines under working loads (SLS), where strict limits on movement and rotation are enforced, assuming linear elastic soil behaviour seems

appropriate and will be used for this FE model and all other FE analyses relating to this research.

When assuming linear elastic soil behaviour, as indicated by numerous authors (Atkinson & Sallfors, 1991; Mair, 1993; Clayton, 2011; Knappett & Craig, 2012), the selection of appropriate and representative stiffness parameters and elastic soil properties is vital. Similar to structural elements, the characterisation of soils in terms of elasticity theory also requires Ioung's modulus (E) and Poisson's ratio (v). A third, and probably the most important parameter, known as the shear modulus (G), is also required. It is typically referred to as soil stiffness, representing the relationship between shear stresses and shear strains within the soil. Stiffness approximations for soil are not as straightforward as in the case of structural steel or concrete elements and are mainly related to and affected by the shear strain level of the soil. Apart from the shear strain level of soil, Knappett and Craig (2012) indicated that it should be appreciated that soil stiffness may not always be constant throughout the soil profile. They indicated that soil stiffness might also vary between soil layers and depth, potentially having higher stiffnesses at higher confining stresses. **Figure 4-2** indicates the typical shape of a graph depicting the non-linear relationship between the shear modulus of soil and shear strain level, as presented by Mair (1993).
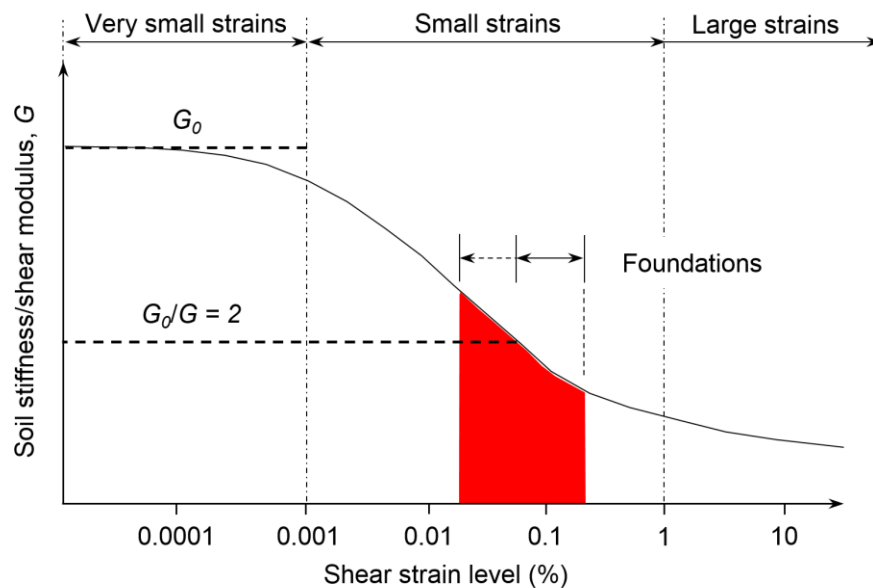
Figure 4-2: Typical stiffness variation and strain range for foundations (adapted from Mair, 1993)

In a paper published in 2011, Clayton indicated that, based on work from Clayton & Heymann (2001), for soils under strain levels of less than about 0.001%, the stiffness behaviour can be considered constant. This region is also known as the very small strain region (see **Figure 4-2**), with the value of the approximate shear modulus in this region

referred to as small strain stiffness (G_0). As the shear strain level increases above this limit into the small and large strain regions, a reduction in the soil stiffness is observed, as seen in **Figure 4-2**.

Based on work presented initially by Atkinson & Sallfour (1991), Mair (1993) indicated a range of approximate soil strain limits for different geotechnical engineering structures. Amongst these structures were the typical operating shear strain limits for foundations, retaining walls and tunnels. Mair (1993) indicated that these limiting values could be used, along with the soil stiffness-shear strain relationship graph, to estimate a representative linearised value for the shear modulus (G) of any soil based on the small strain stiffness of that soil. He indicated that foundations typically operate between a shear strain level of 0.02% and 0.3% (see **Figure 4-2**). On average, the shear modulus of soils exposed to the strain levels typical for foundations could be approximated as half the small strain stiffness value (G_0), also illustrated in **Figure 4-2**. More accurate approximations of G may be obtained using equations presented by Atkinson (2000). The calculated value aligns with the approximation given by Knappett & Craig (2012), with G being between $0.2G_0$ and $0.5G_0$. As indicated in Chapter 3, Continuous Surface Wave (CSW) testing was conducted on the soil supporting the wind turbine and instrumented foundation and allows for determining the in-situ small strain soil stiffness values (G_0). The CSW results from the site indicated different G_0 values at different depths, initially summarised in **Table 3-3** but presented again in **Table 4-2**, with the G_0 being higher for higher confining soil pressures at deeper depths.

Table 4-2: Constitutive material model properties – soil

Soil depth (m)		G_0 (MPa)	Density (kg/m³)	Equivalent small strain Young's modulus (MPa)	Poisson's ratio
0 – 8.2		200	2070	260	0.3
8.2 – 14.1		350	2070	455	0.3
14.1 – 20.8		1100	2070	1430	0.3
> 20.8		> 4000	-	> 5200	0.3

In the case of an isotropic elastic material (uniform behaviour in all directions), the relationship between the elastic soil properties G, E_s and v_s can be expressed by **Equation 4-1**. Therefore, it is typically only necessary to know two of the three properties, as the third can be obtained using the same equation.

$$G = \frac{E_s}{2(1 + v_s)}$$
(4-1)

Using the abovementioned assumption for predicting the shear modulus of soil under typical foundation shear strain levels and **Equation 4-1**, an equivalent small strain Young's modulus of the soil at each depth was determined, assuming a Poisson's ratio of 0.3 for sand (Winterkorn & Fang, 1975). Not much information about soil density with depth was provided in the Geotechnical Report (2014). A constant density of 2070 kg/m^3 was assumed for the soil, with this value corresponding to the density of the soil at a depth of about 14 m. **Table 4-2** indicates the densities, Poisson's ratios, and the equivalent small strain Young's modulus values calculated for each soil layer used in the FE model.

With the soil being modelled as a single part, sections had to be created within the soil part using partitions (mentioned in Section 4.2.1). **Figure 4-3** indicates a cross-section of the 3-D FE model constructed in Abaqus, showing the raft, piles, soil and the 1.1 m soil backfill. The dimensions of the soil's top, middle and bottom layers are indicated, with each layer highlighted in red, green and grey, respectively. The corresponding properties assigned to each of these layers are indicated with the same colours in **Table 4-2**.
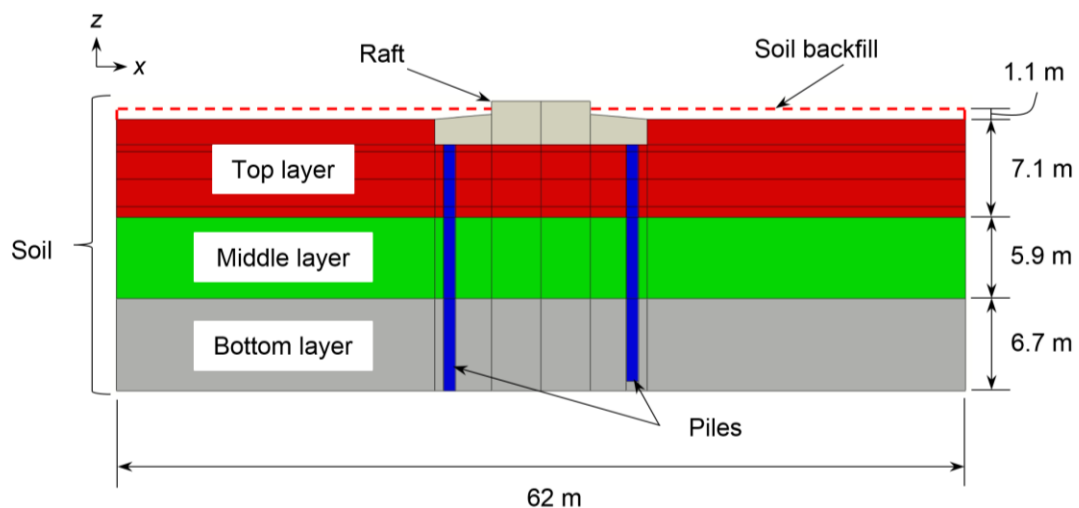
Figure 4-3: Soil profile cross-section

4.2.3   Interaction modelling and contact properties

Accurately modelling the interaction between the different foundation components and the interaction between these components and the surrounding soil was important. These interactions are referred to as structure-structure interaction and soil-structure interaction, with the modelling of these interactions described in the following paragraphs. Surface-to-surface contact discretisation was selected for all interfaces (pile-raft-soil) in the simulation domain. According to Abaqus Online Documentation (2014), it is considered superior to node-to-surface discretisation as it takes the shape of the contact surfaces in the region of the contact constraint into account. However, surface-to-surface discretisation provides better

stress and pressure results only if the surface geometry is well-defined (meshing). Surface-to-surface discretisation works on a master-slave principle, with one of the two contacting surfaces being the master surface and the adjacent surface being the slave surface. As a rule of thumb, the master surface is usually chosen as the surface of the stiffer body or the surface with the coarser mesh (Abaqus Online Documentation, 2014). Master surfaces can also penetrate slave surfaces. However, the opposite is not possible.

Two tracking approaches are available in Abaqus to account for the relative motion between two interacting surfaces in any mechanical contact simulation. These two approaches are finite sliding and small sliding. Finite sliding is the Abaqus default and is the most general as it allows any arbitrary motion between surfaces, whereby small sliding assumes relatively limited sliding of one surface along the other, even though both bodies or surfaces may undergo large motions. Finite sliding was selected as the sliding formation between all interacting surfaces. A surface-to-surface tie constraint was used for the structure-structure interaction between the top of the piles and the base of the raft (pile-raft intersection). Tie constraints allow two surfaces to be fused so that no relative motion between them can occur, regardless of whether these surfaces have dissimilar meshes created on them. This constraint was deemed acceptable for modelling the interaction between the piles and the raft, as piles are typically tied into the raft using reinforcing steel bars extending from the top of the piles after trimming. Tie constraints also work on a master-slave principle at interacting surfaces. The bottom surface of the raft at the position of the piles was selected as the master surface. This was due to the raft having a higher material modulus than the piles. The top of the piles (head) was chosen as the slave surface. All other values, set as defaults by Abaqus, were accepted, except the option to adjust the initial position of the slave surfaces, which was deactivated.

For modelling the soil-structure interaction between the piles and soil (pile-soil intersection), and the raft and soil (raft-soil intersection), respectively, normal and tangential behaviour was assigned at surface interfaces. Similar to the tie constraint, the master-slave principle was applied. The outside contact surfaces of the raft and piles were selected as master surfaces, and all contacting soil surfaces were selected as slave surfaces. For the raft, the master surfaces included the bottom and sides of the raft, whereas, for the piles, the master surfaces only included the circumference (skin) of the piles. The bottom (base) surfaces of the piles were not included as part of the interaction surfaces, as the actual on-site piles were socketed into bedrock and were thus modelled using appropriate boundary conditions (discussed in Section 4.2.5). A penalty friction formation was used for the tangential behaviour, consisting of a Coulomb friction model. A friction coefficient of 0.65 was assigned to all the intersections. This value was obtained from Winterkorn & Fang (1975) as a typical friction

coefficient between rough concrete, cast in situ, and clayey sand soil. On the other hand, the normal behaviour was modelled using the Abaqus default "Hard" contact pressure overclosure, allowing for separation after contact. "Hard" contact was selected as it minimises the penetration of the slave nodes into the master surface and has no limit to the magnitude of contact pressure that can be transmitted when surfaces are in contact. All other default Abaqus settings were accepted.

4.2.4   Meshing

All the parts in the simulation domain were discretised using 10-noded quadratic tetrahedron elements (C3D10), with the decision of the element type based on the geometric nature of the parts. **Figure 4-4** indicates the generated finite element mesh of the FE model developed. The simulation domain was partitioned to get an internal view of the piles and raft meshing. When generating the mesh, it was essential to ensure uniform meshing between contacting parts at all interfaces. This was achieved using partitioning techniques (see **Figure 4-1**) and local edge seeding, allowing for an equal number of elements at intersecting faces. The bias feature available in Abaqus was particularly used for meshing the soil part to reduce computation time. This feature allows for a combined fine-coarse mesh in a single part, gradually increasing the element size from a fine mesh in regions where stresses, strains and deformations are rapidly changing to a coarser mesh where stress concentrations are low. The regions of rapidly changing stresses and deformations are typically near and at pile-raft-soil interfaces.
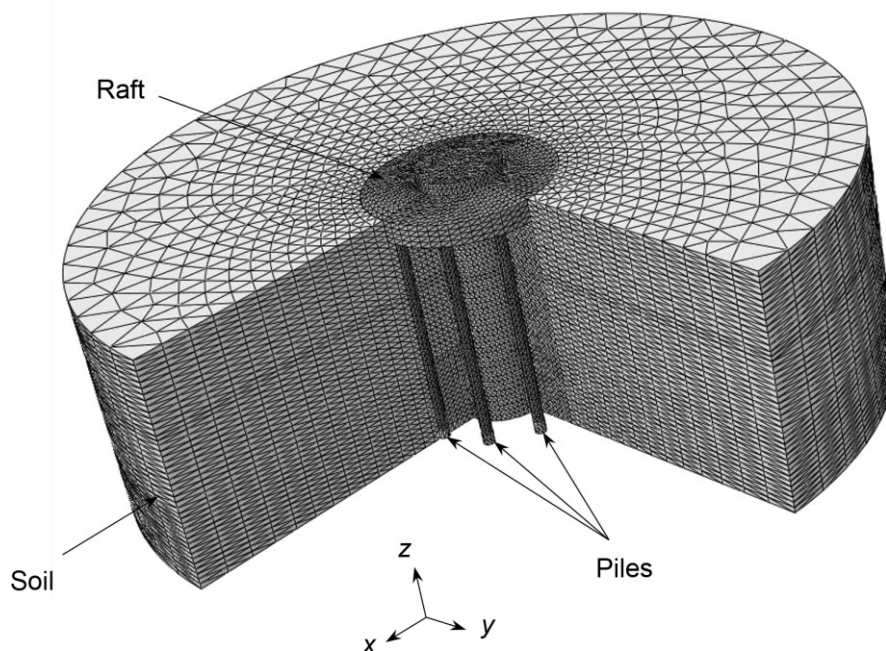
Figure 4-4: Finite element mesh partitioned

In addition, the regions towards the outside perimeter of the soil are generally expected to have low stress concentrations. The gradual increase in element size using the bias function can be seen in **Figure 4-4**. The final finite element mesh consisted of 393 601 quadratic tetrahedron elements and 552 265 nodes.

4.2.5 Boundary conditions

Due to the selection of the elements being 3-D tetrahedrons, each node had a maximum of three degrees of freedom (DOF), all of which are translational. Based on this knowledge, boundary conditions were applied to the soil and piles, as indicated in **Figure 4-5(a)** and **(b)**. As the soil on-site was resting on bedrock, the bottom of the soil part was fixed in all translational directions ($u_x = u_y = u_z = 0$). The sides of the soil part were fixed in the x- and y-translational directions ($u_x = u_y = 0$) and allowed to move freely in the z-direction. As the actual piles on-site were socketed into bedrock, for modelling purposes, it was assumed that the socket connection was fixed. Thus, the bottom of the piles was also fixed in all translational directions ($u_x = u_y = u_z = 0$).

Fixed in x and y translational directions
($u_x = u_y = 0$)

Fixed in all translational directions
($u_x = u_y = u_z = 0$)

(a)

(b)
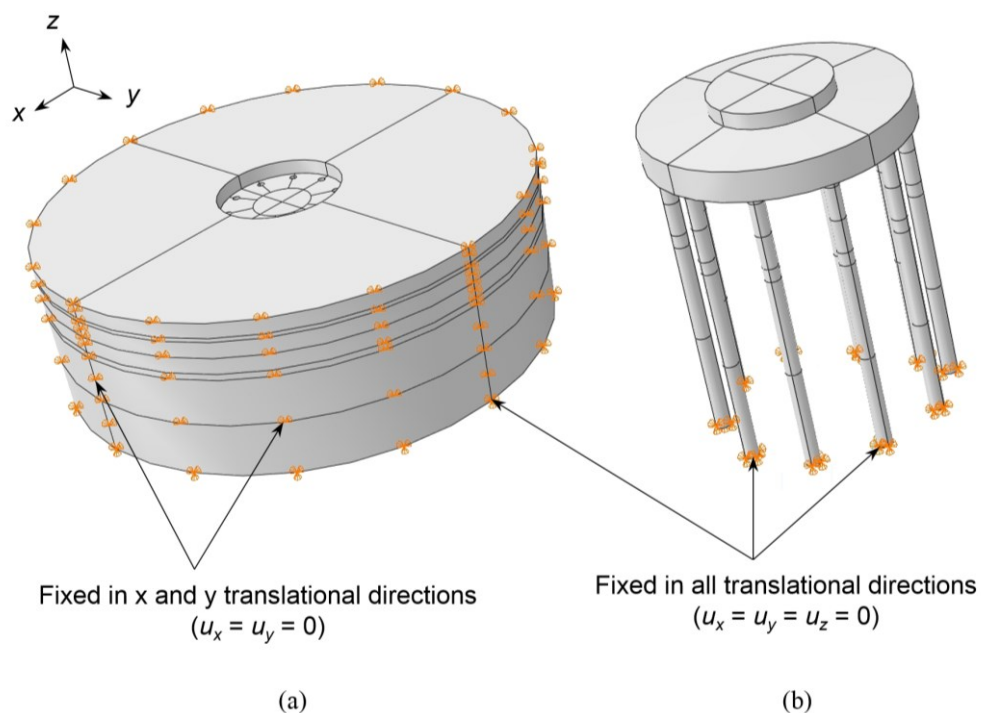
Figure 4-5: FE model boundary conditions: (a) soil; (b) piles

4.2.6 Key simulation steps and loading

The FE model was executed using six separate steps. These steps were carried out in the following order: initial, geostatic, foundation gravity, soil backfill, vertical load, and lastly, a combined coupled horizontal load and overturning moment step, with each step building on

the response of the FE model in the previous step. The initial step is a default step in Abaqus whereby all the boundary conditions, interactions between contacting surfaces, and predefining fields are specified. The geostatic step is a standard step usually included when modelling soil problems in Abaqus and ensures vertical and horizontal equilibrium of the soil before load application and analysis. Gravity loads are applied to only the soil part during this step (g = 9.81 m/s^2), along with a predefined geostatic lateral stress field, which should together equilibrate and produce zero or near-to-zero deformations.

The predefined lateral stress field defines the horizontal confining stresses in the soil with depth (assuming a linear increase with depth), with the magnitude of these stresses depending on the density of the soil and the depth below the soil surface. A lateral earth pressure coefficient is thus required as an input in Abaqus. According to Winterkorn & Fang (1975), the at-rest lateral earth pressure coefficient for cohesionless soils can be approximated using the Poisson's ratio of the soil (v_s), as indicated by **Equation 4-2**. Based on the values presented in **Table 4-2**, K_0 was calculated as 0.429, with this coefficient assumed for the entire soil depth. The calculated K_0 was in the range Whitlow (1995) specified for dense sands and was thus considered representative of the medium-dense to dense soil conditions on the Wesley Wind Farm site.

$$K_0 = \frac{v_s}{1 - v_s} \qquad\qquad\qquad (4\text{-}2)$$

Figure 4-6 indicates a cross-section of the soil part, showing the lateral earth pressure in the soil with depth, with confining pressure presented in megapascal. It should be pointed out that the lateral pressure at the top of the soil is not zero. This was due to the soil backfill being modelled as a separate vertical pressure rather than included in the soil part. Therefore, the additional lateral pressure caused by the 1.1 m soil had to be considered and included in the model to simulate the horizontal pressures of a 'buried' foundation.
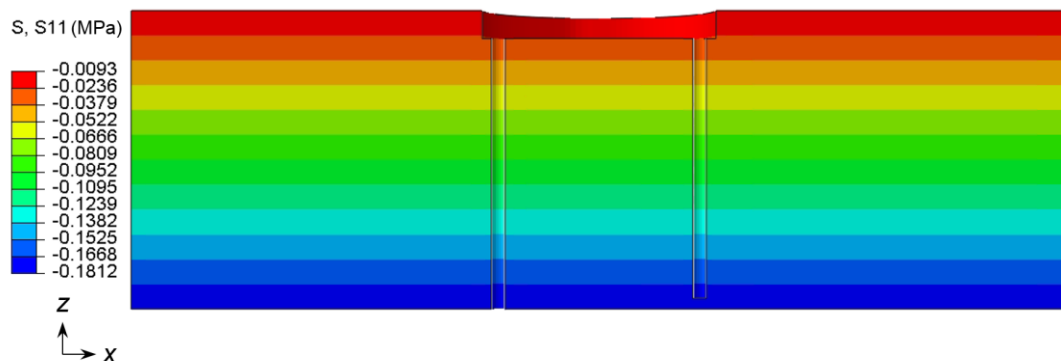
Figure 4-6: Lateral earth pressure with depth cross-section

The additional 1.1 m vertical pressure was applied to the top surface of the soil section as part of the gravity load of the soil to obtain global equilibrium during the geostatic step. As seen in **Figure 4-6**, the piles and raft were deactivated during this step using the model change feature in Abaqus, applying temporary boundary conditions at the piles and raft holes. This allowed the soil to obtain equilibrium before introducing the piles and raft. The piles and raft were re-activated after this step, and the temporary boundary conditions at the holes were removed. After completing the geostatic step, the individual gravity loads ($g = 9.81$ m/s^2) for the two foundation components (piles and raft) were applied during the foundation gravity step (see **Figure 4-7(a)**). This step was followed by applying a uniform vertical pressure load equivalent to the backfill material of 1.1 m during the soil backfill step. This load was applied to the top of the raft, on the sides of the pedestal, as illustrated by **Figure 4-7(b)**. To avoid potential stress concentration with the application of point loads, for the vertical load step, which consisted of the weight of the turbine, the load was modelled as an equivalent pressure applied to the top surface of the pedestal (see **Figure 4-7(c)**).

With the research focusing on static foundation response, the forces and moments caused by the wind were simplified to a single horizontal shear load and moment applied to the top of the foundation pedestal. The coupled horizontal load and overturning moment caused by the wind will occur simultaneously and were therefore combined in the last step. Separating the vertical load from the coupled horizontal load and overturning moment allows for the analysis of the foundation under vertical loading in isolation (simulating a stationary turbine, not in operation). Additionally, simulating the turbine during operations was achieved with the coupled horizontal load and overturning moment along with the imposed vertical load. The horizontal load was applied in the positive x-direction, with the accompanying moment applied in the positive y-direction according to the right-hand rule (see **Figure 4-7(d)**), creating a moment about the y-axis caused by the horizontal load acting in the x-direction. A multi-point constraint, more generally known as an MPC, was used to apply this coupled horizontal load and overturning moment to the foundation without causing stress concentrations or convergence issues. MPCs constrain the motion of the slave nodes of a region to the motion of a single control point (typically a reference point). In addition, they allow constraints to be imposed between different DOFs in the same model (Abaqus Online Documentation, 2014). This means, for example, that bending moments can be applied to a simulation domain consisting of tetrahedron elements with only translational DOFs. A reference point was created in the middle of the top surface of the pedestal, with the horizontal load and overturning moment being applied at this reference point. The MPC beam constraint was then selected (as a bending moment had to be applied), with the top surface of the pedestal taken as the slave surface during step execution. The beam constraint, in

particular, defines a rigid beam connection between the reference point and all the nodes on the slave surface and constrains the displacement and rotation between these points.
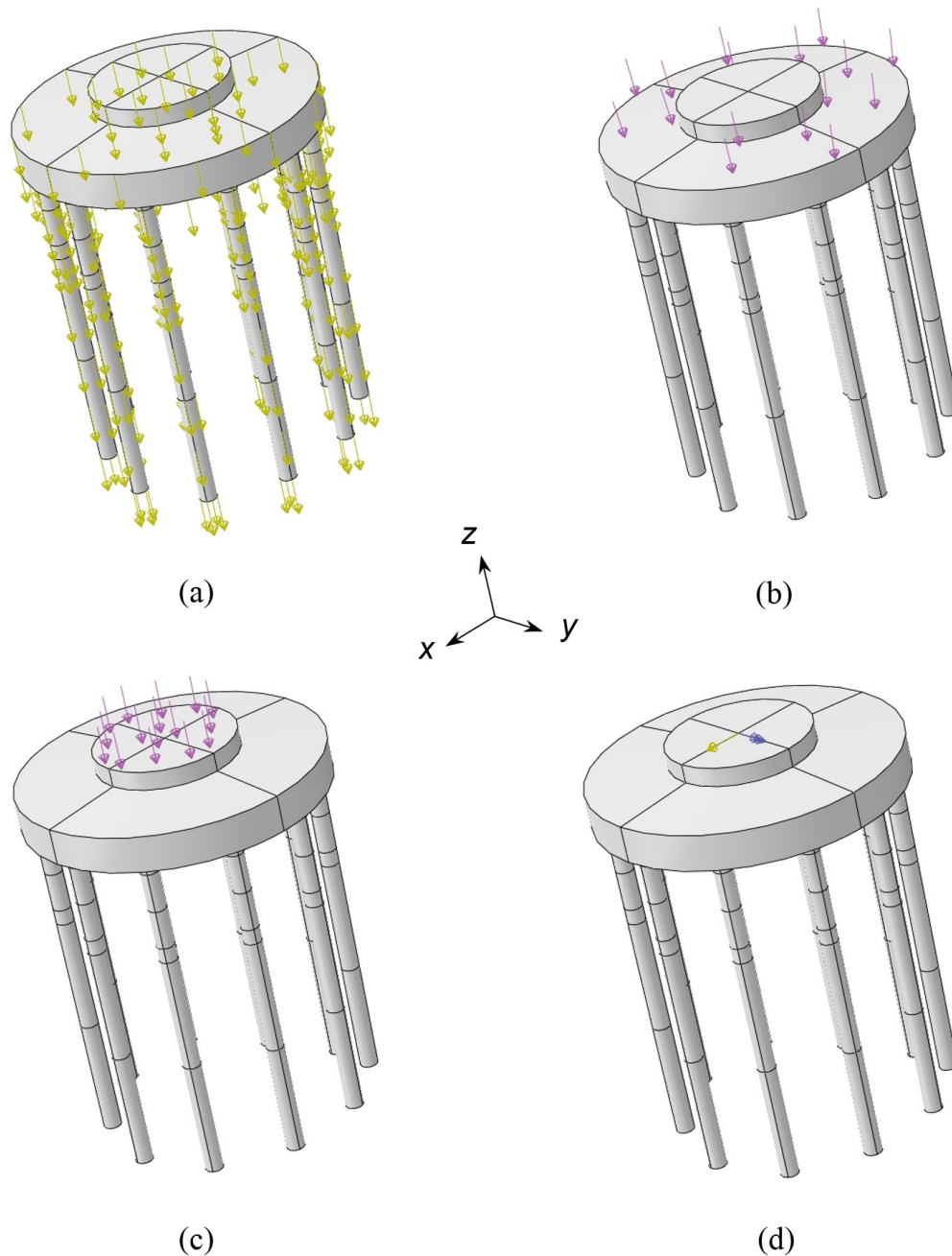
Figure 4-7: Loading steps: (a) raft and piles gravity; (b) backfill soil pressure; (c) vertical load; (d) horizontal load and overturning moment

After completing the construction and assembly of the 3-D piled-raft foundation FE model, a job was created and submitted for analysis using the supercomputer in the Department of Civil Engineering at the University of Pretoria. Due to the linear elastic soil model, a large time step of 1 was used for all the steps as no nonlinear aspects of the soil, potentially causing numerical instability or convergence issues, was present.

4-13

4.3   MODEL COMPARISON

To ensure that the response of the developed FE model in Abaqus represented the response of an in-service onshore wind turbine piled-raft foundation, it was necessary to compare the simulated model outputs against known measured reactions. As the developed model resembled the actual on-site foundation and supporting soil, a direct comparison was made, and the foundation system was calibrated. The comparison eliminated any potential concern about the model validity, allowing for all numerical work conducted in the remainder of this thesis using the same model set-up to be carried out more confidently. Only changes in the response of the FE model during turbine installation and under wind loading were compared with the in-service foundation. As additional factors contributed to the overall raft response, including seasonal thermal effects, as seen in Section 3.9.3 in Chapter 3, the FE model's comparison was based solely on the pile response. With the loads being applied to the raft and the raft acting as the link between the applied loads and the underlying piles, it was assumed that should the response of the piles be captured realistically, the response of the raft would also be representative. Extraction of the model data for post-processing and comparison was done through the use of display groups created in the visualisation module. During model construction, these display groups were generated from node sets specified on the respective geometry and part partitions. As an overview, **Figure 4-8** indicates a typical response of only the simulated foundation under loading, with the soil part excluded from this figure for visualisation. **Figure 4-8(a)** shows deformations of the piled raft in the *z*-direction resulting from the applied vertical load during the vertical load step in millimetres, with the entire foundation moving downwards. **Figure 4-8(b)**, on the other hand, illustrates deformations, again in the *z*-direction, after applying the horizontal load and overturning moment during the last load step. Under these load conditions, deflections on the leading side of the foundation were downwards, whereas the deflections on the trailing side of the foundation were upwards, as expected.

4.3.1   FE model vertical load comparison

With the bottom tower section already installed upon arrival back on site before the final turbine assembly (see Section 3.9.2 in Chapter 3), the applied vertical load in Abaqus had to be split in two, as seen in **Table 4-3**. The first vertical load of 795 kN simulated the weight of the pre-installed bottom tower section, whereas the second vertical load of 3610 kN simulated the weight of the additional turbine components constructed on top. The change in the simulated foundation response before and after the 3610 kN load application could thus be extracted and compared to the change in the strain measured in the actual wind turbine foundation during the installation of the top tower and turbine components. As the vertical

4-14

loads were not applied to the model as a point load, the equivalent vertical pressure for each load applied to the top surface of the pedestal is also indicated in **Table 4-3**.

(a)

(b)
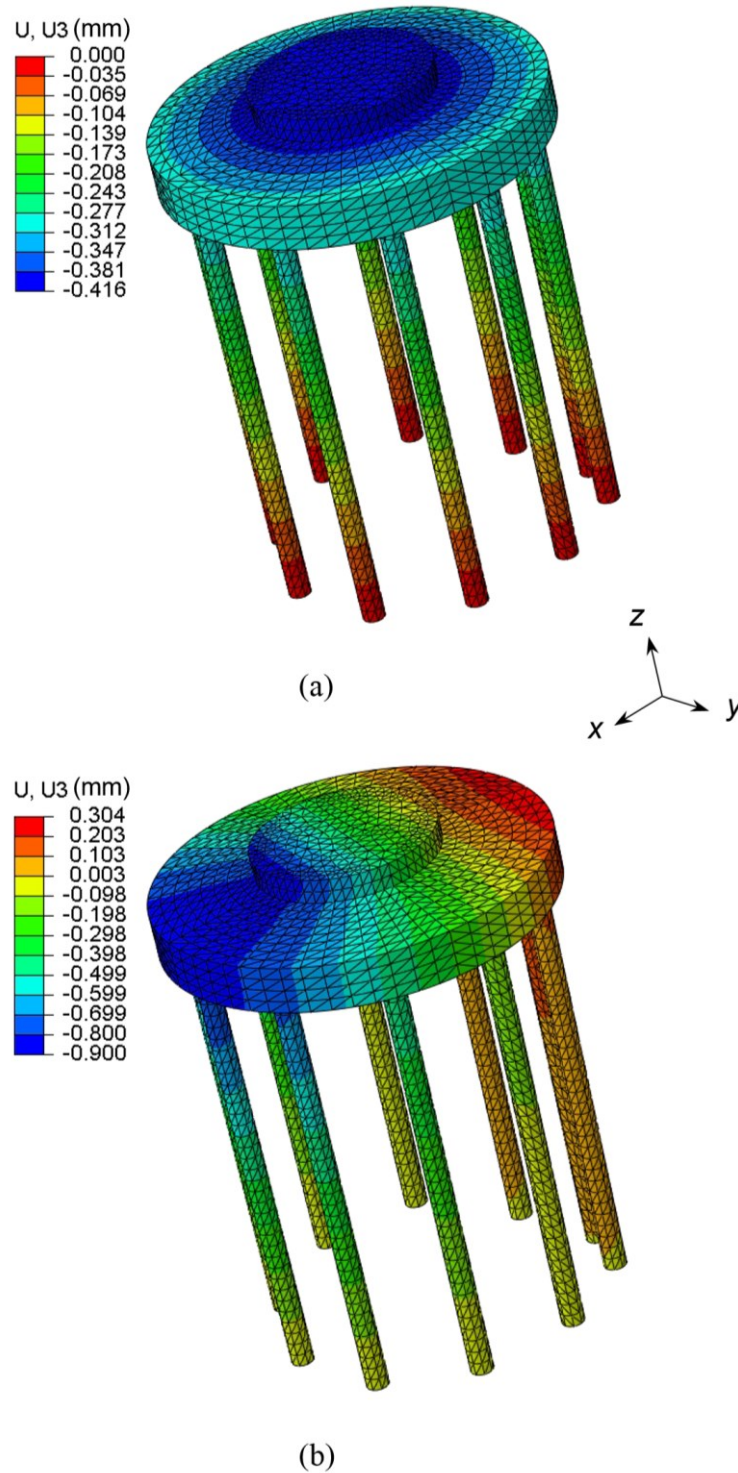
Figure 4-8: FE model deflected shape: (a) vertical load; (b) vertical load, horizontal load and overturning moment

4-15

Table 4-3: Turbine component and corresponding vertical load

Turbine component	Vertical load (kN)	Equivalent vertical pressure on the pedestal (kPa)
Bottom tower section	795	19.5
Top tower sections and additional components	3610	88.7

Obtaining values of the strains measured in the piles for comparison against the FE model under vertical loading, a 24-hour average measured strain reading was taken for each of the 17 sensors installed in the ten piles before turbine installation on 28 January 2021. Additionally, a 24-hour average measured strain reading was again taken from each sensor after turbine installation on 9 February 2021, with the change between the average strain readings taken as the influence of the top turbine tower and components. On both these days, strain measurements in the piles remained relatively constant, allowing for the difference to be calculated and compared. **Table 4-4** indicates the changes in the actual strains measured in each pile from the embedded sensors on both these days. Additionally, the changes in strains observed in each pile of the developed FE model under vertical loading at the location of the embedded sensors are also presented in **Table 4-4**. The sign convention for comparing the measured results to the predicted results obtained from Abaqus used the structural default of positive loads being tensile and compressive loads being negative.

Table 4-4: Piles vertical load comparison

Pile name	Pile length (m)	Actual Δμε		FE model Δμε	
18 P 2.5 L135	17.1	-6.4		-8.7	
54 P 0.5 L112.5	17.2	-8.1		-10.1	
54 P 2.5 L112.5	17.2	-6.2	Δ2.5με	-8.4	Δ2.2με
54 P 4.5 L112.5	17.2	-5.6		-7.9	
54 P 0.5 L292.5	17.2	-7.5		-8.2	
54 P 2.5 L292.5	17.2	-6.5	Δ2.6με	-7.8	Δ2.0με
54 P 4.5 L292.5	17.2	-4.9		-6.2	
90 P 2.5 L45	17.1	-7.4		-7.6	
126 P 2.5 L157.5	16.8	-1.8		-8.9	
162 P 2.5 L157.5	16.8	-1.7		-9.0	
198 P 0.5 L315	17.9	-7.2		-8.2	
198 P 2.5 L315	17.9	-6.1	Δ4.0με	-7.4	Δ3.9με
198 P 4.5 L315	17.9	-3.2		-4.3	
234 P 2.5 L45	17.9	-7.8		-7.4	
270 P 2.5 L180	16.8	-3.4		-9.0	
306 P 2.5 L270	16.7	-5.0		-8.3	
342 P 2.5 L112.5	16.9	-6.3		-8.5	

4-16

Overall, the measured results from the piles compared well with the predicted results from the developed FE model, with the FE model simulating responses within about 2 με from the actual measurements. The most significant difference seemed to occur with the shorter piles (16.8 m), with these piles measuring axial strains that are smaller. This difference was pointed out in Chapter 3 as somewhat strange, as shorter piles typically carry higher loads than longer piles when socketed into bedrock. This significant difference could potentially be attributed to the assumed bearing conditions of the piles in Abaqus.

During FE model construction, boundary conditions applied to the bottom of all the piles assumed complete fixity, with piles unable to move in any direction, which might not have been the case for the actual piles. The piles containing sensors at three depths are highlighted in bold in **Table 4-4**. Considering the measured and simulated strains in these piles, the effect of pile shaft friction under loading is visible (see red arrows in **Table 4-4**), with strain increasing towards the top of the pile under the vertically applied load. The difference in strain measured between the bottom and top sensor in each pile is also comparable to that computed in the FE model, indicating that the interaction modelling produced reasonable results. Thus, the relatively small differences between the measured and computed pile strains indicate that the FE model simulates reality regarding vertical load effects.

4.3.2   FE model horizontal load and overturning bending moment comparison

As indicated previously, a static horizontal shear load and accompanying overturning moment were applied to the FE model to simulate the influence of a wind acting on the turbine and, ultimately, the supporting foundation. However, calibrating the static FE model under the horizontal load and overturning moment was slightly more complicated due to the dynamic nature of the wind turbine in service. Several assumptions regarding the magnitude of the applied horizontal load and overturning moment on the FE model were made, as discussed below, potentially resulting in the differences observed between the actual and simulated results.

According to the site data in Chapter 3, the direction in which the horizontal load and overturning moment were applied to the FE model corresponded to the main wind direction. The main wind direction was taken as to be blowing from a westerly direction (270˚), with the horizontal load acting in the positive *x*-direction according to the model built. Initially, two separate simulations were run to determine and compare the predicted response of the piled-raft foundation to the wind-induced loads. Both simulations had the same set-up, including vertical loading, with the only difference being the magnitude of the applied horizontal load and overturning moment. The first simulation applied a predicted horizontal load and

overturning bending moment to the foundation exposed to a wind speed of 30 km/h, whereas the second applied a load and moment for a typical 50 km/h wind speed. The predictions for the overturning moment at the bottom of the turbine tower at these wind speeds were based on the average linear relationship between the wind speed and the measured tower bending moment presented in **Figure 3-31** in Chapter 3. As the horizontal shear load at the base of the tower was not measured on the in-service wind turbine tower, the applied horizontal load in the FE model was approximated by dividing the applied overturning moment by the hub height of the turbine (117 m). **Table 4-5** indicates the horizontal loads and overturning moments applied to the FE model foundation for the 30 km/h and 50 km/h wind speeds, respectively.

Table 4-5: Wind speed and corresponding applied horizontal load and overturning moment

Wind speed (km/h)	Horizontal load (kN)	Overturning moment (MNm)
30	275.2	32.2
50	458.1	53.6

Similar to the vertical load comparison, average strain results measured from the sensors in the piles were extracted and compared to the predicted results from the FE model. Two wind speeds were considered (30 km/h and 50 km/h), resulting in different horizontal loads and overturning moments acting on the underlying foundation and were modelled as such. For both wind speeds, all the measured site data was examined in search of a day on which the wind blew relatively constant from the 270° direction or nearby. For the 30 km/h wind speed, a 10-hour strain average was obtained on 20 July 2021, whereas measurements for the 50 km/h wind speed were obtained from a 10-hour strain average in the piles on 14 March 2022. **Figure 4-9(a)** and **(b)** indicate the wind speed and corresponding measured bending moment at the tower's base for the two 10-hour data extraction periods. On average, from the two 10-hour periods, the measured bending moments at the base of the tower compared relatively well with the static bending moments applied to the FE model for the 30 km/h wind speed, with the bending moment at 50 km/h varying significantly (see **Figure 4-9**). Thus, given that the relationship between wind speed and the tower base moment is relatively linear up to a wind speed of 30 km/h, deviating at higher wind speeds, for comparison purposes, only the 30 km/h wind speed was considered.

As seen in **Table 4-6**, a larger difference between the measured and simulated strain changes in the piles existed for a 30 km/h wind speed compared to under vertical loading, with differences being between about 5 με to 10 με. These larger differences could potentially be

attributed to the fact that wind speeds and wind directions on-site are highly variable, with tower bending moments changing rapidly over a short time.

(a)   (b)
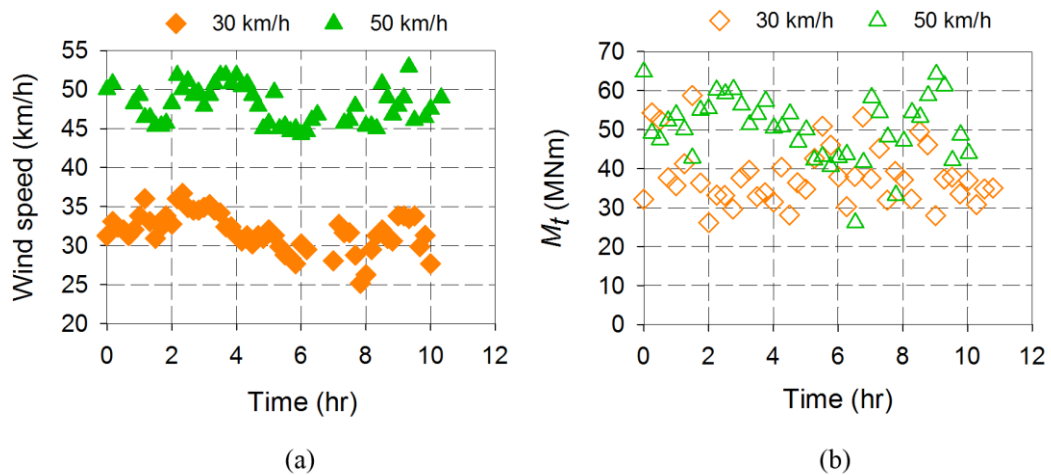
Figure 4-9: Horizontal load and overturning moment comparison: (a) wind speed; (b) tower bending moment

Table 4-6: Piles horizontal load and overturning moment comparison

Pile name	Actual Δμε – 30 km/h		FE model Δμε – 30 km/h	
18 P 2.5 L135	-11.9		-11.3	
54 P 0.5 L112.5	-19.6		-21.4	
54 P 2.5 L112.5	-16.3	Δ1.8με	-21.1	Δ2.4με
54 P 4.5 L112.5	-17.8		-19.0	
54 P 0.5 L292.5	-24.1		-15.5	
54 P 2.5 L292.5	-16.3	Δ13.8με	-16.3	Δ2.3με
54 P 4.5 L292.5	-10.3		-17.8	
90 P 2.5 L45	-18.2		-26.9	
126 P 2.5 L157.5	-11.1		-13.5	
162 P 2.5 L157.5	-5.9		-2.8	
198 P 0.5 L315	11.2		5.3	
198 P 2.5 L315	6.6	Δ8.0με	4.3	Δ2.3με
198 P 4.5 L315	3.2		3.0	
234 P 2.5 L45	22.6		25.0	
270 P 2.5 L180	6.6		17.6	
306 P 2.5 L270	10.1		23.8	
342 P 2.5 L112.5	2.3		-0.1	

Considering the piles containing sensors at three depths (highlighted in bold in **Table 4-6**), the effect of pile shaft friction was also visible, with sensors on the opposing ends of the same pile differing. Additionally, assumptions regarding the magnitude of the horizontal load applied to the FE model may also affect the simulated outcomes. In view of the response of the actual and simulated foundations, piles located on the leading (leeward) end of the raft in

the direction of load application experienced a compressive change in strain. In contrast, piles on the trailing (windward) end experienced a tensile change in strain, as expected. Although not an exact or near-exact match, the overall response of the FE model foundation seems to replicate the in-situ wind turbine foundation response.

4.4 SUMMARY

In this chapter, steps for constructing a representative FE model of a piled-raft foundation and supporting soil in Abaqus were presented and summarised. Several key aspects were incorporated into the developed FE model, the most important being the realistic modelling of the interaction between interfaces. The chapter concluded with a comparative section that compared the simulated FE model results against the actual measured response of an onshore wind turbine piled-raft foundation. A good agreement existed between the predicted FE model strains and the measured strains in the foundation under vertical loading, with the difference being relatively small. Concerning the FE model under horizontal loads and overturning moment, the difference between the measured strain and the predicated model strain was larger. However, the overall response of the foundation was still in line with what was observed on-site, as presented in Chapter 3. The difference could mainly be attributed to calibrating against dynamic loading, with the wind speed, wind direction and the bending moment at the tower's base changing rapidly. Assumptions regarding the applied horizontal load magnitude were also considered a potential contributing factor. In general, the developed FE model seems to replicate the typical response of a piled-raft foundation supporting an onshore wind turbine. However, not an exact match, general behavioural trends could be observed, with the soil-structure interaction concepts further explored in Chapter 5 and Chapter 6.

5   SOIL-STRUCTURE INTERACTION PARAMETRIC STUDY

5.1   INTRODUCTION

Given not only the limited data available for piled-raft foundations under horizontal loads and overturning moments but also the trends observed from the full-scale instrumented foundation in Chapter 3, questions arose about whether the piled-raft foundation's response under these load combinations would have been different if the foundation size and properties or the soil were any different. Additionally, with the strive towards taller but fewer wind turbine structures to obtain the same electricity output, the extent of the consequence of the increase in vertical loads, horizontal loads and overturning moments imposed on the foundation must be quantified. As soil-structure interaction drives foundation response, there is a need to further investigate piled-raft foundations under increasing dominant horizontal loads and overturning moments.

In this chapter, a parametric study, or multivariable analysis, was conducted using FE modelling to investigate these questions. The calibrated FE foundation model discussed in Chapter 4, constructed in Abaqus, was used for this study. The variables considered in this study were based on those deemed necessary regarding wind turbine foundation stiffness and portal frame theory, as highlighted in Chapter 2. The variables included the raft thickness (t_r), the raft radius (R_r) and the pile diameter (d_p), respectively. As the interaction between the foundation and the soil is essential, the Young's modulus of the soil (E_s) was also varied, taking E_s as constant throughout the entire soil part (no layering). In addition, the influence of pile length (L_p), which corresponds to the depth of the compressible soil layer, and hub height (h_h) was also considered for all the above-mentioned variables, taking all piles to have the same lengths.

Figure 5-1 indicates a cross-section of the 3-D FE model, highlighting all the parametric study variables, excluding h_h, as well as some dimensions that were kept fixed during the multivariable analyses. Although technically not a physical dimension or property, in this study, h_h was related to the magnitude of the vertical loads, horizontal loads and overturning moments applied to the foundation during the different simulations. The influence of load and moment magnitude was thus investigated by varying h_h. The author does, however, acknowledge that although h_h is not the only contributing factor influencing the extent of the loads and moments acting on the supporting foundation, it was considered to be for this parametric study. The Young's modulus, Poisson's ratio, and density of the piles and raft were assumed to be the same as that used for the comparative model, with the density and

Poisson's ratio of the soil also taken to be the same, as seen in **Table 4-1** and **Table 4-2** in Chapter 4, respectively. These values remained constant throughout all simulations. Whilst not indicated in **Figure 5-1**, the equivalent uniform vertical pressure applied to the top of the raft, simulating the backfilled soil, was retained at a 1.1 m deep layer.
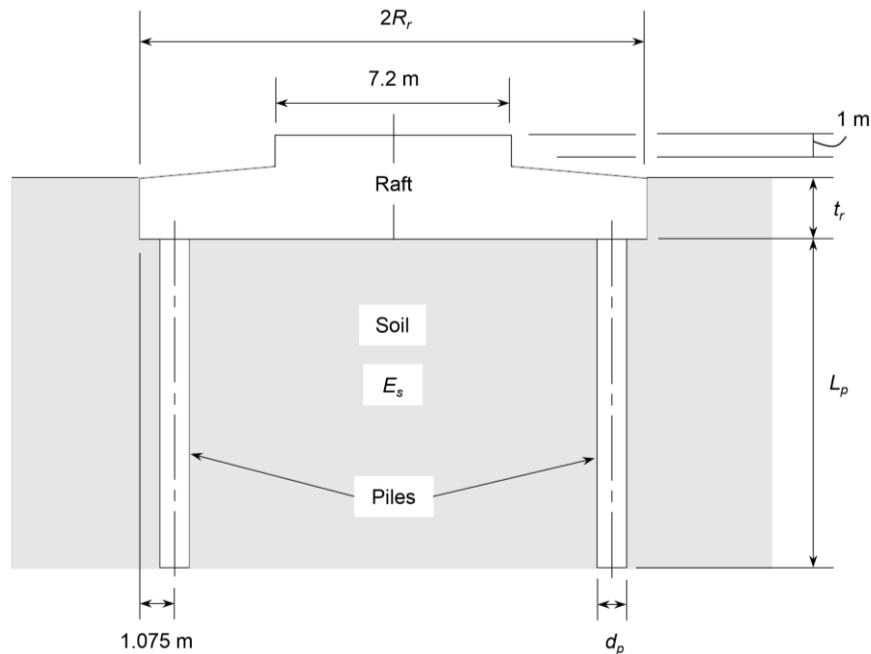
Figure 5-1: Parametric study variables

For each parametric variable (t_r, R_r, d_p and E_s) considered, using Design of Experiment techniques (Montgomery, 2001), h_h was varied simultaneously to investigate load and moment magnitude following a 2-D matrix, as presented in **Figure 5-2**, with h_h varied on the y-axis, with values equalling 20 m, 48 m, 117 m, 186 m and 214 m, respectively. On the x-axis in **Figure 5-2**, the variable under investigation differed, with the range of values (a, b, c, d and e), used in **Figure 5-2**, summarised in **Table 5-1**. Depending on the examined variable, the other variables presented in **Figure 5-1** were fixed at the values indicated in red in **Table 5-1**. In addition, for each variable, the 2-D matrix was repeated for L_p = 10 m and 20 m, respectively, to investigate the influence of pile slenderness.

5.2   LOADS, LOAD CASES AND PLOT DESCRIPTION

Two types of static load cases were considered during this study. The first considered only a vertical load (V) acting on the foundation, representing a stationary wind turbine, with wind effects assumed near zero. This load case also serves as a baseline for the parametric study for each variable considered, as trends should resemble those observed in literature where foundations under vertical loading were primarily investigated. For the second load case, a coupled horizontal load (H) and overturning moment (M) were applied in conjunction with

the vertical load (V), simulating conditions of a wind turbine under operations. Both load cases were considered separately, investigating the change in the foundation's response due to the additional horizontal load and moment. Gravity and overburden soil loads were still applied to each model during computation but zeroed out to isolate the influence of the loads only. **Figure 5-3(a)** and **(b)** contain 2-D representations in the *xz*-plane of the two load cases considered during this investigation.
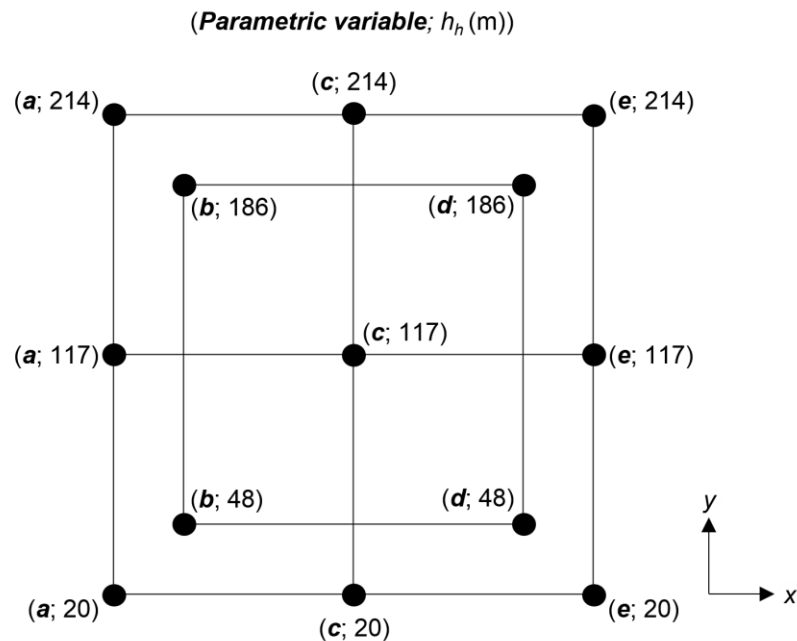
Figure 5-2: Parametric study variables diagram

Table 5-1: Parametric study values for different variables

Parametric variable	a	b	c	d	e
Young's modulus of the soil, E_s (MPa)	10	74	*230*	386	450
Raft thickness, t_r (m)	0.70	1.04	*1.85*	2.66	3.00
Raft radius, R_r (m)	5.5	*7.75*	10	13.5	15
Pile diameter, d_p (mm)	600	688	*900*	1112	1200

As mentioned, the applied loads and moments were expressed in terms of h_h to investigate the effect of load magnitude on the foundation's response. Vertical loads for each h_h were determined through linear extrapolation of the actual 117 m high wind turbine's weight (as presented in Chapter 3) of about 450 tons (4414.5 kN). Based on **Table 2-2** in Chapter 2, under SLS load conditions, the ratio between horizontal and vertical loads for wind turbines seems to be around 10%. Thus, the magnitude of the horizontal load was estimated as 10% of the vertically applied load for each simulation. The accompanying overturning moment was then calculated by multiplying the horizontal load with the h_h considered. **Table 5-2** indicates h_h along with the corresponding vertical load, horizontal load and overturning moment

applied to each FE model. The overturning moment differs somewhat from the actual bending moment measured for a 117 m high h_h in Chapter 3. However, this can largely be attributed to the assumed ratio between the applied horizontal and vertical loads that might not be strictly representative.
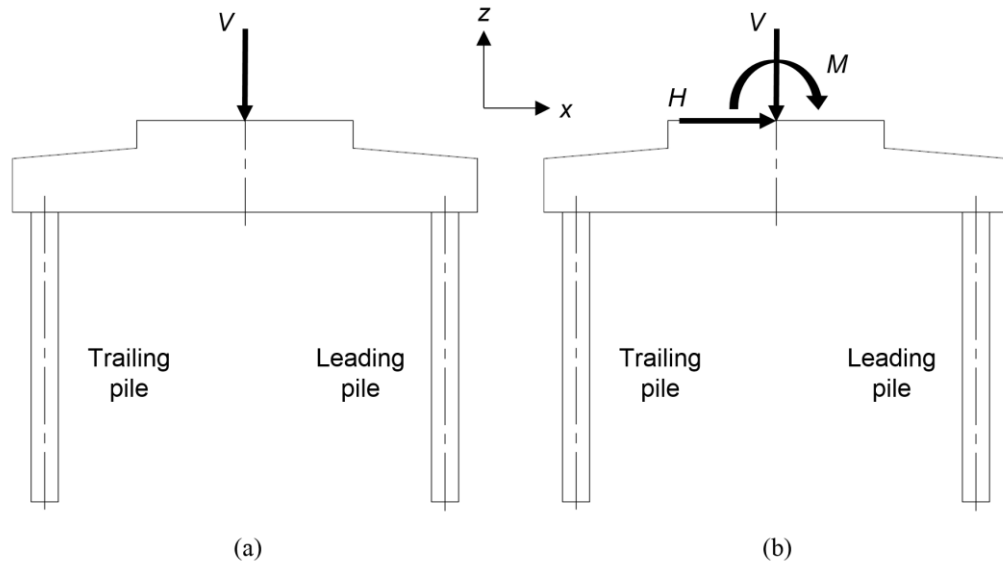
Figure 5-3: Load cases: (a) vertical load (V); (b) vertical load, horizontal load and overturning moment (V-H-M)

Table 5-2: Hub height (h_h) and corresponding loads and moments applied to the FE model

Hub height, h_h (m)	Vertical load, V (kN)	Horizontal load, H (kN)	Overturning moment, M (MNm)
20	754.6	75.5	1.5
48	1826.2	182.6	8.8
117	4414.5	441.5	51.6
186	7002.8	700.3	130.0
214	8074.4	807.4	172.8

For each load case, several output variables, including displacements, deflections, stresses, strains, axial forces and bending moments at specific locations, were extracted from the simulated models for post-processing and plotting. These outputs were extracted using display groups in Abaqus. **Table 5-3** and **Table 5-4** indicate the plot descriptions for the vertical load case (V) and the combined vertical load, horizontal load, and overturning moment load case (V-H-M), respectively. The location of the extracted data for each plot description is also highlighted in red under the plot schematic column in each table. Although the foundation was modelled in 3-D, the plot schematic is indicated in 2-D, as data were plotted in the central xz-plane, with loads and moments acting within this plane in the 3-D model. In terms of the leading and trailing pile descriptions, their assigned positions are

indicated in **Figure 5-3**. Also mentioned in the literature, the leading pile was considered as the pile on the leading (leeward) end of the raft, given the direction of the horizontal load and overturning moment, with the trailing pile positioned on the trailing (windward) end of the raft under loading.

Table 5-3: Plot description and schematic: vertical load
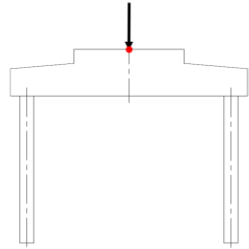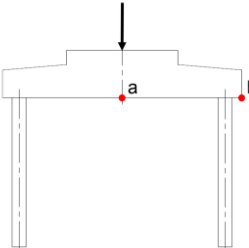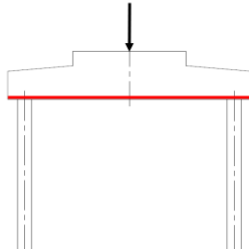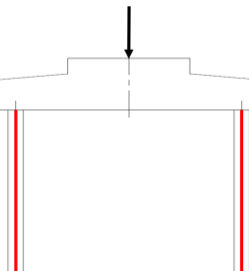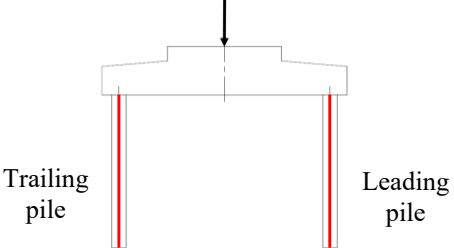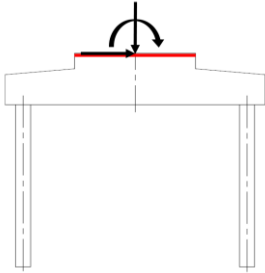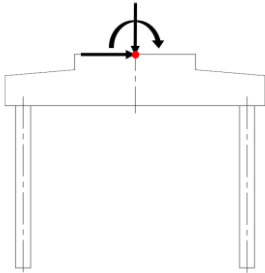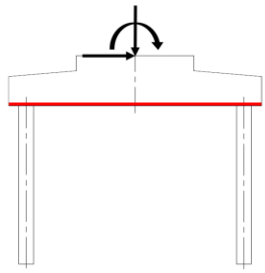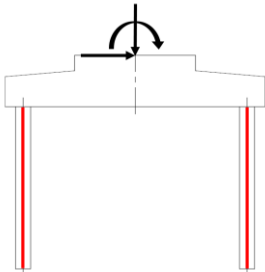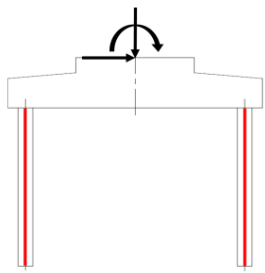
Plot description	Plot schematic
Raft top centre deflection	
Raft differential settlement (a-b)	
Raft stress at raft base	
Total vertical load percentage carried by the piles	
Leading and trailing pile bending moment and axial force	

5-5

Table 5-4: Plot description and schematic: vertical load, horizontal load and overturning moment

Plot description	Plot schematic
Raft pedestal rotation	
Raft top centre horizontal displacement	
Raft stress at raft base	
Total vertical load percentage carried by the piles	
Leading and trailing pile bending moment and axial force	Trailing pile / Leading pile

5.3 SIGN CONVENTION

Similar to Chapter 4, the sign convention adopted for plotting the data in this chapter was the default Abaqus sign convention, which aligns with standard structural practices. **Figure 5-4**

presents the different sign conventions adopted for the output variables. **Figure 5-4(a)** indicates the convention for deflection and displacement in the *xz*-plane, whereby deflections in the positive *z*-direction and displacements in the positive *x*-direction are both positive. Additionally, **Figure 5-4(b)** shows the convention adopted for plotting bending moments in the piles and stresses at the base of the raft. Bending moments and stresses are plotted on the tension side of members, with the positive or negative signs assumed, as indicated in **Figure 5-4(b),** based on moment equilibrium at the nodes/joints. Lastly, **Figure 5-4(c)** shows the sign convention for a tensile and compressive load being positive and negative, respectively.
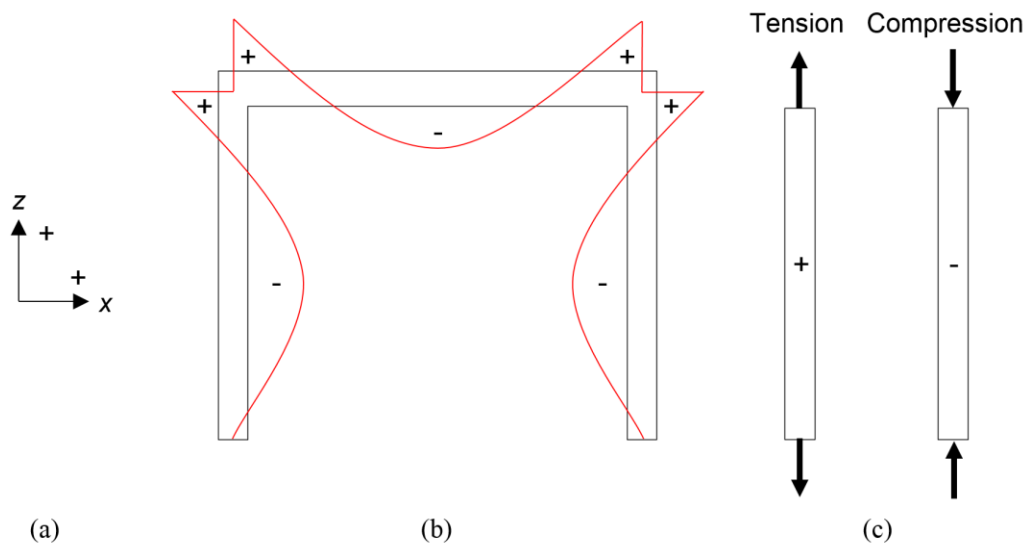
Figure 5-4: Sign convention: (a) deflection/displacement; (b) bending moment/stress; (c) axial force

5.4   YOUNG'S MODULUS OF THE SOIL

This section considers the influence of Young's modulus of the soil (E_s) on the response of a piled-raft foundation under dominant horizontal loads and overturning moments. **Table 5-5** indicates the Young's modulus values of the soil considered, with the placement of *a*, *b*, *c*, *d* and *e* shown in **Figure 5-2**. Two load cases were investigated, with the first being the impact of only vertical loading (*V*), while the second considered the influence of the combined vertical load, horizontal load and the overturning moment (*V-H-M*). Apart from the Young's modulus of the soil, the other parametric variables were kept at the values indicated in red in **Table 5-1**.

Table 5-5: Parametric study values – Young's modulus of the soil

Parametric variable	*a*	*b*	*c*	*d*	*e*
Young's modulus of the soil, E_s (MPa)	10	74	230	386	450

5.4.1   Vertical load, V

Figure 5-5(a) and **(b)** present the surface plots showing the influence of h_h and E_s on the top central vertical deflection of the raft (v_{rv}) for $L_p = 10$ m and 20 m, respectively. Under vertical loading, larger v_{rv} values resulted from higher turbine heights. The Young's modulus of the soil also influenced v_{rv}, with less stiff soil resulting in more significant deflections, as expected due to the reduction in the relative stiffness between the raft and the soil. The relationship between v_{rv}, h_h and E_s seems relatively linear. Longer piles, or deeper compressible soil layers, resulted in higher vertical deflections regardless of E_s and h_h, justifying the responses observed by Poulos & Mattes (1969) and the arguments raised in Chapter 2 regarding buckling.
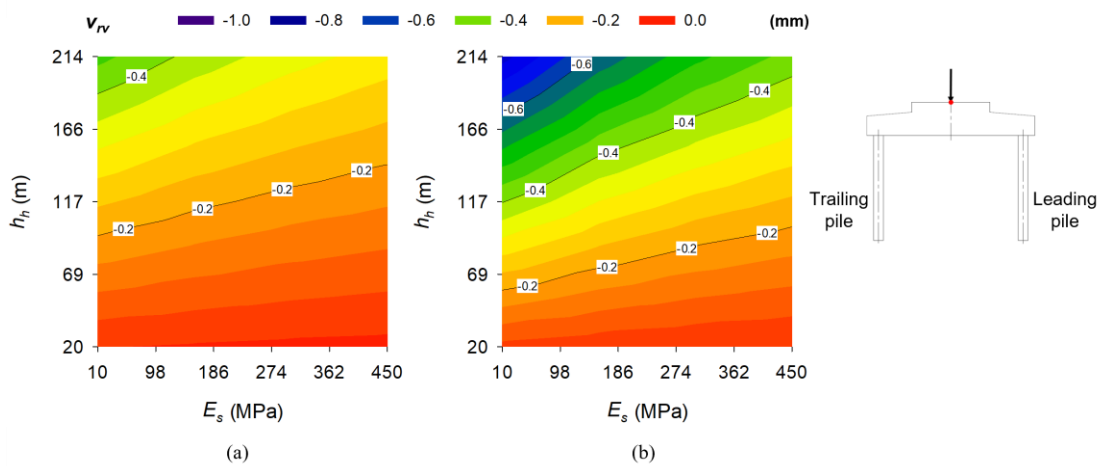
Figure 5-5: Raft top centre vertical deflection (v_{rv}) – h_h vs E_s [V]: (a) $L_p = 10$ m; (b) $L_p = 20$ m

Regarding the differential settlement of the raft (v_{rd}), which, in this case, is taken as the difference between the central and side deflection at the base of the raft, **Figure 5-6(a)** and **(b)** present the surface plots showing the influence of h_h and E_s for $L_p = 10$ m and 20 m, respectively. Like the central vertical deflection, v_{rd} is more significant for higher h_h and lower E_s and, hence, lower relative raft-soil stiffness values. However, pile slenderness does not seem to have any effect.

Due to the circular nature of the raft and the moment of inertia not being constant throughout the section, bending moments were not plotted for the raft, with only the horizontal stresses at the base of the raft (σ_r) considered for discussion. **Figure 5-7** shows the influence of E_s by keeping h_h constant at 117 m. **Figure 5-7(a)** and **(b)** present the stresses in the central xz-plane for $L_p = 10$ m and 20 m, plotted in 2-D against the distance from the centre of the raft, respectively.
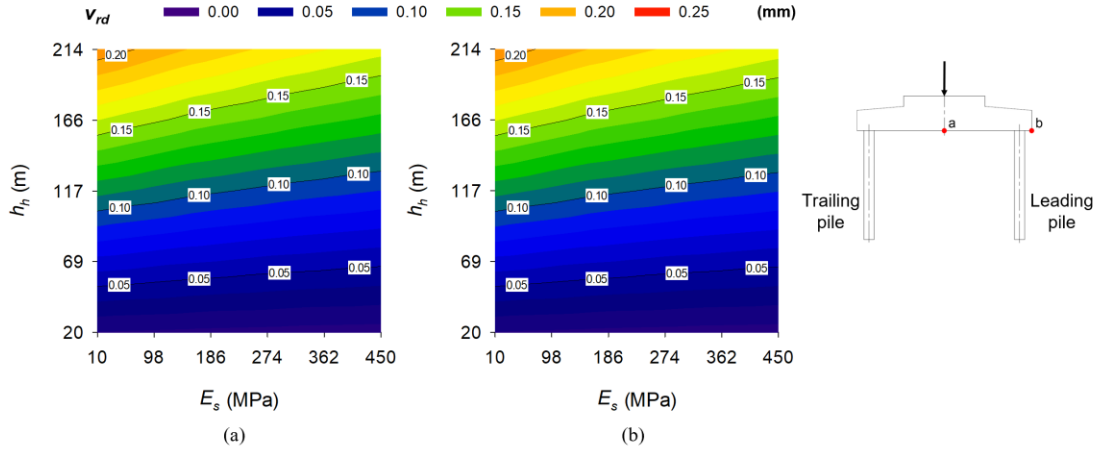
Figure 5-6: Raft differential settlement (v_{rd}) – h_h vs E_s [V]: (a) L_p = 10 m; (b) L_p = 20 m
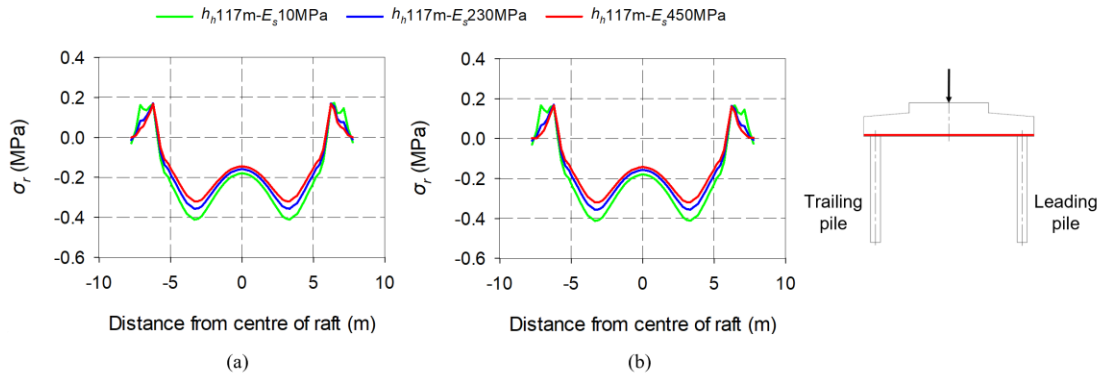
Figure 5-7: Raft stress at raft base (σ_r) – influence of E_s [V]: (a) L_p = 10 m; (b) L_p = 20 m

Additionally, **Figure 5-8(a)** and **(b)** indicate the same bottom raft stresses for the two pile lengths considered, showing the effect of h_h by keeping E_s constant at 230 MPa. As expected, **Figure 5-7** and **Figure 5-8** indicate 'sagging' horizontal tensile stresses over the part of the raft spanning between the piles, with substantial horizontal compressive stresses over the pile-raft interfaces, similar to the works presented by Deb & Pal (2021). These compressive stresses will have equivalent 'hogging' tensile stresses towards the top of the raft over the pile-raft interface. The maximum tensile stress within the region between the piles seems to occur where the pedestal connects to the raft at a distance of 3.6 m from the raft's centre. These stresses are well below concrete's typical splitting tensile strength of around 2 MPa to 3 MPa. Thus, no cracking should occur for the foundation size and properties considered. From **Figure 5-7**, it is clear that E_s had a relatively small influence on σ_r, at the same h_h, with slightly higher stresses at less stiff soils. This insignificant change can potentially be ascribed to the significant rigidity of the raft, having t_r equalling 1.85 m and R_r equalling 7.75 m, respectively, and K_{rs} values greater than 1.3 for all E_s values considered. In contrast, h_h affected the stresses at the base of the raft, with higher h_h resulting in higher σ_r values, as

5-9

indicated in **Figure 5-8**. In both these figures, pile length, or depth of the compressible soil layer, again did not seem to affect raft stress response.
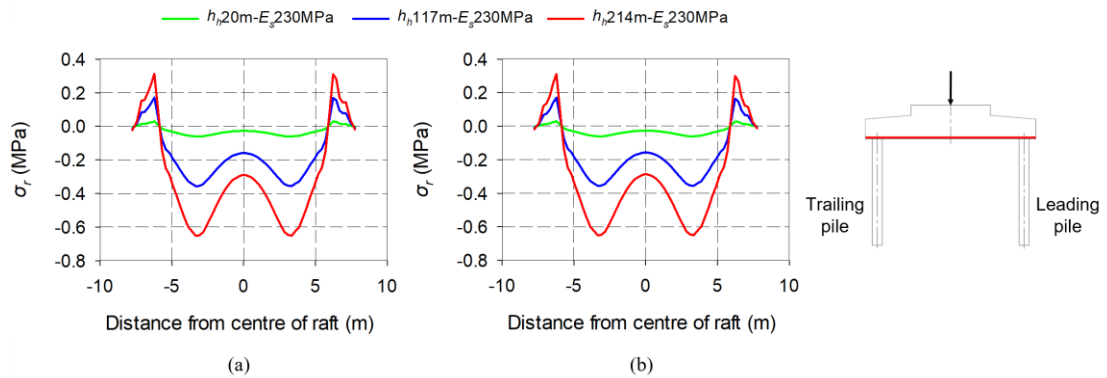
Figure 5-8: Raft stress at raft base (σ_r) – influence of h_h [V]: (a) $L_p = 10$ m; (b) $L_p = 20$ m

Extracting the maximum 'sagging' tensile stresses ($\sigma_{r,max}$) at 3.6 m from the centre of the raft for all the E_s-h_h combinations, **Figure 5-9(a)** and **(b)** were plotted for $L_p = 10$ m and 20 m, respectively. In both surface plots, $\sigma_{r,max}$ is primarily influenced by h_h, as observed previously, with higher h_h resulting in higher stresses at the base of the raft. Although not as significant, more stiff soils resulted in smaller stresses. However, E_s had a more substantial impact when h_h exceeded 117 m for the foundation size investigated.
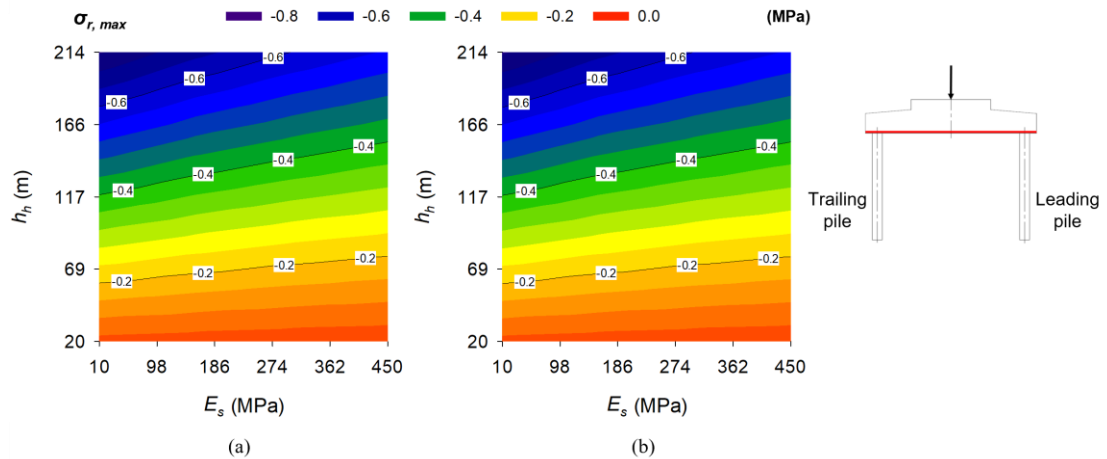
Figure 5-9: Maximum raft stress at raft base ($\sigma_{r,max}$) – h_h vs E_s [V]: (a) $L_p = 10$ m; (b) $L_p = 20$ m

Moving on to the response of the piles, **Figure 5-10** indicates surface plots showing the combined influence of h_h and E_s on the percentage of the total vertical load carried by the piles (F_p/F_t). Load data was extracted from all ten piles in Abaqus. As seen in **Figure 5-10(a)** for $L_p = 10$ m and **Figure 5-10(b)** for $L_p = 20$ m, only E_s influences this percentage, with less stiff soil resulting in the piles having to carry higher loads. Both figures show that an E_s value of 10 MPa resulted in the piles carrying about 100% of the vertically applied load, as

expected. As indicated by the literature, shorter piles carried higher loads, with an E_s value equal to 450 MPa, resulting in the shorter piles carrying 60% of the load compared to the piles, having twice the length, only carrying about 40%.
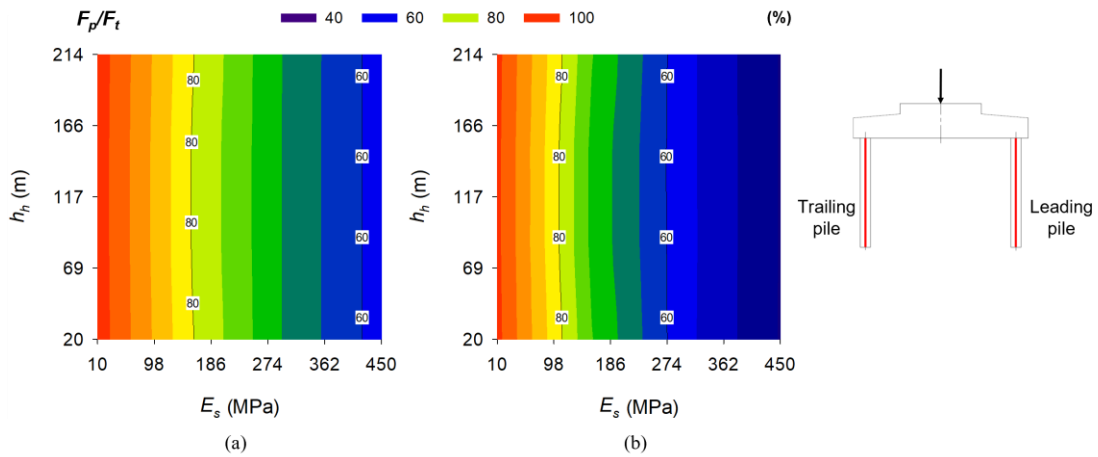
Figure 5-10: Total vertical load percentage carried by piles (F_p/F_t) – h_h vs E_s [V]: (a) L_p = 10 m; (b) L_p = 20 m

For the leading and trailing piles in the *xz*-plane, axial force and bending moment diagrams with depth were determined from the strain data in Abaqus with depth, as seen in **Figure 5-11**. The effect of E_s was determined by keeping h_h constant at 117 m. As before, **(a)** presents the bending moment (M_p) and axial force (F_p) diagrams with depth in the leading and trailing pile, both having lengths equal to 10 m, whereas **(b)** presents these diagrams for when L_p = 20 m. In all figures, the solid lines represent the leading pile response, and the dashed lines represent the trailing pile response. In the case of the bending moment diagrams, the leading and trailing piles were also plotted on different axes, given the sign convention adopted in Section 5.3 and bending moments plotted on the tension side of members. The top 0.5 m of the computed data for the axial force and bending moment plots were excluded from all the figures to avoid displaying stress concentrations near where the piles connected to the raft. The same conventions were applied to all pile data presented in the remainder of this chapter. As seen in **Figure 5-11(a)** and **(b)**, M_p in the leading and trailing piles are symmetrical under vertical loading, with both piles experiencing positive bending moments towards the top. At the same h_h, the influence of E_s is noticeable for both pile lengths, with M_p in the leading and trailing piles decreasing at a reducing rate throughout the entire pile length as E_s increases, with the distribution of bending moments along the length of the piles being greater for lower E_s values.

A reasonably linear relationship between M_p and depth below the raft was observed when E_s = 10 MPa and L_p = 10 m. Given this low soil stiffness, the response was similar to the expected response of a 2-D portal frame under vertical loading without any supporting soil.

However, this was not the case at the same E_s value when L_p equalled 20 m due to soil confinement at deeper depths. As expected, the maximum M_p occurred towards the top of the pile, with the value not changing significantly with E_s or L_p. M_p was present at the bottom of both pile lengths, with M_p being more significant for the shorter piles, or shallower compressible soil layers. The leading and trailing piles also showed symmetry regarding the axial forces in the piles with depth. Lower E_s values resulted in higher compressive axial loads carried by the piles. Shorter piles also carried higher compressive loads, except when E_s was equal to 10 MPa. The effect of shaft friction between the piles and the surrounding soil can also be observed in **Figure 5-11**, which was more significant for the longer piles, with the axial loads in the piles decreasing with depth.
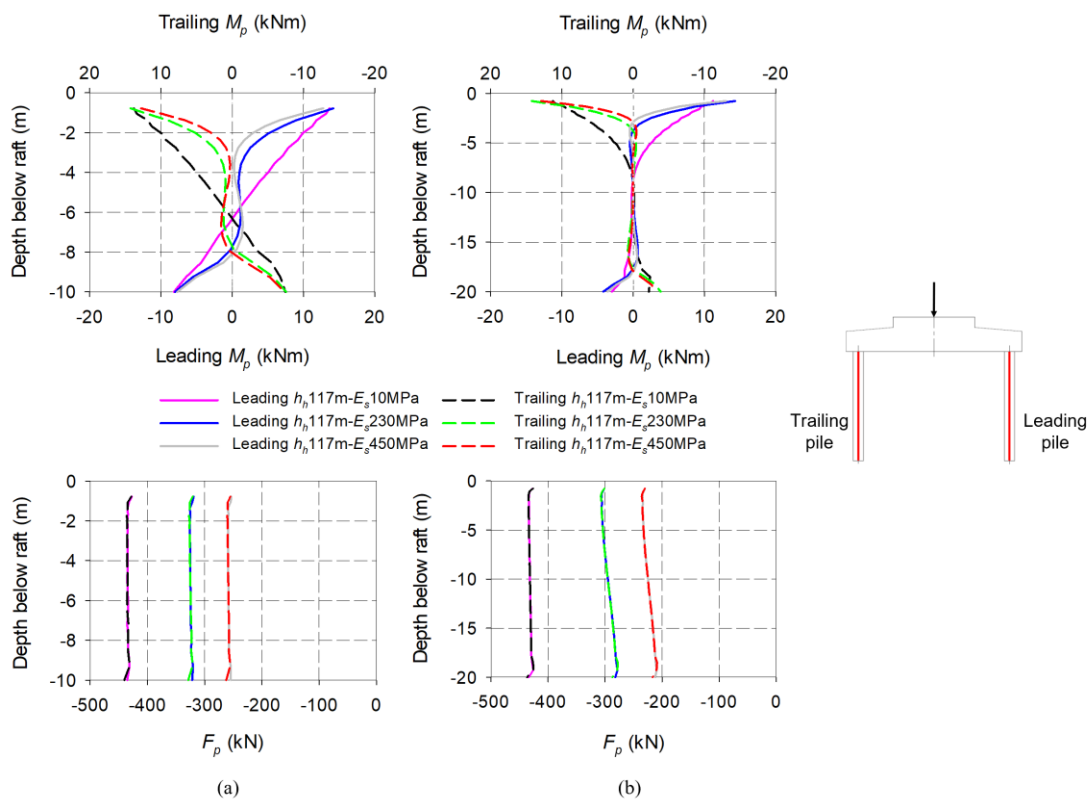
Figure 5-11: Leading and trailing pile bending moment (M_p) and axial force (F_p) – influence of E_s [V]: (a) L_p = 10 m; (b) L_p = 20 m

The effect of h_h was plotted by keeping E_s constant at 230 MPa. **Figure 5-12(a)** and **(b)** indicate M_p and F_p against depth below the raft for L_p = 10 m and 20 m, respectively. Both M_p and F_p are greatly influenced by h_h, with higher h_h resulting in more significant bending moments and axial compressive forces in the piles. Higher bending moments were also observed at the base of the piles as the applied vertical load increased, with the magnitude of the M_p being larger for the shorter piles. Again, the symmetry between the leading and trailing piles was observed, with shorter piles carrying higher axial loads.
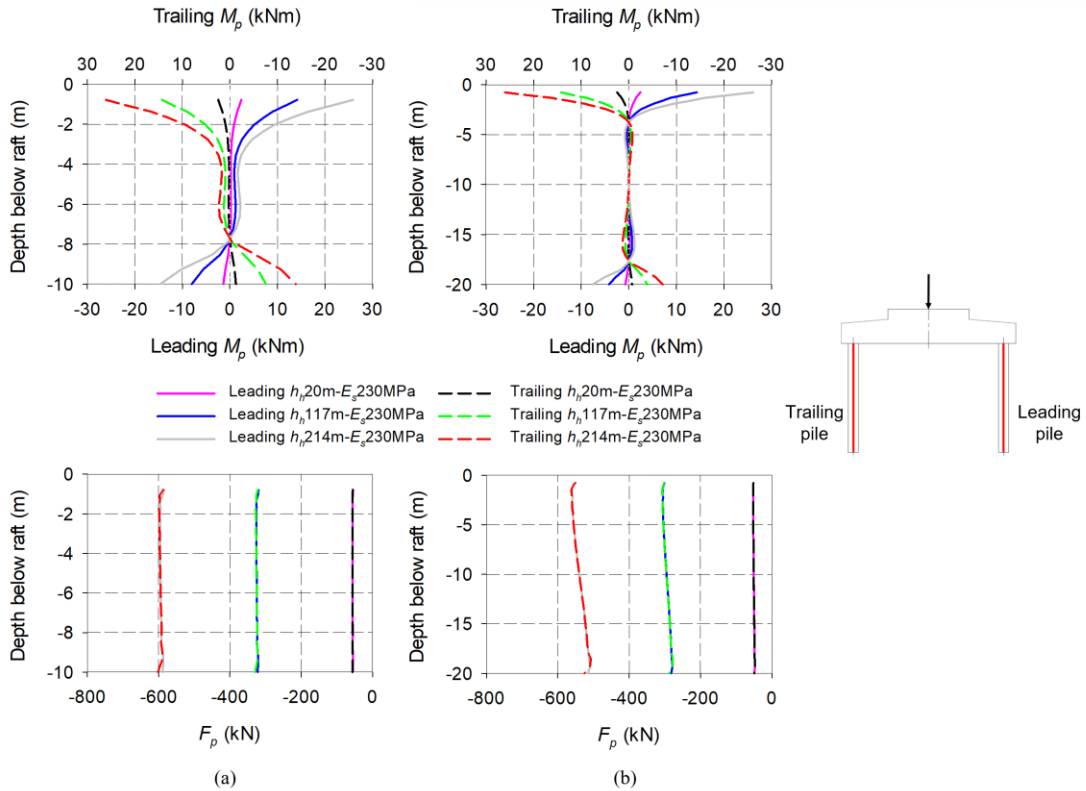
Figure 5-12: Leading and trailing pile bending moment (M_p) and axial force (F_p) – influence of h_h [V]: (a) L_p = 10 m; (b) L_p = 20 m

Extracting the maximum bending moments ($M_{p,max}$) and axial forces ($F_{p,max}$) in the leading and trailing piles at 0.5 m from the base of the raft for all the E_s-h_h combinations, **Figure 5-13(a)** and **(b)** were plotted for L_p = 10 m and 20 m, respectively. Given the symmetry of the piles under vertical loading, both the leading and trailing piles yielded the same results and surface plots and were, thus, not plotted separately. For $M_{p,max}$, h_h largely governed response. For both L_p = 10 m and 20 m, if h_h values were smaller than 117 m, $M_{p,max}$ seems to converge to a constant value for E_s greater than 186 MPa. However, for E_s values lower than 186 MPa, $M_{p,max}$ was lower when the soil was stiffer, which can be attributed to the increased relative stiffness between the Young's modulus of the pile and that of the soil. Near zero bending moments were observed when h_h = 20 m. With the pile diameter being constant at 900 mm, assuming that the concrete's tensile strength is roughly 2 MPa, the bending moment at which cracking would occur (M_{crack}) could be calculated using the flexure formula ($\sigma = My/I$). This allowed the magnitude of the bending moments presented in **Figure 5-13** to be assessed. In this case, M_{crack} was calculated as 143 kNm, with all E_s-h_h combinations falling below this value under vertical loading for the foundation size considered. For $F_{p,max}$, a reasonably linear relationship seems to exist between h_h, E_s and $F_{p,max}$, with the same observations as discussed in **Figure 5-11** and **Figure 5-12**.
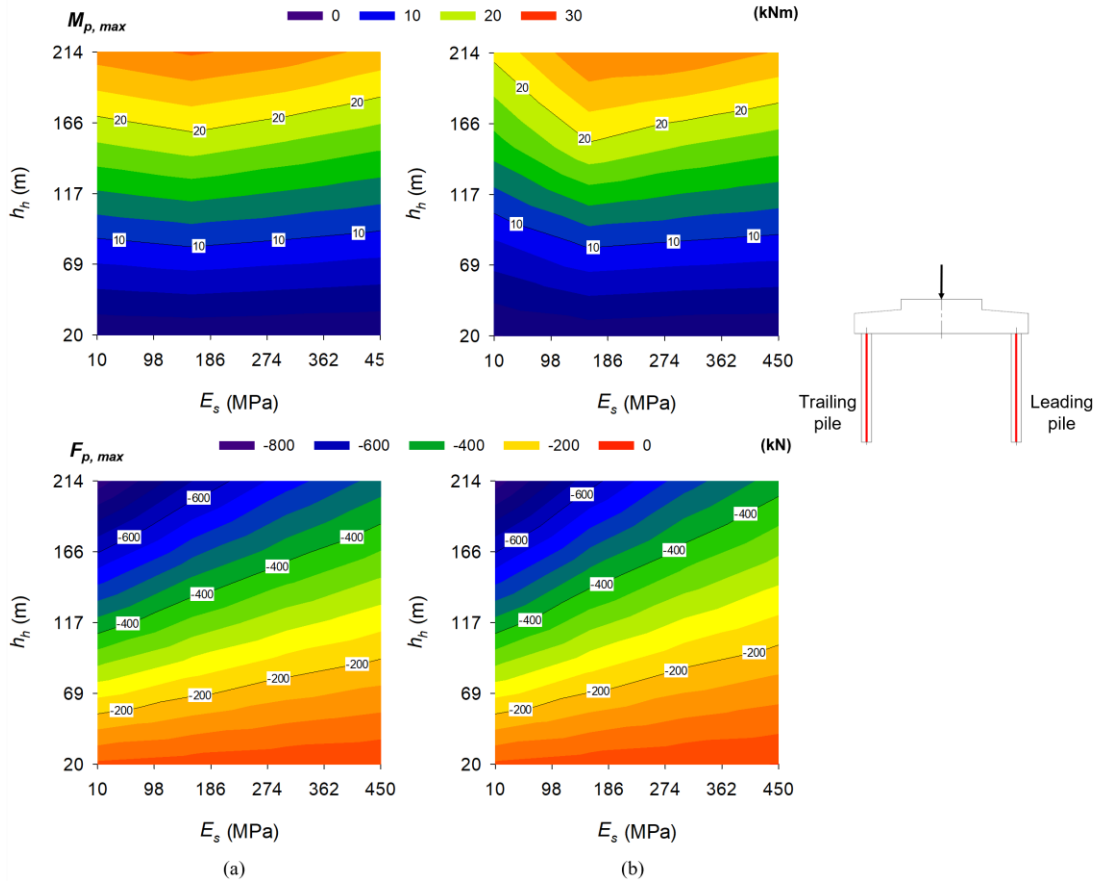
Figure 5-13: Leading and trailing pile maximum bending moment ($M_{p,max}$) and axial force ($F_{p,max}$) – h_h vs E_s [V]: (a) $L_p = 10$ m; (b) $L_p = 20$ m

5.4.2 Vertical load, horizontal load and overturning moment, *V-H-M*

Moving on to the second load case, which considered the combined effect of the vertical load, horizontal load and overturning moment, several foundation responses were investigated. **Figure 5-14(a)** and **(b)** present the surface plots showing the influence of h_h and E_s on the rotation of the raft pedestal (θ_r) for $L_p = 10$ m and 20 m, respectively. For both pile lengths, as h_h increases, the rotation of the raft increases due to the magnitude of the applied overturning bending moment increasing. As a result of the slenderness of the piles, longer pile lengths, or deeper compressible soil layers, also resulted in higher foundation rotation, which justifies the comparison made in the literature arguing that the amount of rotation of a portal frame, in this case, a piled-raft foundation, is related to the rigidity of the joint (or pile-raft interface). Alternatively, higher E_s values caused smaller foundation rotation, with limited rotation occurring for $h_h < 69$ m.

As the foundation is subjected to horizontal loads, the raft's horizontal displacement (v_{rh}) was also considered. v_{rh} was affected by both E_s and h_h, as seen by the surface plots in **Figure 5-15(a)** and **(b)** for pile lengths of 10 m and 20 m, respectively. Longer piles supported by

less stiff soil resulted in higher v_{rh} values than shorter piles at the same E_s values. Limited movement occurred for h_h smaller than 69 m when L_p was equal to 10 m, compared to when L_p equalled 20 m, only experiencing limited movement at h_h less than 20 m.
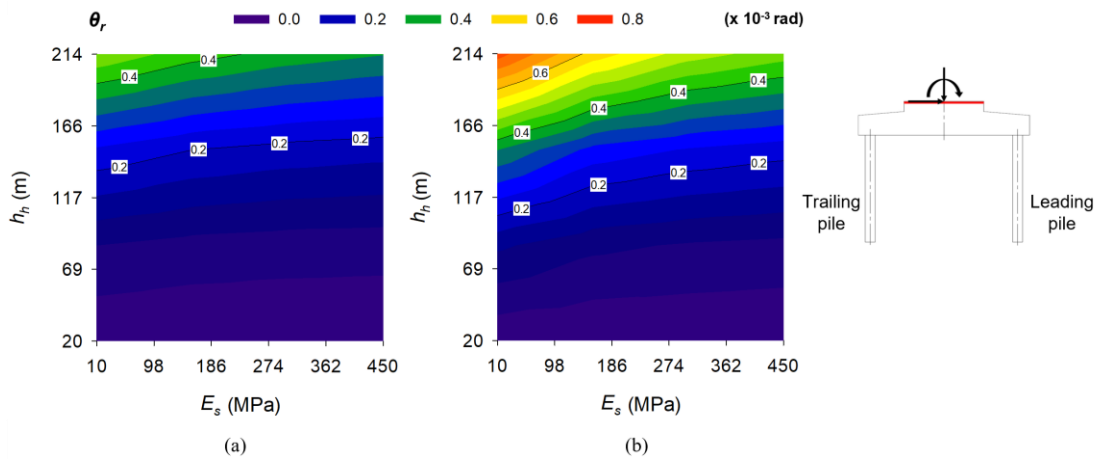
Figure 5-14: Raft pedestal rotation (θ_r) – h_h vs E_s [V-H-M]: (a) $L_p = 10$ m; (b) $L_p = 20$ m
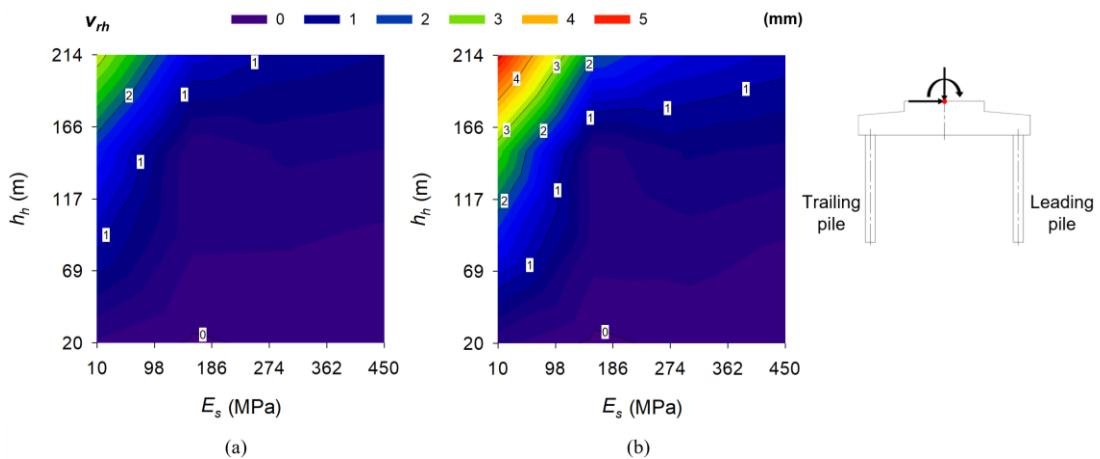
Figure 5-15: Raft top centre horizontal displacement (v_{rh}) – h_h vs E_s [V-H-M]: (a) $L_p = 10$ m; (b) $L_p = 20$ m

Figure 5-16 and **Figure 5-17** present the horizontal stresses at the base of the raft (σ_r) against the distance from the centre of the raft, indicating the influence of E_s by keeping h_h constant and displaying the result of h_h by keeping E_s constant, respectively. For both sets of figures, **(a)** shows the response of the raft supported by 10 m long piles, whereas **(b)** shows the response if the piles are 20 m long. Considering the part of the raft spanning between the piles, as before, both tensile and compressive horizontal stresses are observed, with the tensile stresses occurring on the bottom of the leading end of the raft in the direction of the horizontal load and overturning moment. These stresses are substantially higher than those observed when only the vertical loading was acting on the foundation. As with the case when only the vertical load was applied, the maximum tensile stresses in the raft are located about 3.6 m from the centre of the raft, with tensile stresses also present at the base of the raft over the

raft-trailing pile interface. Compressive forces were observed over the raft-leading pile interface at the base of the raft, having an equivalent tensile stress at the top of the raft at the same location. From **Figure 5-16**, it is again clear that E_s had a relatively small influence on σ_r, given the same h_h, potentially due to the significant rigidity of the raft with slightly higher stresses for less stiff soils. The magnitude of these stresses nearly exceeds the limit for cracking if the assumed tensile stress of concrete is about 2 MPa. Thus, the raft should be safe from cracking for any h_h up to about 117 m when t_r equals 1.85 m and pile lengths, or depth of the compressible soil layer, do not exceed 20 m.
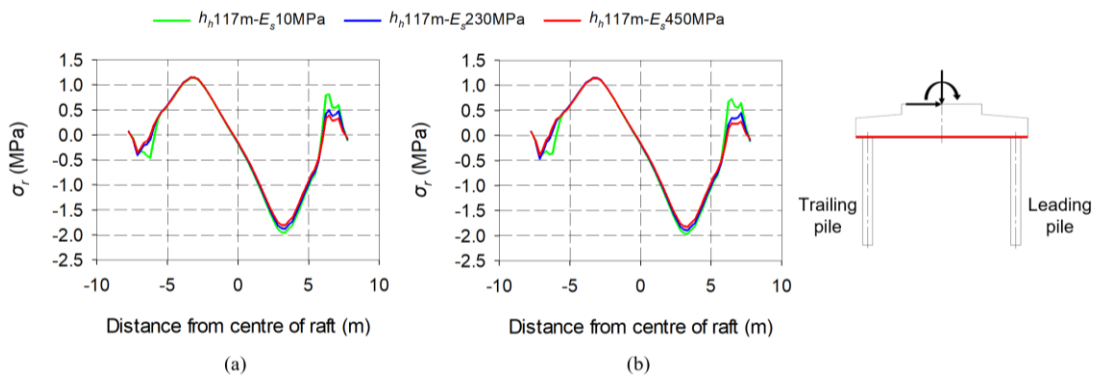
Figure 5-16: Raft stress at raft base (σ_r) – influence of E_s [*V-H-M*]: (a) L_p = 10 m; (b) L_p = 20 m
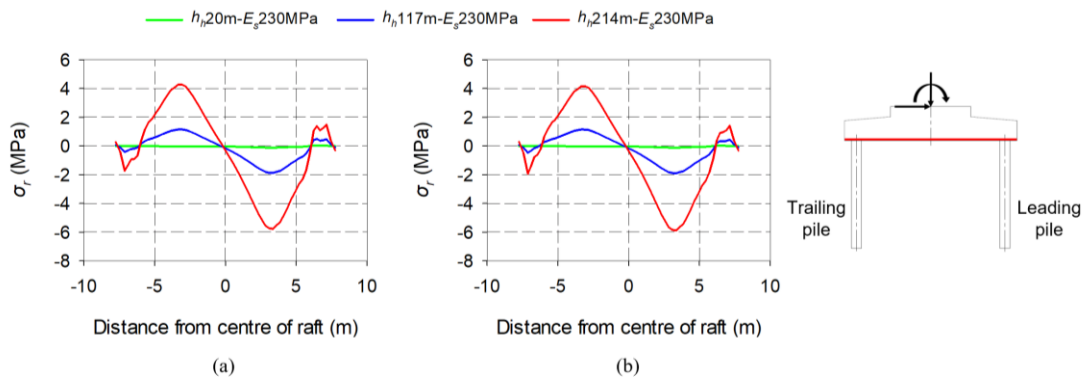
Figure 5-17: Raft stress at raft base (σ_r) – influence of h_h [*V-H-M*]: (a) L_p = 10 m; (b) L_p = 20 m

Considering the influence of h_h by keeping E_s constant at 230 MPa (see **Figure 5-17**), a significant effect can be observed. Given the size of the raft, a h_h of 20 m had nearly no noticeable impact on the σ_r. As h_h, however, increased, the horizontal tensile stresses in the base of the raft at the leading end of the raft increased, exceeding the cracking stress of the concrete when h_h equalled 214 m. Similarly, the horizontal compressive stresses at the trailing end of the raft increased, which will have an equivalent tensile stress at the top of the raft, potentially exceeding the cracking stress of concrete. Although the steel reinforcing in the raft should absorb most of these tensile stresses, consideration should be given at these hub heights.

5-16

To assess these stresses, the maximum horizontal 'sagging' tensile stresses ($\sigma_{r,max}$) 3.6 m from the centre of the raft for all the E_s-h_h combinations were extracted and plotted. **Figure 5-18(a)** and **(b)** indicate the surface plots showing the simultaneous effect of E_s and h_h on $\sigma_{r,max}$ for L_p = 10 m and 20 m, respectively. In both figures, $\sigma_{r,max}$ is mainly influenced by h_h, with increasing h_h resulting in an increased $\sigma_{r,max}$ regardless of E_s. Pile length (depth of the compressible soil layer), again, did not affect raft response, even under these load combinations. As mentioned, given the size of the raft, any h_h larger than 117 m could result in the concrete in the base of the raft cracking under the combined vertical load, horizontal load and overturning moment for the E_s values considered.
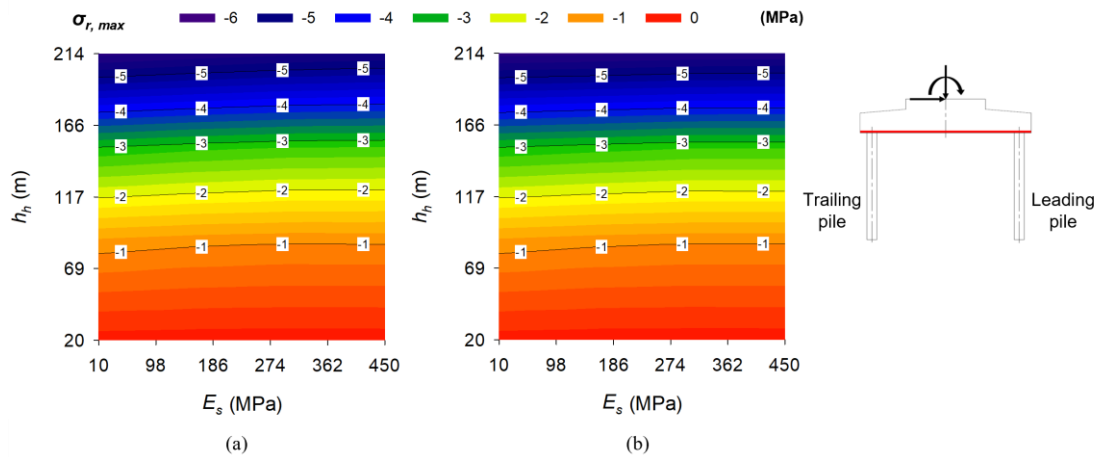
Figure 5-18: Maximum raft stress at raft base ($\sigma_{r,max}$) – h_h vs E_s [*V-H-M*]: (a) L_p = 10 m; (b) L_p = 20 m

Moving on to the response of the piles, **Figure 5-19** indicates surface plots showing the influence of h_h and E_s on the percentage of the total vertical load carried by the piles (F_p/F_t) under the *V-H-M* load combination. As seen in **Figure 5-19(a)** for L_p = 10 m and **Figure 5-19(b)** for L_p = 20 m, E_s mainly influences this percentage, with less stiff soil resulting in the piles having to carry higher loads. Overall, compared to the load carried by the piles under pure vertical loading, a slight decrease in load percentage was observed with the addition of the horizontal load and overturning moment. This reduction can be attributed to the increased raft bearing on the supporting soil resulting from the applied overturning moment.

For the leading and trailing piles in the *xz*-plane, axial force and bending moment data were again calculated and plotted with depth, as seen in **Figure 5-20**, showing the effect of E_s by keeping h_h constant at 117 m. In **Figure 5-20**, **(a)** presents the bending moment (M_p) and axial force (F_p) diagrams with depth in the leading and trailing pile having lengths equal to 10 m, whereby **(b)** presents these diagrams for L_p = 20 m. As seen in **Figure 5-20(a)** and **(b)**, the magnitude and direction of the bending moment in the leading and trailing piles are affected

by both E_s and L_p and are also highly dependent on the relative stiffness between the raft and the piles and the piles and the soil.
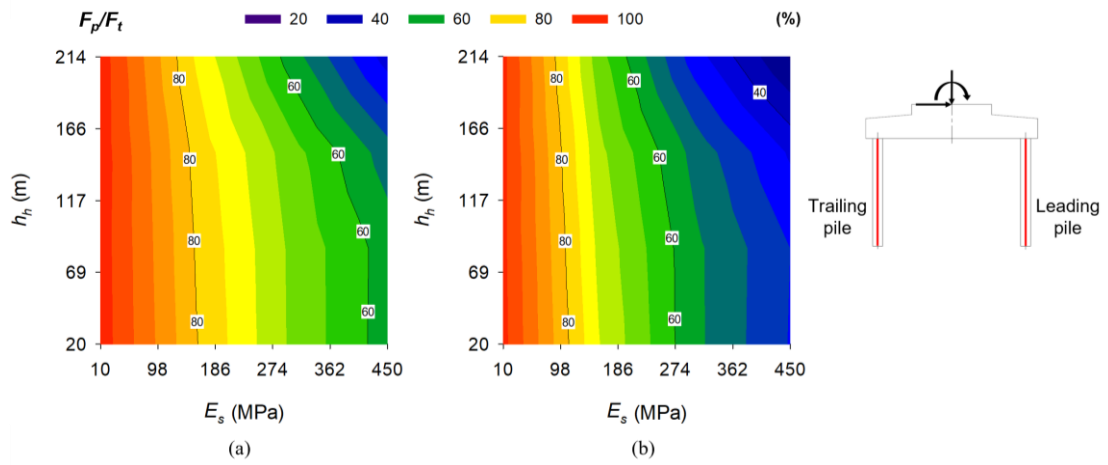
Figure 5-19: Total vertical load percentage carried by piles (F_p/F_t) – h_h vs E_s [V-H-M]: (a) L_p = 10 m; (b) L_p = 20 m

Figure 5-20: Leading and trailing pile bending moment (M_p) and axial force (F_p) – influence of E_s [V-H-M]: (a) L_p = 10 m; (b) L_p = 20 m

For the shorter piles, the addition of the horizontal load and overturning moment did not affect M_p much when $E_s \geq 230$ MPa. In the case where $E_s = 10$ MPa, higher bending moments

5-18

were observed, with the M_p in the leading pile becoming more positive and M_p in the trailing pile changing from positive to negative. Again, the observed relationship between M_p and depth at this low Young's modulus value was near linear, similar to the expected response of a portal frame without any supporting soil under the combined horizontal load and overturning moment. The linear response was less evident for $L_p = 20$ m, mainly due to the soil's confinement at deeper depths. As a result of the slenderness of the longer piles and the rigidity of the raft, M_p towards the top of the leading pile became less positive, and M_p in the trailing pile more positive. M_p was still evident at the bottom of the piles for both pile lengths, with M_p being more significant for the shorter piles, especially when $E_s = 10$ MPa.

Regarding the axial forces in the piles with depth (see **Figure 5-20(a)** and **(b)**), the leading and trailing piles showed push-pull responses similar to that observed from the full-scale instrumented foundation in Chapter 3. Piles on the leading end of the raft experienced an increase in compressive loads, whereas the piles on the trailing side of the raft experienced tensile loads. For both pile lengths considered, F_p in the leading and trailing piles showed similar results when $E_s = 10$ MPa. Thus, low E_s values do not seem to impact axial response. **Figure 5-20(a)** and **(b)** show that the compressive and tensile loads are smaller if E_s is larger. However, the reader should be reminded that the influence of the backfilled soil and foundation gravity was omitted in these displays, as the study only focuses on the change in the pile's response due to the applied loads. Thus, the tensile stresses on an in-service foundation might be smaller due to these excluded effects, as seen in Chapter 3.

Figure 5-21(a) and **(b)** indicate the M_p and F_p against depth below the base of the raft for $L_p = 10$ m and 20 m, respectively, showing the influence of h_h. Both M_p and F_p are heavily influenced by h_h, with higher h_h, resulting in more significant bending moments and push-pull axial forces in the leading and trailing piles. Again, the direction of the bending moment is dependent on the relative stiffness between the raft and piles, with the longer piles being more slender, resulting in larger M_p values close to the raft-pile interface. M_p towards the top of the leading pile became less positive, and M_p in the trailing pile more positive with the addition of the horizontal load and overturning moment at the same E_s. Shaft friction effect is also visible, considering the observed axial forces in the piles. Given the size of the raft, significant tensile loads in the trailing pile are observed for $h_h = 214$ m, exceeding the cracking limit of the concrete.

Extracting the maximum bending moments ($M_{p,max}$) and axial forces ($F_{p,max}$) in the leading and trailing piles at 0.5 m from the base of the raft for all the E_s-h_h combinations, **Figure 5-22** and **Figure 5-23** were plotted. In both figures, **(a)** and **(b)** represent the response when $L_p = 10$ m and $L_p = 20$ m, respectively.
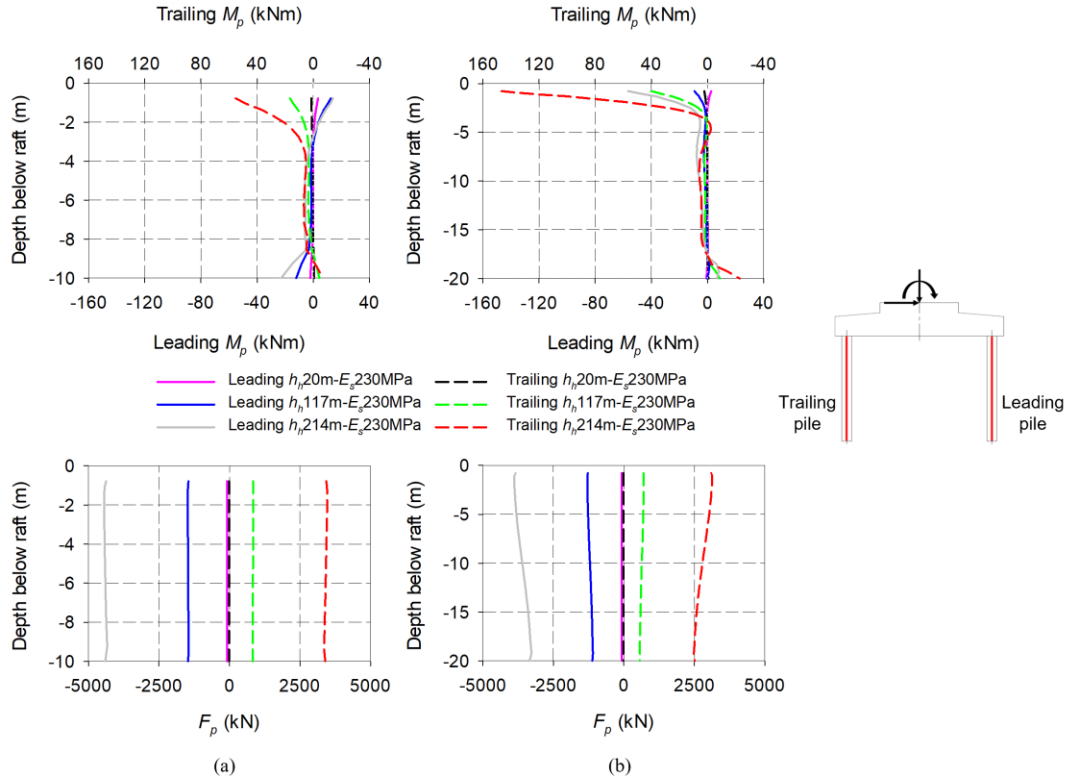
Figure 5-21: Leading and trailing pile bending moment (M_p) and axial force (F_p) – influence of h_h [V-H-M]: (a) $L_p = 10$ m; (b) $L_p = 20$ m

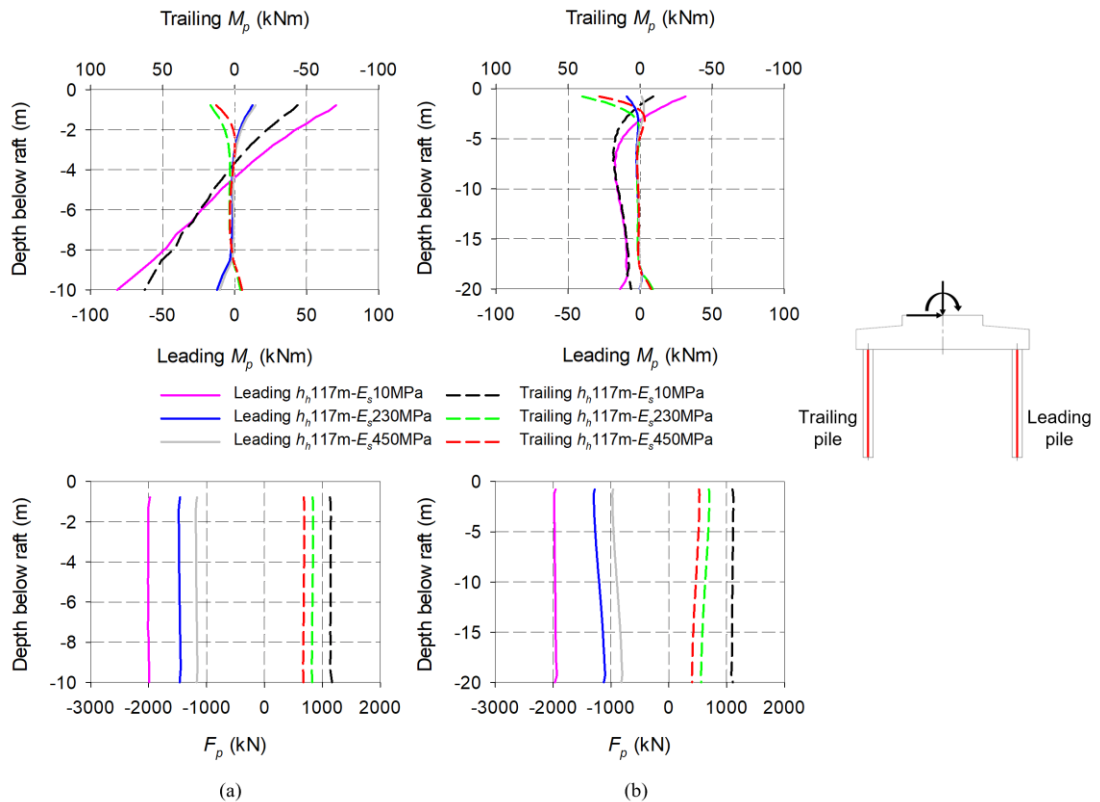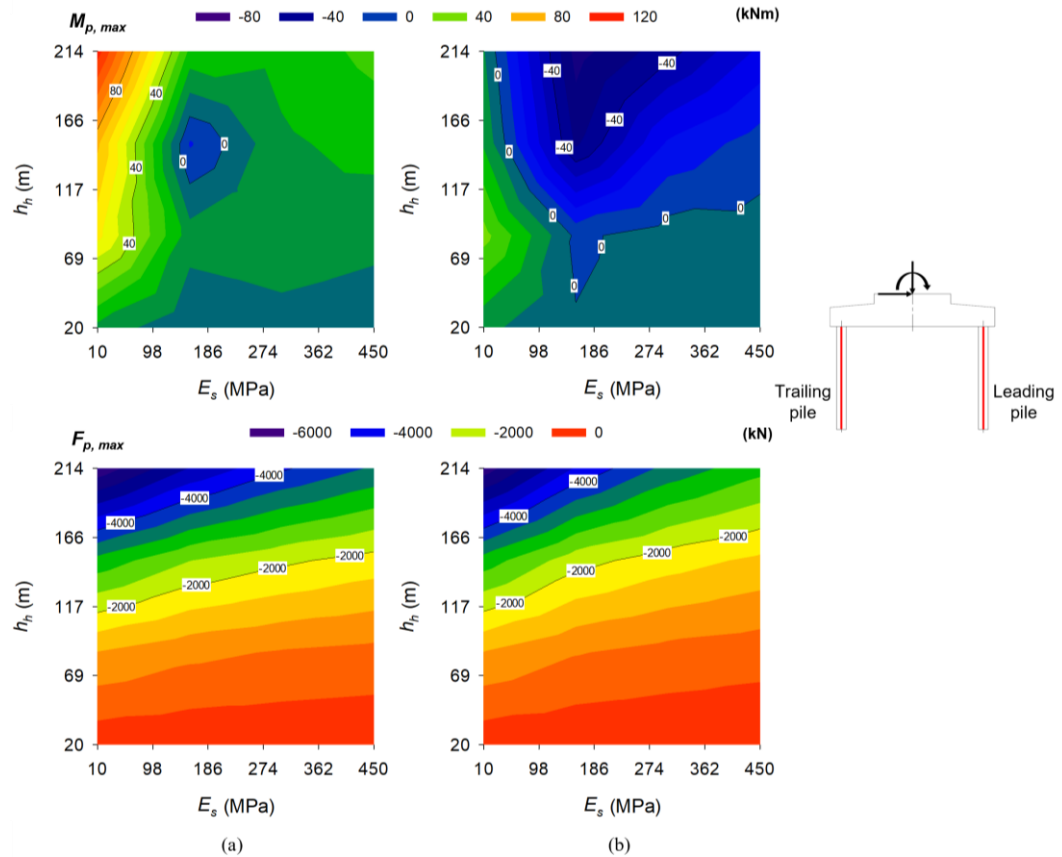**Figure 5-22:** Leading pile maximum bending moment ($M_{p,max}$) and axial force ($F_{p,max}$) – h_h vs E_s [V-H-M]: (a) $L_p = 10$ m; (b) $L_p = 20$ m

Looking at the leading pile first (see **Figure 5-22**), the magnitude and sign of the bending moment mainly depend on the length of the pile and, hence, the relative stiffness between the pile and the raft. For $L_p = 10$ m, larger h_h and the smaller E_s values resulted in higher positive bending moments given the size of the overall foundation. Negative bending moments were observed in the leading pile when L_p was equal to 20 m, with maximum bending moment observed when $h_h = 214$ m and E_s was between 98 MPa and 186 MPa, respectively. These responses aligned with the expected outcome considering the relative stiffness between the pile and the raft in portal frame theory subjected to horizontal loads and bending moments. Regarding the axial compressive force in the leading pile under this load combination, the force was the highest when the soil was the least stiff, and the applied vertical load, horizontal load and overturning bending moment were the highest (see **Figure 5-22**). Even under these load conditions, the shorter piles carried higher axial loads.
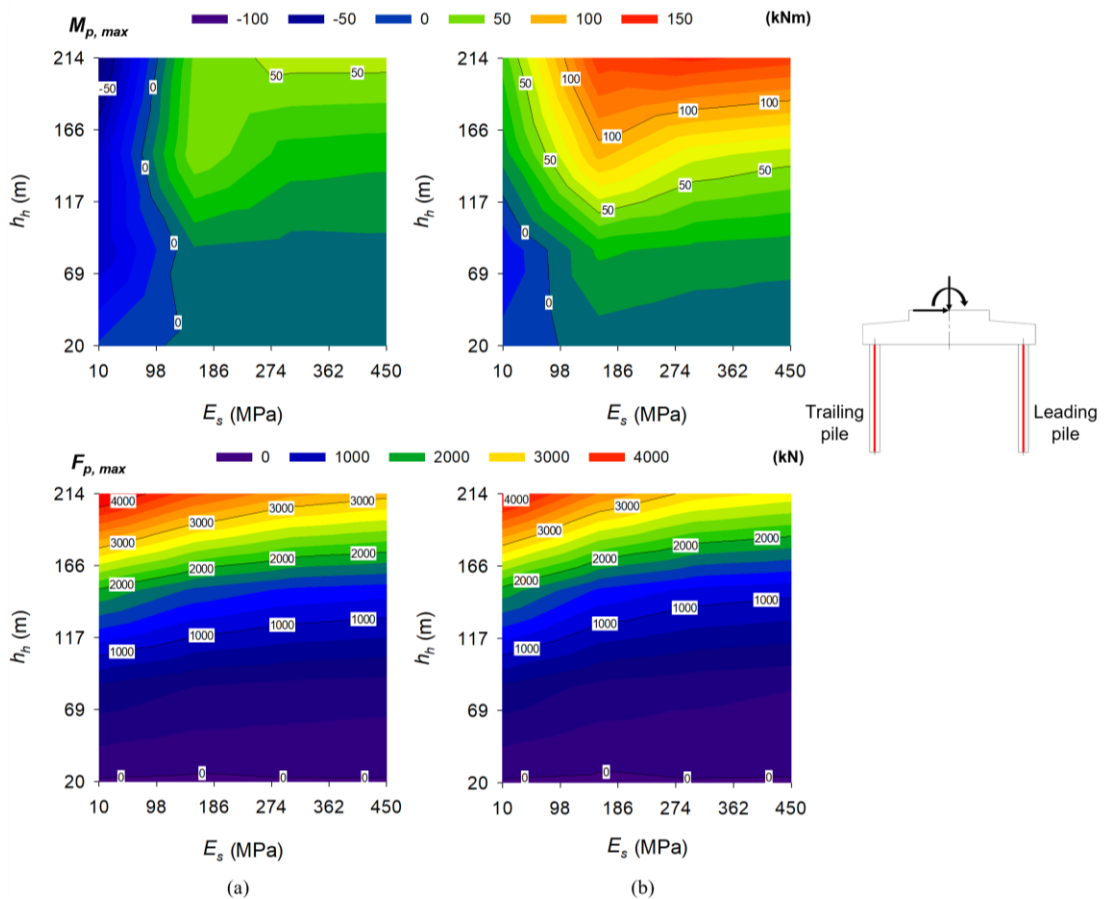
Figure 5-23: Trailing pile maximum bending moment ($M_{p,max}$) and axial force ($F_{p,max}$) – h_h vs E_s [V-H-M]: (a) $L_p = 10$ m; (b) $L_p = 20$ m

For the trailing pile (see **Figure 5-23**), the direction of the bending moment was, again, mainly dependent on the length and, hence, the slenderness of the pile and the relative stiffness between the raft and pile. $M_{p,max}$ was the highest for both pile lengths when $h_h = 214$ m and E_s was greater than 186 MPa, with bending moments for $L_p = 20$ m exceeding

M_{crack} = 143 kNm calculated in Section 5.4.1 for d_p = 900 mm. Axial forces in this pile also proved significant due to the applied loads and moment on the foundation, as seen in **Figure 5-23**. High tensile forces are generated in the pile, with the magnitude increasing when h_h increases and E_s decreases. Doing a simple calculation using the axial stress formula ($\sigma = F/A$), the axial load at which cracking will occur can be determined, assuming that the tensile strength of concrete is about 2 MPa. For d_p = 900 mm, this value was calculated as 1272 kN. Thus, based on this, for the E_s values considered, if h_h exceeded 117 m, the possibility exists that the trailing pile might experience tensile cracking under turbine operation loading.

5.5   RAFT THICKNESS

This section considers the influence of raft thickness (t_r) on the response of a piled-raft foundation under dominant horizontal loads and overturning moments. As before, two load cases were explored (V and V-H-M), presented separately in Sections 5.5.1 and 5.5.2, respectively. **Table 5-6** indicates the raft thickness values investigated in this parametric study, with the placement of a, b, c, d and e as indicated in **Figure 5-2** and the accompanying h_h considered. The other parametric variables, excluding the raft thickness, were kept at the values indicated in red in **Table 5-1**.

Table 5-6: Parametric study values – raft thickness

Parametric variable	a	b	c	d	e
Raft thickness, t_r (mm)	0.70	1.04	1.85	2.66	3.00

5.5.1   Vertical load, V

Figure 5-24(a) and **(b)** present the surface plots showing the influence of h_h and t_r on the top central vertical deflection of the raft (v_{vr}) for L_p = 10 m and 20 m, respectively. Under vertical loading, v_{rv} is affected by both h_h and t_r, with larger deflections resulting from higher turbine heights. In addition, due to the flexibility of the raft, thinner rafts resulted in higher vertical deflections. Due to the slenderness of the supporting piles, longer piles resulted in higher vertical deflections, with the maximum deflection observed when L_p = 20 m, h_h = 214 m and t_r = 0.70 m, respectively.

Regarding the differential settlement of the raft (v_{rd}), **Figure 5-25(a)** and **(b)** present the surface plot showing the influence of h_h and t_r for L_p = 10 m and 20 m, respectively. Similar to the central vertical deflection, v_{rd} is more significant with higher h_h values and smaller t_r values, similar to the trends highlighted in the literature review. Thus, differential settlement can potentially be reduced by regulating the thickness of the raft. Pile slenderness does not seem to have any effect, as with E_s.
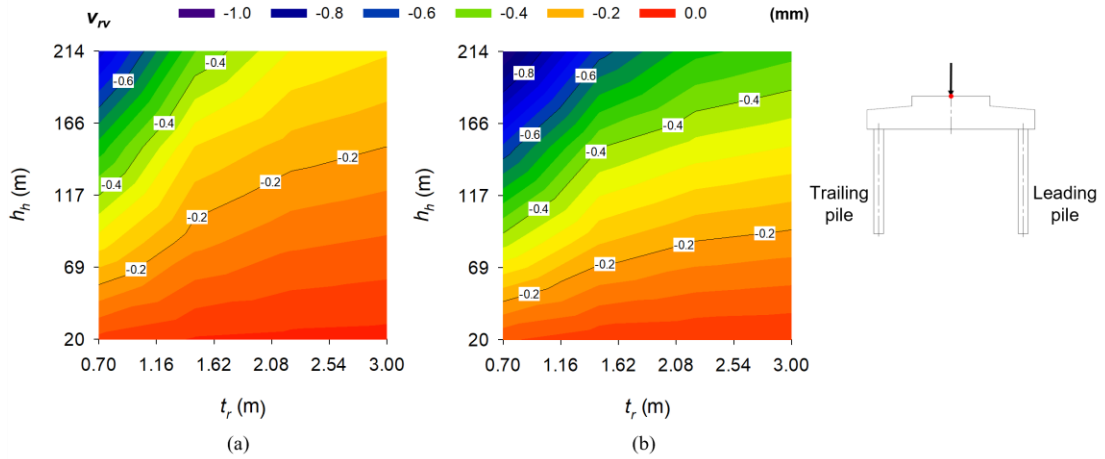
Figure 5-24: Raft top centre vertical deflection (v_{rv}) – h_h vs t_r [V]: (a) L_p = 10 m; (b) L_p = 20 m
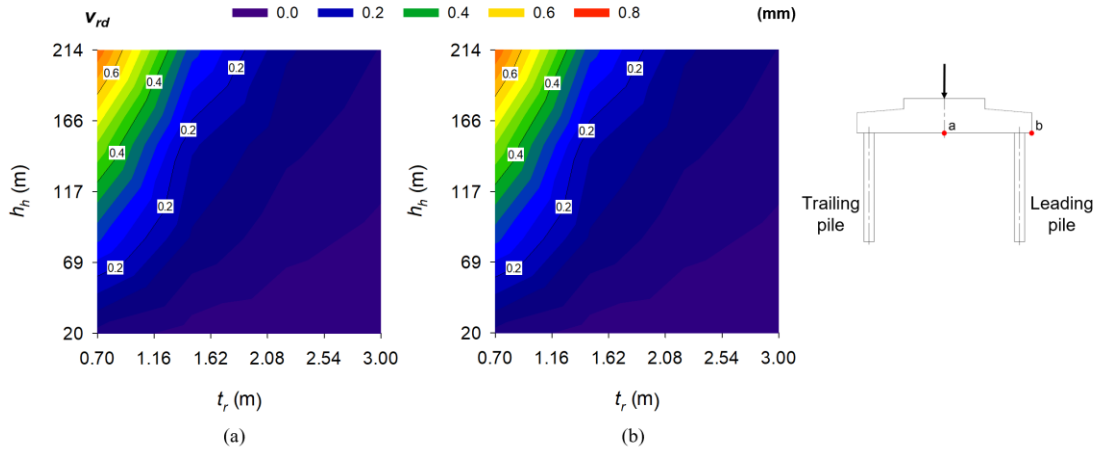
Figure 5-25: Raft differential settlement (v_{rd}) – h_h vs t_r [V]: (a) L_p = 10 m; (b) L_p = 20 m

Figure 5-26(a) and **(b)** present the bottom raft horizontal stresses (σ_r) in the central *xz*-plane for L_p = 10 m and 20 m plotted in 2-D against the distance from the centre of the raft, respectively. **Figure 5-26** indicates the influence of t_r by keeping h_h constant at 117 m. As before, the part of the raft between the piles showed 'sagging' tensile stresses, with substantial compressive stresses observed in the base of the raft over the pile-raft interfaces. The magnitude of these stresses was substantially higher when t_r was low and reduced at a decreasing rate as t_r increased. The largest tensile stress within the region between the piles occurred where the pedestal connects to the raft at a distance of 3.6 m from the raft's centre. These stresses were below concrete's typical splitting tensile strength of around 2 MPa to 3 MPa, even with the raft having a thickness of 0.70 m. Thus, the raft should not crack under vertical loading for the foundation sizes considered.

Extracting the maximum 'sagging' horizontal tensile stresses ($\sigma_{r,max}$) at 3.6 m from the centre of the raft for all the t_r-h_h combinations, **Figure 5-27(a)** and **(b)** were plotted for L_p = 10 m

and 20 m, respectively. In both surface plots, $\sigma_{r,max}$ is influenced by h_h and t_r, as observed previously, with higher h_h resulting in higher tensile stresses at the base of the raft. Thinner raft sections also resulted in higher σ_r values. Regarding L_p, more slender piles resulted in slightly increased stress at the base of the raft. All t_r-h_h combinations yielded tensile stresses below that required for cracking.
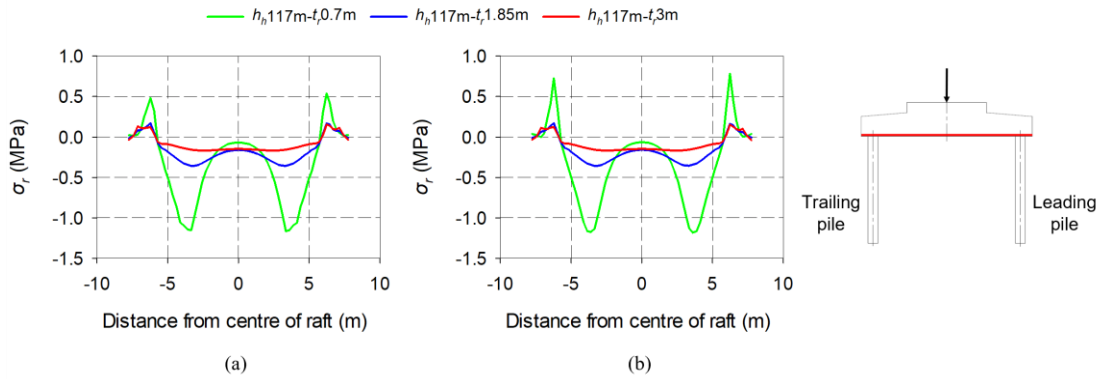
Figure 5-26: Raft stress at raft base (σ_r) – influence of t_r [V]: (a) L_p = 10 m; (b) L_p = 20 m
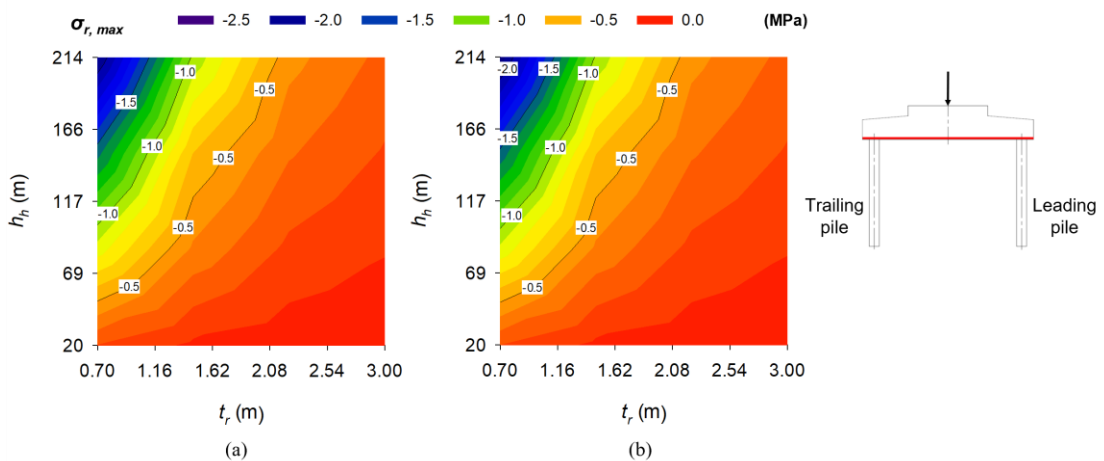
Figure 5-27: Maximum raft stress at raft base ($\sigma_{r,max}$) – h_h vs t_r [V]: (a) L_p = 10 m; (b) L_p = 20 m

Considering the percentage of the total vertical load carried by the piles (F_p/F_t), **Figure 5-28** indicates the surface plots showing the combined influence of h_h and t_r. As seen in **Figure 5-28(a)** for L_p = 10 m and **Figure 5-28(b)** for L_p = 20 m, raft thickness mainly influenced this percentage. For t_r values higher than 1.62 m (when L_p equalled 10 m), this percentage remained constant at about 75%, slightly reducing below this raft thickness. For piles having twice the length, the percentage remained constant at about 65% for all the thicknesses considered. For the leading and trailing piles in the xz-plane, axial forces and bending moments were determined from the strain data with depth, as seen in **Figure 5-29**, showing the effect of t_r by keeping h_h constant at 117 m. **Figure 5-29(a)** presents the bending moment (M_p) and axial force (F_p) diagrams with depth in the leading and trailing pile having lengths

equal to 10 m, whereby **(b)** presents these diagrams for $L_p = 20$ m. Given the sign convention assumed in Section 5.3, the bending moment diagrams for the two piles were plotted on separate axes.
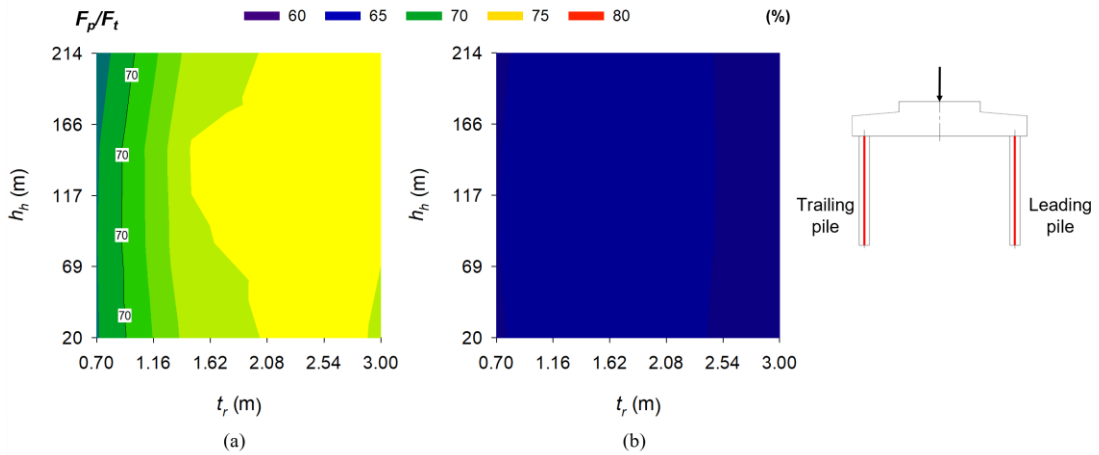
Figure 5-28: Total vertical load percentage carried by piles (F_p/F_t) – h_h vs t_r [V]: (a) $L_p = 10$ m; (b) $L_p = 20$ m
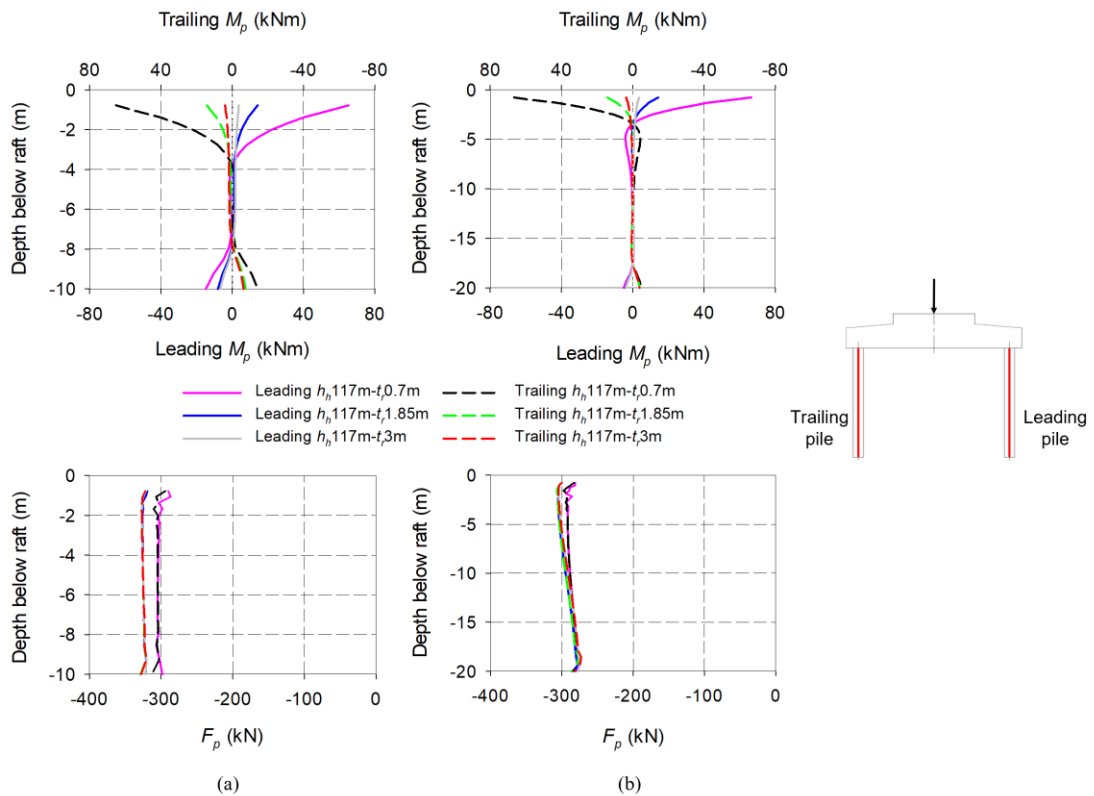
Figure 5-29: Leading and trailing pile bending moment (M_p) and axial force (F_p) – influence of t_r [V]: (a) $L_p = 10$ m; (b) $L_p = 20$ m

As seen in **Figure 5-29**, the bending moment in the leading and trailing piles are symmetrical under pure vertical loading, with both piles experiencing positive bending moments towards the top. At the same h_h, the influence of t_r is noticeable for both pile lengths, with the bending

moment in the leading and trailing piles being more significant if the thickness of the raft is smaller. This was to be expected as the relative stiffness of the pile-raft interface reduced, resulting in the amount of rotation at the joint increasing. These significant bending moments also correspond with the high tensile stresses observed at the base of the raft over the raft-pile interface mentioned previously. As expected, maximum M_p values occurred towards the top of the piles for the t_r values considered, with the value not changing significantly with L_p. M_p was also present at the base of the piles, being more significant for shorter piles. Furthermore, the leading and trailing piles showed symmetry regarding the axial forces in the piles with depth. However, t_r did not seem to influence the magnitude of these compressive axial forces that much, except for when $t_r = 0.7$ m and $L_p = 10$ m, respectively.

Extracting the maximum bending moments ($M_{p,max}$) and axial forces ($F_{p,max}$) in the leading and trailing piles at 0.5 m from the base of the raft for all the t_r-h_h combinations, **Figure 5-30(a)** and **(b)** were plotted for $L_p = 10$ m and 20 m, respectively.
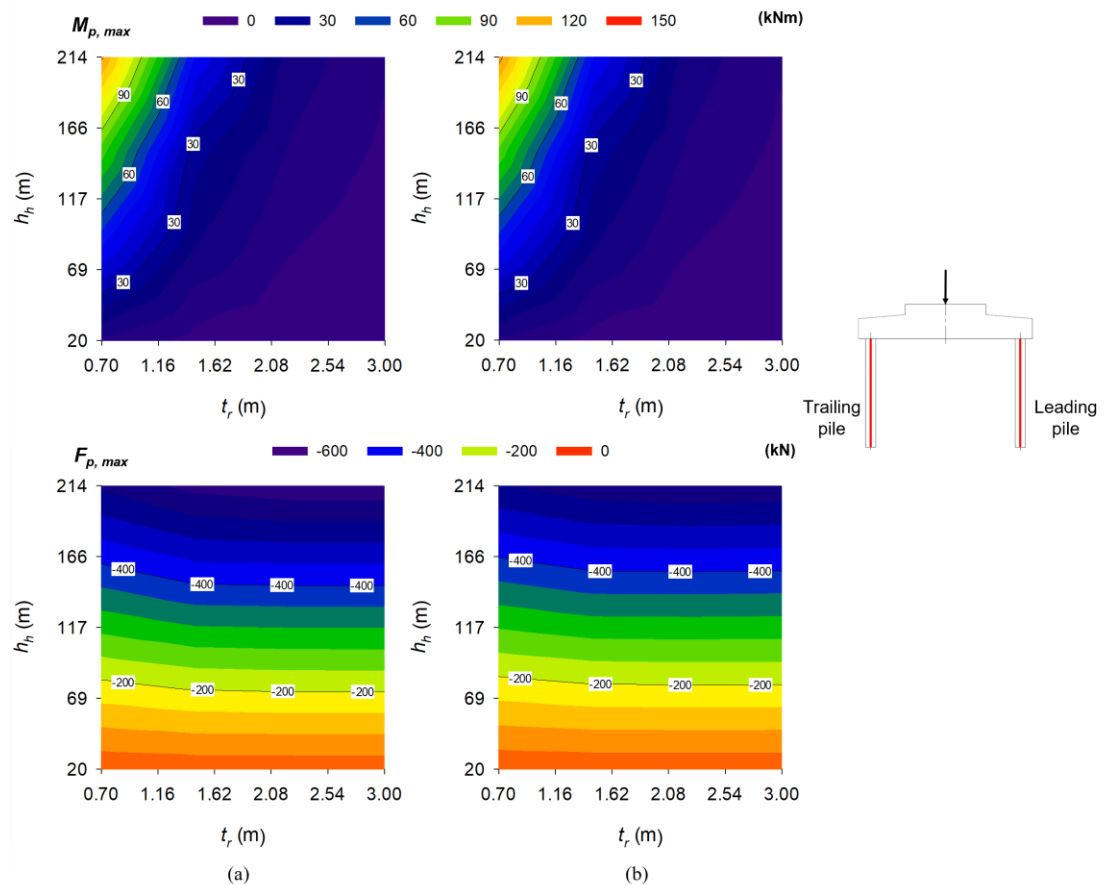
Figure 5-30: Leading and trailing pile maximum bending moment ($M_{p,max}$) and axial force ($F_{p,max}$) – h_h vs t_r [V]: (a) $L_p = 10$ m; (b) $L_p = 20$ m

Given the symmetry of the piles under vertical loading, the leading and trailing piles yielded the same results and were not plotted separately. $M_{p,max}$ was the most significant if h_h was high

and t_r was low, with the largest bending moment of about 120 kNm observed when h_h = 214 m for both pile lengths, which is smaller than M_{crack} = 143 kNm calculated for a 900 mm diameter pile and a concrete tensile strength of 2 MPa. Pile length, or the depth of the compressible soil layer, did not seem to have an influence. As seen in **Figure 5-12** and **Figure 5-29**, $F_{p,max}$ seemed to be only affected by h_h, except when t_r was less than 1.16 m, whereby a slight decrease in the compressive force in the piles was observed under loading for the same h_h.

5.5.2   Vertical load, horizontal load and overturning moment, *V-H-M*

The combined effect of the vertical load, horizontal load, and overturning moment was investigated with varying raft thicknesses for the second load case. **Figure 5-31(a)** and **(b)** present the surface plots showing the influence of h_h and t_r on the rotation of the raft pedestal (θ_r) for L_p = 10 m and 20 m, respectively. For both pile lengths, as h_h increases, θ_r also increases due to the magnitude of the applied overturning moment increasing. However, h_h lower than 69 m resulted in nearly no rotation. Additionally, thicker raft sections and short pile lengths resulted in lower pedestal rotations, aligning with the observations in the literature regarding the relative stiffness at the pile-raft interface, which should ultimately reduce the amount of the tensile forces in the trailing pile.

Figure 5-31: Raft pedestal rotation (θ_r) – h_h vs t_r [*V-H-M*]: (a) L_p = 10 m; (b) L_p = 20 m

The horizontal displacement of the raft (v_{rh}) for the different t_r-h_h combinations is presented in **Figure 5-32(a)** and **(b)** for pile lengths of 10 m and 20 m, respectively. v_{rh} is only affected by h_h, as seen in **Figure 5-32**, with higher horizontal loads and overturning moments resulting in larger horizontal displacements, regardless of the thickness of the raft. Longer piles also resulted in higher v_{rh} values due to slenderness.

Figure 5-32: Raft top centre horizontal displacement (v_{rh}) – h_h vs t_r [*V-H-M*]: (a) L_p = 10 m; (b) L_p = 20 m

Figure 5-33 presents the horizontal stresses at the base of the raft (σ_r) in the central *xz*-plane against the distance from the centre of the raft, indicating the influence of t_r by keeping h_h constant at 117 m. For both sets of figures, **(a)** shows the response of the raft supported by 10 m long piles, whereas **(b)** shows the response if the piles are 20 m long. Considering the part of the raft spanning between the piles, both tensile and compressive stresses are observed, with the tensile stresses occurring on the leading end of the raft in the direction of the horizontal load and overturning moment. The inflection point where these tensile stresses changed to compressive in the base of the raft occurred in the centre of the raft. These stresses are also substantially higher than when only the vertical load was acting on the foundation. The highest stresses were observed when t_r = 0.7 m, exceeding 2 MPa (tensile strength) at a hub height of 117 m. These stresses, however, decreased at a reducing rate as the raft's thickness and, ultimately, the raft rigidity increased. As with the case when only the vertical load was applied, the maximum 'sagging' and 'hogging' stresses are located about 3.6 m from the centre of the raft.

Figure 5-33: Raft stress at raft base (σ_r) – influence of t_r [*V-H-M*]: (a) L_p = 10 m; (b) L_p = 20 m

The maximum horizontal tensile stresses ($\sigma_{r,max}$) at 3.6 m from the centre of the raft for all the t_r-h_h combinations were extracted and plotted in **Figure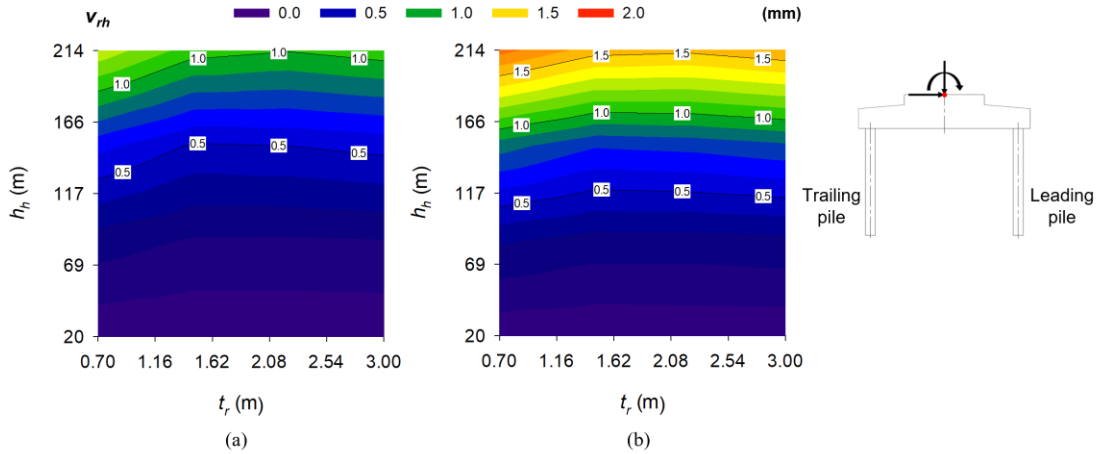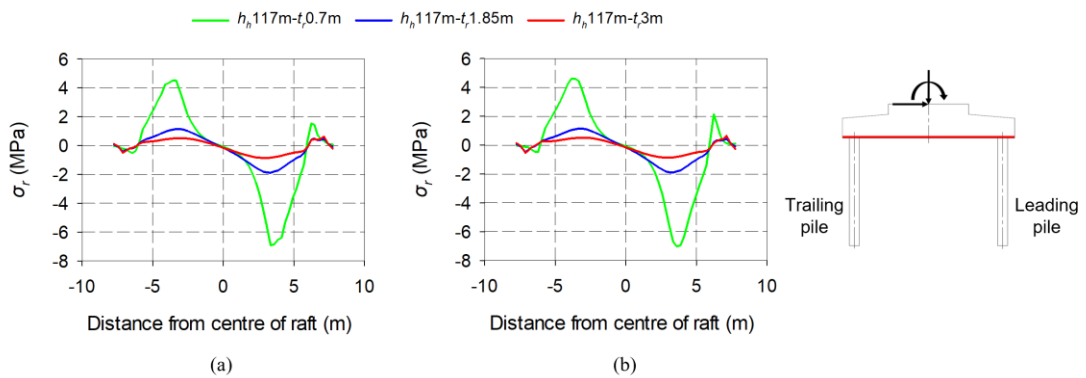 5-34(a)** and **(b)** for L_p = 10 m and L_p = 20 m, respectively. In both figures, $\sigma_{r,max}$ is influenced by both t_r and h_h, with increasing h_h and decreasing t_r resulting in a substantially increased $\sigma_{r,max}$. Pile length slightly affected raft response, with longer piles resulting in higher σ_r values. Again, this can potentially be ascribed to the amount of rotation that the foundation undergoes during loading, which is linked to the combined stiffness of the members and the interaction of these stiffnesses with the surrounding soil. Given the foundation's size and the soil's properties, any h_h larger than 69 m could result in the raft cracking under the combined vertical load, horizontal load and overturning moment, with the risk being higher if the raft is thin.
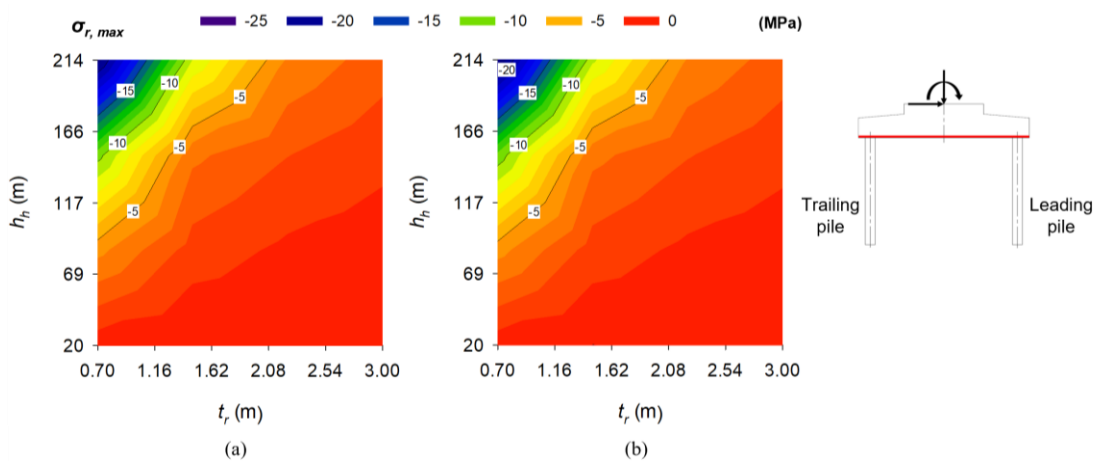
Figure 5-34: Maximum raft stress at raft base ($\sigma_{r,max}$) – h_h vs t_r [V-H-M]: (a) L_p = 10 m; (b) L_p = 20 m

Moving on to the response of the piles, **Figure 5-35** contains surface plots showing the influence of h_h and t_r on the percentage of the total vertical load carried by the piles (F_p/F_t) under the V-H-M load combination. **Figure 5-35(a)** for L_p = 10 m and **Figure 5-35(b)** for L_p = 20 m show a slightly different response than when only the vertical load acted on the foundation. F_p/F_t is now influenced by both h_h and t_r, with the effect being more significant for shorter piles. As with E_s, under the combined vertical load, horizontal load and overturning moment, the overall percentage was reduced, with the load bearing more on the supporting soil under the raft.

For the leading and trailing piles in the xz-plane, axial forces and bending moments were determined from the strain data with depth, as seen in **Figure 5-36**, showing the effect of t_r by keeping h_h constant at 117 m. **Figure 5-36(a)** presents the bending moment (M_p) and axial force (F_p) diagrams with depth for the leading and trailing piles having lengths equal to 10 m, whereas **Figure 5-36(b)** presents these diagrams for L_p = 20 m, respectively. Given the sign convention assumed in Section 5.3, the bending moment diagrams for the two piles were

plotted on separate axes. As seen in **Figure 5-36(a)** and **(b)**, the magnitude and direction of M_p in the leading and trailing piles are affected by t_r and the relative stiffness between the pile, raft and supporting soil. When the raft was thin, the positive bending moment in the leading pile under pure vertical loading became more positive with the addition of the horizontal load and overturning moment. Additionally, the positive bending moment in the trailing pile became negative. However, as the raft increased in thickness and became more rigid, the opposite was observed with M_p for both the leading and trailing piles. Regarding the axial forces in the piles with depth, the leading and trailing piles showed push-pull responses under loading. However, t_r did not influence the magnitude of these push-pull compressive and tensile axial forces much. This insignificant difference could result from the significant Young's foundation's modulus. A thicker raft slightly reduced both these forces.
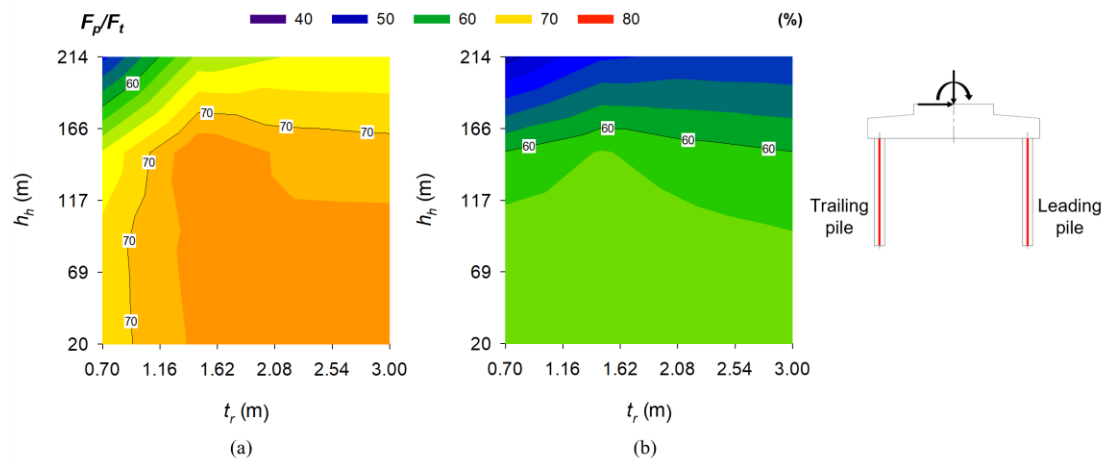
Figure 5-35: Total vertical load percentage carried by piles (F_p/F_t) – h_h vs t_r [*V-H-M*]: (a) L_p = 10 m; (b) L_p = 20 m

Extracting the maximum bending moments $(M_{p,max})$ and axial forces $(F_{p,max})$ in the leading and trailing piles at 0.5 m from the base of the raft for all the t_r-h_h combinations **Figure 5-37** and **Figure 5-38** were plotted, respectively. Due to the asymmetrical response, the leading and trailing piles were plotted separately for this load configuration, as seen in **Figure 5-37** and **Figure 5-38**. In both figures, **(a)** and **(b)** represent the response when L_p = 10 m and L_p = 20 m, respectively. Looking at the leading pile first (see **Figure 5-37**), the magnitude of the bending moments increased for both pile lengths, becoming more positive with the addition of H and M. Additionally, these moments were more significant when h_h was high, t_r was small, and the pile length was short. Bending moments exceeded M_{crack} = 143 kNm when h_h exceeded 117 m, and t_r was less than 1.62 m for the foundation size and soil properties considered. Regarding the axial compressive force in the leading pile under this load combination, the compressive force was the highest when the piles were the shortest and h_h the greatest, regardless of t_r.

Figure 5-36: Leading and trailing pile bending moment (M_p) and axial force (F_p) – influence of t_r [V-H-M]: (a) $L_p = 10$ m; (b) $L_p = 20$ m
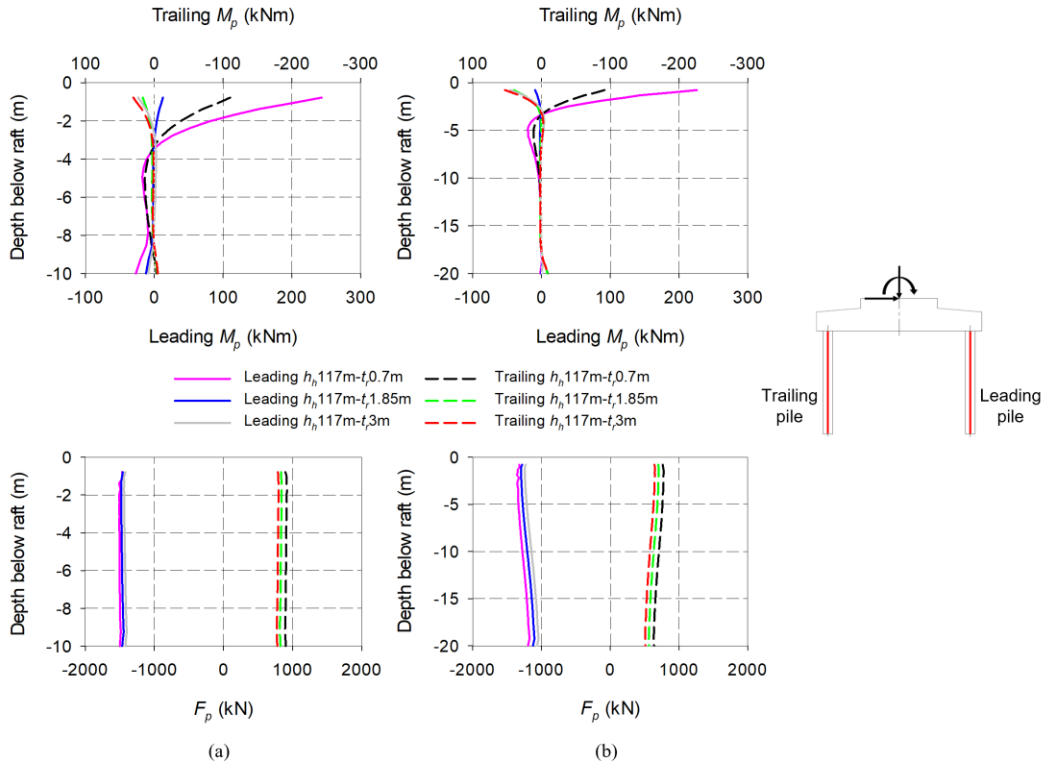

Figure 5-37: Leading pile maximum bending moment ($M_{p,max}$) and axial force ($F_{p,max}$) – h_h vs t_r [V-H-M]: (a) $L_p = 10$ m; (b) $L_p = 20$ m
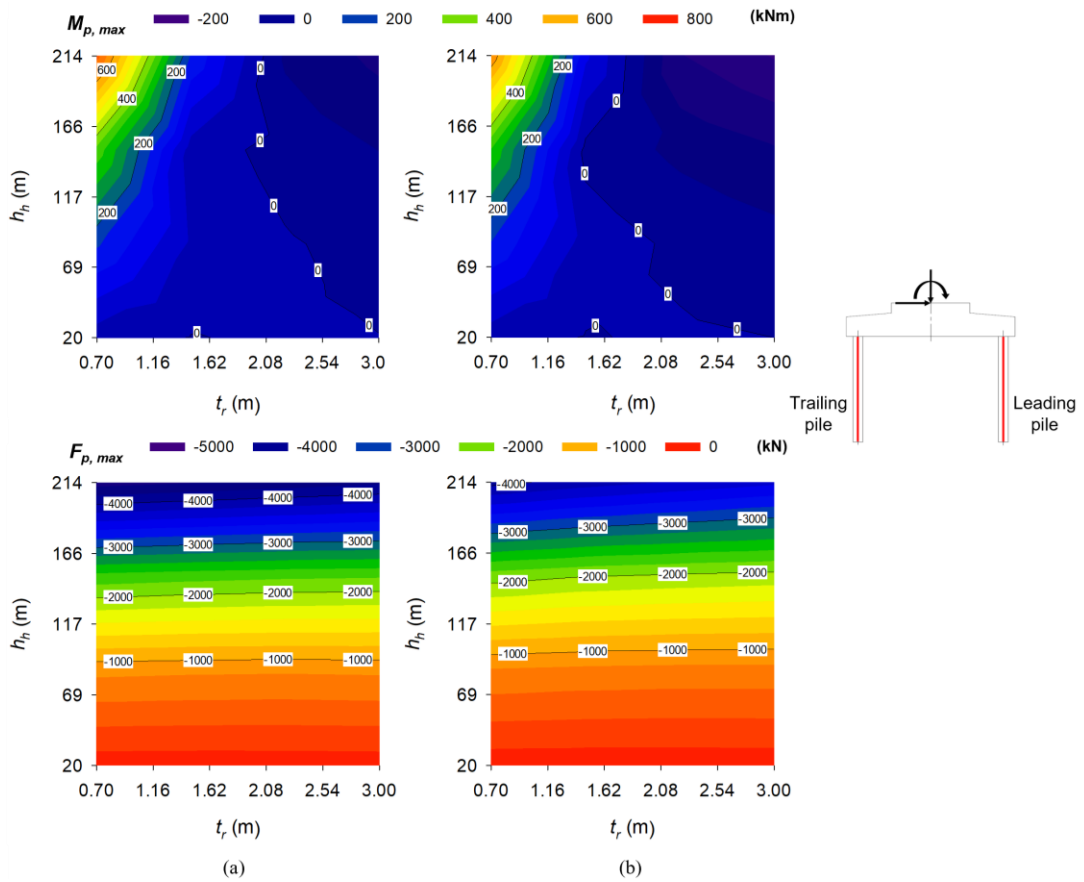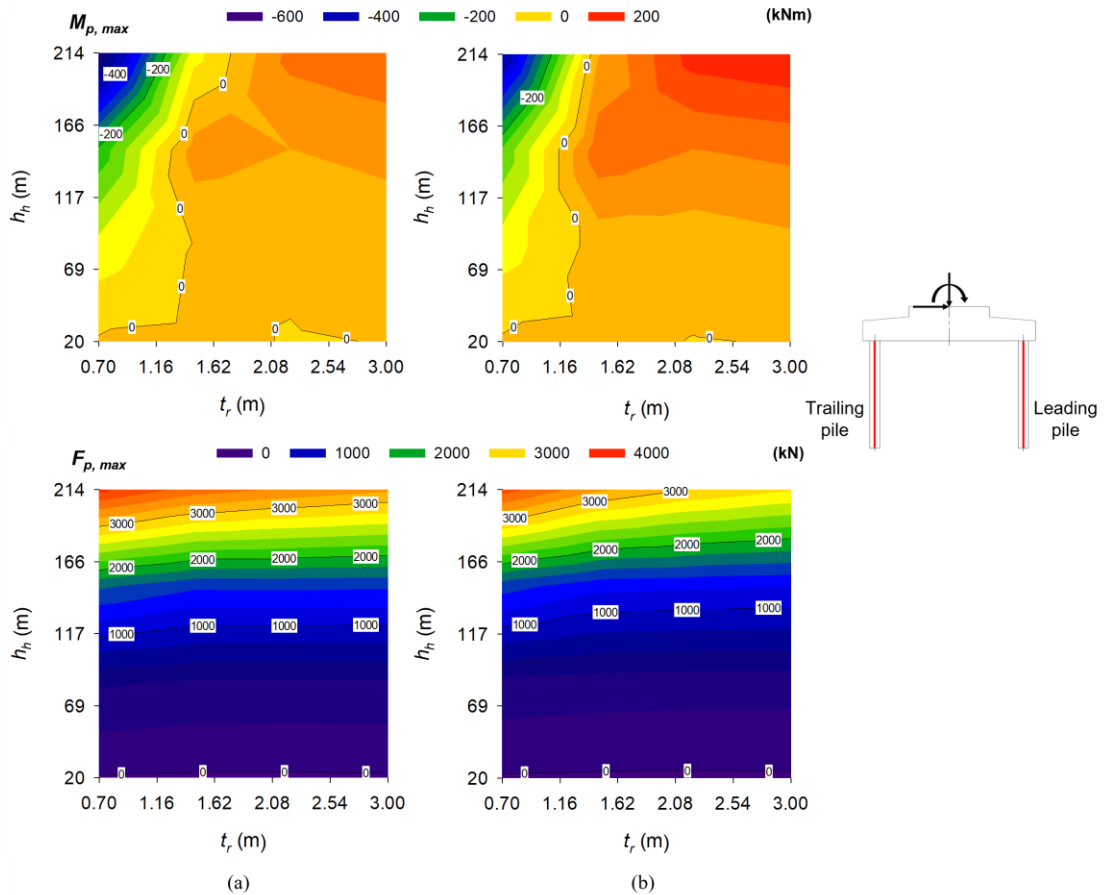
Figure 5-38: Trailing pile maximum bending moment ($M_{p,max}$) and axial force ($F_{p,max}$) – h_h vs t_r [*V-H-M*]: (a) $L_p = 10$ m; (b) $L_p = 20$ m

For the trailing pile (see **Figure 5-38**), similar responses were observed to that of the leading pile, with the only difference being the direction of the bending moments and axial forces. The direction of the bending moments changed for both pile lengths, becoming more negative with the addition of *H* and *M*, compared to the positive bending moment induced on the trailing pile under pure vertical loading. Higher h_h values resulted in more significant negative $M_{p,max}$ values when the raft was thinner. Shorter, stockier piles also resulted in higher $M_{p,max}$ values. Positive axial tensile forces were observed in the trailing pile, primarily influenced by h_h, regardless of t_r, with nearly no tensile forces observed when $h_h = 20$ m. For h_h exceeding 117 m, these axial forces exceeded the calculated axial cracking strength of the pile at 1272 kN for a 900 mm diameter pile and a concrete cracking stress of 2 MPa.

5.6   RAFT RADIUS

The second last variable considered in this study was the effect of raft radius (R_r) on the response of a piled-raft foundation under dominant horizontal loads and overturning moments. As before, two load cases were explored (*V* and *V-H-M*), presented separately in Sections 5.6.1 and 5.6.2, respectively. **Table 5-7** indicates the raft radius values investigated

in this parametric study, with the placement of *a*, *b*, *c*, *d* and *e* as indicated in **Figure 5-2** and the accompanying h_h considered. The plots summarised in Section 5.2 will be presented for each load case, with the other parametric variables, excluding the raft radius, kept at the values indicated in red in **Table 5-1**.

Table 5-7: Parametric study values – raft radius

Parametric variable	*a*	*b*	*c*	*d*	*e*
Raft radius, R_r (m)	5.5	7.75	10	13.5	15

5.6.1   Vertical load, *V*

Figure 5-39(a) and **(b)** present the surface plots showing the influence of h_h and R_r on the top central vertical deflection of the raft (v_{rv}) for $L_p = 10$ m and 20 m, respectively. Under vertical loading, v_{rv} is affected by both h_h and R_r, with more considerable deflections resulting from higher turbine heights and increased R_r, with the raft being more flexible at these R_r values. Due to the slenderness of the supporting piles, longer piles also resulted in higher vertical deflections. For both pile lengths, limited deflection was experienced when h_h equalled 20 m, and R_r was equal to 5.5 m, respectively.
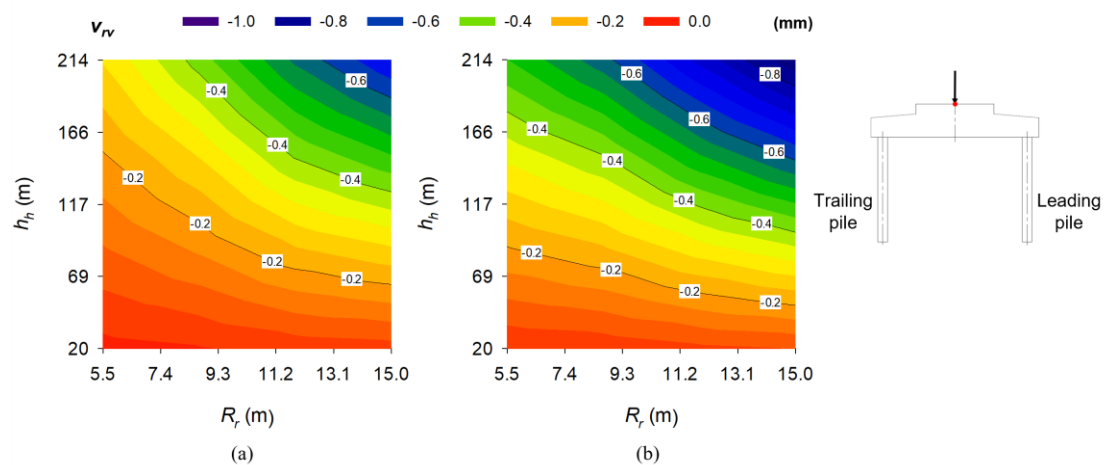
Figure 5-39: Raft top centre vertical deflection (v_{rv}) – h_h vs R_r [*V*]: (a) $L_p = 10$ m; (b) $L_p = 20$ m

Regarding the differential settlement of the raft (v_{rd}), **Figure 5-40(a)** and **(b)** present the surface plots showing the influence of h_h and R_r for $L_p = 10$ m and 20 m, respectively. Like the central vertical deflection, v_{rd} was more significant with higher h_h and larger R_r values. Pile slenderness has a slight effect, with more slender piles resulting in larger settlements.

Figure 5-41(a) and **(b)** present the bottom raft horizontal stresses (σ_r) in the central *xz*-plane for $L_p = 10$ m and 20 m plotted in 2-D against the distance from the centre of the raft, respectively. **Figure 5-41** indicates the influence of R_r on σ_r by keeping h_h constant at 117 m.

The part of the raft between the piles showed 'sagging' tensile stresses, with substantial compressive horizontal stresses over the pile-raft interfaces. The magnitude of these stresses was substantially higher when R_r was larger due to the significant flexibility of the raft. However, for radius values greater than 10 m, σ_r did not increase significantly, with values seeming to converge as raft rigidity decreases. The largest tensile stress within the region between the piles occurred where the pedestal connects to the raft at a distance of 3.6 m from the raft's centre. These stresses were below concrete's typical splitting tensile strength of around 2 MPa to 3 MPa, even with the raft having a radius of 15 m. Thus, the raft should not crack under vertical loading for the foundation sizes and soil properties considered.
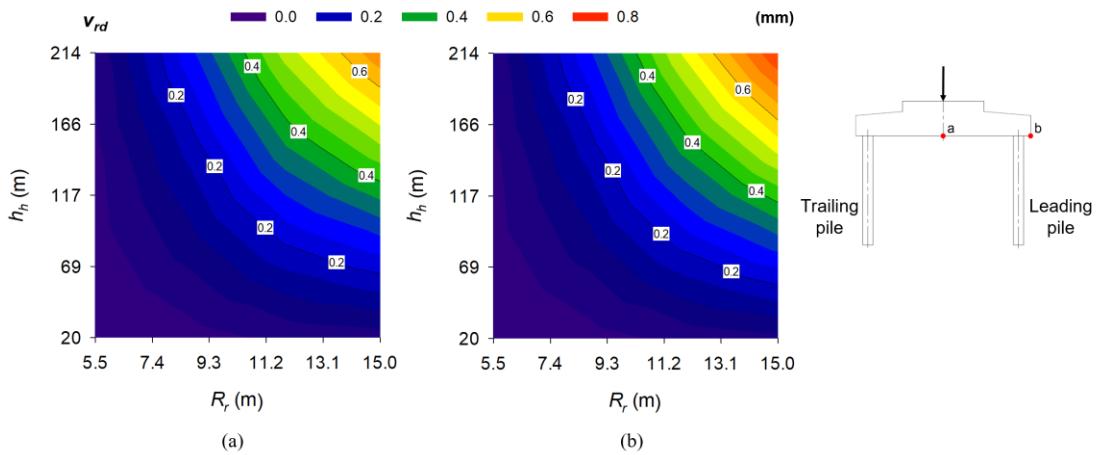
Figure 5-40: Raft differential settlement (v_{rd}) – h_h vs R_r [V]: (a) L_p = 10 m; (b) L_p = 20 m
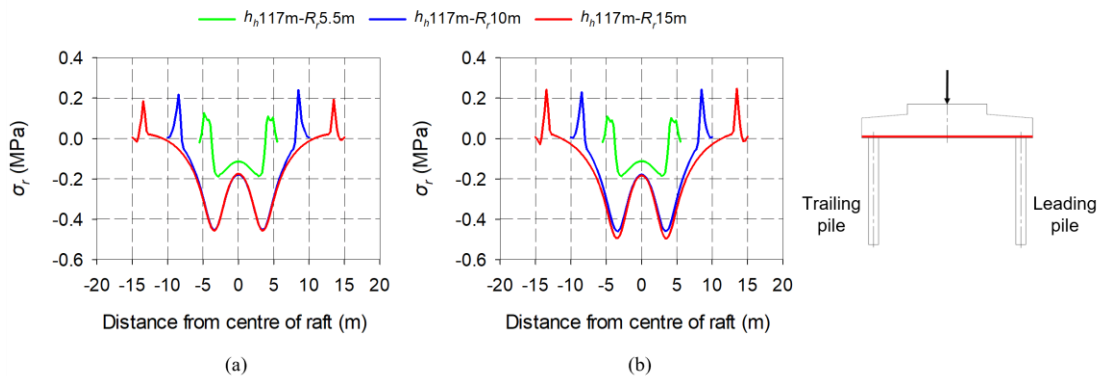
Figure 5-41: Raft stress at raft base (σ_r) – influence of R_r [V]: (a) L_p = 10 m; (b) L_p = 20 m

Extracting the maximum tensile horizontal stresses ($\sigma_{r,max}$) at 3.6 m from the centre of the raft for all the R_r-h_h combinations, **Figure 5-42(a)** and **(b)** were plotted for L_p = 10 m and 20 m, respectively. In both surface plots, $\sigma_{r,max}$ is influenced by h_h and R_r, as observed previously, with higher h_h resulting in higher tensile stresses at the base of the raft. As the raft radius, however, increases, $\sigma_{r,max}$ also increases up to a radius equal to about 11 m. After this point, $\sigma_{r,max}$ remains constant regardless of R_r. Less slender piles resulted in a slight decrease in the

stress at the base of the raft, with all R_r-h_h combinations yielding tensile stresses below cracking.
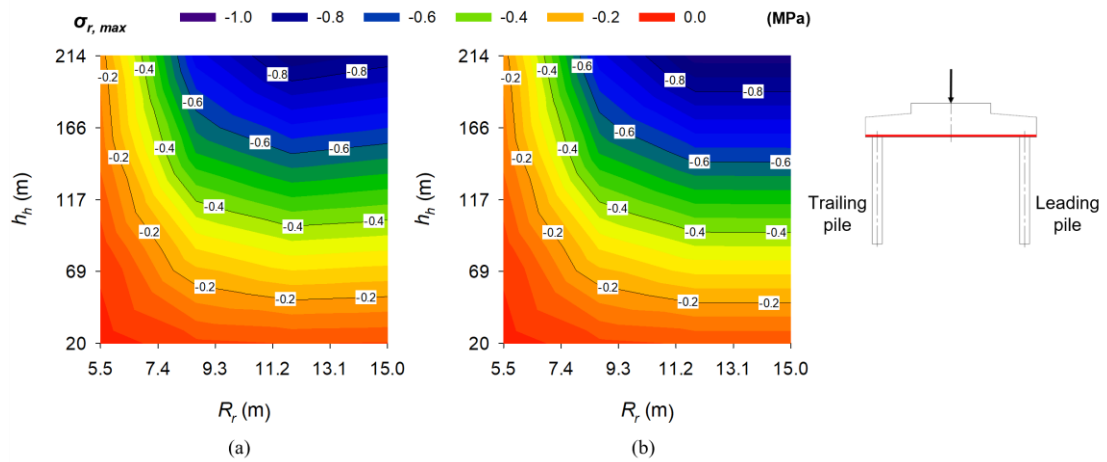
Figure 5-42: Maximum raft stress at raft base ($\sigma_{r,max}$) – h_h vs R_r [V]: (a) L_p = 10 m; (b) L_p = 20 m

Considering the percentage of the total vertical load carried by the piles (F_p/F_t), **Figure 5-43** indicates the surface plots showing the combined influence of h_h and R_r. As seen in **Figure 5-43(a)** for L_p = 10 m and **Figure 5-43(b)** for L_p = 20 m, only R_r influenced this percentage, with rafts having smaller radii resulting in the piles having to carry higher loads, similar to the observation from literature, with increasing pile spacings resulting in the pile carrying less load. Longer piles carried smaller loads than shorter piles, with L_p = 10 m carrying 80% of the vertically applied load when R_r = 5.5 m.
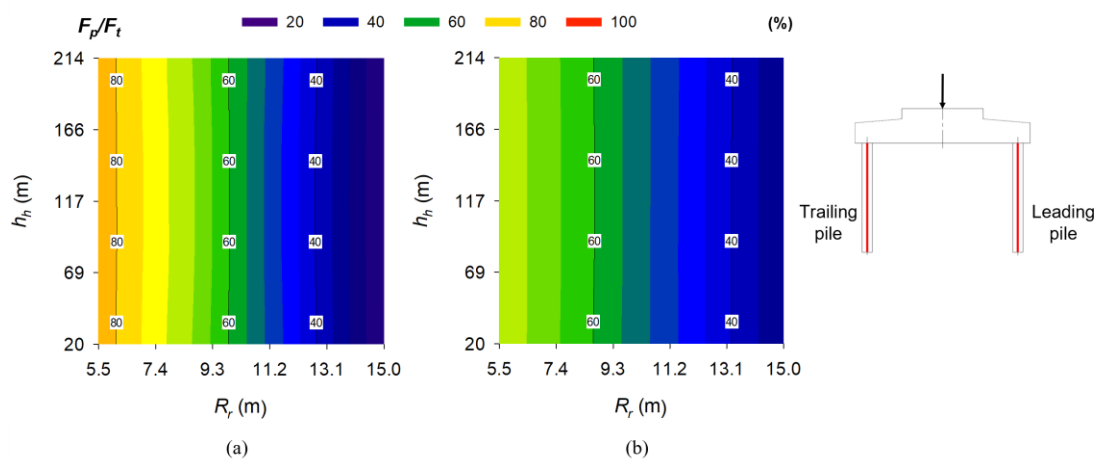
Figure 5-43: Total vertical load percentage carried by piles (F_p/F_t) – h_h vs R_r [V]: (a) L_p = 10 m; (b) L_p = 20 m

For the leading and trailing piles in the *xz*-plane, axial forces and bending moments were determined from the strain data with depth, as seen in **Figure 5-44**, showing the effect of R_r by keeping h_h constant at 117 m.

5-35

Figure 5-44: Leading and trailing pile bending moment (M_p) and axial force (F_p) – influence of R_r [V]: (a) L_p = 10 m; (b) L_p = 20 m

Figure 5-44(a) presents the bending moment (M_p) and axial force (F_p) diagrams with depth in the leading and trailing pile having lengths equal to 10 m, whereby **Figure 5-44(b)** presents these diagrams for L_p = 20 m, respectively. Given the sign convention assumed in Section 5.3, the bending moment diagrams for the 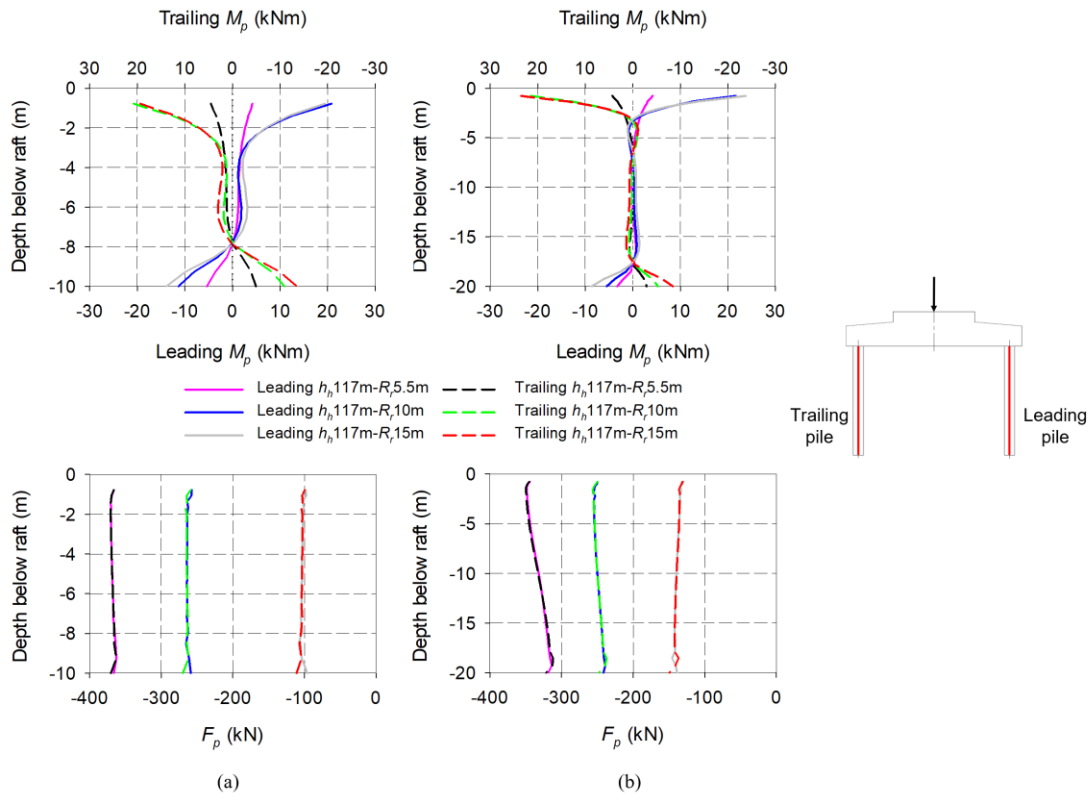two piles were plotted on separate axes. As seen in **Figure 5-44**, the bending moment in the leading and trailing piles are symmetrical under pure vertical loading, with both piles experiencing positive bending moments towards the top. At the same h_h, the influence of R_r is noticeable for both pile lengths, with the bending moment in the leading and trailing piles being more significant if the raft radius was larger. However, similar to σ_r, no significant increase was observed for a radius greater than 10 m. This convergence is similar to that observed for the stresses in the raft earlier. As expected, maximum M_p values occurred towards the top of the piles for the R_r values considered, with the value not changing significantly with L_p. M_p was also present at the foot of the piles, being more significant for shorter piles. Regarding the axial forces in the piles with depth, the leading and trailing piles showed symmetry, with both piles experiencing compressive loads. Smaller raft radii resulted in higher axial forces experienced by the pile.

Extracting the maximum bending moments ($M_{p,max}$) and axial forces ($F_{p,max}$) in the leading and trailing piles at 0.5 m from the base of the raft for all the R_r-h_h combinations, **Figure 5-45(a)** and **(b)** were plotted for L_p = 10 m and 20 m, respectively. Given the symmetry of the piles

under vertical loading, both the leading and trailing piles yielded the same results and were, thus, not plotted individually. $M_{p,max}$ was the most significant if h_h and R_r were high. However, as with σ_r, $M_{p,max}$ did not increase significantly for radii more significant than 11 m. Greater pile lengths also resulted in higher bending moments due to slenderness. As seen in **Figure 5-45**, $F_{p,max}$ seemed to be affected by h_h and R_r, with higher h_h and lower R_r resulting in larger axial compressive loads under pure vertical loading.
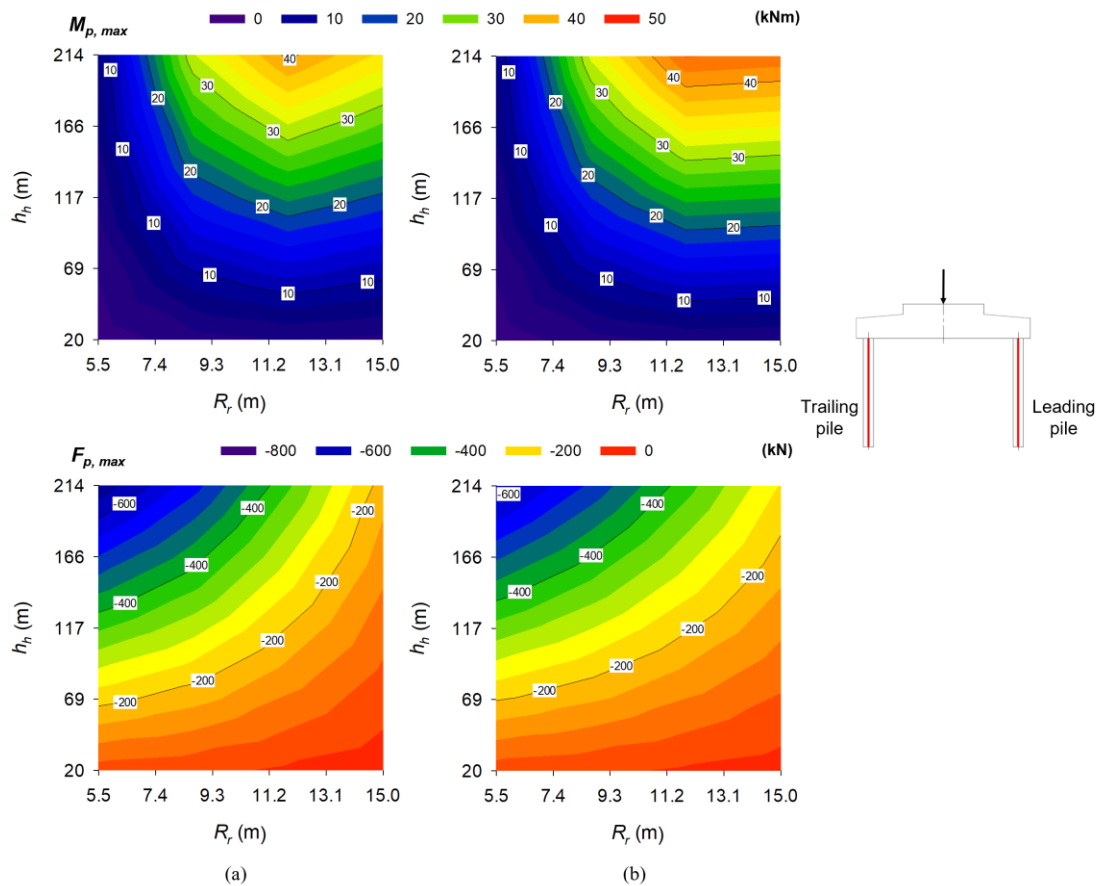
Figure 5-45: Leading and trailing pile maximum bending moment ($M_{p,max}$) and axial force ($F_{p,max}$) – h_h vs R_r [V]: (a) $L_p = 10$ m; (b) $L_p = 20$ m

5.6.2 Vertical load, horizontal load and overturning moment, *V-H-M*

The combined effect of the vertical load, horizontal load, and overturning moment was investigated with varying raft radii for the second load case. **Figure 5-46(a)** and **(b)** present the surface plots showing the influence of h_h and R_r on the rotation of the raft pedestal (θ_r) for $L_p = 10$ m and 20 m, respectively. For both pile lengths, as h_h increased, θ_r also increased due to the magnitude of the applied overturning moment increasing. However, only for R_r smaller than 11 m. This data suggests that as raft radius increases, raft rotation and foundation rotational stiffness tend to become unaffected under loading. Comparing it to the arguments in the literature review on portal frames, the stiffness of that member decreases as member

length increases. Additionally, large radii and short pile lengths resulted in lower pedestal rotations due to the reduced slenderness.
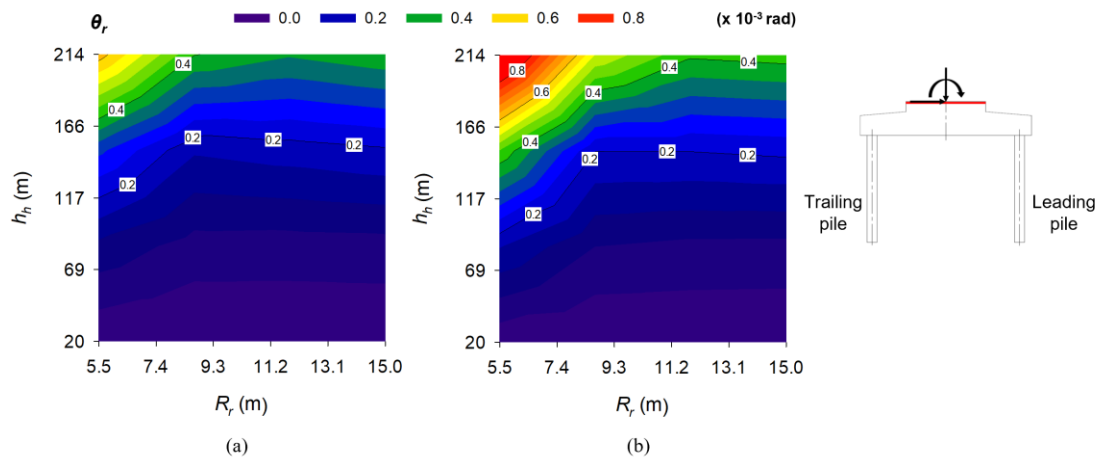
Figure 5-46: Raft pedestal rotation (θ_r) – h_h vs R_r [V-H-M]: (a) L_p = 10 m; (b) L_p = 20 m

The horizontal displacement of the raft (v_{rh}) for the different R_r-h_h combinations is presented in **Figure 5-47(a)** and **(b)** for pile lengths of 10 m and 20 m, respectively. v_{rh} is affected by both R_r and h_h, as seen in **Figure 5-47**, with higher horizontal loads and overturning moments resulting in larger horizontal displacements. Lower raft radii resulted in higher displacements and can be ascribed to the reduction in the area of the raft in contact with the soil.
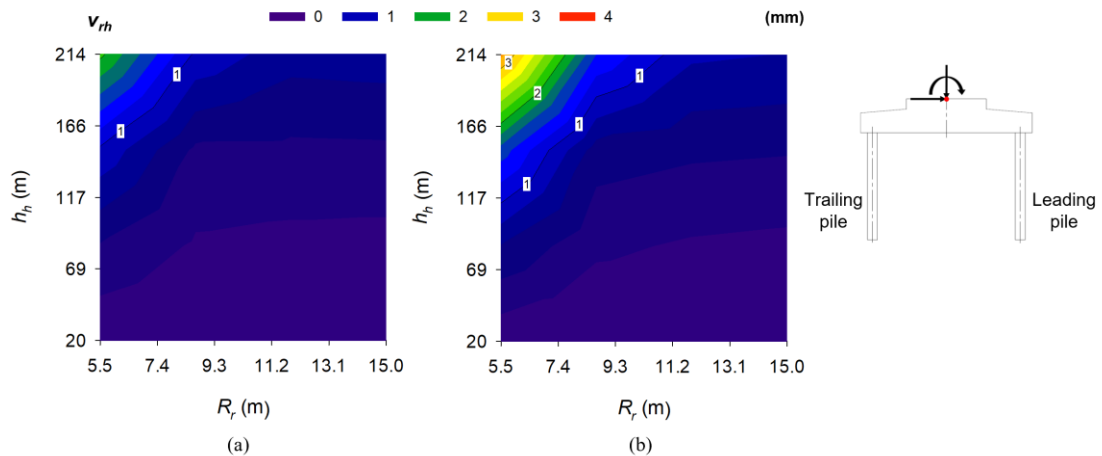
Figure 5-47: Raft top centre horizontal displacement (v_{rh}) – h_h vs R_r [V-H-M]: (a) L_p = 10 m; (b) L_p = 20 m

Figure 5-48 presents the horizontal stresses at the base of the raft (σ_r) in the central xz-plane against the distance from the centre of the raft, indicating the influence of R_r by keeping h_h constant at 117 m. Considering the part of the raft spanning between the piles, both tensile and compressive stresses are observed, with the tensile horizontal stresses occurring on the leading end of the raft in the direction of the horizontal load and overturning moment.
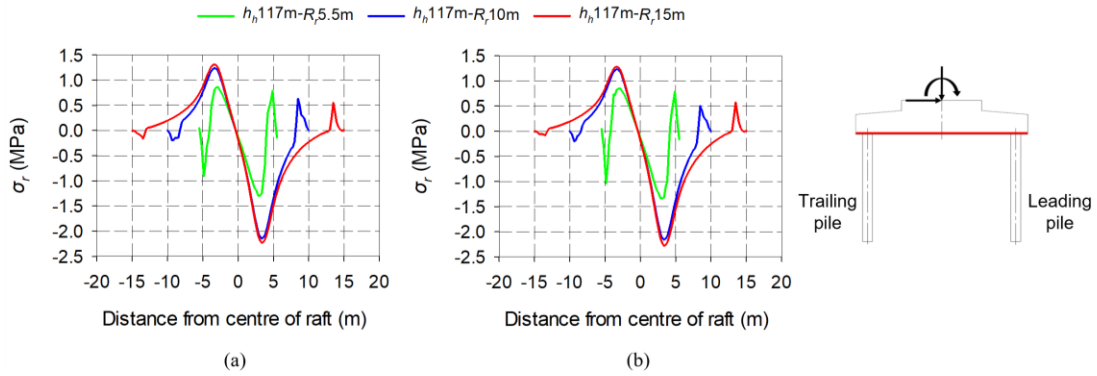
Figure 5-48: Raft stress at raft base (σ_r) – influence of R_r [V-H-M]: (a) L_p = 10 m; (b) L_p = 20 m

Again, the inflection point, where these tensile stresses changed to compressive stresses, occurred in the centre of the raft. The stresses were substantially higher than when only the vertical load was acting on the foundation. The highest stresses were observed when R_r = 15 m. However, these values were not significantly higher than the value observed when R_r equalled 10 m. The stresses decreased as the raft radius decreased. As with the case when only the vertical load was applied, the maximum tensile and compressive stresses are located about 3.6 m from the centre of the raft, with stresses not exceeding 2 MPa for h_h = 117 m.

The maximum tensile horizontal stresses ($\sigma_{r,max}$) at 3.6 m from the centre of the raft for all the R_r-h_h combinations were extracted and plotted. **Figure 5-49(a)** and **(b)** indicate the surface plots showing the effect of R_r and h_h on $\sigma_{r,max}$ for L_p = 10 m and 20 m, respectively. In both figures, $\sigma_{r,max}$ is influenced by both R_r and $h_h$, with increasing h_h and R_r resulting in an increasing $\sigma_{r,max}$. However, as before, no significant increase was observed for radii larger than 11 m. The depth of the compressible soil layer, or pile length, slightly affected raft response, with longer piles resulting in higher σ_r values. Given the foundation's size and the soil's properties, any h_h larger than 117 m could result in the concrete in the raft cracking under the combined vertical load, horizontal load and overturning moment, with the risk being higher if the raft radius is higher.

Figure 5-50 contains surface plots showing the influence of h_h and R_r on the percentage of the total vertical load carried by the piles (F_p/F_t) under the V-H-M load combination. **Figure 5-50(a)** for L_p = 10 m and **Figure 5-50(b)** for L_p = 20 m show a slightly different response than when only the vertical load acted on the foundation. F_p/F_t is now influenced by both h_h and R_r when R_r was less than 9 m. Below these radii, higher h_h resulted in less load being carried by the pile, which can be attributed to the large tensile forces generated in the trailing piles under loading, as discussed in the following paragraphs.

For the leading and trailing piles in the xz-plane, axial forces and bending moments were determined from the strain data with depth, as seen in **Figure 5-51**, showing the effect of R_r

by keeping h_h constant at 117 m. **Figure 5-51(a)** presents the bending moment (M_p) and axial force (F_p) diagrams with depth in the leading and trailing pile having lengths equal to 10 m, whereby **Figure 5-51(b)** presents these diagrams for L_p = 20 m, respectively. Given the sign convention assumed in Section 5.3, the bending moment diagrams for the two piles were plotted on separate axes.
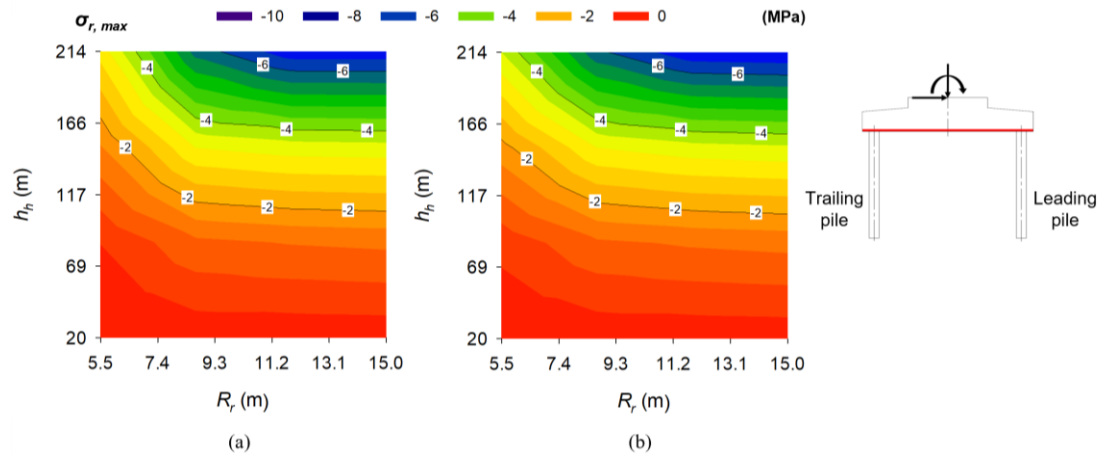
Figure 5-49: Maximum raft stress at raft base ($\sigma_{r,max}$) – h_h vs R_r [*V-H-M*]: (a) L_p = 10 m; (b) L_p = 20 m
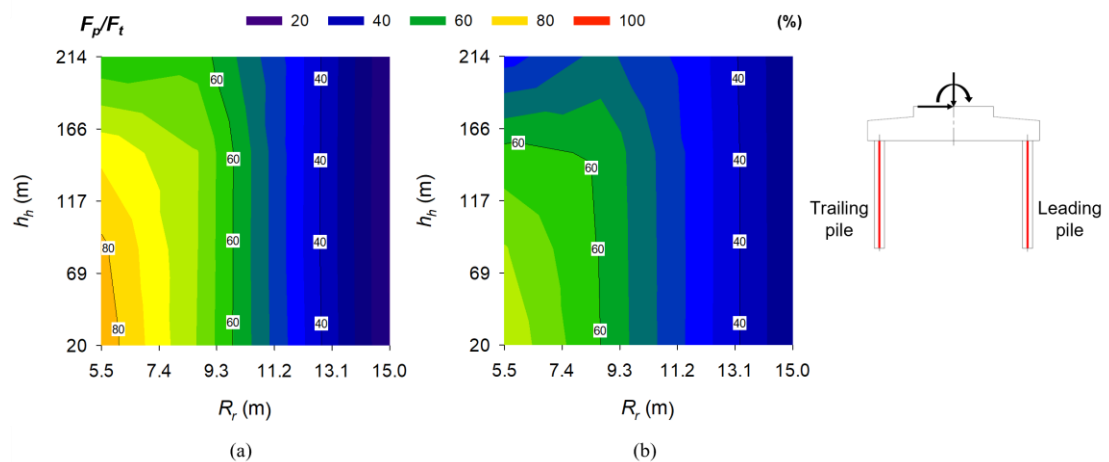
Figure 5-50: Total vertical load percentage carried by piles (F_p/F_t) – h_h vs R_r [*V-H-M*]: (a) L_p = 10 m; (b) L_p = 20 m

As seen in **Figure 5-51(a)** and **(b)**, the magnitude and direction of M_p in the leading and trailing piles are affected by R_r and the relative stiffness between the pile, raft and supporting soil. When the raft radius was small, the positive bending moment in the leading pile under pure vertical loading became substantially negative with the addition of the horizontal load and overturning moment. The effect was more significant when L_p = 20 m. M_p remained relatively constant for R_r values greater than 10 m. The positive bending moment in the trailing pile became more positive when R_r was small. However, as the raft radius increased,

M_p in the trailing pile reduced to zero. Thus, the amount of rotation is a function of the relative stiffness between the raft, the piles and the soil. Regarding the axial forces in the piles with depth, the leading and trailing piles showed push-pull responses under loading. As R_r decreased, the compressive and tensile forces in the leading and trailing piles increased. This observation seems linked to the combined member stiffnesses at the pile-raft interface.
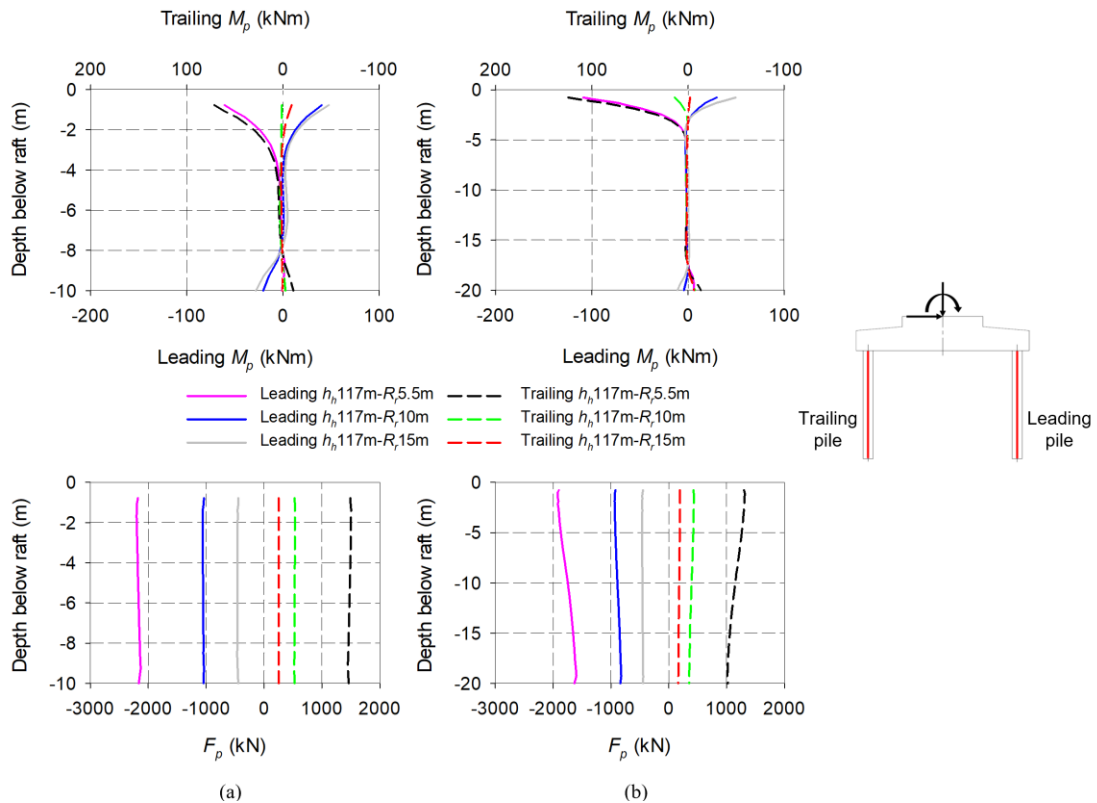
Figure 5-51: Leading and trailing pile bending moment (M_p) and axial force (F_p) – influence of R_r [V-H-M]: (a) L_p = 10 m; (b) L_p = 20 m

Extracting the maximum bending moments ($M_{p,max}$) and axial forces ($F_{p,max}$) in the leading and trailing piles at 0.5 m from the base of the raft for all the R_r-h_h combinations, **Figure 5-52** and **Figure 5-53** were plotted, respectively. Due to the asymmetrical response, the leading and trailing piles were plotted separately for this load configuration. In both figures, **(a)** and **(b)** represent the response when L_p = 10 m and L_p = 20 m, respectively. Looking at the leading pile first (see **Figure 5-52**), the magnitude of the maximum bending moments decreased for both pile lengths, becoming more negative with the addition of H and M. Additionally, these moments were more significant when h_h was high, R_r was small, and the pile length was long. Bending moments only exceeded M_{crack} = 143 kNm when L_p was equal to 20 m, h_h exceeded 117 m, and R_r was less than 7.3 m for the foundation size and soil properties considered. Regarding the axial compressive force in the leading pile under this load combination, the compressive force was the highest when the leading piles were the shortest, h_h the greatest and R_r the smallest.

Figure 5-52: Leading pile maximum bending moment ($M_{p,max}$) and axial force ($F_{p,max}$) – h_h vs R_r [V-H-M]: (a) $L_p = 10$ m; (b) $L_p = 20$ m

For the trailing pile (see **Figure 5-53**), similar responses were observed to that of the leading pile, with the only difference being the direction of the bending moments and axial forces. The direction of the bending moments changed for both pile lengths, becoming more positive with the addition of H and M, compared to the positive bending moment induced on the trailing pile under pure vertical loading. Higher h_h values resulted in more significant positive $M_{p,max}$ values when the raft radius was small. More extended, slender piles also resulted in higher $M_{p,max}$ values. Positive axial tensile forces were observed in the trailing pile, influenced by both h_h and R_r, with lower raft radii resulting in higher tensile forces in the pile. For h_h exceeding 117 m, these axial forces exceeded the calculated axial cracking strength of the pile at 1272 kN for a 900 mm diameter pile and a concrete cracking stress of 2 MPa.
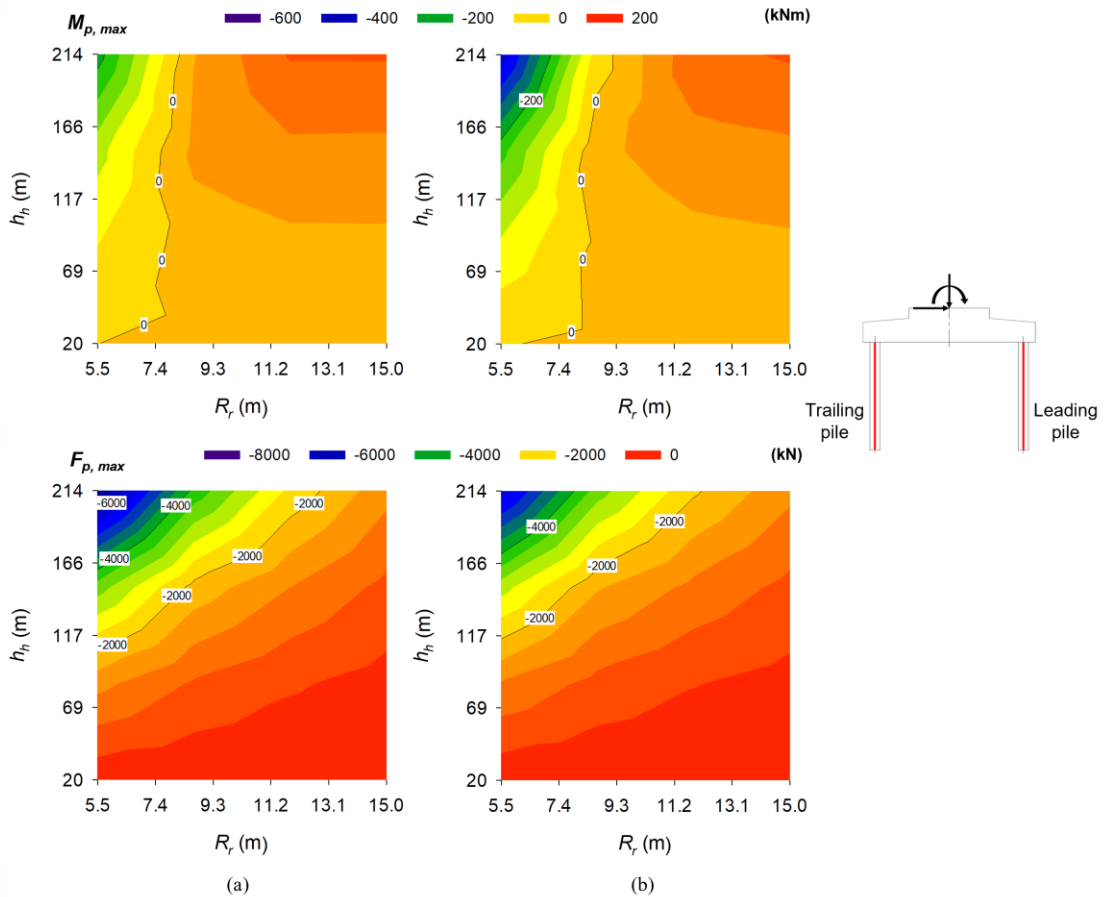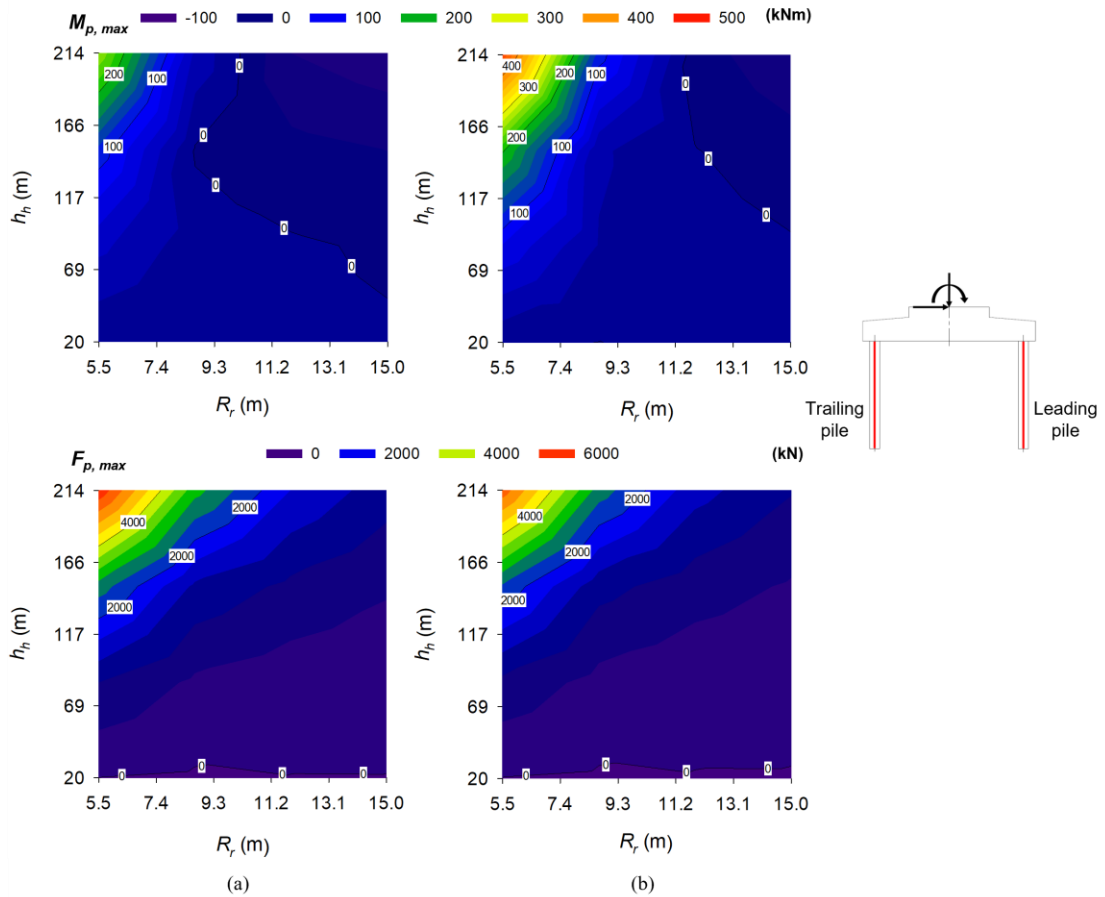
Figure 5-53: Trailing pile maximum bending moment ($M_{p,max}$) and axial force ($F_{p,max}$) – h_h vs R_r [*V-H-M*]: (a) $L_p = 10$ m; (b) $L_p = 20$ m

5.7 PILE DIAMETER

Pile diameter (d_p) was the last variable considered in this parametric study investigating the response of a piled-raft foundation under dominant horizontal loads and overturning moments. Two load cases were explored, namely, *V* and *V-H-M*. Both cases are presented separately in Sections 5.7.1 and 5.7.2, respectively. **Table 5-8** indicates the pile diameter values considered in the parametric study, with the placement of *a*, *b*, *c*, *d* and *e* as indicated in **Figure 5-2** and the accompanying h_h considered. The plots summarised in Section 5.2 will be presented for each load case. The other parametric variables, excluding the pile diameter, were kept at the values indicated in red in **Table 5-1**.

Table 5-8: Parametric study values – pile diameter

Parametric variable	*a*	*b*	*c*	*d*	*e*
Pile diameter, d_p (mm)	600	688	900	1112	1200

5-43

5.7.1   Vertical load, V

Figure 5-54(a) and **(b)** present the surface plots showing the influence of h_h and d_p on the top central vertical deflection of the raft (v_{rv}) for $L_p = 10$ m and 20 m, respectively. Under vertical loading, v_{rv} is affected by both h_h and d_p, with more considerable deflections resulting from higher turbine heights and smaller pile diameters. At smaller pile diameters, the slenderness of the pile is also increased, which results in higher deflections, as seen with longer piles previously, resulting in larger deflections.
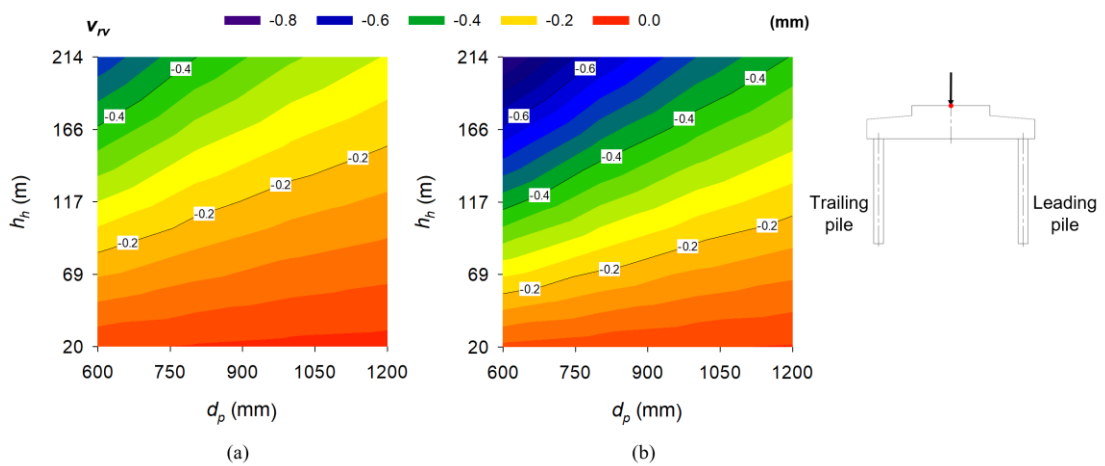
Figure 5-54: Raft top centre vertical deflection (v_{rv}) – h_h vs d_p [V]: (a) $L_p = 10$ m; (b) $L_p = 20$ m

Regarding the differential settlement of the raft (v_{rd}), which is taken as the difference between the bottom central deflection and bottom side deflection of the raft, **Figure 5-55(a)** and **(b)** present the surface plots showing the influence of h_h and d_p for $L_p = 10$ m and 20 m, respectively. v_{rd} seemed to be only influenced by h_h, with d_p and L_p not having an effect.
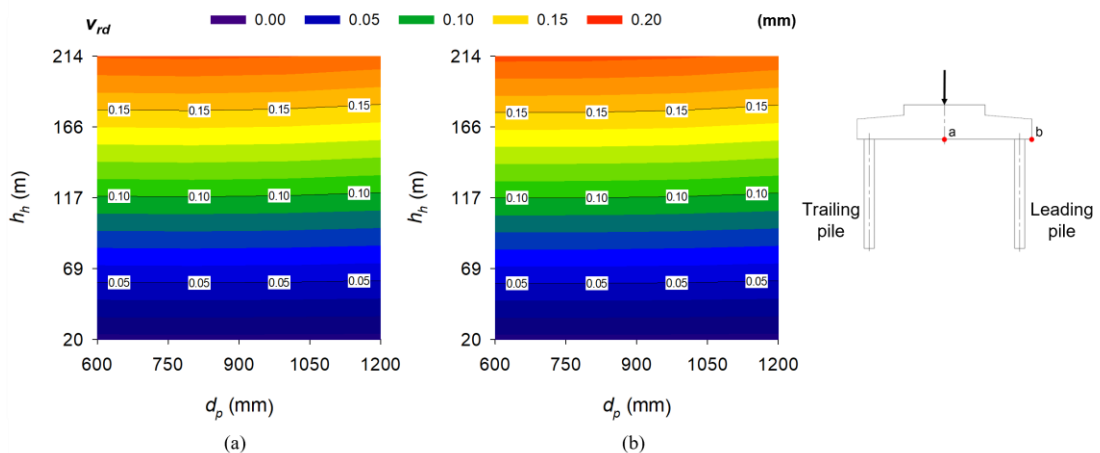

Figure 5-55: Raft differential settlement (v_{rd}) – h_h vs d_p [V]: (a) $L_p = 10$ m; (b) $L_p = 20$ m

Figure 5-56(a) and **(b)** present the horizontal stresses in the base of the raft (σ_r) in the central *xz*-plane for L_p = 10 m and 20 m plotted in 2-D against the distance from the centre of the raft. **Figure 5-56** indicates the influence of d_p on σ_r by keeping h_h constant at 117 m. As before, the part of the raft between the piles showed tensile stresses, with substantial compressive stresses over the pile-raft interfaces, having an equivalent tensile stress at the top of the raft over this interface. As seen in **Figure 5-56**, both d_p and L_p did not influence σ_r, which could be ascribed to the significant raft-soil stiffness compared to the stiffness of the pile. The most considerable tensile stress within the region between the piles still occurred where the pedestal connects to the raft at a distance of 3.6 m from the raft's centre. These stresses were substantially below concrete's typical splitting tensile strength of around 2 MPa to 3 MPa. Thus, the raft should not crack under vertical loading for the foundation sizes and soil properties considered.
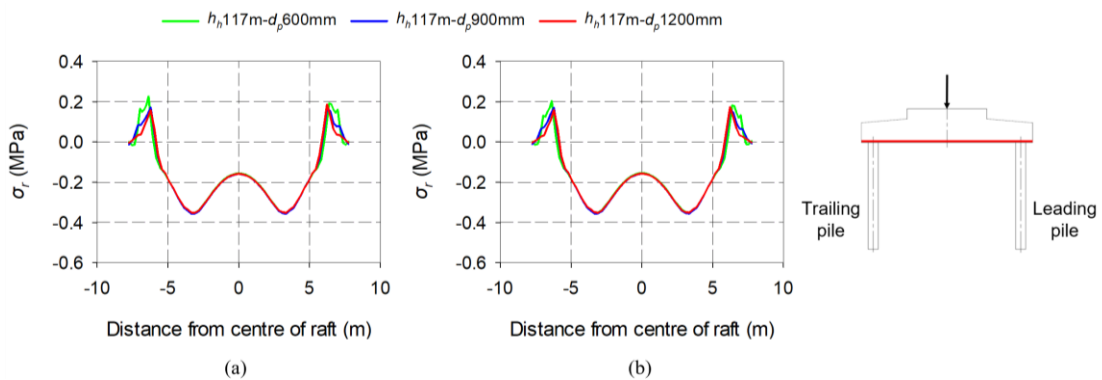
Figure 5-56: Raft stress at raft base (σ_r) – influence of d_p [*V*]: (a) L_p = 10 m; (b) L_p = 20 m

Extracting the maximum tensile stresses ($\sigma_{r,max}$) at 3.6 m from the centre of the raft for all the d_p-h_h combinations, **Figure 5-57(a)** and **(b)** were plotted for L_p = 10 m and 20 m, respectively. In both surface plots, $\sigma_{r,max}$ is influenced only by h_h, as observed previously, with higher h_h resulting in higher tensile stresses at the base of the raft. For all d_p-h_h combinations considered, tensile stresses were below the cracking limit stress.

Considering the percentage of the total vertical load carried by the piles (F_p/F_t), **Figure 5-58** indicates the surface plots showing the combined influence of h_h and d_p. As seen in **Figure 5-58(a)** for L_p = 10 m and **Figure 5-58(b)** for L_p = 20 m. Only d_p influenced this percentage, with piles having larger diameters carrying higher loads. As before, longer piles carried smaller loads than shorter piles, with L_p = 10 m carrying 85% of the vertically applied load when d_p = 1200 mm.
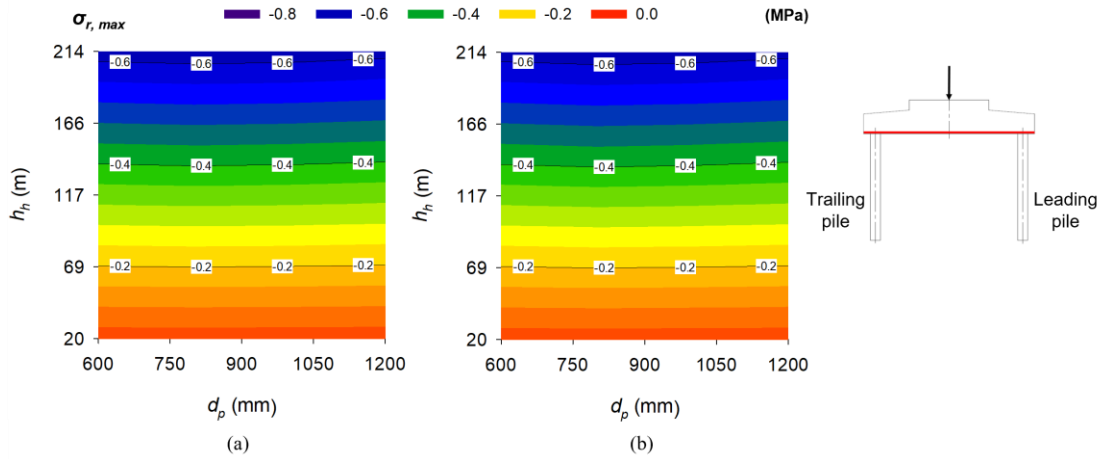
Figure 5-57: Maximum raft stress at raft base ($\sigma_{r,max}$) – h_h vs d_p [V]: (a) L_p = 10 m; (b) L_p = 20 m

For the leading and trailing piles in the *xz*-plane, axial forces and bending moments were determined from the strain data with depth, as seen in **Figure 5-59**, showing the effect of d_p by keeping h_h constant at 117 m. Again, investigating the effect of h_h by keeping d_p constant at 900 mm was not considered here, as it was already discussed in **Figure 5-12**, where d_p equalled 900 mm and E_s equalled 230 MPa, respectively. In **Figure 5-59**, **(a)** presents the bending moment (M_p) and axial force (F_p) diagrams with depth in the leading and trailing pile having lengths equal to 10 m, whereby **(b)** presents these diagrams for L_p = 20 m, respectively. Given the sign convention assumed in Section 5.3, the bending moment diagrams for the two piles were plotted on separate axes.

Figure 5-58: Total vertical load percentage carried by piles (F_p/F_t) – h_h vs d_p [V]: (a) L_p = 10 m; (b) L_p = 20 m

As seen in **Figure 5-59**, the bending moment in the leading and trailing piles are symmetrical under pure vertical loading, with both piles experiencing positive bending moments towards the top. At the same h_h, the influence of d_p is noticeable for both pile lengths, with the

bending moment in the leading and trailing piles being more significant for larger pile diameters. As expected, maximum M_p values occurred towards the top of the piles for the d_p values considered, with the value not changing significantly with L_p. M_p was also present at the foot of the piles, being more significant for shorter piles. Regarding the axial forces in the piles with depth, the leading and trailing piles also showed symmetry, with both piles experiencing compressive loads. Greater pile diameters resulted in higher axial loads, with shaft friction being more visible for the longer piles.
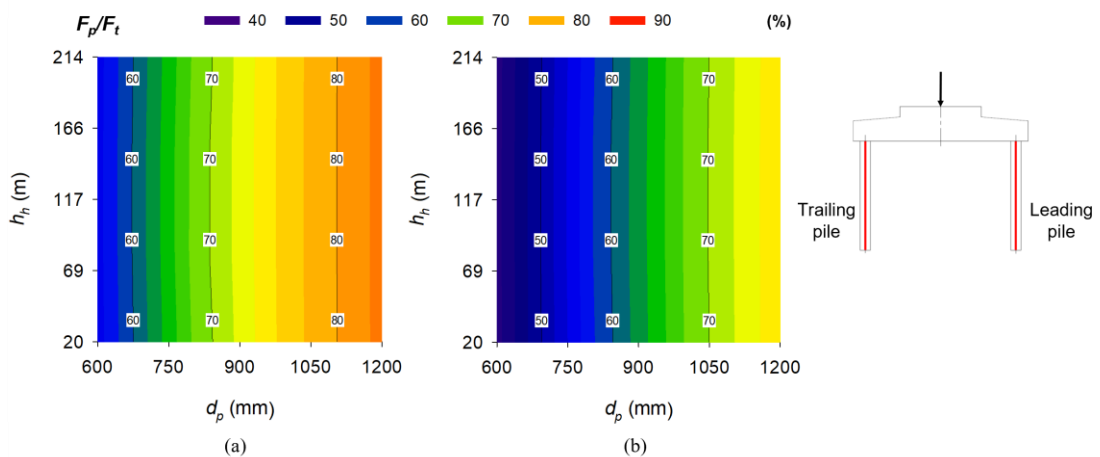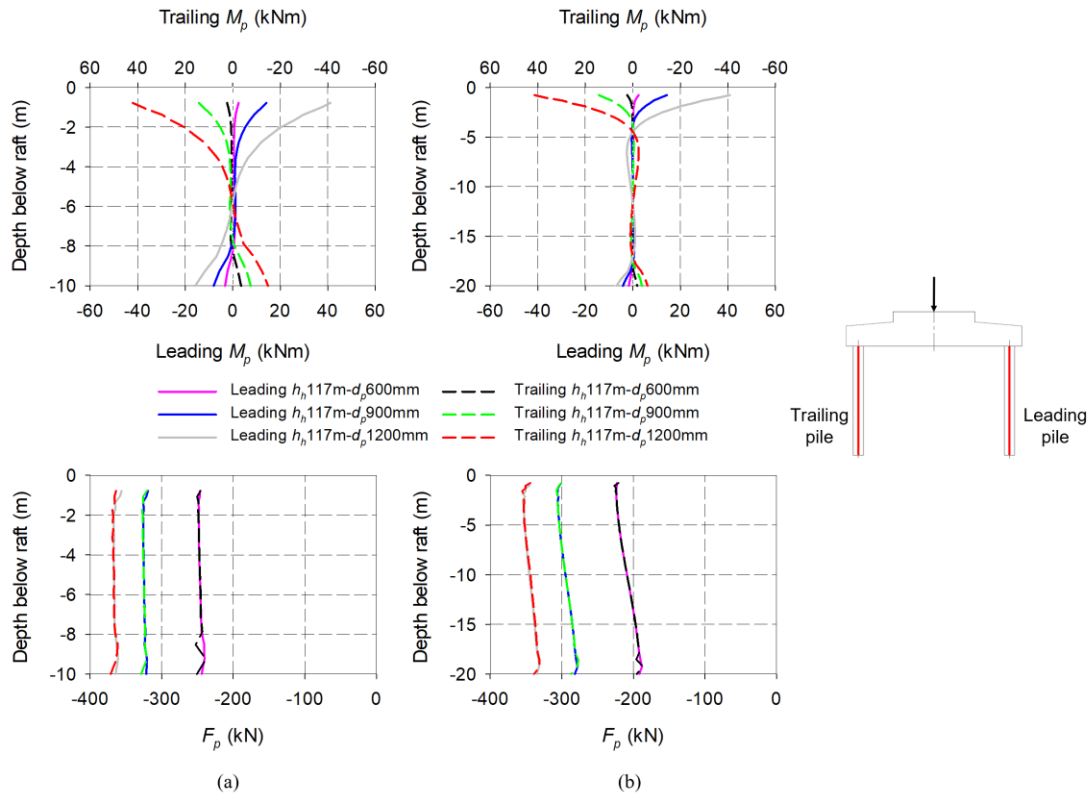

Figure 5-59: Leading and trailing pile bending moment (M_p) and axial force (F_p) – influence of d_p [V]: (a) $L_p = 10$ m; (b) $L_p = 20$ m

Extracting the maximum bending moments ($M_{p,max}$) and axial forces ($F_{p,max}$) in the leading and trailing piles at 0.5 m from the base of the raft for all the d_p-h_h combinations, **Figure 5-60(a)** and **(b)** were plotted for $L_p = 10$ m and 20 m, respectively. Given the symmetry of the piles under vertical loading, both the leading and trailing piles yielded the same results and were, thus, not plotted individually. $M_{p,max}$ was the most significant if h_h and d_p were high, owing to a greater combined connection stiffness at the pile-raft interface. As seen in **Figure 5-60**, $F_{p,max}$ is also affected by both h_h and d_p, with higher h_h and d_p resulting in larger axial compressive loads under pure vertical loading. Shorter piles, again, carried higher loads.
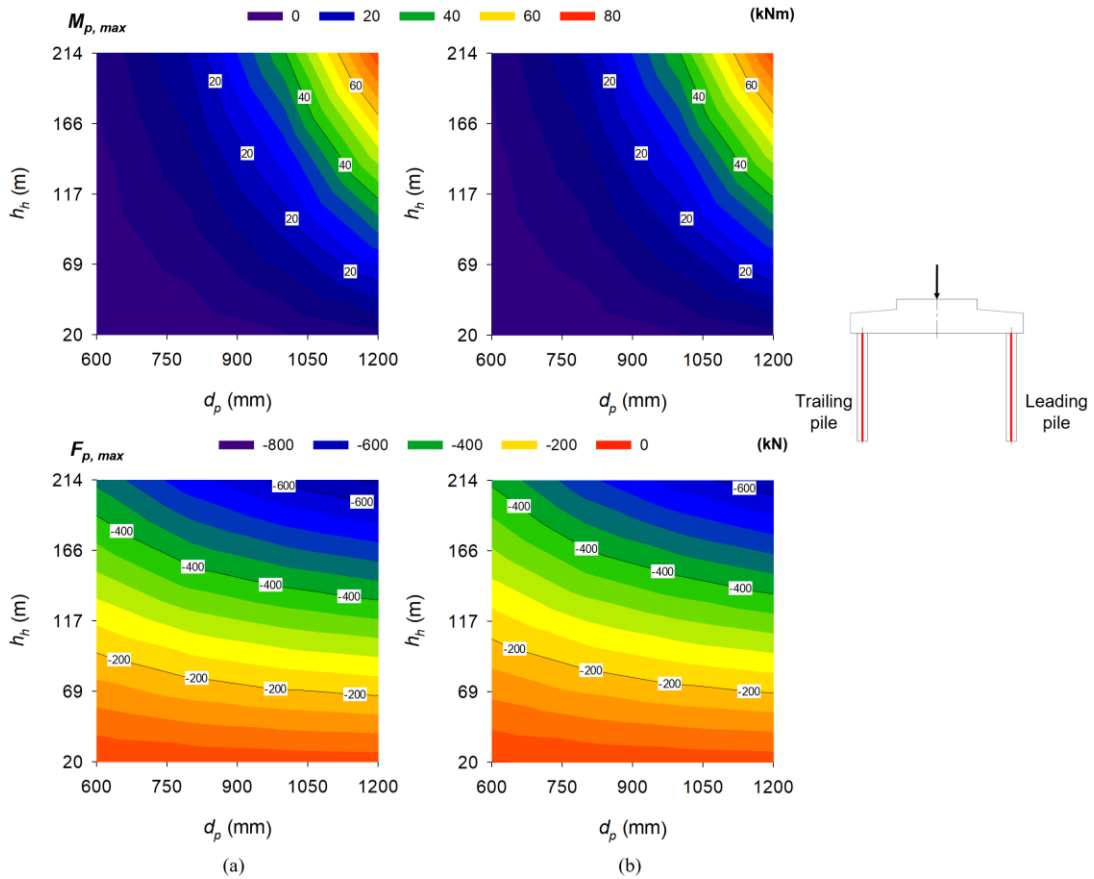
Figure 5-60: Leading and trailing pile maximum bending moment ($M_{p,max}$) and axial force ($F_{p,max}$) – h_h vs d_p [V]: (a) L_p = 10 m; (b) L_p = 20 m

5.7.2 Vertical load, horizontal load and overturning moment, *V-H-M*

The combined effect of the vertical load, horizontal load, and overturning moment was investigated with varying pile diameters for the second load case. **Figure 5-61(a)** and **(b)** present the surface plots showing the influence of h_h and d_p on the rotation of the raft pedestal (θ_r) for L_p = 10 m and 20 m, respectively. For both pile lengths, as h_h increased, θ_r also increased due to the magnitude of the applied overturning moment increasing. Additionally, as d_p decreased, θ_r also increased due to pile slenderness and, thus, the relative stiffness between the piles, raft and soil.

The horizontal displacement of the raft (v_{rh}) for the different d_p-h_h combinations is presented in **Figure 5-62(a)** and **(b)** for pile lengths of 10 m and 20 m, respectively. v_{rh} is affected by both d_p and h_h, as seen in **Figure 5-62**, with higher h_h, hence higher horizontal loads and overturning moments resulting in larger horizontal displacements. Larger pile diameters resulted in lower displacements, with less slender piles also having smaller displacements.
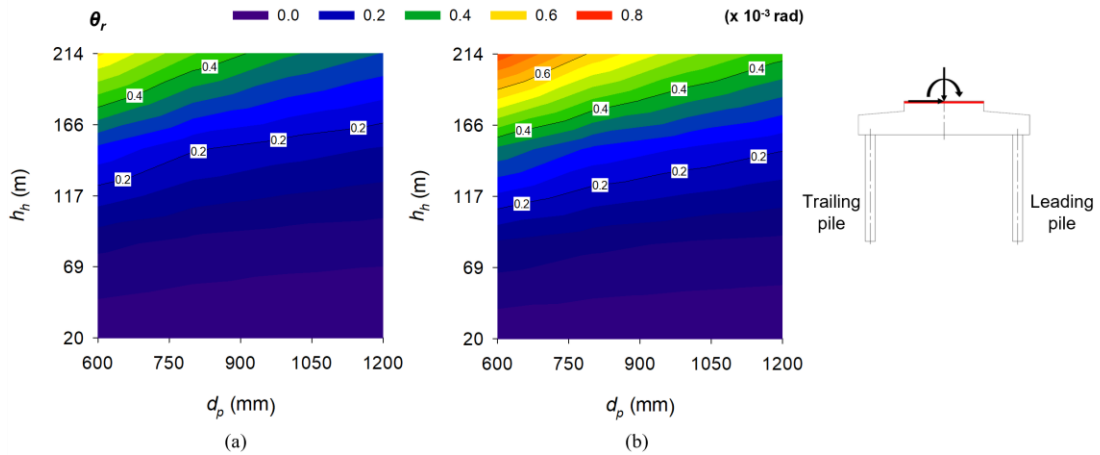
Figure 5-61: Raft pedestal rotation (θ_r) – h_h vs d_p [*V-H-M*]: (a) L_p = 10 m; (b) L_p = 20 m
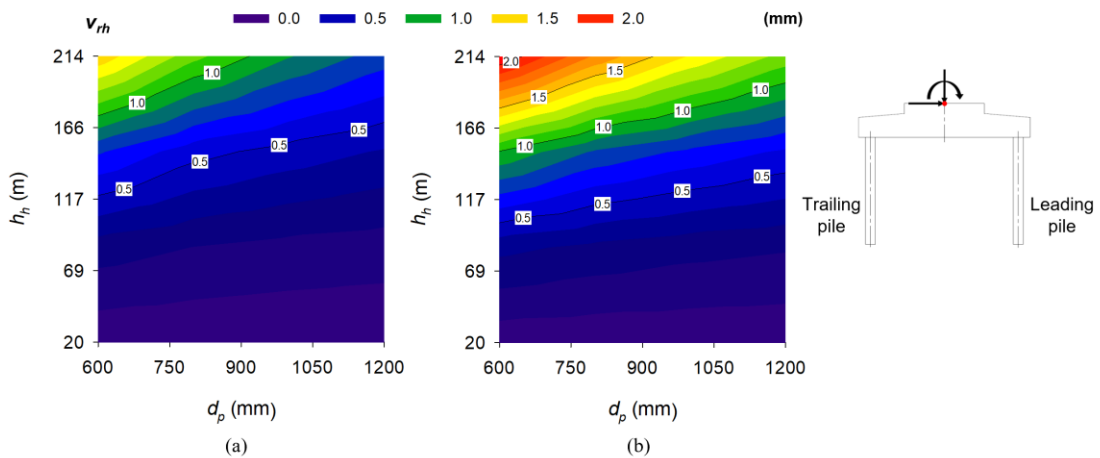
Figure 5-62: Raft top centre horizontal displacement (v_{rh}) – h_h vs d_p [*V-H-M*]: (a) L_p = 10 m; (b) L_p = 20 m

Figure 5-63 presents the horizontal stresses at the base of the raft (σ_r) in the central *xz*-plane against the distance from the centre of the raft, indicating the influence of d_p by keeping h_h constant at 117 m. For both sets of figures, **(a)** shows the response of the raft supported by 10 m long piles, whereas **(b)** shows the response if the piles are 20 m long. Considering the part of the raft spanning between the piles, as before with the addition of the horizontal load and overturning moment, both tensile and compressive stresses are observed, with the tensile stresses occurring on the leading end of the raft in the direction of the horizontal load and overturning moment. Again, the inflection point where these tensile stresses changed to compressive occurred in the centre of the raft. The stresses were also substantially higher than when only the vertical load was acting on the foundation. However, as with the vertical loading case, these values were not influenced by d_p or L_p. The maximum tensile and compressive stresses are about 3.6 m from the centre of the raft, with stresses not exceeding 2 MPa for h_h = 117 m. The maximum tensile stresses ($\sigma_{r,max}$) from the base of the raft for all the d_p-h_h combinations were extracted and plotted.
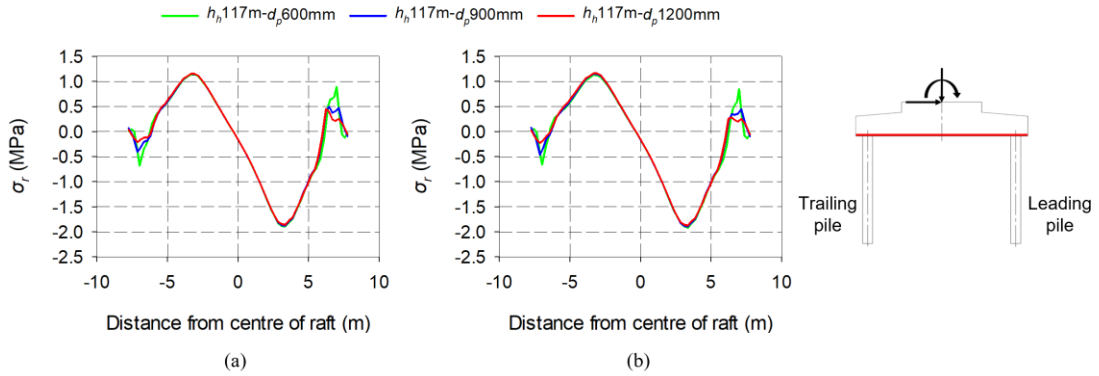
Figure 5-63: Raft stress at raft base (σ_r) – influence of d_p [*V-H-M*]: (a) L_p = 10 m; (b) L_p = 20 m

Figure 5-64(a) and **(b)** indicate the surface plots showing the effect of d_p and h_h on $\sigma_{r,max}$ for L_p = 10 m and 20 m, respectively. In both figures, $\sigma_{r,max}$ is only influenced by h_h, with increasing h_h resulting in an increasing $\sigma_{r,max}$. Given the foundation's size and the soil's properties, any h_h larger than 117 m could result in the concrete in the raft cracking under the combined vertical load, horizontal load and overturning moment.
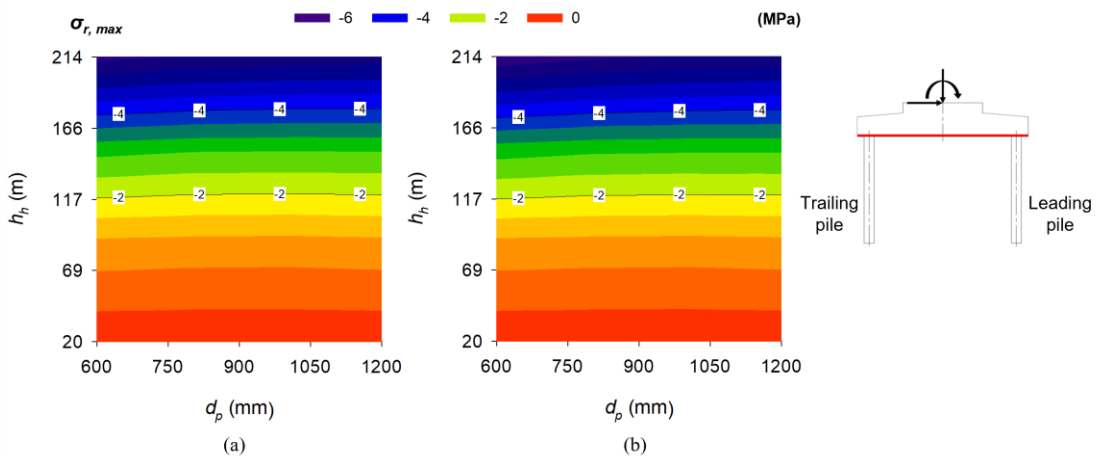
Figure 5-64: Maximum raft stress at raft base ($\sigma_{r,max}$) – h_h vs d_p [*V-H-M*]: (a) L_p = 10 m; (b) L_p = 20 m

Figure 5-65 indicates surface plots showing the influence of h_h and d_p on the percentage of the total vertical load carried by the piles (F_p/F_t) under the *V-H-M* load combination. **Figure 5-65(a)** for L_p = 10 m and **Figure 5-65(b)** for L_p = 20 m show a slightly different response than when only the vertical load acted on the foundation. F_p/F_t is now influenced by both h_h and d_p when h_h was greater than 69 m. Above these h_h, piles carried less vertical loads, with this percentage being smaller if the piles were longer.

For the leading and trailing piles in the *xz*-plane, axial forces and bending moments were determined from the strain data with depth, as seen in **Figure 5-66**, showing the effect of d_p by keeping h_h constant at 117 m. In **Figure 5-66**, **(a)** presents the bending moment (M_p) and

5-50

axial force (F_p) diagrams with depth in the leading and trailing pile having lengths equal to 10 m, while **(b)** presents these diagrams for $L_p = 20$ m, respectively.
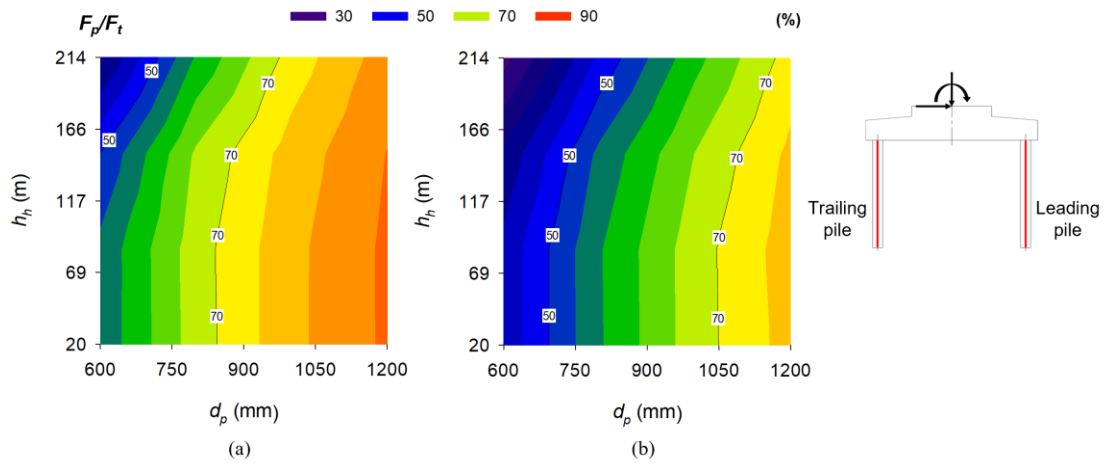
Figure 5-65: Total vertical load percentage carried by piles (F_p/F_t) – h_h vs d_p [*V-H-M*]: (a) $L_p = 10$ m; (b) $L_p = 20$ m
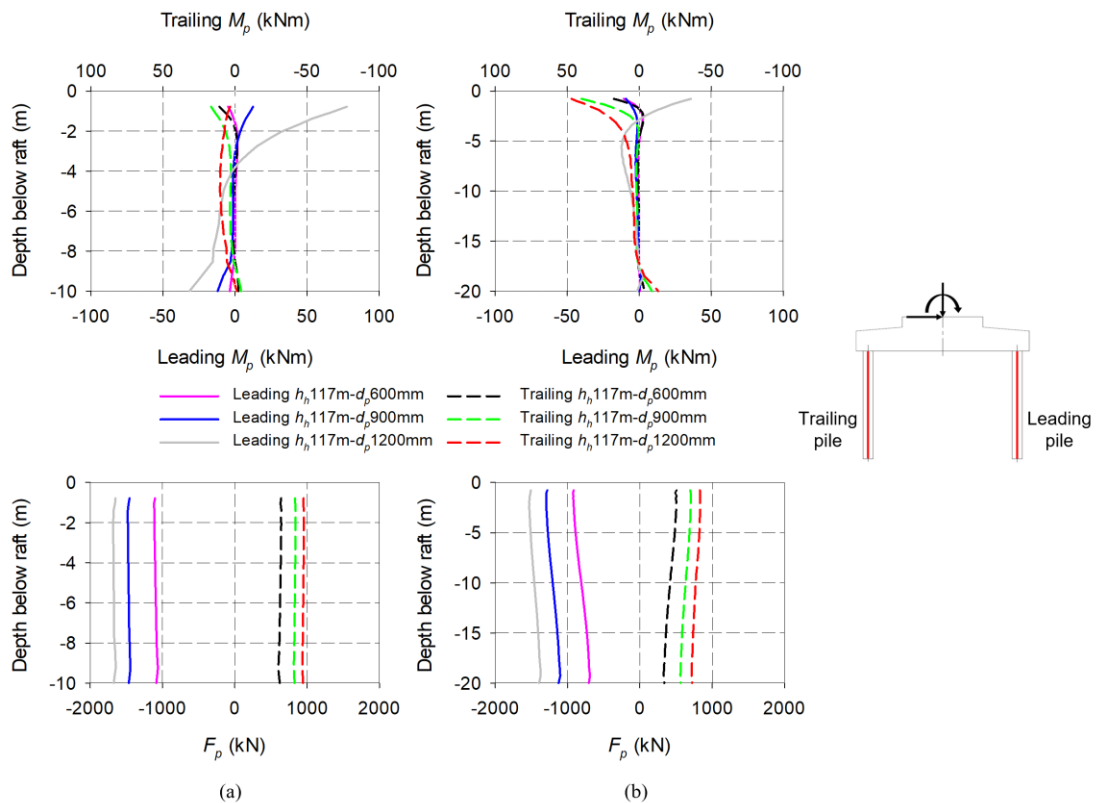
Figure 5-66: Leading and trailing pile bending moment (M_p) and axial force (F_p) – influence of d_p [*V-H-M*]: (a) $L_p = 10$ m; (b) $L_p = 20$ m

Given the sign convention assumed in Section 5.3, the bending moment diagrams for the two piles were plotted on separate axes. As seen in **Figure 5-66(a)** and **(b)**, the magnitude and direction of M_p in the leading and trailing piles are affected by d_p and the relative stiffness

5-51

between the pile, raft and supporting soil. When the pile diameter was large, the positive bending moment in the leading pile under pure vertical loading became substantially more positive with the addition of the horizontal load and overturning moment. The effect was more significant when L_p = 10 m. M_p remained relatively constant for d_p values less than 900 mm in the leading pile, with a slight negative bending moment observed when d_p = 600 mm. The positive bending moment in the trailing pile became more positive when d_p was increased when L_p = 20 m, with M_p being unaffected for L_p = 10 m. Regarding the axial forces in the piles with depth, the leading and trailing piles showed push-pull responses under loading. As d_p decreased, the compressive and tensile forces in the leading and trailing piles decreased.

Extracting the maximum bending moments ($M_{p,max}$) and axial forces ($F_{p,max}$) in the leading and trailing piles at 0.5 m from the base of the raft for all the R_r-h_h combinations, **Figure 5-67** and **Figure 5-68** were plotted. Due to the asymmetrical response, the leading and trailing piles were plotted separately for this load configuration. In both figures, **(a)** and **(b)** represent the response when L_p = 10 m and L_p = 20 m, respectively.
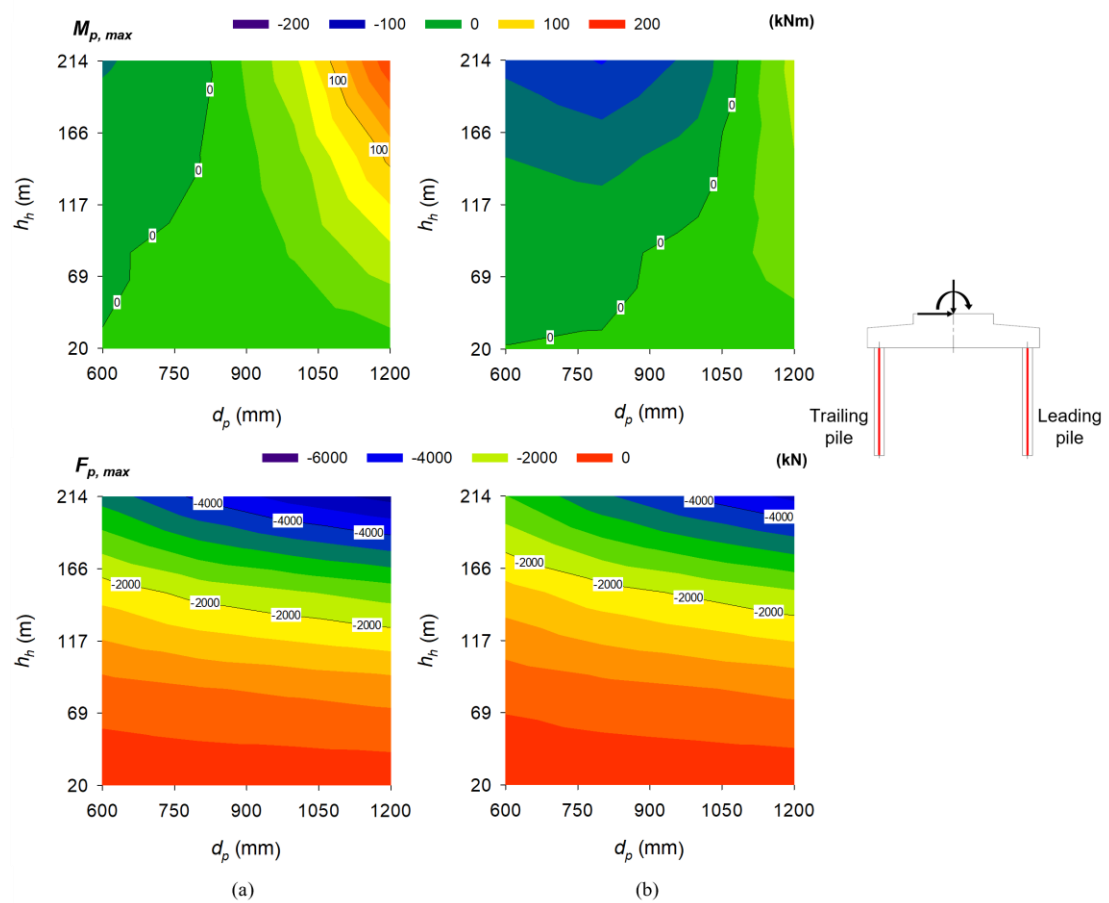
Figure 5-67: Leading pile maximum bending moment ($M_{p,max}$) and axial force ($F_{p,max}$) – h_h vs d_p [V-H-M]: (a) L_p = 10 m; (b) L_p = 20 m
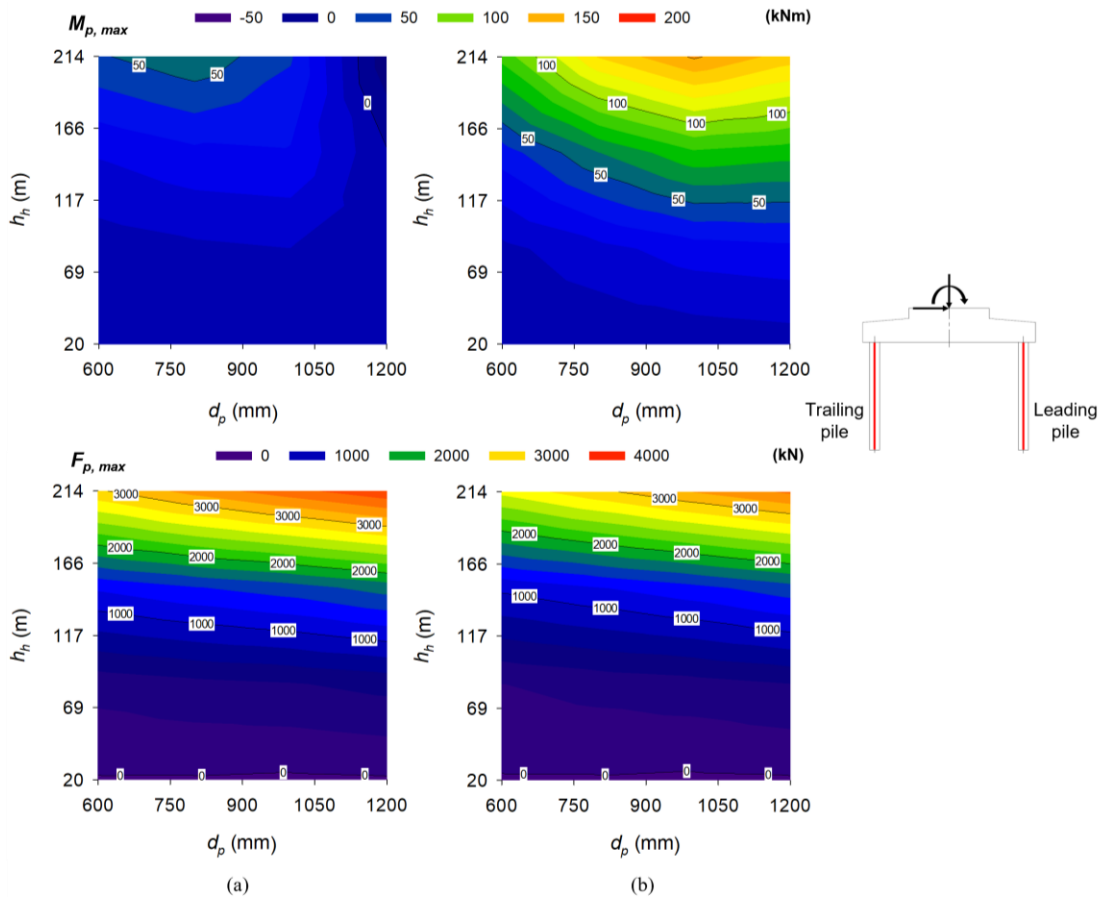
Figure 5-68: Trailing pile maximum bending moment ($M_{p,max}$) and axial force ($F_{p,max}$) – h_h vs d_p [V-H-M]: (a) $L_p = 10$ m; (b) $L_p = 20$ m

Looking at the leading pile first (see **Figure 5-67**), the magnitude of the maximum bending moments only increased for the shorter piles, becoming more positive with the addition of H and M. Additionally, these moments were more significant when h_h and d_p were higher. In addition, due to the slenderness of the longer piles and the relative stiffness between the raft and the piles, negative bending moments developed within these piles when d_p was low and h_h exceeded 117 m. For the pile diameters considered, bending moments did not exceed M_{crack}. Regarding the axial compressive force in the leading pile under this load combination, the compressive force was the highest when the leading piles were the shortest, h_h the greatest and d_p the largest. These forces were not significantly affected when h_h was smaller than 69 m. For the trailing pile (see **Figure 5-68**), the effect of V-H-M on M_p was more significant when L_p was longer. $M_{p,max}$ becomes more positive with adding H and M, compared to the positive bending moment already induced on the trailing pile under pure vertical loading. Higher h_h values resulted in more significant positive $M_{p,max}$ values when the pile diameters were high. For most d_p-h_h combinations considered, $M_{p,max}$ in the trailing pile reduced to zero when $L_p = 10$ m. Positive axial tensile forces were observed in the trailing pile, influenced by both h_h and d_p, with lower pile diameters resulting in lower tensile forces. For h_h exceeding

5-53

117 m, these axial forces exceeded the calculated axial cracking strength of the pile at 1272 kN for a 900 mm diameter pile and a concrete cracking stress of 2 MPa.

5.8   SUMMARY

A parametric study was conducted considering the effect of varying foundation sizes and soil properties on the response of piled-raft foundations under vertical loading and combined vertical loading, horizontal loading and overturning moments. Particular consideration was given to investigating the influence of the Young's modulus of the soil, the raft thickness and radius, pile diameter, and pile length, with pile length equivalent to the depth of the compressible soil layer. All models also considered the effect of hub height, which was ultimately linked to the magnitude of the applied loads and moments, investigating the effect of increased wind turbine sizes.

As evident from the literature and also observed in this chapter, the response of a piled-raft foundation is highly dependent on soil-structure interaction and the relative stiffness between the foundation and the soil. Under vertical loading, greater vertical deflections and differential settlements was observed when the size of wind turbines increased. Similarly, as the Young's modulus of the soil, the thickness of the raft and the diameter of the piles decreased, and the radius of the raft increased, the vertical deflections and differential settlements also increased, with all these parameters linking to slenderness of the individual foundation members and the relative stiffness between these members and the surrounding soil. In addition, pile length, or depth of the compressible soil layers, influenced vertical deflections, but not differential settlement, with longer pile lengths resulting in higher vertical deflections. The horizontal stresses at the base of the raft increased with increased load magnitudes, with 'sagging' tensile stresses observed between the piles, and substantial 'hogging' tensile stresses observed over the pile-raft interface. Larger stresses were observed for thinner rafts having larger radii and piles having smaller diameters, with the Young's modulus of the soil only affecting the stresses in the raft if the relative stiffness between the raft and the soil is low. Larger turbines resulted in greater stresses at the base of the raft exceeding the tensile stress of concrete, increasing the risk for cracking. Longer piles also showed a slight increase in the stresses in the raft, however only when the relative stiffness between the raft and piles were low.

A greater portion of the loads were carried by the piles when the Young's modulus of the soil was low, the radius of the raft small and the diameter of the piles large, with the raft thickness not seeming to have an effect. Shorter piles, or shallower compressible soil layers, also resulted in greater loads to be carried by the piles. In addition, bending moments in the piles were more significant for larger turbine sizes and when the raft thickness was low and the

diameter of the piles and radius of the raft larger. Again, this can be ascribed to the relative stiffness between the piles and the raft and the amount of rotation possible at the raft-pile interface, similar to the responses observed for portal frames in Chapter 2. The distribution of bending moments in the piles was also greater when the Young's modulus of the soil was low.

With the addition of the horizontal load and overturning moment, the rotation of the foundation was also considered given the limited rotation allowed for foundations supporting wind turbines. As expected, as turbine size increased, the rotation of the raft increased, with the rotation also being higher when the Young's modulus of the soil and pile diameter were low, the depth of the compressible layer (pile length) was large, and the raft thickness and radius were greater. Similar responses were observed considering horizontal displacement compared to that observed for the foundation rotation, with the only difference being larger raft radii resulting in less horizontal displacements due to the increase in the area of the raft in contact with the soil. Greater 'sagging' and 'hogging' horizontal stresses were observed in the raft than under pure vertical loading, with the risk of raft cracking increasing as turbine size increases, depending on the rigidity of the foundation and the properties of the soil. Longer piles resulted in slightly greater stresses, which is also linked to the relative stiffness between the raft, piles and the surrounding soil. With the presence of the horizontal load and overturning moment on the foundation, bending moments in the supporting piles increased, with the magnitude and direction of these moments being dependent on the relative stiffness between the raft, piles and soil. Similar to the results presented in Chapter 3 on the full-scale instrumented wind turbine foundation, the leading and trailing piles experienced the push-pull effect, with the leading piles experiencing an increase in compressive forces under the additional horizontal load and overturning moment and the trailing piles reduced compressive forces or even tensile forces, depending on the magnitude of the applied load and the size of the foundation. The push-pull effect was greater when the Young's modulus of the soil was lower, the piles were shorter, raft radius was smaller and the pile diameter larger.

Most notably, the pile-raft interface stiffness showed interesting trends, with majority of the results observed related to and dependent on this interaction in particular, especially with the addition of the horizontal load and overturning moment, strengthening the arguments made in Chapter 2 regarding portal frames and joint stiffness. This, and the relative stiffness concept, however, needs further exploration for wind turbine foundations supporting ever-growing wind turbine models. Thus, Chapter 6 focuses on larger turbine models, combining all the parameters mentioned in this chapter, providing some guidelines for meeting foundation rotational stiffnesses and deflections and limiting axial tension forces in piles, as these are some of the biggest concerns regarding the design of piled-raft foundations for wind turbines.

6 RELATIVE STIFFNESS AND PILE-RAFT-SOIL INTERACTION

6.1 INTRODUCTION

In light of the parametric study results in Chapter 5, it is evident that the response of a piled-raft foundation depends on not only the relative stiffness between the foundation and soil, but also the relative stiffness between the different foundation components. Previously, the focus was on investigating individual foundation and soil parameters, including the Young's modulus of the soil, the raft radius and thickness, and pile diameter and length, and how they affected several foundation responses and outcomes. However, in this chapter, a more general study was conducted, combining these parameters and investigating relative stiffness, pile-raft-soil interaction and foundation rigidity. The first part of the chapter considers pile-raft-soil interaction, particularly relating to the existing soil-structure interaction principles defined by Clancy & Randolph (1993). These principles are typically used for assessing piled-raft foundations under vertical loading. However, in this case, consideration was also given to the scenario when the dominant loads are horizontal forces and overturning moments. Although the foundation response is influenced by several factors simultaneously, including raft-soil, pile-soil, raft-pile and pile-pile interaction, conclusions could only be made from a select few combinations as only a limited number of numerical analyses were conducted. The last portion of the chapter deals with the relative stiffness between the piles and raft and how this interaction can be used for designing future piled-raft foundations for onshore wind turbines increasing in size. This section, in particular, focused on foundation size and the elements critical to design, including vertical deflection, differential settlement, horizontal displacement and rotational foundation stiffness under loading. Given the strict limitations set on foundation design for these dynamically sensitive structures, consideration was also given to raft cracking and the potential of axial tensile forces developing in the trailing piles under the dominant horizontal load and overturning moment, which became significant for larger wind turbine models.

For all future explanations, **Figure 6-1** illustrates how the spacing (s) between the piles were calculated. The angle (β) between neighbouring piles was determined by dividing 2π rad by the number of piles (n), with s then calculated from the isosceles triangle (indicated in red in **Figure 6-1**) and the Sine Rule. The long edge of the triangle was taken as the raft radius (R_r) minus the distance to the pile centre from the raft edge (= 1.075 m), which remained constant in all analyses. Thus, given that only a single row of piles along the perimeter of the rafts was considered, with the edge distance remaining unchanged and the number of piles being kept constant at 10, the spacing between the piles increased as the radius of the raft increased.
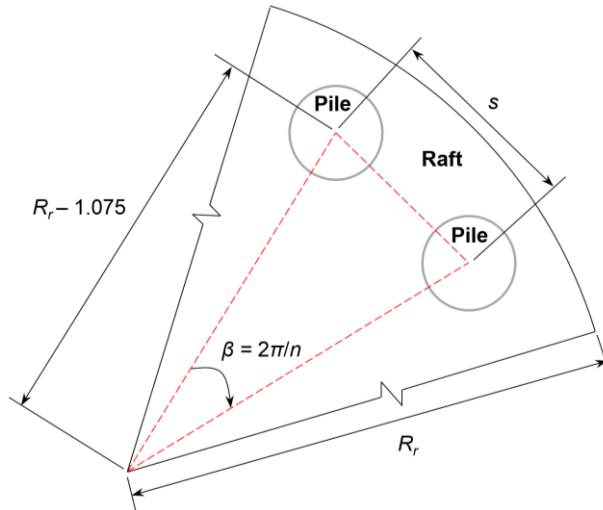
Figure 6-1: Pile-raft foundation segment – pile spacing calculation

6.2 PILE-RAFT-SOIL INTERACTION FOR VERTICAL LOADING

Figure 6-2 indicates the effect of raft-soil stiffness (K_{rs}) and pile-soil stiffness (K_{ps}) on the vertical deflection (v_{rv}) of the raft under vertical loading. **Figure 6-2(a)** and **(b)** consider these effects for $L_p/d_p = 11.11$ and $L_p/d_p = 22.22$, respectively.
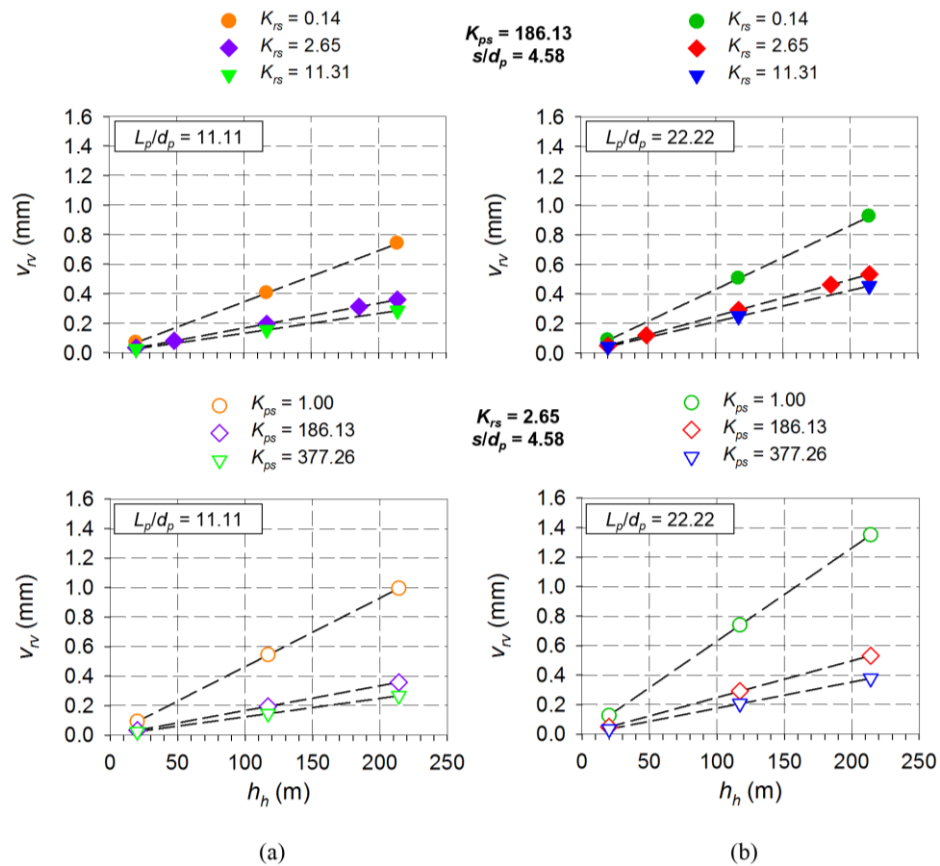
Figure 6-2: Raft vertical deflection for K_{rs} and K_{ps}: (a) $L_p/d_p = 11.11$; (b) $L_p/d_p = 22.22$

For the top two graphs (K_{ps} = 186.13 and s/d_p = 4.58), the influence of K_{rs} is evident and similar to the responses observed in the literature. Lower K_{rs} values resulted in higher vertical deflection, which increased when L_p/d_p was higher. As mentioned in the previous chapter, this increase was linked to the buckling stiffness of columns, given that the piles are modelled as resting on bedrock, effectively behaving as columns. As expected, more considerable deflections were also visible as h_h increased, with a significant increase observed when h_h exceeded 117 m. The effect of K_{rs} on vertical deflection appears to become smaller as K_{rs} increases, especially for K_{rs} values greater than 2.65, where response resembles more rigid behaviour. For the bottom two graphs (K_{rs} = 2.65 and s/d_p = 4.58), the effect of K_{ps} on the vertical deflection of the raft under vertical loading can also be seen. For both the pile slenderness ratios considered, the vertical deflection decreased as K_{ps} increased and seemed to converge past a value of 186.13. As before, vertical deflections also increased as h_h and L_p/d_p increased. Similarly, **Figure 6-3(a)** and **(b)** consider the differential settlement (v_{rd}) of the raft under vertical loading for L_p/d_p = 11.11 and L_p/d_p = 22.22, respectively, while keeping K_{ps} and s/d_p constant at 186.13 and 4.58.
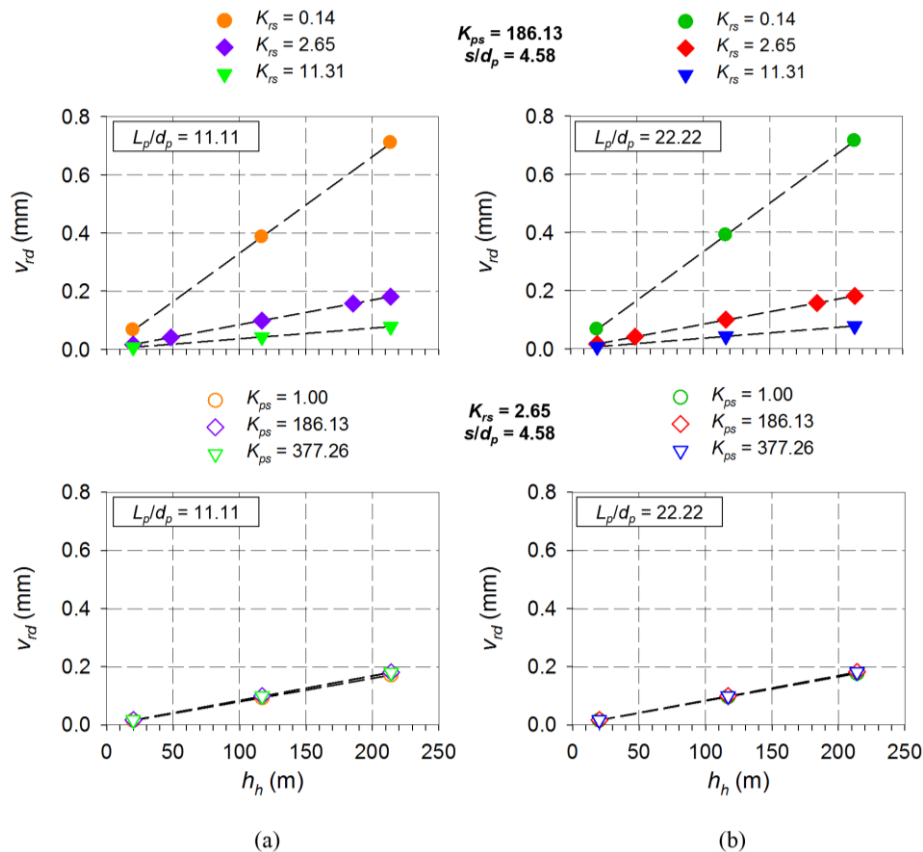

Figure 6-3: Raft differential settlement for K_{rs} and K_{ps}: (a) L_p/d_p = 11.11; (b) L_p/d_p = 22.22

As K_{rs} increased, the differential settlement decreased, with differential settlement increasing as h_h increased. Again, the effect of K_{rs} on the differential settlement seems to become smaller

as K_{rs} increases, especially for foundations with K_{rs} values greater than 2.65. As before, L_p/d_p did not influence differential settlement. For K_{rs} = 2.65 and s/d_p = 4.58, neither K_{ps} nor L_p/d_p influenced differential settlement, with the only factor being h_h.

6.3 PILE-RAFT-SOIL INTERACTION FOR LARGE HORIZONTAL LOADS AND OVERTURNING MOMENTS

Under the applied vertical load, horizontal load and overturning moment, the horizontal displacement (v_{rh}) of the raft was plotted considering the effect of K_{rs} and K_{ps}. **Figure 6-4(a)** and **(b)** indicate the horizontal displacement for L_p/d_p = 11.11 and L_p/d_p = 22.22, respectively. From the top two graphs, the horizontal displacement is unaffected by K_{rs}, with an increase in L_p/d_p resulting in a slight increase in horizontal displacement for the K_{ps} and s/d_p values investigated. Correspondingly, from the bottom two graphs, keeping K_{rs} constant and varying K_{ps}, horizontal displacement decreases as K_{ps} increases, with v_{rh} increasing slightly as L_p/d_p is doubled. For K_{ps} values greater than 186.13, no significant decrease was observed, with horizontal displacements being significant for h_h exceeding 117 m when K_{ps} was small. In both instances, horizontal displacement increased as h_h increased due to the larger applied loads.
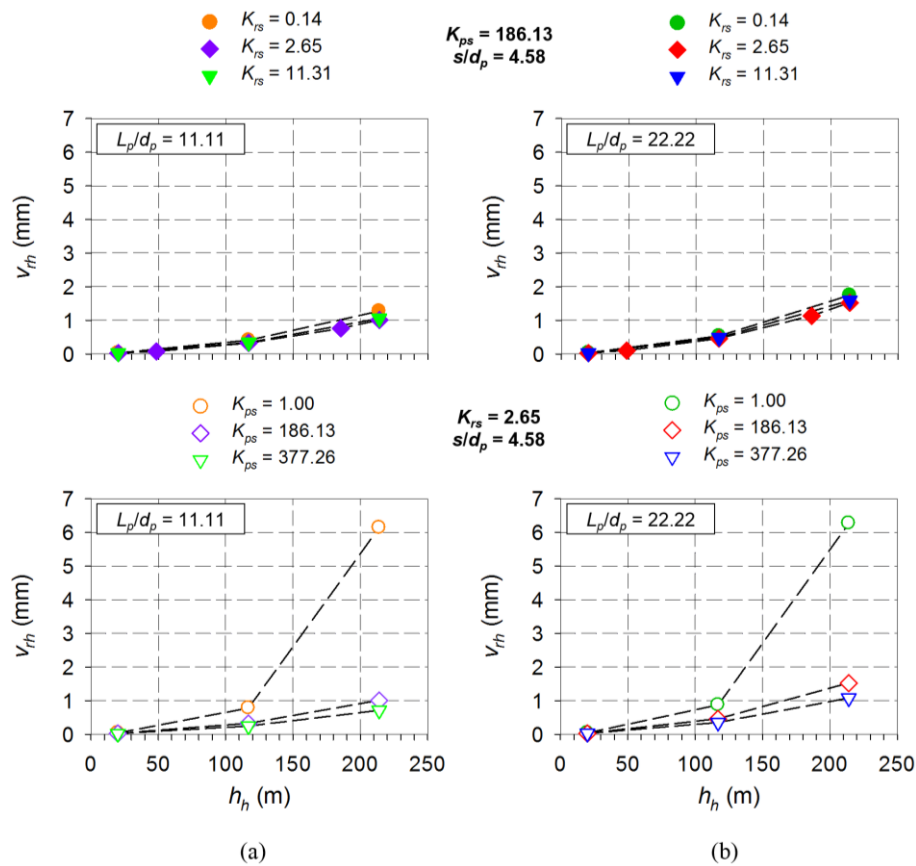

Figure 6-4: Raft horizontal displacement for K_{rs} and K_{ps}: (a) L_p/d_p = 11.11; (b) L_p/d_p = 22.22

Figure 6-5(a) and **(b)** present the rotational (rocking) foundation stiffness (K_θ) calculated from the different foundation models considered for $L_p/d_p = 11.11$ and $L_p/d_p = 22.22$, respectively, investigating the effect of K_{rs} and K_{ps}. Similar to Wojtowitz & Vorster (2014), this value was calculated by dividing the applied overturning moment by the resulting rotation of the foundation. At a constant K_{ps} and pile spacing, increasing K_{rs} increased the rotational stiffness of the foundation. Shorter piles also resulted in higher rotational stiffnesses, except when $h_h = 20$ m. Given that linear elastic material models were considered, the rotational stiffness of the foundation seems to remain unaffected by h_h. Similarly, at a constant K_{rs} and s/d_p, as K_{ps} increased, the rotational stiffness of the foundation increased, with the effect being more significant when piles were less slender. Again, the rotational stiffness seems unaffected by h_h for $h_h < 117$ m. A sharp decline in K_θ was observed when $K_{ps} = 1.00$ and $h_h = 214$ m, indicating that low pile-soil stiffness ratios should, especially, be avoided for larger turbines exceeding a hub height of 117 m.
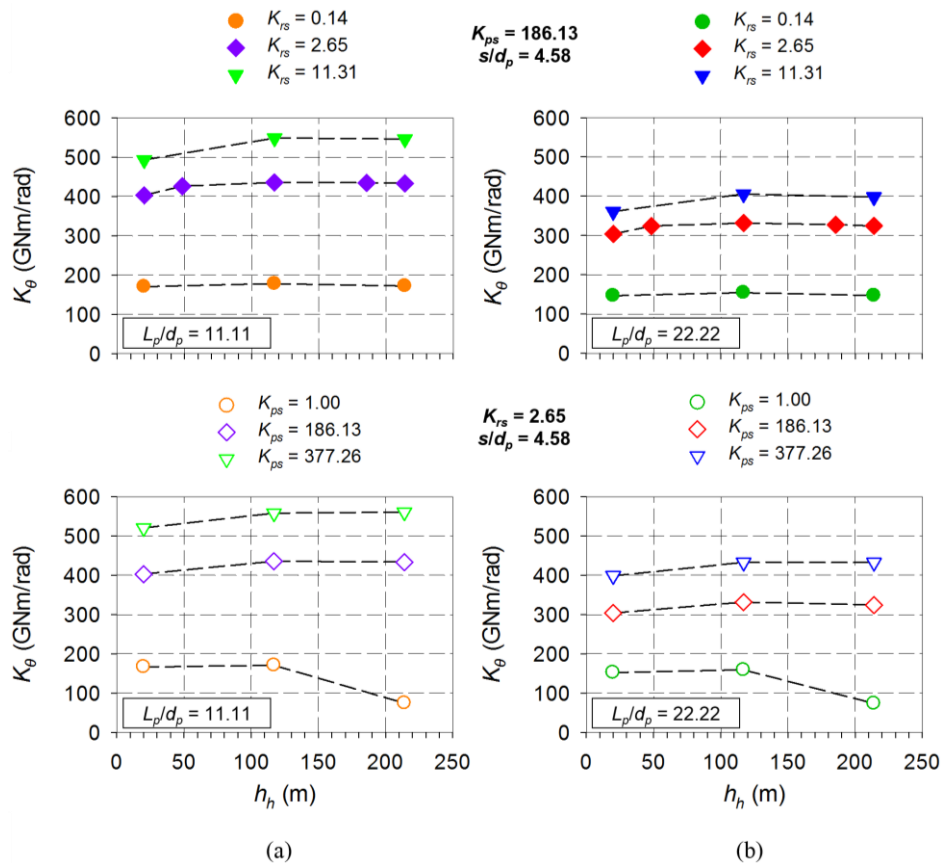
Figure 6-5: Foundation rotational stiffness for K_{rs} and K_{ps}: (a) $L_p/d_p = 11.11$; (b) $L_p/d_p = 22.22$

Lastly, the axial tensile forces in the trailing pile under the applied vertical load, horizontal load and overturning moment are presented in **Figure 6-6(a)** and **(b)** for $L_p/d_p = 11.11$ and $L_p/d_p = 22.22$, respectively. Investigating the effect of K_{rs} on the axial tensile forces in the trailing pile, it is evident that, although small, as K_{rs} is increased, the axial force decreases. A

slight increase in the tensile force was also observed as the pile slenderness decreased. As expected, the corresponding axial tensile forces also increased with h_h increasing. However, this relationship is exponential, having significantly greater effects on the axial tensile forces in the trailing piles for taller turbine models. The effect of varying K_{ps} was more profound. As K_{ps} increased, the tensile force in the trailing pile increased, with the effect becoming smaller as K_{ps} increases. Nearly no tensile forces were observed when $K_{ps} = 1.00$, as the foundation responds as a raft given that $E_p = E_s$. Shorter piles also resulted in slightly higher forces in the tailing piles.
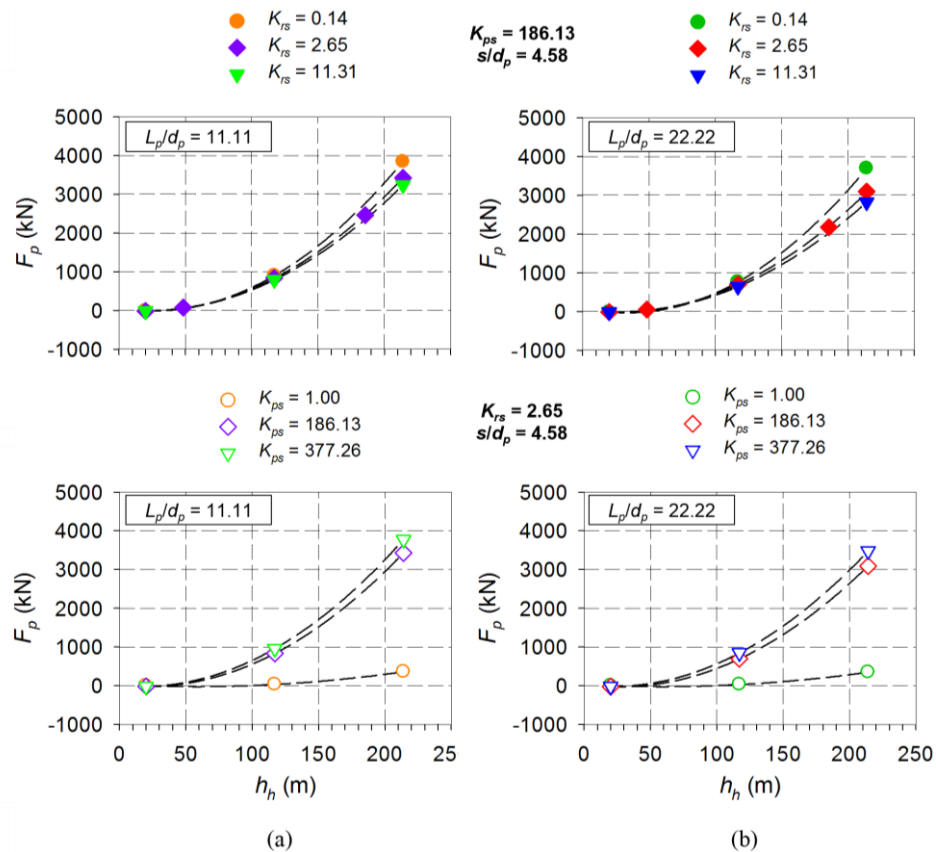
Figure 6-6: Trailing pile axial force for K_{rs} and K_{ps}: (a) $L_p/d_p = 11.11$; (b) $L_p/d_p = 22.22$

6.4 RELATIVE PILE-RAFT STIFFNESS – INCREASED WIND TURBINE SIZES

From the combination of trends observed, what does this, however, mean for the future design of onshore wind turbine foundations comprising piled rafts? Although increasing the thickness of the raft would provide benefits towards both differential settlement and rotational stiffness, the effect of increasing turbine height and size on foundation behaviour is still unknown. To accommodate these significant overturning moments, an increased raft radius would be required to limit tensile stresses in the trailing piles, yet increasing the radius without taking the thickness of the raft or the spacing between the piles into consideration

might lead to a decrease in the raft rigidity, resulting in increased settlement that is not desirable. The following sections attempt to address these types of questions, proposing a more balanced design approach when considering piled rafts for supporting onshore wind turbines. Several graphs are provided that can be used to make a preliminary prediction on the size of the raft and piles that would be required for a given turbine size.

Figure 6-7 presents the horizontal tensile stresses in the base of the raft (σ_r) against h_h for different raft thicknesses under the combined vertical load, horizontal load and overturning moment. **Figure 6-7(a)** and **(b)** indicate these relationships for $L_p/d_p = 11.11$ and $L_p/d_p = 22.22$, respectively, for a constant raft radius, pile diameter, pile spacing and Young's modulus of the soil. As expected, rafts having greater thicknesses resulted in lower tensile stresses, with these tensile stresses unaffected by the L_p/d_p ratio. These stresses seem to converge for raft thicknesses greater than 1.85 m, with a negligible difference observed between the tensile stresses in the base of the raft when $t_r = 1.85$ m and 3 m for $h_h < 75$ m. To assess the magnitude of these stresses, the tensile cracking limit of concrete of approximately 2 MPa was also included in the figures. Thus, given that the current focus is on turbines exceeding hub heights of 130 m, a raft thickness greater than 1.85 m would be required to limit raft cracking for the given pile spacing, pile diameter, raft radius and Young's modulus of the soil. The relationship between h_h and σ_r is also exponential, thus resulting in significantly higher stresses for a slight change in hub height.
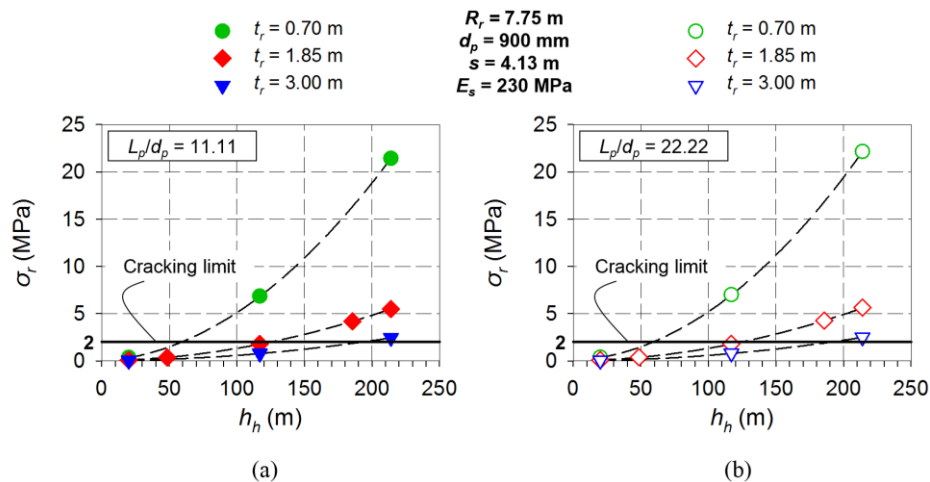
Figure 6-7: Tensile σ_r versus h_h for different t_r: (a) $L_p/d_p = 11.11$; (b) $L_p/d_p = 22.22$

To assess the effect of raft radius (R_r) and pile spacing (s) on the stresses in the base of the raft under the combined loading, **Figure 6-8(a)** and **(b)** indicate these results for $L_p/d_p = 11.11$ and $L_p/d_p = 22.22$. As mentioned before, given that the pile spacing increased as the radius of the raft increased (the number of piles remained the same), the results presented in **Figure 6-8** indicate the combined effect by considering the equivalent pile-raft area (sR_r) carried by each

pile. Typically, piles are located towards the edge of a piled raft when supporting wind turbines to accommodate the sizeable overturning moment. Thus, the assumption of plotting responses using this equivalent pile-raft area was deemed representative. As seen in **Figure 6-8**, as sR_r increased, the tensile stresses in the base of the raft increased but tended to converge beyond a value of 55.16 m^2 for the raft thickness, pile diameter and Young's modulus of the soil considered. As with raft thickness, σ_r was unaffected by L_p/d_p ratios. Thus, limiting the potential cracking of the concrete in the raft for large wind turbine models, sR_r needs to be reduced, which can either be achieved by decreasing pile spacing or raft radius. However, as will become apparent later, reducing pile spacing would potentially be the more viable option, as reducing the radius of the raft will result in more significant tensile stresses in the trailing piles.
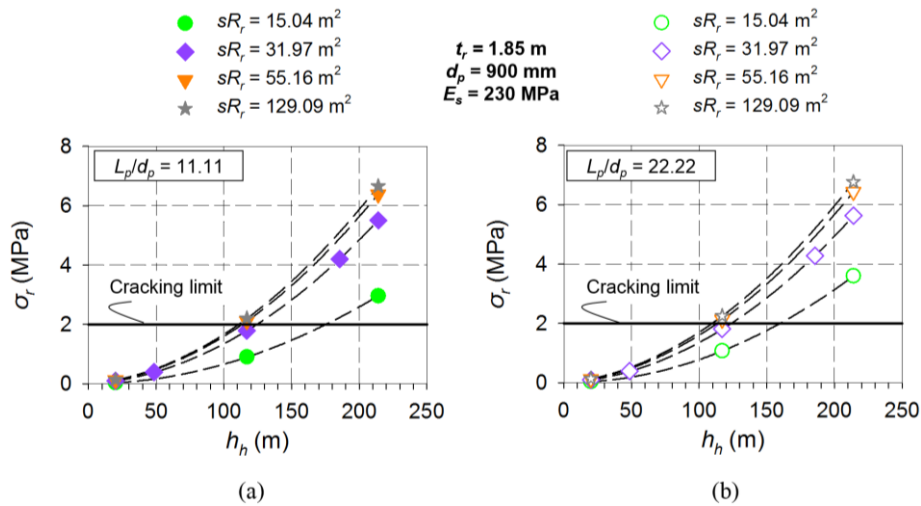
Figure 6-8: Tensile σ_r versus h_h for different sR_r: (a) $L_p/d_p = 11.11$; (b) $L_p/d_p = 22.22$

To investigate the influence of the Young's modulus of the soil, **Figure 6-9(a)** and **(b)** illustrate the effect of E_s for $L_p/d_p = 11.11$ and $L_p/d_p = 22.22$, for $t_r = 1.85$ m and $R_r = 7.75$ m. Regardless of h_h, E_s does not influence the horizontal stresses at the base of the raft, with L_p/d_p, as before, not affecting the stresses at the base of the raft. Increasing h_h will result in potential cracking in the base of the raft, increasing the risk of the turbine destabilising. However, limiting this risk can be achieved by increasing raft thickness or by either reducing the spacing of the piles or the radius of the raft.

Under vertical loading, **Figure 6-10(a)** and **(b)** shows the influence of t_r on the vertical deflection in the raft (v_{rv}) for $L_p/d_p = 11.11$ and $L_p/d_p = 22.22$. As before, greater hub heights and L_p/d_p ratios resulted in more considerable vertical deflections in the centre of the raft, however, this decreased as t_r increased.
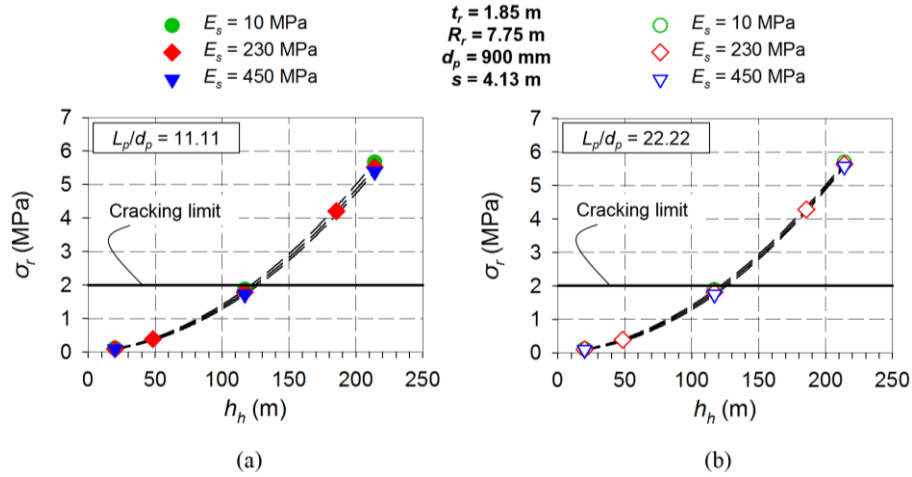
Figure 6-9: Tensile σ_r versus h_h for different E_s: (a) $L_p/d_p = 11.11$; (b) $L_p/d_p = 22.22$

For both L_p/d_p ratios, no significant reduction was observed for t_r greater than 2 m, where response resembles more rigid behaviour. Thus, as with the stresses in the base of the raft, foundations with raft thicknesses greater than 2 m react as if rigid for the diameter investigated. Soils having greater Young's moduli also resulted in less vertical deflection of the raft, with the effect being more significant when L_p/d_p was larger. The Young's modulus of the soil values considered in all analyses ranged between 10 MPa and 450 MPa, with its influence indicated as a range in **Figure 6-10** and in all subsequent figures for a hub height of 117 m. Thus, piles with larger diameters and shorter lengths will be less affected by the Young's modulus of the soil. Vertical deflection does not seem critical for the combinations considered, given that all deflections were well below the limit to achieve a minimum vertical stiffness (K_v) of 5000 MN/m (obtained from **Table 2-2**).

Figure 6-10: v_{rv} versus t_r for different h_h: (a) $L_p/d_p = 11.11$; (b) $L_p/d_p = 22.22$

Figure 6-11(a) and **(b)** present the effect of equivalent pile-raft area (sR_r) on the vertical deflection of the raft. As sR_r increased, the vertical deflection of the raft increased, with the

6-9

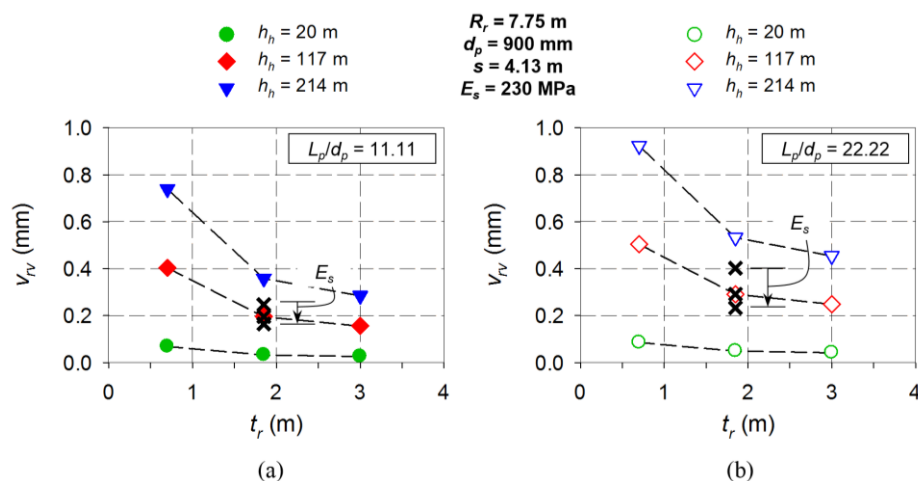effect amplified with increasing hub heights. Greater L_p/d_p ratios resulted in more significant deflections, with the effect of E_s being more noticeable for longer piles or smaller pile diameters. Thus, in light of increasing wind turbine sizes, reducing the radius of the raft or pile spacing will result in reduced vertical deflection. Increasing the diameter of the pile would have the same effect. However, considering the magnitudes of the deflections observed for the combinations considered, vertical deflection does not seem critical.
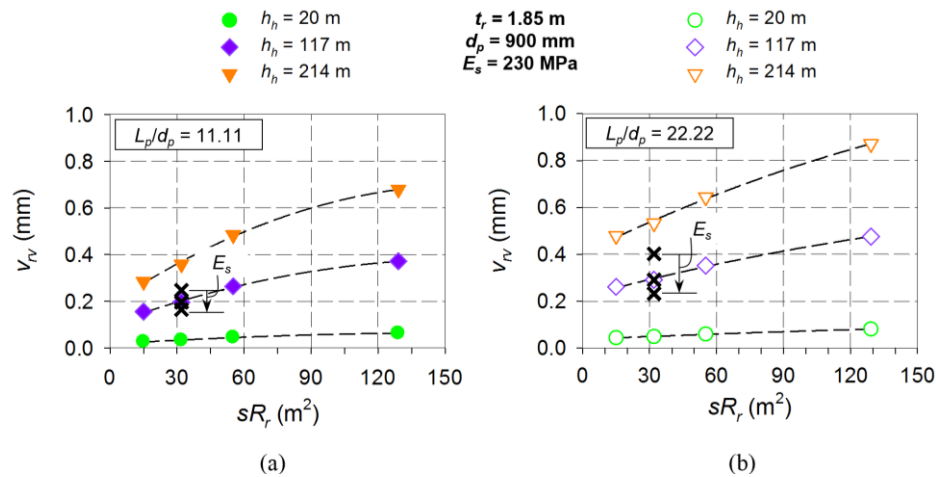
Figure 6-11: v_{rv} versus sR_r for different h_h: (a) $L_p/d_p = 11.11$; (b) $L_p/d_p = 22.22$

Similarly, the horizontal displacement of the raft was plotted for different t_r and h_h values. **Figure 6-12(a)** and **(b)** presents v_{rh} for $L_p/d_p = 11.11$ and $L_p/d_p = 22.22$, for $s = 4.13$, $R_r = 7.75$ m, $d_p = 900$ mm and $E_s = 230$ MPa. Greater h_h resulted in higher horizontal displacements due to the increased magnitude of the horizontal load and overturning moment acting at the foundation level. However, t_r did not significantly affect horizontal displacement, with lower L_p/d_p ratios resulting in smaller displacements.

Figure 6-12: v_{rh} versus t_r for different h_h: (a) $L_p/d_p = 11.11$; (b) $L_p/d_p = 22.22$

As E_s increased from 10 MPa to 450 MPa, the v_{rd} also reduced significantly for E_s values up to 230 MPa, converging to a constant value past this value, with the influence being greater when L_p/d_p was larger. Thus, regarding taller wind turbines, given that the length of the piles are subjective and dependent on the depth of the compressible soil layer, greater pile diameters would assist in limiting horizontal displacement, especially when the Young's modulus of the soil is less than 230 MPa.

Considering the horizontal displacement of the foundation by varying the equivalent pile-raft area (sR_r), **Figure 6-13(a)** and **(b)** illustrate these results for $L_p/d_p = 11.11$ and $L_p/d_p = 22.22$, respectively. As the spacing between the piles, and effectively the radius of the raft, is increased, the horizontal displacement of the raft decreases, with no significant change observed for sR_r values greater than 60 m^2 for both pile slenderness ratios. As before, greater pile lengths or smaller pile diameters resulted in higher horizontal displacements, with the effect of the Young's modulus of the soil being greater for larger L_p/d_p values. However, even at small Young's modulus values of the soil, the horizontal displacement was limited for the foundation sizes considered for $h_h < 117$ m, resulting in the minimum horizontal stiffness (K_h) value to be achieved (obtained from **Table 2-2**). Consideration should be given when hub heights increase beyond this height.

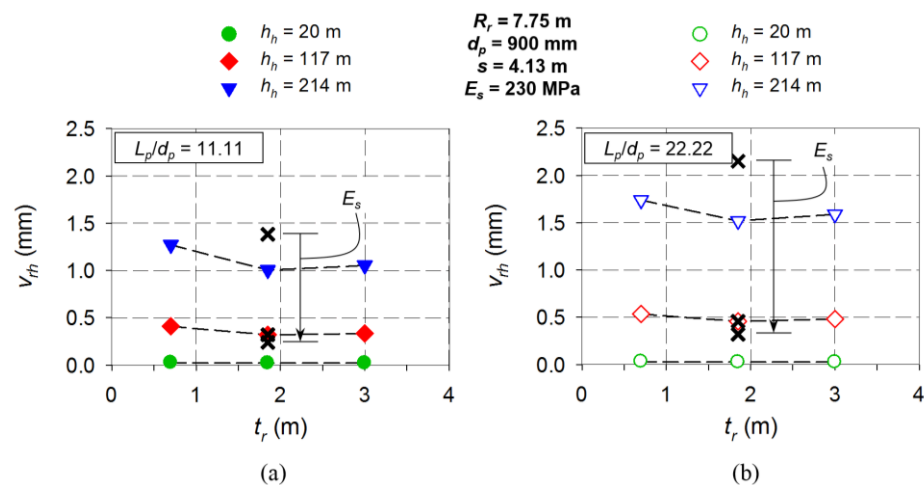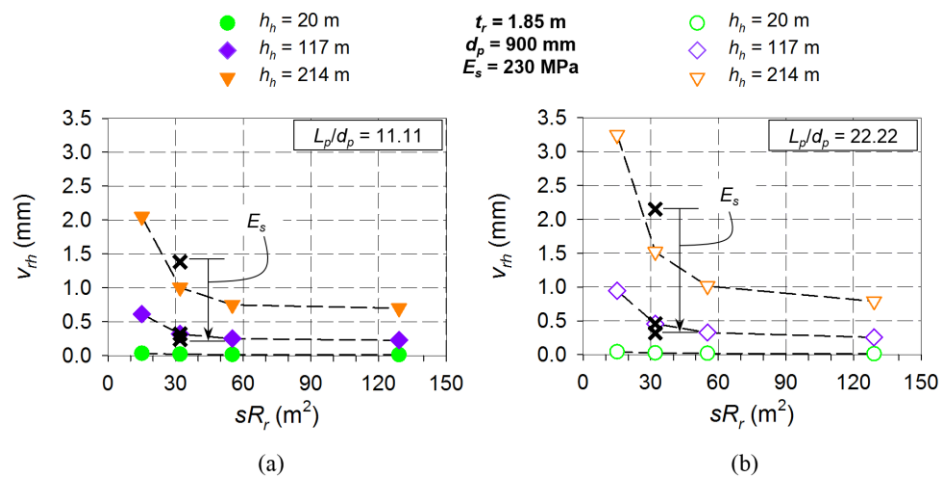**Figure 6-13:** v_{rh} versus sR_r for different h_h: (a) $L_p/d_p = 11.11$; (b) $L_p/d_p = 22.22$

More importantly, **Figure 6-14** illustrates the influence of t_r on the rotational stiffness (K_θ) of the foundation, where **(a)** indicates the results for $L_p/d_p = 11.11$ and **(b)** for $L_p/d_p = 22.22$. For the given pile spacing, pile diameter, and raft radius, as t_r increased, K_θ increased at a decreasing rate, with the magnitude of h_h having a limited effect. Higher L_p/d_p ratios also resulted in smaller rotational stiffness of the foundation. As expected, as the Young's modulus of the soil increased, K_θ also increased, with the effect being greater for $L_p/d_p = 22.22$.
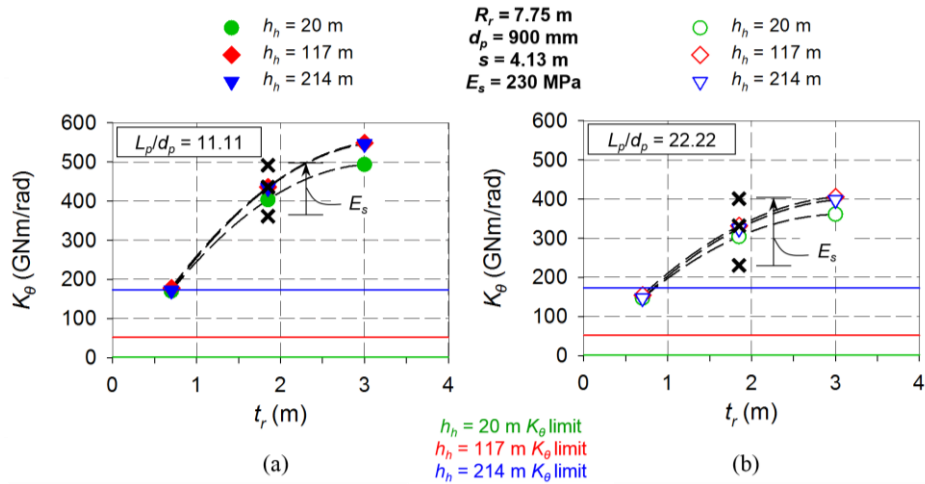
Figure 6-14: K_θ versus t_r for different h_h: (a) $L_p/d_p = 11.11$; (b) $L_p/d_p = 22.22$

Based on the SLS rotation limit of 1 mm/m specified in Chapter 2, the minimum K_θ values for the different hub heights were calculated and also indicated in **Figure 6-14**. With the exception of t_r less than 1 m for $h_h = 214$ m, the rotational stiffness of the combinations considered passes the minimum requirements. Based on the trends observed, increasing the diameter of the pile will increase the rotational stiffness of the piled raft, with thicker rafts also proving beneficial.

Figure 6-15(a) and **(b)** present the rotational stiffness of the foundation for different hub heights by varying the equivalent pile-raft area (sR_r). As with the equation from DNV/RisØ (2002) (see **Equation 2-3**), as the radius of the raft increased, the rotational stiffness of the raft increased, with the effect being higher when L_p/d_p was smaller for the raft thickness of 1.85 m and pile diameter of 900 mm.

Figure 6-15: K_θ versus sR_r for different h_h: (a $L_p/d_p = 11.11$; (b) $L_p/d_p = 22.22$

Similarly, as pile spacing increased, the data suggests that the rotational stiffness of the raft also increased. For sR_r values greater than 60 m², no significant increase in K_θ was observed for L_p/d_p = 22.22, however, a small reduction was observed for L_p/d_p = 11.11. For all equivalent pile-raft areas considered, the rotational stiffness of the foundations exceeded the minimum limit for each hub height. Thus, increased raft radii and pile spacing would benefit larger turbine models (up to a limit). If this is not possible, increasing the diameter of the piles would be helpful, given that the length of the pile is subjective to the depth of the compressible soil layer.

Lastly, **Figure 6-16(a)** and **(b)** indicates the effect of t_r on the axial tensile force in the trailing pile under the combined vertical load, horizontal load and overturning moment for L_p/d_p = 11.11 and L_p/d_p = 22.22. As evident from the data, raft thickness had minimal effect on the magnitude of the tensile forces in the trailing pile, with thicker rafts reducing the magnitude of the force for h_h = 214 m. The Young's modulus of the soil had minimal effect on the axial tensile force in the trailing pile, with stiffer soils reducing these loads slightly for R_r = 7.75 m, d_p = 900 mm and s = 4.13 m. As before, the Young's modulus values of the soil considered were 10 MPa, 230 MPa and 450 MPa.
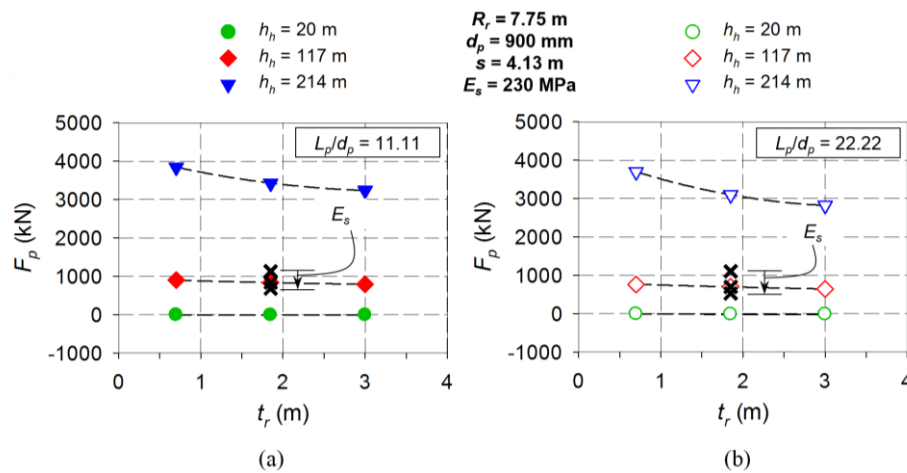
Figure 6-16: F_p versus t_r for different h_h: (a) L_p/d_p = 11.11; (b) L_p/d_p = 22.22

Figure 6-17(a) and **(b)** illustrates the effect of the equivalent pile-raft area on the axial forces developing on the trailing piles under the load combination. For the given raft thickness of 1.85 m (considered relatively rigid according to vertical deflections), as sR_r increased, the axial tensile forces in the trailing pile decreased, with no significant decrease observed for sR_r values greater than 60 m² for h_h less than 117 m. Higher L_p/d_p ratios resulted in slightly less axial forces in the piles, which can be attributed to the increased shaft friction between the pile and the soil. As before, the Young's modulus of the soil had minimal effect on the magnitude of the axial force. Thus, for taller wind turbine models, increasing the radius of the

raft and the spacing of the piles for a $t_r = 1.85$ m will limit axial forces, with sR_r values greater than 120 m^2 required for h_h exceeding 214 m regardless of L_p/d_p.
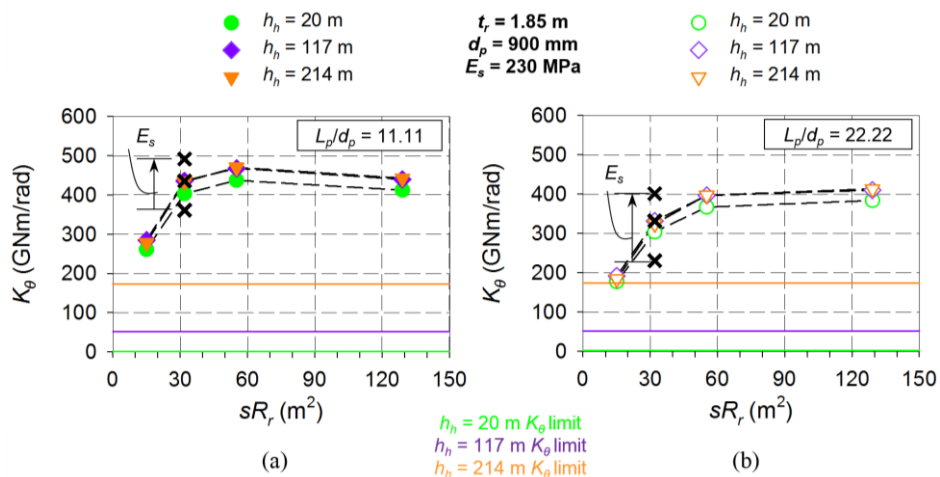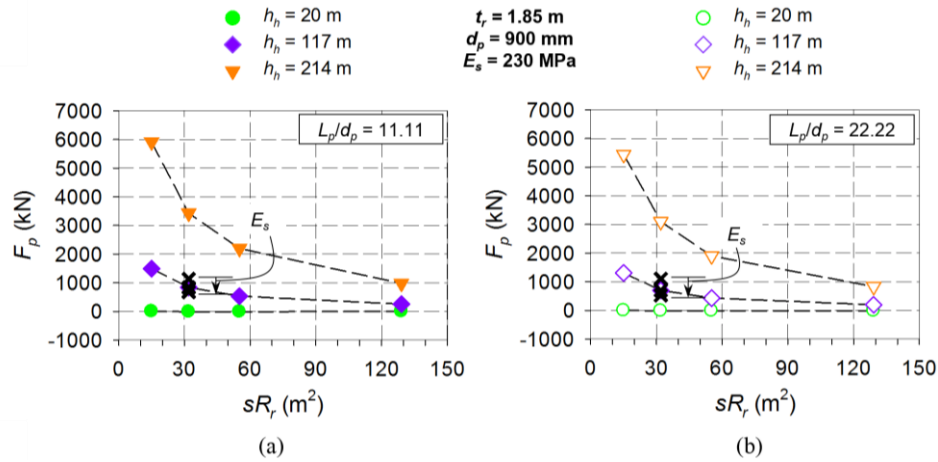

Figure 6-17: F_p versus sR_r for different h_h: (a) $L_p/d_p = 11.11$; (b) $L_p/d_p = 22.22$

Based on the results presented, for larger wind turbine models with increased magnitude of the horizontal load and overturning moment, the following is considered critical foundation design aspects that need to be limited to ensure turbine stability:

- Significant tensile stresses in the base of the raft, increasing the risk of concrete cracking.
- Development of large tensile forces in the trailing piles under the significant horizontal load and overturning moment.
- Horizontal displacements and foundation rotation, which exceed serviceability limits.

6.5   SUMMARY

In this chapter, a more general investigation was conducted on the pile-raft-soil interactions and how these interactions influence the response of the foundations under the dominant horizontal load and overturning moment. The results concerning the known principles of soil-structure interaction of piled-raft foundations compared well with the trends observed in literature. Under vertical loading, both the raft-soil (K_{rs}) and pile-soil (K_{ps}) stiffnesses influenced foundation response in limiting vertical settlement, with only K_{rs} affecting differential settlement. Under the combined vertical load, horizontal load and overturning moment, K_{rs} had little effect on the horizontal displacement of the foundation, with larger K_{ps} values limiting these displacements. Increasing both the raft-soil and pile-soil stiffnesses resulted in increased rotational stiffness of the foundation, with the effect being higher for shorter piles or larger pile diameters. Limiting the axial tensile forces in the trailing piles can be achieved by decreasing K_{ps}, with K_{rs} having little effect. Results indicate that wind turbines

with hub height exceeding 117 m will require adjustments to current design assumptions for piled-raft foundations.

Regarding the design of piled-raft foundations for future taller onshore wind turbines, the following recommendations are made:

- To prevent potential cracking in the base of the raft, either the thickness of the raft should be increased, or the equivalent pile-raft area should be reduced. No significant reduction was observed for thicknesses greater than 2 m, where response resembles more rigid behaviour, with pile length and diameter not having an effect. It is advised that reducing the potential tensile stresses in the raft should be achieved by increasing the number of piles rather than the radius of the raft due to the potential axial forces that might develop in the trailing piles. The Young's modulus of the soil did not affect these results.

- Under vertical loading, the vertical deflection can be limited by either increasing the thickness of the raft or reducing the equivalent pile-raft area (sR_r). Given that the piles investigated are socketed into bedrock, the length of the pile is subjective. Thus, deflections can be limited by increasing the diameter of the piles.

- Similar results were observed for horizontal displacements than for vertical deflections. The Young's modulus of the soil had a more significant effect on horizontal displacement, with less stiff soils requiring greater raft thicknesses or larger raft radii. Increasing the diameter of the piles also limited the amount of horizontal displacement.

- The rotational stiffness of the foundation can be increased by either increasing the thickness of the raft or the equivalent pile-raft area. However, for rigid rafts ($t_r >$ 2 m), the rotational stiffness started converging, with less stiff soils also requiring greater thicknesses. Increasing the raft radius and pile spacing also increased the rotational stiffness, with values converging to a constant value for sR_r values greater than 60 m^2 for a rigid raft.

- The axial tensile forces in the trailing piles can be controlled by increasing the radius of the raft, with raft thickness having minimal effect. For sR_r values greater than 60 m^2, tensile forces reduced minimally for $h_h \leq 117$ m. However, this value must be increased to 120 m^2 for $h_h = 214$ m to obtain the same equivalent tensile force in the piles.

7 CONCLUSIONS AND RECOMMENDATIONS

7.1 INTRODUCTION

This chapter summarises the main conclusions based on the results from the full-scale instrumented onshore wind turbine foundation and the numerical FE modelling conducted in Abaqus, all investigating the effects of dominant horizontal loads and overturning moments on piled-raft foundation response. Based on these findings, a list of recommendations for future research is also provided.

7.2 CONCLUSIONS

The main aim of this research was to establish whether the conventional soil-structure interaction models used for analysing and predicting piled-raft foundation response under vertical loading are still relevant when horizontal loading and overturning moments become the dominant foundation actions (as in the case of wind turbines). For years, designing the foundations for supporting these dynamically sensitive structures has been based on simplified and semi-empirical methods not initially developed for wind turbine application, raising several concerns given modern technologies, developments and computational power.

After considering the relevant literature and establishing the current assumptions regarding the design of onshore wind turbine foundations, a full-scale onshore wind turbine piled-raft foundation was successfully instrumented and monitored for an extended period of time. The foundation supported a 117 m high wind turbine located on a newly constructed wind farm near Wesley in South Africa. The response of the in-service piled-raft foundation was monitored, with the data focusing on the foundation's response during construction, turbine installation and turbine operations after commissioning. The presented data showed the possibility of calibrating the foundation system using know turbine weights, allowing for the estimation of load sharing between the piles and the raft.

During construction, the foundation's response was dominated by thermal effects caused by the concrete's heat of hydration process, with the raft's size contributing to thermal gradients in the concrete section. The full-scale testing showed that the foundation response was dominated by the dynamic horizontal load and overturning moment caused by the wind, compared to the vertical self-weight of the turbine, with the loads shared by both the raft and the piles, which differs from the conservative design assumption that the piles carry all the loads. Thus, the size of these foundations can potentially be reduced if the contribution of the raft is not neglected. During turbine installation, the piles carried approximately 35% of the

applied vertical load, increasing at a reduced rate to about 60% after one year of turbine operations. This increase in the loads on the piles could potentially be attributed to the soil below the raft settling, or densifying, with the raft having to bridge the 'gap' between the piles. The response of the piles under turbine operations were dominated by the push-pull effect under the dynamic horizontal load and overturning moment. This push-pull effect was due to the significant rigidity of the raft connecting the piles, which is expected for wind turbines (limiting differential settlement and rotation), with the relationship between the moment and the axial forces in the piles remaining unaffected by the number of load cycles. Although, as the number of wind load cycles increased, permanent bending moments develop towards the top of the piles. Wind-induced cyclic loading seemed to have no noticeable influence on the strain measured in the raft for the period of measurement. Seasonal temperature variations and thermally induced strains also affect foundation response, which is typically neglected due to the foundation being buried.

Based on the parametric study conducted on the FE models in Abaqus, it was evident that the response of a piled-raft foundation depends on not only the relative stiffness between the foundation and soil but also the relative stiffness between the different foundation components (pile-raft interface). During this study, particular consideration was given to investigating the influence of the overall foundation-soil system rigidity on the response of a piled-raft foundation under dominant horizontal loads and overturning moments, with the overall foundation-soil system rigidity evaluated by varying the Young's modulus of the soil, the raft thickness and radius, pile diameter and pile length, which is related to the depth of the compressible soil layer as all piles were assumed to be socketed into bedrock. The influence of increased turbine sizes was also examined.

The results concerning the known principles of soil-structure interaction of piled-raft foundations compared well with the trends observed in literature. Under vertical loading, both the raft-soil (K_{rs}) and pile-soil (K_{ps}) stiffnesses influenced foundation response in limiting vertical settlement, with only K_{rs} affecting differential settlement. Under the combined vertical load, horizontal load and overturning moment, K_{rs} had little effect on the horizontal displacement of the foundation, with larger K_{ps} values limiting these displacements. Increasing both the raft-soil and pile-soil stiffnesses resulted in increased rotational stiffness of the foundation, with the effect being higher for shorter piles or larger pile diameters. Limiting the axial tensile forces in the trailing piles, under horizontal loads and overturning moments, can be achieved by decreasing K_{ps}, with K_{rs} having little effect.

Based on the responses observed from the full-scale testing and the results from the relevant FE models, it is clear that the upper limit has been reached regarding our current approaches

to designing these foundations. In addition to the regular checks for restricting foundation settlement, differential settlement, horizontal displacement and meeting the minimum rotational stiffness requirements of the foundation, larger wind turbine models have presented additional critical design checks that cannot be ignored. These include the potential cracking of the raft under loading and the development of significant tensile forces in the trailing piles, both of which must be limited. It was found that limiting cracking of the raft can be achieved by either increasing the thickness of the raft, or reducing the equivalent pile-raft area by means of increasing the number of piles installed, as reducing the radius of the raft could potentially yield large unwanted tensile stresses in trailing piles. Reducing the presence of tensile forces developing in the trailing piles under the applied horizontal load and overturning moment can be achieved by increasing the raft radius or the pile-raft area.

Vertical deflection of the foundation can be reduced by increasing the raft thickness or pile diameter, or reducing the equivalent pile-raft area, similar to reducing the potential cracking tensile stresses in the base of the raft. Reducing horizontal displacements in the piled-raft can be achieved by increasing the thickness or radius of the raft, or the diameter of the piles, with the rotational stiffness of the foundation increased by increasing either the raft thickness or the equivalent pile-raft area. Especially for larger turbine models, considering a balanced soil-structure interaction approach was shown to be beneficial. However, as observed from the full-scale instrumented foundation, consideration should still be given to the constructability of these foundations, as larger foundations might result in more significant thermal gradients with the concrete section that can lead to premature cracking.

7.3 RECOMMENDATIONS

From the research conducted and the results obtained, some recommendations for future research include the following:

- Validate the instrumented and numerical results with more full-scale instrumentation, testing and numerical work or even scaled models in the geotechnical centrifuge to investigate the cyclic response of the supporting soil.
- Investigate whether the floating piles have a different outcome than socketed end-bearing piles.
- Study the fatigue behaviour of the concrete foundation under cyclic loading caused by the wind.
- Establish the effect of dynamic load effects, including torsional effects, caused by the wind on the external structure and the rotation of the blades on the supporting foundation.

REFERENCES

Alexander M and Mindess S (2005) *Aggregates in Concrete*. Taylor & Francis Group, Oxon, UK.

American Wind Energy Association (2011) Recommended Practice for Compliance of Large Land-based Wind Turbine Support Structures (ASCE/AWEA RP2011).

Atkinson JH (2000) Non-linear soil stiffness in routine design. *Géotechnique* **50(5)**: 487-508, https://doi.org/10.1680/geot.2000.50.5.487.

Atkinson JH and Sallfors G (1991) Experimental determination of stress-strain-time characteristic in laboratory and in situ tests. General report to Session 1. In *Proceedings of the 10th European Conference on Soil Mechanics and Foundation Engineering, Florence* (Associazione Geotecnica Italiana (eds)). AA Balkema, Rotterdam, Netherlands, vol. 3, pp. 915-956.

Azenha M and Faria R (2008) Temperatures and stresses due to cement hydration on the R/C foundation of a wind tower – a case study. *Engineering Structures* **30(9)**: 2392-2400, https://doi.org/10.1016/j.engstruct.2008.01.018.

Bai X, He M, Ma R and Huang D (2017) Structural condition monitoring of wind turbine foundations. *Proceedings of the Institution of Civil Engineers – Energy* **170(3)**: 116-134, https://doi.org/10.1680/jener.16.00012.

Barry-Macaulay D, Bouazza A, Singh RM, Wang B and Ranjith PG (2013) Thermal conductivity of soils and rocks from the Melbourne (Australia) region. *Engineering Geology* **164**: 131-138, http://dx.doi.org/10.1016/j.enggeo.2013.06.014.

Bhaduri A and Choudhury D (2020) Serviceability-based finite-element approach on analyzing combined pile-raft foundation. *International Journal of Geomechanics* **20(2)**: 04019178, https://doi.org/10.1061/(ASCE)GM.1943-5622.0001580.

Borowicka H (1939) Influence of rigidity of a circular foundation slab on the distribution of pressures over the contact surface. In *Proceedings of the 1st International Conference on Soil Mechanics and Foundation Engineering, Cambridge*. Vol. 2, pp. 144-149.

Brown PT (1969a) Numerical analyses of uniformly loaded circular rafts on elastic layers of finite depth. *Géotechnique* **19(2)**: 301-306, https://doi.org/10.1680/geot.1969.19.2.301.

Brown PT (1969b) Numerical analyses of uniformly loaded circular rafts on deep elastic foundations. *Géotechnique* **19(3)**: 399-404, https://doi.org/10.1680/geot.1969.19.3.399.

BSI (2009) BS EN 12390-6:2009 Testing Hardened Concrete. Tensile Splitting Strength of Test Specimens. BSI, London, UK.

BSI (2014) BS EN 1992-1-1:2004+A1:2014 Eurocode 2: Design of Concrete Structures – General Rules and Rules for Buildings. BSI, London, UK.

BSI (2019) BS EN 12390-3:2019 Testing Hardened Concrete. Compressive Strength of Test Specimens. BSI, London, UK.

BSI (2021) BS EN 12390-13:2021 Testing Hardened Concrete. Determination of Secant Modulus of Elasticity in Compression. BSI, London, UK.

Bu DS (2005) Engineering considerations for design of wind farm foundations. *Technical Note, Ground Engineering*.

Burland JB, Broms BB and De Mello VFB (1977) Behaviour of foundations and structures. In *Proceedings of the 9th International Conference on Soil Mechanics and Foundation Engineering, Tokyo*. Japanese Society of Soil Mechanics and Foundation Engineering, pp. 495-546.

Burton T, Jenkins N, Sharpe D and Bossanyi E (2011) *Wind Energy Handbook.* John Wiley & Sons, West Sussex, UK.

Butterfield R and Banerjee PK (1971) The problem of pile group-pile cap interaction. *Géotechnique* **21(2)**: 135-142, https://doi.org/10.1680/geot.1971.21.2.135.

Chanda D, Saha R and Haldar S (2020) Behaviour of piled raft foundation in sand subjected to combined *V-M-H* loading. *Ocean Engineering* **216**: 107596, https://doi.org/10.1016/j.oceaneng.2020.107596.

Chen HP (2018) *Structural Health Monitoring of Large Civil Engineering Structures.* John Wiley & Sons, West Sussex, UK.

Chow YK (1986) Analysis of vertically loaded pile groups. *International Journal for Numerical and Analytical Methods in Geomechanics* **10(1)**: 59-72, https://doi.org/10.1002/nag.1610100105.

Clancy P (1993) *Numerical analysis of piled raft foundations*. PhD thesis, University of Western Australia, Australia.

Clancy P and Randolph MF (1993) An approximate analysis procedure for piled raft foundations. *International Journal for Numerical and Analytical Methods in Geomechanics* **17(12)**: 849-869, https://doi.org/10.1002/nag.1610171203.

Clancy P and Randolph MF (1996) Simple design tools for piled raft foundations. *Géotechnique* **46(2)**: 313-328, https://doi.org/10.1680/geot.1996.46.2.313.

Clayton CRI (2011) Stiffness at small strain: research and practice. *Géotechnique* **61(1)**: 5-37, https://doi.org/10.1680/geot.2011.61.1.5.

Clayton CRI and Heymann G (2001) Stiffness of geomaterials at very small strains. *Géotechnique* **51(3)**: 245-255, https://doi.org/10.1680/geot.2001.51.3.245.

Conceicao J, Faria R, Azenha M, Mamede F and Souza F (2014) Early-age behaviour of the concrete surrounding a turbine spiral case: monitoring and thermo-mechanical modelling. *Engineering Structures* **81**: 327-340, https://doi.org/10.1016/j.engstruct.2014.10.009.

Cools JE (2015) Geotechnical foundation design for onshore wind turbines. In *Special Editon of the 16th European Conference on Soil Mechanics and Geotechnical Engineering, Edinburgh*. GEOTECHNIEK, pp. 18-22.

Cross H (1932) Analysis of continuous frames by distributing fixed-end moments. *Transactions of the American Society of Civil Engineers* **96(1)**: 919-928, https://doi.org/10.1061/TACEAT.0004333.

Currie M, Saafi M, Tachtatzis C and Quail F (2013) Structural health monitoring for wind turbine foundations. *Proceedings of the Institution of Civil Engineers – Energy* **166(4)**: 162-169, https://doi.org/10.1680/ener.12.00008.

Currie M, Saafi M, Tachtatzis C and Quail F (2015) Structural integrity monitoring of onshore wind turbine concrete foundations. *Renewable Energy* **83**: 1131-1138, https://doi.org/10.1016/j.renene.2015.05.006.

Dassault Systèmes Simulia Corp. (2014) *ABAQUS Online Documentation*. Providence, RI, USA.

Dassault Systèmes Simulia Corp. (2021) *ABAQUS*. Johnston, RI, USA.

Deb P and Pal SK (2021) Structural and geotechnical aspects of piled raft foundation through numerical analysis. *Marine Georesources & Geotechnology* **40(7)**: 823-846, https://doi.org/10.1080/1064119X.2021.1943083.

Det Norske Veritas and RisØ National Laboratory (2002) *Guidelines for the design of wind turbines*. DNV/RisØ, Copenhagen, Denmark.

EDF Renewables (2022) *Wesley-Ciskei Wind Farm*. See https://www.edf-re.co.za/projects/wesley-ciskei/ (accessed 19/02/2022).

Fang HY (1991) *Foundation Engineering Handbook.* Chapman & Hall, New York, NY, USA.

Fleming K, Weltman A, Randolph M and Elson K (2009) *Piling Engineering*. Taylor & Francis Group, Oxon, UK.

Florides G and Kalogirou (2007) Ground heat exchangers – A review of systems, models and applications. *Renewable Energy* **32(15)**: 2461-2478, https://doi.org/10.1016/j.renene.2006.12.014.

Fraser RA and Wardle LJ (1976) Numerical analysis of rectangular rafts on layered foundations. *Géotechnique* **26(4)**: 613-630, https://doi.org/10.1680/geot.1976.26.4.613.

Geotechnical Report (2014) *Geotechnical Site Investigation for the Proposed Wesley Wind Energy Facility, Eastern Cape.*

Gere JM and Goodno BJ (2013) *Mechanics of Materials.* Cengage Learning, Stamford, CT, USA.

Giroud JP (1968) Settlement of a linearly loaded rectangular area. *Journal of Soil Mechanics and Foundation Engineering – Division of the American Society of Civil Engineers* **94(4)**: 813-831, https://doi.org/10.1061/JSFEAQ.0001174.

Global Wind Energy Council (2022) *Global Wind Report 2022*. GWEC, Brussels, Belgium.

Google Earth (2022) *Wind turbine position*, 1:36000. See https://earth.google.com/web/@-33.29524911,27.3657843,113.18980884a,8866.23425631d,35y,359.99993784h,0t,0r (accessed 19/02/2022).

Google Maps (2022) *Wind farm location*, 1:10000000. See https://www.google.com/maps/@-28.7221848,22.8964847,5.94z (accessed 19/02/2022).

Griffiths DV, Clancy P and Randolph MF (1991) Piled raft foundation analysis by finite elements. In *Proceedings of the 7th International Conference on Computer Methods and Advances in Geomechanics, Cairns* (Booker JR, Carter JP and Beer G (eds)). AA Balkema, Rotterdam, Netherlands, pp. 1153-1157.

Hain SJ and Lee IK (1978) The analysis of flexible raft-pile systems. *Géotechnique* **28(1)**: 65-83, https://doi.org/10.1680/geot.1978.28.1.65.

Hanna AM and Vakili R (2021) Load-sharing mechanism of non-displacement piled-raft foundation in sand. *Proceedings of the Institution of Civil Engineers – Ground Improvement* **174(2)**: 105-115, https://doi.org/10.1680/jgrim.17.00072.

He M, Bai X, Ma R and Huang D (2019) Structural monitoring of onshore wind turbine foundation using strain sensors. *Structure and Infrastructure Engineering* **15(3)**: 314-333, https://doi.org/10.1080/15732479.2018.1546325.

Hettler A (1981) *Verschiebungen starrer und elastischer Gründungskörper in Sand bei monotoner und zyklischer Belastung.* Veröffentlichungen des Institutes für Bodenmechanik und Felsmechanik der Universität Fridericiana in Karlsruhe, Heft 90, Karlsruhe, Germany (in German).

Horikoshi K, Matsumoto T, Hashizume Y, Watanabe T and Fukuyama H (2003a) Performance of piled raft foundations subjected to static horizontal loads. *International Journal of Physical Modelling in Geotechnics* **3(2)**: 37-50, https://doi.org/10.1680/ijpmg.2003.030204.

Horikoshi K, Matsumoto T, Hashizume Y and Watanabe T (2003b). Performance of piled raft foundations subjected to dynamic loading. *International Journal of Physical Modelling in Geotechnics* **3(2)**: 51-62, https://doi.org/10.1680/ijpmg.2003.030205.

Horikoshi K and Randolph MF (1997) On the definition of raft-soil stiffness ratio for rectangular rafts. *Géotechnique* **47(5)**: 1055-1061, https://doi.org/10.1680/geot.1997.47.5.1055.

Horikoshi K and Randolph MF (1998) A contribution to optimum design of piled rafts. *Géotechnique* **48(3)**: 301-317, https://doi.org/10.1680/geot.1998.48.3.301.

Hu WH, Thons S, Rohrmann RG, Said S and Rucker W (2015) Vibration-based structural health monitoring of a wind turbine system. Part I: resonance phenomenon. *Engineering Structures* **89**: 260-272, https://doi.org/10.1016/j.engstruct.2014.12.034.

Johnson KL (1986) Plastic flow, residual stresses and shakedown of rolling contacts. In *Proceedings of the 2nd International Conference on Contact Mechanics and Wear of Rail/Wheel Systems, Kingston* (Gladwell GML, Ghonem H and Kalousek J (eds)). University of Waterloo Press, Ontario, Canada, pp. 83-97.

Kassimali A (2015) *Structural Analysis*. Cengage Learning, Stamford, CT, USA.

Katzenbach R, Arslan U, Moormann C and Reul O (1998) Piled raft foundation – interaction between piles and raft. *Darmstadt Geotechnics* **4**: 279-296.

Kirkwood PB and Haigh SK (2014). Centrifuge testing of monopiles subject to cyclic lateral loading. In *Proceedings of the 8th International Conference on Physical Modelling in Geotechnics, Perth* (Gaudin C and White D (eds)). Taylor & Francis Group, London, UK, vol. 2, pp. 827-831.

Klar A, Vorster TEB, Soga K and Mair RJ (2005) Soil-pipe interaction due to tunnelling: comparison between winkler and elastic continuum solutions. *Géotechnique* **55(6)**: 461-466, https://doi.org/10.1680/geot.2005.55.6.461.

Knappett JA and Craig RF (2012) *Craig's Soil Mechanics*. Spon Press, Oxon, UK.

Kusel F, Kearsley EP, Butler LJ, Skorpen SA and Elshafie MZEB (2018) Measured temperature effects during the construction of a prestressed precast concrete bridge beam. In *Proceedings of the 5th International Conference on Concrete Repair, Rehabilitation and Retrofitting, Cape Town* (Alexander MG, Beushausen H, Dehn F and Moyo P (eds)). MATEC Web of Conferences, vol. 199, pp. 11013.

Kuwabara F (1989) An elastic analysis for piled raft foundations in a homogeneous soil. *Soils and Foundations* **29(1)**: 82-92, https://doi.org/10.3208/sandf1972.29.82.

Lantz E, Wiser R and Hand M (2012) *IEA Wind Task 26: The Past and Future Cost of Wind Energy* (Technical Report NREL/TP-6A20-53510). National Renewable Energy Laboratory, Denver, CO, USA.

Leblanc C, Houlsby GT and Byrne BW (2010) Response of stiff piles in sand to long-term cyclic lateral loading. *Géotechnique* **60(2)**: 79-90, https://doi.org/10.1680/geot.7.00196.

Lee CJ, Bolton MD and Al-Tabbaa A (2002) Numerical modelling of group effects on the distribution of dragloads in pile foundations. *Géotechnique* **52(5)**: 325-335, https://doi.org/10.1680/geot.2002.52.5.325.

Lee JH, Kim Y and Jeong S (2010) Three-dimensional analysis of bearing behavior of piled raft on soft clay. *Computers and Geotechnics* **37(1-2)**: 103-114, https://doi.org/10.1016/j.compgeo.2009.07.009.

Li Z, Haigh SK and Bolton MD (2010) Centrifuge modelling of mono-pile under cyclic lateral loads. In *Proceedings of the 7th International Conference on Physical Modelling*

in Geotechnics, Zurich (Springman S, Laue J and Seward L (eds)). CRC Press, London, UK, vol. 2, pp. 965-970.

Little RL and Briaud JL (1988) *Full Scale Cyclic Lateral Load Tests on Six Single Piles in Sand.* Geotechnical Division, Department of Civil Engineering, Texas A and M University. College Station, TX, USA, Miscellaneous Paper GL-88-27.

Long JH and Vanneste G (1994) Effects of cyclic lateral loads on piles in sand. *Journal of Geotechnical Engineering* **120(1)**: 225-244, https://doi.org/10.1061/(ASCE)0733-9410(1994)120:1(225).

Louw H, Kearsley E and Jacobsz SW (2022a) Modelling horizontally loaded piles in a geotechnical centrifuge. *International Journal on Physical Modelling in Geotechnics* **22(1)**: 14-25, https://doi.org/10.1680/jphmg.20.00016.

Louw H, Broekman A and Kearsley E (2022b) MADV-DAQ: Multi-channel Arduino-based differential voltage data acquisition system for remote strain measurement applications. *HardwareX* **12**: e00360, https://doi.org/10.1016/j.ohx.2022.e00360.

Mair RJ (1993) Developments in geotechnical engineering research: applications to tunnels and deep excavations. Unwin Memorial Lecture 1992. *Proceedings of the Institution of Civil Engineers – Civil Engineering* **97(1)**: 27-41, https://doi.org/10.1016/0148-9062(93)92167-o.

Maney GA (1915) *Studies in Engineering,* Bulletin 1. University of Minnesota, Minneapolis.

Mawer B and Kalumba D (2016) Stability of wind turbine foundations – accounting for gapping and eccentric loading. *Civil Engineering Magazine of the South African Institution of Civil Engineering* **24(3)**: 63-67.

Mawer B, Kalumba D and Warren-Codrington C (2017) Loading and dynamic response considerations for the design of wind turbine foundations on South African soils. *Geotechnical Engineering Journal of the SAEGE & AGSSEA* **48(3)**: 110-117.

Mayne PW and Poulos HG (1999) Approximate displacement influence factors for elastic shallow foundations. *Journal of Geotechnical and Geoenvironmental Engineering* **125(6)**: 453-460, https://doi.org/10.1061/(ASCE)1090-0241(1999)125:6(453).

McAlorum J, Perry M, Fusiek G, Niewczas P, McKeeman I and Rubert T (2018) Deterioration of cracks in onshore wind turbine foundations. *Engineering Structures* **167**:121-131, https://doi.org/10.1016/j.engstruct.2018.04.003.

Mindlin RD (1936) Force at a point in the interior of a semi-infinite solid. *Physics* **7**: 195-202, https://doi.org/10.1063/1.1745385.

Mohamed W and Austrell PE (2018) A comparative study of three onshore wind turbine foundation solutions. *Computers and Geotechnics* **94**: 46-57, https://doi.org/10.1016/j.compgeo.2017.08.022.

Montgomery DC (2001) *Design and Analysis of Experiments.* John Wiley & Sons, New York, NY.

Morgan K and Ntambakwa E (2008) Wind turbine foundation behavior and design considerations. In *Proceedings of AWEA Windpower Conference, Houston.* Prentice Hall, Englewood Cliffs, NJ, USA, pp. 1-14.

Mosley B, Bungey J and Hulse R (2012) *Reinforced Concrete Design to Eurocode 2.* Palgrave Macmillan, London, UK.

Moss RES, Caliendo JA and Anderson LR (1998) Investigation of a cyclic laterally loaded model pile group. *Soil Dynamics and Earthquake Engineering* **17(7-8)**: 519-523, https://doi.org/10.1016/S0267-7261(98)00003-7.

Niemann C, O'Loughlin C, Tian Y, Cassidy M and Reul O (2019) Response of pile groups in sand due to lateral cyclic loading. *International Journal of Physical Modelling in Geotechnics* **19(6)**: 318-330, https://doi.org/10.1680/jphmg.18.00027.

Noor FA and Boswell LF (1992) *Small scale modelling of concrete structures.* Elsevier Applied Science, London, UK.

Norris CH, Wilbur JB and Utku S (1976) *Elementary Structural Analysis.* McGraw-Hill, New York, NY, USA.

Novak LJ, Reese LC and Wang ST (2005) Analysis of piled-raft foundations with 3-D finite-element method. In *Structures Congress 2005: Metropolis and Beyond, New York.* American Society of Civil Engineers (ASCE), pp. 1-12, https://doi.org/10.1061/40753(171)93.

Novak M and Sheta M (1982) Dynamic response of piles and pile groups. In *Proceedings of the 2nd International Conference on Numerical Methods in Offshore Piling, Austin* (University of Texas at Austin and Institution of Civil Engineers (eds)). University of Texas, Austin, TX, USA, pp. 1-18.

Perry M, Fusiek G, Niewczas P, Rubert T and McAlorum J (2017) Wireless concrete strength monitoring of wind turbine foundations. *Sensors* **17(12)**: 2928, https://doi.org/10.3390/s17122928.

Pham HV, Dias D, Miranda T, Cristelo N and Araujo N (2018) 3D numerical modelling of foundation solutions for wind turbines. *International Journal of Geomechanics* **18(12)**: 04018164, https://doi.org/10.1061/(ASCE)GM.1943-5622.0001318.

Popiel CO, Wojtkowaik J and Biernacka B (2001) Measurements of temperature distribution in ground. *Experimental Thermal and Fluid Science* **25(5)**: 301-309, https://doi.org/10.1016/S0894-1777(01)00078-4.

Poulos HG (1982) Single pile response to cyclic lateral load. *Journal of Geotechnical and Geoenvironmental Engineering* **108(3)**: 355-375, https://doi.org/10.1061/AJGEB6.0001255.

Poulos HG (1989) Pile behaviour – theory and application. *Géotechnique* **39(3)**: 365-415, https://doi.org/10.1680/geot.1989.39.3.365.

Poulos HG (2001) Methods of analysis of piled raft foundations. *A Report Prepared on Behalf of Technical Committee TC18 on Piled Foundations.*

Poulos HG (2002) Simplified design procedure for piled raft foundations. In *Deep Foundations 2002: An International Perspective on Theory, Design, Construction, and Performance, Orlando.* American Society of Civil Engineers (ASCE), pp. 441-458, https://doi.org/10.1061/40601(256)32.

Poulos HG (2010) The design of foundations for high-rise buildings. *Proceedings of the Institution of Civil Engineers – Civil Engineering* **163(6)**: 27-32, https://doi.org/10.1680/cien.2010.163.6.27.

Poulos HG (2016) Tall building foundations: design methods and applications. *Innovative Infrastructure Solutions* **1(10)**: 1-51, https://doi.org/10.1007/s41062-016-0010-2.

Poulos HG and Davis EH (1980). *Pile Foundation Analysis and Design.* John Wiley & Sons, Toronto, Canada.

Poulos HG and Mattes NS (1969) The behaviour of axially loaded end-bearing piles. *Géotechnique* **19(2)**: 285-300, https://doi.org/10.1680/geot.1969.19.2.285.

Prakoso WA and Kulhawy FH (2001) Contribution to piled raft foundation design. *Journal of Geotechnical and Geoenvironmental Engineering* **127(1)**: 17-24, https://doi.org/10.1061/(ASCE)1090-0241(2001)127:1(17).

Randolph MF (1977) *A theoretical study of the performance of piles*. PhD thesis, University of Cambridge, UK.

Randolph MF (1983) Design of piled raft foundations. In *Proceedings of the International Symposium on Recent Developments in Laboratory and Field Tests and Analysis of Geotechnical Problems, Bangkok* (Balasubramaniam AS, Chandra S and Bergado DT (eds)). AA Balkema, Rotterdam, Netherlands, pp. 525-537.

Randolph MF (1994) Design methods for pile groups and piled rafts. In *Proceedings of the 13th International Conference on Soil Mechanics, New Delhi*. Taylor & Francis, pp. 61-82.

Randolph MF (2003) Science and empiricism in pile foundation design. *Géotechnique* **53(10)**: 847-875, https://doi.org/10.1680/geot.2003.53.10.847.

Ravichandran N and Shrestha S (2019) Comparison of settlement response of piled-raft foundation subjected to combined loads computed from finite element and analytical models. In *Geo-Congress 2019: Foundations (GSP 307), Philadelphia* (Meehan CL, Kumar S, Pando MA and Coe JT (eds)). American Society of Civil Engineers (ASCE), pp. 63-73.

Reese LC and Wang ST (2008) Design of foundations for a wind turbine employing modern principles. In *GeoCongress 2008: From Research to Practice in Geotechnical Engineering (GSP 180), New Orleans* (Laier JE, Crapps DK and Hussein MH (eds)). American Society of Civil Engineers (ASCE), pp. 351-365, https://doi.org/10.1061/40962(325)10.

Reul O (2004) Numerical study of the bearing behavior of piled raft. *International Journal of Geomechanics* **4(2)**: 59-68, https://doi.org/10.1061/(ASCE)1532-3641(2004)4:2(59).

Reul O and Randolph MF (2003). Piled rafts in overconsolidated clay: comparison of in situ measurements and numerical analysis. *Géotechnique* **53(3)**: 301-315, https://doi.org/10.1680/geot.2003.53.3.301.

REVE (2023) Vestas wins an order for 373 MW of wind power in South Africa with V163-4.5 MW wind turbines. See https://www.evwind.es/2023/03/14/vestas-wins-an-order-

for-373-mw-of-wind-power-in-south-africa-with-v163-4-5-mw-wind-turbines/90716 (accessed 01/04/2023).

Reynolds CE and Steedman JC (1988) *Reinforced Concrete Designer's Handbook.* E & FN Spon, Taylor & Francis Group, London, UK.

Rowe PW (1952) Anchored sheet-pile walls. *Proceedings of the Institute of Civil Engineers* **1(1)**: 27-70, https://doi.org/10.1680/iicep.1952.10942.

Rubert T, Perry M, Fusiek G, McAlorum J, Niewczas P, Brotherston A and McCallum D (2018) Field demonstration of real-time wind turbine foundation strain monitoring. *Sensors* **18(1)**: 97, https://doi.org/10.3390/s18010097.

Sabnis GM, Harris HG, White RN and Saeed Mirza M (1983) *Structural Modelling and Experimental Techniques.* Prentice Hall, Englewood Cliffs, NJ, USA.

Sakellariadis L and Anastasopoulos I (2022) On the mechanisms governing the response of pile groups under combined VHM loading. *Géotechnique* (published online ahead of print 12 September), https://doi.org/10.1680/jgeot.21.00236.

Schiegg Y and Steiner L (2010) Cost effectiveness and application of online monitoring in reinforced concrete structures. *Materials and Corrosion* **61(6)**: 490-493, https://doi.org/10.1002/maco.200905556.

Schofield AH (1980) Cambridge geotechnical centrifuge operations. *Géotechnique* **30(3)**: 227-268, https://doi.org/10.1680/geot.1980.30.3.227.

Shrestha S and Ravichandran N (2019) 3D Nonlinear finite element analysis of piled-raft foundation for tall wind turbines and its comparison with analytical model. *Journal of GeoEngineering* **14(4)**: 259-276, http://dx.doi.org/10.6310/jog.201912_14(4).5.

Shrestha S, Ravichandran N and Rahbari P (2018) Geotechnical design and design optimization of a pile-raft foundation for tall onshore wind turbines in multilayered clay. *International Journal of Geomechanics* **18(2)**: 04017143, https://doi.org/10.1061/(ASCE)GM.1943-5622.0001061.

Sinha A and Hanna AM (2016) 3D Numerical Model of Piled Raft Foundation. *International Journal of Geomechanics* **17(2)**: 04016055, https://doi.org/10.1061/(ASCE)GM.1943-5622.0000674.

Skorpen SA (2020) *Temperature effects and the behaviour of long reinforced concrete integral bridges*. PhD thesis, University of Pretoria, Pretoria.

Skorpen SA, Kearsley EP, Clayton CRI and Kruger EJ (2021) Structural monitoring of an integral bridge in South Africa. *Proceedings of the Institution of Civil Engineers – Smart Infrastructure and Construction* **173(3)**: 63-72, https://doi.org/10.1680/jsmic.20.00001.

Small JC and Poulos HG (2007) Non-linear analysis of piled raft foundations. In *Geo-Denver 2007: Contemporary Issues in Deep Foundations (GSP 158), Denver*. American Society of Civil Engineers (ASCE), pp. 1-9, https://doi.org/10.1061/40902(221)14.

Small JC and Zhang HH (2002) Behavior of piled raft foundations under lateral and vertical loading. *International Journal of Geomechanics* **2(1)**: 29-45, https://doi.org/10.1061/(ASCE)1532-3641(2002)2:1(29).

Smith IM and Griffiths DV (1988) *Programming the finite element method.* Wiley, Chichester, West Sussex, UK.

Soutsos M and Domone P (2018) *Construction Materials: Their Nature and Behaviour*. Taylor & Francis Group, Boca Raton, FL, USA.

Swartz RA, Lynch JP, Zerbst S, Sweetman B and Rolfes R (2010) Structural monitoring of wind turbines using wireless sensor networks. *Smart Structures and Systems* **6(3)**: 183-196, http://dx.doi.org/10.12989/sss.2010.6.3.183.

Tang YJ, Pei J and Zhao XH (2014) Design and measurement of piled-raft foundation. *Proceedings of the Institution of Civil Engineers – Geotechnical Engineering* **167(5)**: 461-475, https://doi.org/10.1680/geng.13.00004.

Timoshenko S and Woinowsky-Krieger S (1959) *Theory of Plates and Shells.* McGraw-Hill, New York, NY, USA.

Tinjum JM and Christensen RW (2011) 2 - Site investigation, characterization and assessment for wind turbine design and construction. *Wind Energy Systems*. Woodhead Publishing, Cambridge, UK, https://doi.org/10.1533/9780857090638.1.28.

Tomlinson MJ (1986) *Foundation Design and Construction*. Longman Scientific & Technical, London, UK.

Truong P, Lehane BM, Zania V and Klinkvort RT (2019) Empirical approach based on centrifuge testing for cyclic deformations of laterally loaded piles in sand. *Géotechnique* **69(2)**: 133-145, https://doi.org/10.1680/jgeot.17.P.203.

Ugural AC and Fenster SK (2012) *Advanced Mechanics of Materials and Applied Elasticity.* Prentice Hall, Upper Saddle River, NJ, USA.

Verdure L, Garnier J and Levacher D (2003) Lateral cyclic loading of single piles in sand. *International Journal of Physical Modelling in Geotechnics* **3(3)**: 17-28, https://doi.org/10.1680/ijpmg.2003.030303.

Vesic AS (1969) Experiments with instrumented pile groups in sand. In *Performance of deep foundations*. ASTM International, pp. 177-222.

Vestas (2022) *Vestas V126-3.45 MW*. See https://www.vestas.com/en/products/4-mw-platform/V126-3-45-MW (accessed 01/12/2022).

Viggiani C (2001) Analisi e progetto delle fondazioni su pali. Prima Conferenza Arrigo Croce, *Rivista Italiana di Geotecnica* **35**: 17-45 (in Italian).

Vorster TEB and Wojtowitz G (2019) Innovative foundation design for super-tall buildings. In *Proceedings of the 17th African Regional Conference on Soil Mechanics and Geotechnical Engineering, Cape Town* (Jacobsz SW (ed)). International Society for Soil Mechanics and Geotechnical Engineering (ISSMGE), pp. 1-8.

Wang P, Yan Y, Tian GY, Bouzid O and Ding Z (2012) Investigation of wireless sensor networks for structural health monitoring. *Journal of Sensors* **2012**: 156329, https://doi.org/10.1155/2012/156329.

Werkmeister S, Dawson AR and Wellner F (2001) Permanent deformation behaviour of granular materials and the shakedown concept. *Transportation Research Record* **1757(1)**: 75-81, https://doi.org/10.3141/1757-09.

Werkmeister S, Dawson AR and Wellner F (2004) Pavement design model for unbound granular materials. *Journal of Transportation Engineering* **130(5)**: 665-674, https://doi.org/10.1061/(ASCE)0733-947X(2004)130:5(665).

Westergaard HM (1926) Stresses in concrete pavements computed by theoretical analysis. *Public Roads Magazine of the US Department of Transportation Federal Highway Administration.*

Whitlow R (1995) *Basic Soil Mechanics.* Longman Group Limited, London, UK.

Winterkorn HF and Fang HY (1975) *Foundation Engineering Handbook.* Van Nostrand Reinhold Company, New York, NY, USA.

Wiser R and Bolinger M (2011) *2010 Wind Technologies Market Report*. US Department of Energy - Energy Efficiency and Renewable Energy, Washington DC, USA.

Wojtowitz G and Foster J (2020) Wind energy powering a changing landscape for South Africa. *Civil Engineering Magazine of the South African Institution of Civil Engineering* **28(3)**: 19-24.

Wojtowitz G and Vorster E (2014) The design of gravity foundations for wind turbines for West Coast 1 Wind Farm. In *Proceeding of the 8ᵗʰ South African Young Geotechnical Engineers Conference, Stellenbosch*, pp. 379-388.

World Meteorological Organization (1970) *The Beaufort Scale of Wind Force: Technical and Operational Aspects*. Commission of Maritime Meteorology, WMO, Geneva, Switzerland.

Wymore ML, Van Dam JE, Ceylan H and Qiao D (2015) A survey of health monitoring systems for wind turbines. *Renewable and Sustainable Energy Reviews* **52**: 976-990, https://doi.org/10.1016/j.rser.2015.07.110.

Yilmaz M, Eun J, Tinjum JM and Fratta D (2022) In-service response of shallow on-shore wind turbine generator foundation. *Geotechnical and Geological Engineering* **40(2)**: 977-994, https://doi.org/10.1007/s10706-021-01938-1.

Zeevaert L (1991) Foundation problems in earthquake regions. *Foundation Engineering Handbook*, pp. 673-678.

Zhang HH and Small JC (2000) Analysis of capped pile groups subjected to horizontal and vertical loads. *Computers and Geotechnics* **26(1)**: 1-21, https://doi.org/10.1016/S0266-352X(99)00029-4.
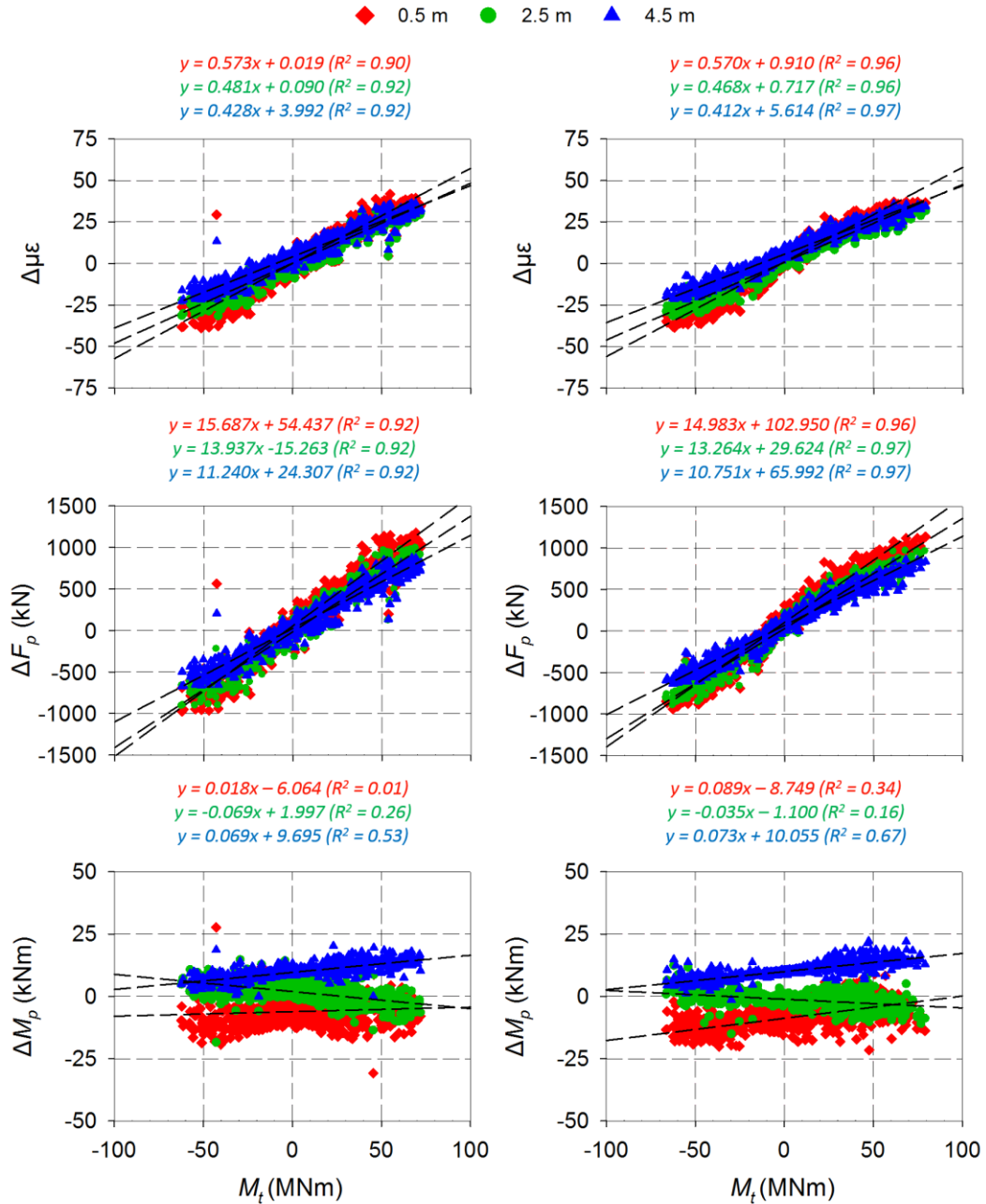
APPENDIX: MONITORING OF A PILED-RAFT FOUNDATION

This appendix accompanies the results and discussions in Chapter 3 regarding the instrumentation and monitoring of an onshore wind turbine piled-raft foundation.

Section 3.7.3 – Thermal expansion coefficient
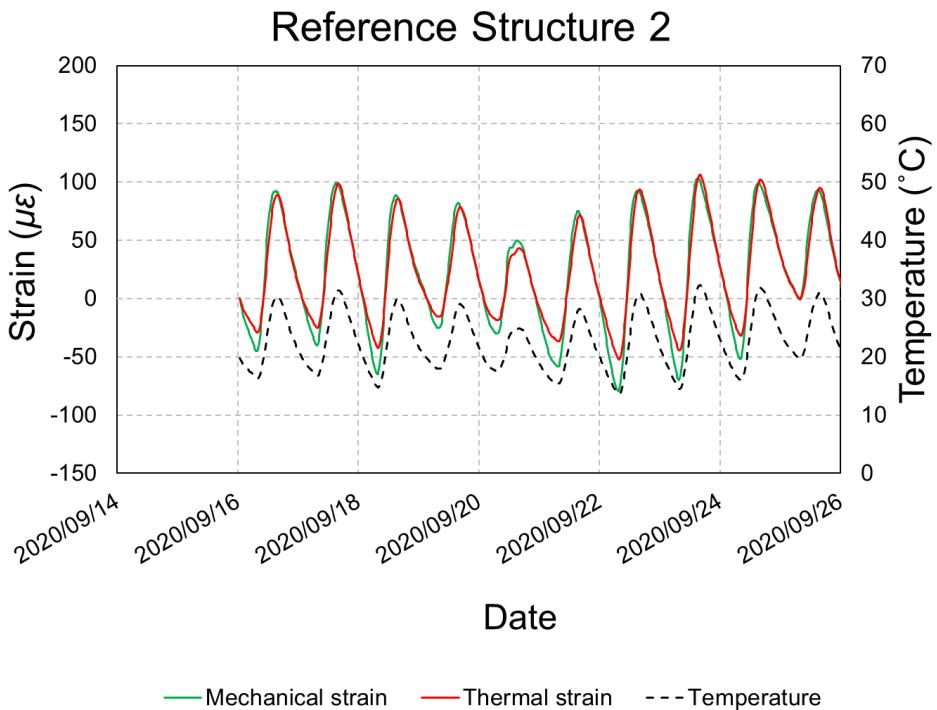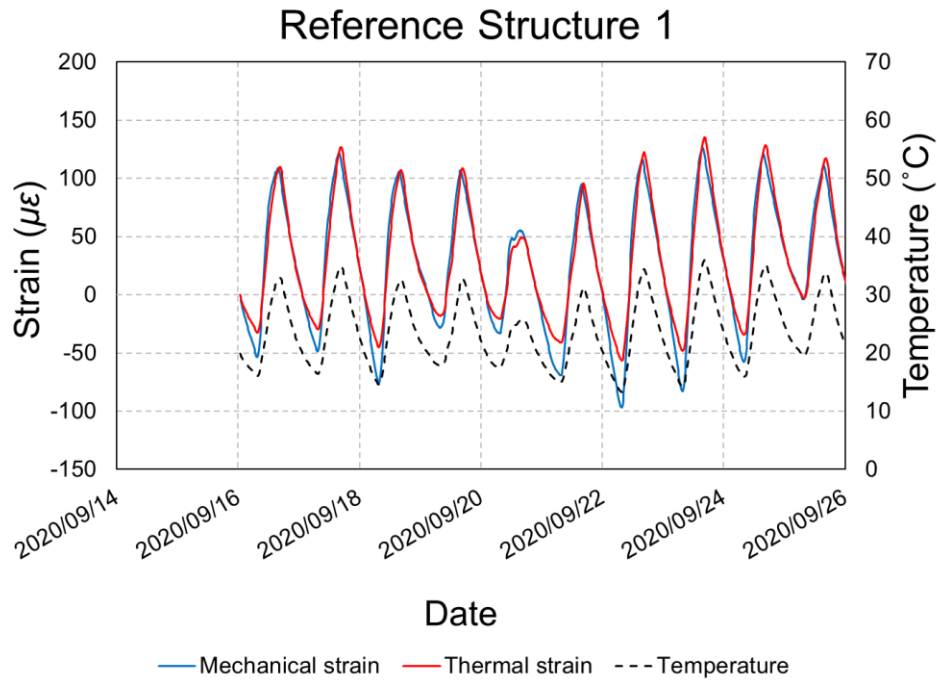
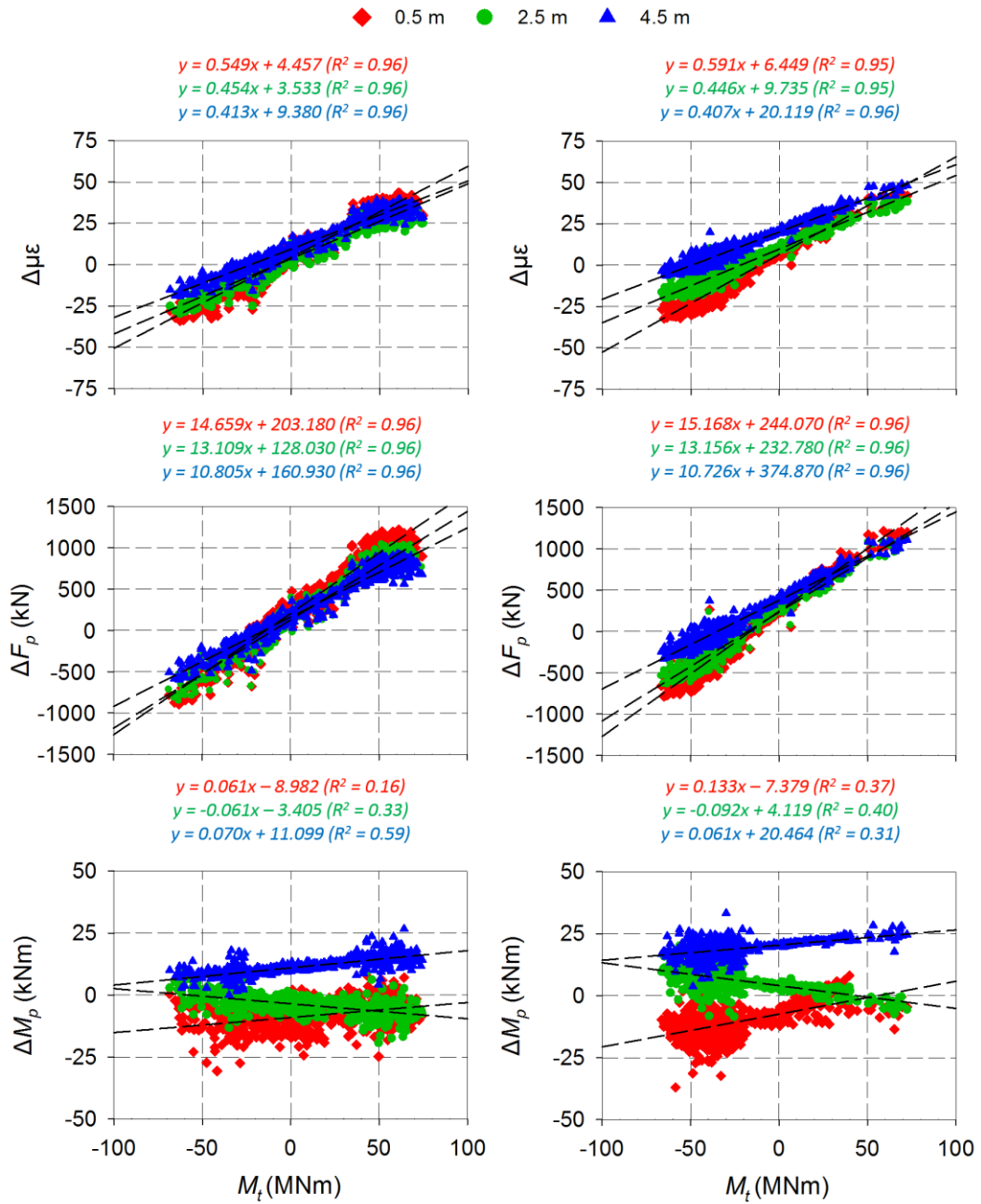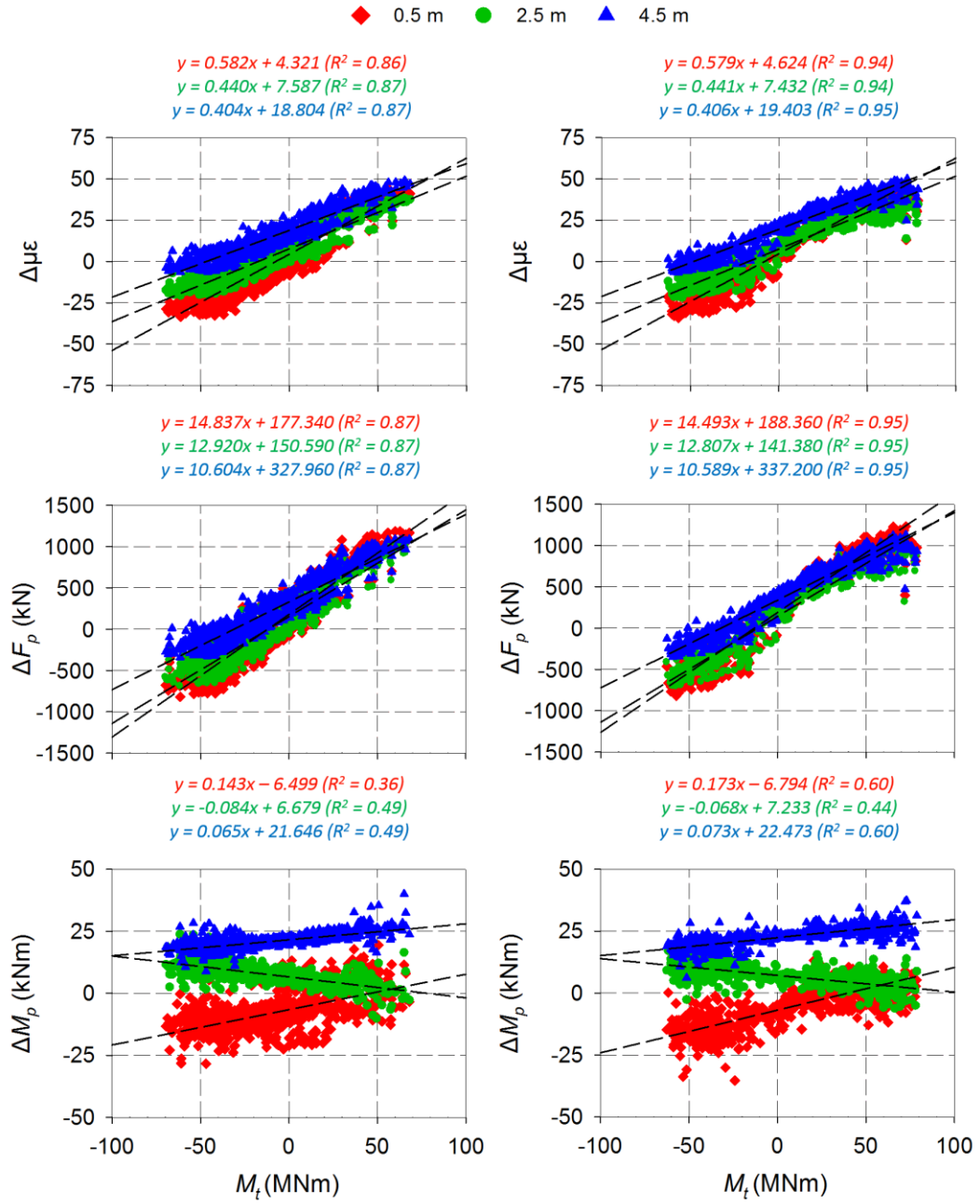**Section 3.9.3 – Commercial operation after commissioning**

July 2021

August 2021

September 2021

February 2022

March 2021

April 2022